ANALYSIS OF MODE MATCHED GYROSCOPES

A Dissertation

by

Hakan Çetin

Submitted to the
Graduate School of Sciences and Engineering
In Partial Fulfillment of the Requirements for
the Degree of

Doctor of Philosophy

in the
Department of Electrical and Electronics Engineering

Özyeğin University
June 2021

Copyright © 2021 by Hakan Çetin

ANALYSIS OF MODE MATCHED GYROSCOPES

Advisor: Asst. Prof. Polat Şendur
Co-Advisor: Dr. Göksen Göksenin Yaralıoğlu

Approved by:

Asst. Prof. Polat Şendur, Advisor
Department of Mechanical Engineering
Özyeğin University

Assoc. Prof. Ayhan Bozkurt
Faculty of Engineering and Natural Sciences
Sabancı University

Assoc. Prof. Cenk Demiroğlu
Department of Electrical and Electronics Engineering
Özyeğin University

Asst. Prof. Birkan Tunç
Department of Mechanical Engineering
Yeditepe University

Date Approved:

Asst. Prof. Özgür Ertunç
Department of Mechanical Engineering
Özyeğin University

To my love Jülide

ABSTRACT

The aim of this thesis is to characterize the mode matched vibratory gyroscopes in terms of noise and stability. Furthermore, the mode matched wave coupling in rotating rod systems due to the Coriolis Effect is explored in order to provide a basis for novel gyroscope structures. This thesis is composed of two parts. In the first part, the noise analysis of the mode matched vibratory gyroscope is discussed with emphasis on MEMS gyroscope. MEMS (Micro-electromechanical System) vibratory gyroscopes have attracted a lot of interest recently and these gyroscopes made their way through portable devices and smart phones. However, their performance is not enough to cope with the demanding requirements of applications such as dead reckoning. Mode-matched gyroscopes are considered to be a solution for this problem. Various mode-matched gyroscope architectures have been proposed and their noise performances have been analyzed in the literature. However, in most of these analyses zero-rate output was considered and the noise analysis for dynamic cases were ignored. In the first part, we demonstrate the noise analysis of mode-matched vibratory gyroscope using the power spectral density (PSD) and the Allan deviation methods while non-zero rate is applied to the gyroscope. We show that for mode-matched gyros the noise performance of a rotating gyro can be significantly different from that of a gyro that does not experience any rotation. We also show that this difference is due to the coupling between the drive and sense systems via Coriolis force. This sets a fundamental limit for the noise performance of mode-matched vibratory gyroscopes where ARW (Angle Random Walk) increases proportionally with the rotation rate for the open loop and the force to rebalance operation modes.

In the second part, vibration analysis of rods that are subjected to rotation is

presented. It is shown that flexural-flexural, longitudinal-flexural and torsional-flexural wave coupling occur due to the Coriolis Effect. First, we carried out our analysis for thin rods where the wavelength is much larger than the radius. It is shown that the wavenumbers change due to the Coriolis Effect. Then, we characterize the 3-D wave propagation in rotating rods by using the Finite Element Method (FEM) in order to determine the corresponding wavenumber shifts for each type of wave. We show that for different drive frequency (ω_0) and rotation rate (Ω), wave couplings exhibit different characteristics. For flexural-flexural wave coupling, the wavenumber increases for the primary flexural wave whereas the wave number decreases for the coupled flexural wave where $\Omega < \omega_0$. For the Coriolis coupling between flexural-longitudinal waves, the wavenumber increases for the flexural wave and decreases for the longitudinal wave where $\Omega < \omega_0$. For the Coriolis coupling between flexural-torsional waves, the wavenumber increases for both flexural and torsional waves. Based on the several case studies, it is found that the sizes of the rod structures are not suitable enough for the sensor applications, except for the case of flexural-flexural wave coupling. Thus, the flexural wave that couples with its conjugate flexural mode can be used to measure the rotation rate applied about the direction of propagation, where the gyro structure can be miniaturized in small scales by the MEMS technology. Based on this observation, we proposed a novel cylindrical rod gyroscope using the coupled flexural-flexural wave propagation. The new gyroscope will consist of a straight circular rod waveguide and piezoelectric transducers; one of which will excite the flexural wave from one end of the rod and the other will receive the corresponding signal. When the waveguide is subjected to a rotational motion, due to the Coriolis force the flexural wave is modulated by its conjugate flexural mode. This causes phase change in the transmitted signal and the relative phase change will increase in proportional to the angular velocity of the waveguide. In other words, by measuring the phase difference in the modulated signal, one can monitor the rate of rotational motion.

Keywords: Coriolis force; Rotation; MEMS vibratory gyroscopes; Mode matched gyroscopes; Noise analysis; Stability of vibratory gyroscopes; Power spectral density; Allan deviation; Cylindrical rod; Coriolis coupling; Elastic waves; Wavenumber shift.

ÖZETÇE

Bu tezin amacı eşlenik modlu titreşimli jiroskopları gürültü ve stabilite açısından karakterize etmektir. Ayrıca, yeni jiroskop yapıları için bir temel sağlamak amacıyla Coriolis etkisine bağlı olarak dönen çubuk sistemlerinde eşlenik modlu dalga etkileşimi (wave coupling) araştırılmıştır. Bu tez iki bölümden oluşmaktadır. İlk bölümde, eşlenik modlu titreşimli jiroskopun gürültü analizi MEMS jiroskop vurgulanarak tartışılmıştır. MEMS (Mikro-elektromekanik Sistem) titreşimli jiroskopları son zamanlarda çok ilgi görmüştür ve bu jiroskoplar taşınabilir cihazlar ve akıllı telefonlar aracılığıyla kendilerine yer bulmuştur. Ancak, performansları kaba kompas hesabı gibi uygulamaların zorlu gereksinimlerini karşılamak için yeterli değildir. Eşlenik modlu jiroskopların bu soruna bir çözüm olduğu düşünülmektedir. Çeşitli eşlenik modlu jiroskop mimarileri önerilmiş ve literatürde gürültü performansları analiz edilmiştir. Bununla birlikte, bu analizlerin çoğunda statik durumlar dikkate alınmış ve dinamik durumlar için gürültü analizi göz ardı edilmiştir. İlk bölümde, spektral güç yoğunluğu (Powet Spectral Density) ve Allan sapma yöntemlerini kullanarak eşlenik modlu titreşimli jiroskopun gürültü analizini dinamik durumlar için gösteriyoruz. Eşlenik modlu jiroskoplar için dönen bir jiroskopun gürültü performansının herhangi bir dönüş yaşamayan bir jiroskopunkinden önemli ölçüde farklı olabileceğini gösteriyoruz. Ayrıca bu farkın Coriolis kuvveti aracılığıyla sürücü ve algılama sistemleri arasındaki bağlantıdan kaynaklandığını da gösteriyoruz. Bu eşlenik modlu titreşimli jiroskopların gürültü performansı için temel bir sınır belirler; açı rastgele yürüme (Angle Random Walk) açık döngü ve yeniden dengeleme kapalı döngü çalışma modları için dönüş hızı ile orantılı olarak artar.

İkinci bölümde dönmeye tabi tutulan çubukların titreşim analizi sunulmuştur. Bükülme-bükülme (flexural-flexural), uzunlamasına-bükülme (longitudinal-flexural)

ve burulma-bükülme (torsional-flexural) dalga etkileşimleri Coriolis etkisine bağlı olarak ortaya çıktığı gösterilmiştir. İlk olarak, dalga boyunun yarıçaptan çok daha büyük olduğu ince çubuklar için analizimizi gerçekleştirdik. Coriolis etkisine bağlı olarak dalga sayılarının (wavenumber) değiştiği gösterilmiştir. Ardından, her bir dalga türü için karşılık gelen dalga sayısı kaymalarını belirlemek için Sonlu Elemanlar Yöntemi (Finite Element Method) kullanarak dönen çubuklardaki 3-D dalga yayılımını karakterize ettik. Farklı sürücü frekansı (ω_0) ve dönüş hızı (Ω) için dalga etkileşimlerinin farklı özellikler sergilediğini gösteriyoruz. Bükülme-bükülme dalga etkileşimi için, dalga sayısı birincil bükülme dalgası için artar, buna karşılık dalga sayısı ikincil bükülme dalgası için azalır ($\Omega < \omega_0$). Bükülme-uzunlamasına dalgalar arasındaki Coriolis etkileşimi için dalga sayısı bükülme dalgası için artar ve uzunlamasına dalga için azalır ($\Omega < \omega_0$). Bükülme-burulma dalgaları arasındaki Coriolis etkileşimi için dalga sayısı hem bükülme hem de burulma dalgaları için artar. Birkaç vaka incelemesine dayanarak çubuk yapılarının boyutlarının bükülme-bükülme dalga etkileşimi durumu dışında sensör uygulamaları için yeterince uygun olmadığı bulunmuştur. Bu nedenle, eşlenik bükülme modu ile etkileşen bükülme dalgası yayılma yönü etrafında uygulanan dönme oranını ölçmek için kullanılabilir ve bu durumda jiroskop yapısı MEMS teknolojisi ile küçük ölçeklerde minyatürleştirilebilir. Bu gözleme dayanarak, etkileşen bükülme-bükülme dalga yayılımını kullanan yeni bir silindirik çubuk jiroskop önerdik. Yeni jiroskop düz dairesel çubuk dalga kılavuzu ve piezoelektrik dönüştürücülerden oluşacak; bunlardan biri çubuğun bir ucundan bükülme dalgasını uyaracak ve diğeri karşılık gelen sinyali alacaktır. Dalga kılavuzu Coriolis kuvveti nedeniyle bir dönme hareketine maruz kaldığında, bükülme dalgası eşlenik bükülme modu tarafından modüle edilir. Bu iletilen sinyalde faz değişikliğine neden olur ve göreceli faz değişikliği dalga kılavuzunun açısal hızıyla orantılı olarak artacaktır. Diğer bir deyişle, modüle edilmiş sinyaldeki faz farkı ölçülerek dönme hareketinin hızı izlenebilir.

Anahtar Kelimeler: Coriolis kuvveti; Rotasyon; MEMS titreşimli jiroskoplar; Eşlenik modlu jiroskoplar; Gürültü analizi; Titreşimli jiroskopların stabilitesi; Spektral güç yoğunluğu; Allan sapması; Silindirik çubuk; Coriolis etkileşi; Elastik dalgalar; Dalga numarası kayması.

ACKNOWLEDGEMENTS

For the last five years, I have had the privilege and honor of working with Dr. G. Goksenin Yaralıoğlu, my research advisor. I have learned so much from his impressive technical knowledge, his research philosophy, and his incredible humility, generosity, and kindness. I thank him for patiently listening to me whether the subject matter was technical or not and sharing his insight. I consider myself extremely lucky to have known such a technical pioneer and a wonderful person. I am also deeply grateful to Dr. Polat Şendur for providing invaluable guidance through the final year of my Ph.D..

I would like to thank my peer, Erkan Kemal, in the OzU MEMS Group for his valuable friendship. We have shared a lot of memorable moments and worked night and day for the last five years.

Special thanks to my family for their invaluable supports. I am so grateful for their encouragements and sacrifices during my educational life. Lastly, most special thanks to my fiancé, Jülide Arıkan. I am so lucky to have such a special person in my life. For the last five years, I have been so grateful to know that she always stands beside me with all her support when I needed in the most difficult times including the pandemic period. Without her invaluable support and sacrifices, it would be impossible for me to complete my study.

This research was done in the MEMS Laboratory at Ozyegin University; supported by the Scientific and Technical Research Council of Turkey (TÜBİTAK) under Grant No. 114E592.

TABLE OF CONTENTS

DEDICATION . . . . . **iii**

ABSTRACT . . . . . **iv**

ÖZETÇE . . . . . **vii**

ACKNOWLEDGEMENTS . . . . . **x**

LIST OF TABLES . . . . . **xiii**

LIST OF FIGURES . . . . . **xiv**

I INTRODUCTION **1**

1.1 MEMS Vibratory Gyroscopes 3

1.2 Applications of MEMS Gyroscopes 8

1.3 Performance Specifications of Gyroscopes 9

1.4 The Robustness Challenge 10

1.5 Thesis Contribution 12

II BACKGROUND **13**

2.1 Micromachined Vibratory Gyroscopes 13

2.1.1 Coriolis Effect 13

2.1.2 Basic Modelling of Vibratory Gyroscopes 15

2.1.3 Mode Matching 18

2.1.4 Mode Matched Vibratory Rate Gyroscopes 23

2.1.5 Operation Modes of the Sense System 35

2.1.6 Mode Matched Vibratory Rate Integrating Gyroscopes . . . 41

2.2 Waveguide Based Gyroscopes 49

2.2.1 Wave Propagation In Elastic Solids 49

2.2.2 Coriolis Effect On Propagating Waves 49

2.2.3 Elastic Wave Based Gyroscopes 52

2.2.4 SAW Based MEMS Gyroscopes 54

III NOISE ANALYSIS OF MODE MATCHED VIBRATORY GYROSCOPES **59**

3.1 Vibratory Gyroscopes System Model 62

3.1.1 Dynamic Model of Vibratory Gyroscopes 62
3.1.2 MATLAB Simulink Model of Vibratory Gyroscopes 66
3.2 Allan Variance 71
3.3 Simulation and Results 73
3.3.1 Open Loop Operation Mode 73
3.3.2 Force to Rebalance Operation Mode 76
3.4 Application of the Model 80
3.5 Discussion 86
IV CORIOLIS EFFECT ON PROPAGATING WAVES IN RODS 87
4.1 Theory 90
4.1.1 Waveguide modes of solid cylindrical rods 90
4.1.2 Governing Equations 92
4.1.3 Elastic waves in rotating rods 95
4.2 Materials and Methods 103
4.2.1 Numerical Methods 103
4.2.2 Numerical Examples of Coupled Elastic Waves 105
4.3 Results 106
4.3.1 Example 1: Flexural wave - Flexural wave Coupling 107
4.3.2 Example 2: Longitudinal wave - Flexural wave Coupling . . 113
4.3.3 Example 3: Torsional wave - Flexural wave Coupling 121
4.4 A Novel Cylindrical Rod Gyroscope Using Coupled Flexural-Flexural Wave Propagation 130
4.5 Discussion 133
V CONCLUSION AND FUTURE WORK 134
REFERENCES 136
VITA 152

LIST OF TABLES

1 Performance requirements for different classes of gyroscopes [24]. . . 10

2 Vibratory rate gyroscopes studied between 1991 and 2002. Gray colored rows represent the mode matched gyro systems and white colored rows represent the split mode gyro systems. 24

3 Vibratory rate gyroscopes studied between 2003 and 2021. Gray colored rows represent the mode matched gyro systems and white colored rows represent the split mode gyro systems. 25

4 Mode matched vibratory rate integrating gyroscopes. 45

5 The mode matched vibratory gyroscope parameters. 63

6 MATLAB Simulink model parameters. 70

7 The mode matched vibratory gyroscope parameters of the experiment presented in [16]. 81

8 MATLAB Simulink model parameters for gyro system presented in [16]. 84

9 Design parameters for a cylindrical aluminum rod with the radius of r. 102

10 Example 1: Flexural wave - Flexural wave Coupling. 107

11 Example 2: Longitudinal wave - Flexural wave Coupling. 113

12 Example 3: Torsional wave - Flexural wave Coupling. 121

LIST OF FIGURES

1 Lumped-mass systems; **(a)** linear vibratory gyroscope [10], and **(b)** torsional vibratory gyroscope [22]. 4

2 Mode matched vibratory gyroscope architectures; **(a)** lumped-mass system, **(b)** tuning fork system, **(c)** torsional vibratory/gimbal system, **(d)** ring/disk system and **(e)** hemispherical shell/wineglass system. 6

3 Representation of the position vector relative to the inertial reference frame (Frame A) and the rotating reference frame (Frame B). 14

4 **(a)** Mass-spring-damper system of the 2-DOF vibratory gyroscope, where the rotation axis is going through the point mass, and **(b)** the steady-state response of vibratory rate gyroscopes for various input rates. 16

5 Bode diagram of the transfer function given in Eq. (2.16). **(a)** The mechanical output is modest when $\omega_x < \omega_y$. **(b)** The mechanical output reaches its maximum when $\omega_x = \omega_y$. **(c)** The mechanical output is low when $\omega_x > \omega_y$. 20

6 **(a)** Configuration of the frequency tuning electrodes, and **(b)** frequency tuning characteristics of the drive and sense modes as a function of voltage. 21

7 Mode matched vibratory rate gyroscope examples; **(a)** lumped-mass system [42], **(b)** tuning fork system [43, 15], **(c)** torsional vibratory/gimbal system [44], **(d)** ring/disk system [25] and **(e)** hemispherical shell/wineglass system [45]. 26

8 Block diagram of **(a)** the drive mode oscillation control with the open loop operation mode, and **(b)** the drive mode oscillation control with force to rebalance operation mode. 37

9 Block diagram of **(a)** vibratory gyroscope box, phase locked loop (PLL) box, and **(b)** quadrature box and force to rebalance (FTR) box. 38

10 **(a)** Orbital trajectory of a proof-mass motion in response to the rotation rate Ω_z in x–y plane, where the amplitude of the proof-mass motion, the quadrature of the proof-mass motion, the inclination angle, the vibration frequency and the phase are denoted as a, q, θ, ω and ϕ respectively, and **(b)** the steady-state response of vibratory rate integrating gyroscopes. 40

11 Mode matched vibratory rate integrating gyroscope examples; **(a)** lumped-mass system [101], **(b)** tuning fork system [91], **(c)** ring and disk systems [98], **(d)** cylindrical shell system [92] and **(e)** wineglass system [96]. 47

12 Particle motions of **(a)** the dilatational wave and **(b)** the shear wave. 50

13 (a) Surface wave in a semi-infinite solid; (b) u_z vs. z at the surface; (c) u_y vs. z at the surface; (d) variation of particle displacement with depth [120]. 55

14 Piezoelectric substrate with IDTs [124]. 56

15 SAW based gyroscope [128]. 57

16 Block diagram of the drive mode oscillation control with the open loop operation mode. 68

17 Block diagram of the drive mode oscillation control with the force to rebalance operation mode. 68

18 Block diagram of the vibratory gyroscope box. 69

19 Block diagram of the phase locked loop (PLL) box. 69

20 Block diagram of the force to rebalance (FTR) box. 69

21 Allan variance analysis of gyroscope output. 72

22 Frequency response of the mode matched vibratory gyroscope for the open loop operation mode where 0 dB = 1 $(^\circ/\text{hr})^2/\text{Hz}$. 74

23 Normalized scale factor K_{SF} as a function of input rate for the open loop operation mode. 74

24 Allan deviation of the mode matched vibratory gyroscope for the open loop operation mode. 75

25 Frequency response of the mode matched vibratory gyroscope for the force to rebalance operation mode where 0 dB = 1 $(^\circ/\text{hr})^2/\text{Hz}$. . 77

26 Allan deviation of the mode matched vibratory gyroscope for the force to rebalance operation mode. 77

27 Frequency response of the mode matched vibratory gyroscope for $\Omega_z = 50$ rad/s with and without the Coriolis effect where 0 dB = 1 $(^\circ/\text{hr})^2/\text{Hz}$. 78

28 Allan deviation of the mode matched vibratory gyroscope for $\Omega_z = 50$ rad/s with and without the Coriolis Effect. 78

29 Linearity of the mode matched vibratory gyroscope. 79

30 Angle random walk of the mode matched vibratory gyroscope. . . . 80

31 Frequency response of the mode matched vibratory gyroscope model of the experiment for both open loop and force to rebalance operation modes where $\Omega_z = 0$ rad/s and 0 dB = 1 $(^\circ/\text{hr})^2/\text{Hz}$. 82

32 Allan deviation of the mode matched vibratory gyroscope model of the experiment for the force to rebalance operation mode where $\Omega_z = 0$ rad/s. 82

33 Frequency shift of the drive and sense modes for the mode matched vibratory gyroscope model of the experiment where $\Omega_z \neq 0$ rad/s. . 83

34 Frequency response of the mode matched vibratory gyroscope model of the experiment for the force to rebalance operation mode where 0 dB = 1 $(^\circ/\text{hr})^2/\text{Hz}$. 85

35 Allan deviation of the mode matched vibratory gyroscope model of the experiment for the force to rebalance operation mode. 85

36 Fundamental modes in a cylindrical waveguide. 90

37 Dispersion curves for a 1 mm thick aluminum cylindrical rod. . . . 91

38 A thin rod with linear displacements u, v and angular displacements θ, ψ where the differential element of rod subjected to **(a)** various transverse loads, **(b)** longitudinal load, and **(c)** torsional load. . . . 93

39 **(a)** Flexural wave-flexural wave coupling between primary flexural wave (F1) and secondary flexural wave (F2), **(b)** flexural wave-longitudinal wave coupling between flexural wave (F2) and longitudinal wave (L1), and **(c)** flexural wave-torsionl wave coupling between flexural wave (F2) and torsional wave (T1). 96

40 **(a)** Finite element model of the cylindrical rod, **(b)** y-displacement at the top y-nodes of cylindrical aluminum rod along the x-axis for loss factor $\beta = 3 \times 10^{-3}$, and **(c)** for loss factor $\beta = 3 \times 10^{-5}$. . . . 104

41 For the cylindrical aluminum rod induced by the constant rotation (Ω_x) in Example 1, **(a)** wavenumbers of F1 and F2 calculated from Eq.(4.14) and the ANSYS results, **(b)** wavenumber, amplitude and phase calculations of the numerical result by fitting the sinusoidal wave of $B\cos(kx - \Phi)$ to the real part of the y-displacement (same blue curve as in Fig.40c). 107

42 For $\Omega_x = 2\pi 100$ rad/s in Example 1, the displacement at the top y-nodes of lossless cylindrical aluminum rod along the x axis **(a)** in the y direction, **(b)** in the z direction, and **(c)** wavenumber, amplitude and phase calculations of the numerical result by fitting the sinusoidal wave of $B_{F1}\cos(k_{F1}x - \Phi_{F1}) + B_{F2}\cos(k_{F2}x - \Phi_{F2})$ to the real part of the y-displacement (same blue curve as in Fig.42a)). The length of lossy aluminum part equals to $60\lambda_{F0}$ with loss factor $\beta = 10^{-5}$. 109

43 For $\Omega_x = 2\pi 500$ rad/s in Example 1, the displacement at the top y-nodes of lossless cylindrical aluminum rod along the x axis **(a)** in the y direction, **(b)** in the z direction, and **(c)** wavenumber, amplitude and phase calculations of the numerical result by fitting the sinusoidal wave of $B_{F1}\cos(k_{F1}x - \Phi_{F1}) + B_{F2}\cos(k_{F2}x - \Phi_{F2})$ to the real part of the y-displacement (same blue curve as in Fig.43a)). The length of lossy aluminum part equals to $60\lambda_{F0}$ with loss factor $\beta = 2 \times 10^{-5}$. 110

44 For $\Omega_x = 2\pi 1100$ rad/s in Example 1, the displacement at the top y-nodes of lossless cylindrical aluminum rod along the x axis **(a)** in the y direction, **(b)** in the z direction, and **(c)** wavenumber, amplitude and phase calculations of the numerical result by fitting the sinusoidal wave of $B_{F1}\cos(k_{F1}x - \Phi_{F1}) + B_{F2}\cos(k_{F2}x - \Phi_{F2})$ to the real part of the y-displacement (same blue curve as in Fig.44a)). The length of lossy aluminum part equals to $60\lambda_{F0}$ with loss factor $\beta = 3 \times 10^{-5}$. 111

45 For the cylindrical aluminum rod induced by the constant rotation (Ω_y) in Example 2, the wavenumbers of F2 and L1 calculated from Eq.(4.25) and the ANSYS results. 113

46 For $\Omega_y = 0$ in Example 2, the displacement at the top z-nodes of lossless cylindrical aluminum rod along the x axis **(a)** in the z direction for Case 1, **(b)** in the x direction for Case 2, **(c)** wavenumber, amplitude and phase calculations of the numerical result by fitting the sinusoidal wave of $B\cos(kx - \Phi)$ to the real part of the z-displacement (same blue curve as in Fig.46a), and **(d)** to the real part of the x-displacement (same blue curve as in Fig.46b). The length of lossy aluminum part equals to $6\lambda_{L0}$ with loss factor $\beta = 2 \times 10^{-3}$. 115

47 For $\Omega_y = 2\pi 5$ rad/s in Case 1 of Example 2, the displacement at the top z-nodes of lossless cylindrical aluminum rod along the x axis **(a)** in the z direction, **(b)** in the x direction, **(c)** wavenumber, amplitude and phase calculations of the numerical result by fitting the sinusoidal wave of $B_{F2}\cos(k_{F2}x - \Phi_{F2}) + B_{L1}\cos(k_{L1}x - \Phi_{L1})$ to the real part of the z-displacement (same blue curve as in Fig.47a), and **(d)** to the real part of the x-displacement (same blue curve as in Fig.47b). The length of lossy aluminum part equals to $6\lambda_{L0}$ with loss factor $\beta = 4 \times 10^{-3}$. 116

48 For $\Omega_y = 2\pi 12.5$ rad/s in Case 1 of Example 2, the displacement at the top z-nodes of lossless cylindrical aluminum rod along the x axis **(a)** in the z direction, **(b)** in the x direction, **(c)** wavenumber, amplitude and phase calculations of the numerical result by fitting the sinusoidal wave of $B_{F2}\cos(k_{F2}x - \Phi_{F2}) + B_{L1}\cos(k_{L1}x - \Phi_{L1})$ to the real part of the z-displacement (same blue curve as in Fig.48a), and **(d)** to the real part of the x-displacement (same blue curve as in Fig.48b). The length of lossy aluminum part equals to $6\lambda_{L0}$ with loss factor $\beta = 2 \times 10^{-3}$. 118

49 For $\Omega_y = 2\pi 5$ rad/s in Case 2 of Example 2, the displacement at the top z-nodes of lossless cylindrical aluminum rod along the x axis **(a)** in the z direction, **(b)** in the x direction, **(c)** wavenumber, amplitude and phase calculations of the numerical result by fitting the sinusoidal wave of $B_{L1}\cos(k_{L1}x - \Phi_{L1}) + B_{F2}\cos(k_{F2}x - \Phi_{F2})$ to the real part of the z-displacement (same blue curve as in Fig.49a), and **(d)** to the real part of the x-displacement (same blue curve as in Fig.49b). The length of lossy aluminum part equals to $6\lambda_{L0}$ with loss factor $\beta = 4 \times 10^{-3}$. 119

50 For $\Omega_y = 2\pi 12.5$ rad/s in Case 2 of Example 2, the displacement at the top z-nodes of lossless cylindrical aluminum rod along the x axis **(a)** in the z direction, **(b)** in the x direction, **(c)** wavenumber, amplitude and phase calculations of the numerical result by fitting the sinusoidal wave of $B_{L1}\cos(k_{L1}x - \Phi_{L1}) + B_{F2}\cos(k_{F2}x - \Phi_{F2})$ to the real part of the z-displacement (same blue curve as in Fig.50a), and **(d)** to the real part of the x-displacement (same blue curve as in Fig.50b). The length of lossy aluminum part equals to $6\lambda_{L0}$ with loss factor $\beta = 7 \times 10^{-3}$. 120

51 For the cylindrical aluminum rod induced by the constant rotation (Ω_z) in Example 3, the wavenumbers of F2 and T1 calculated from Eq.(4.32) and the ANSYS results. 123

52 For $\Omega_z = 0$ in Example 3, the displacement at the top z-nodes of lossless cylindrical aluminum rod along the x axis **(a)** in the z direction for Case 1, **(b)** in the y direction for Case 2, **(c)** wavenumber, amplitude and phase calculations of the numerical result by fitting the sinusoidal wave of $B\cos(kx - \Phi)$ to the real part of the z-displacement (same blue curve as in Fig.52a), and **(d)** to the real part of the y-displacement (same blue curve as in Fig.52b). The length of lossy aluminum part equals to $4\lambda_{T0}$ with loss factor $\beta = 4 \times 10^{-3}$. 124

53 For $\Omega_z = 2\pi 5$ rad/s in Case 1 of Example 3, the displacement at the top z-nodes of lossless cylindrical aluminum rod along the x axis **(a)** in the z direction, **(b)** in the y direction, **(c)** wavenumber, amplitude and phase calculations of the numerical result by fitting the sinusoidal wave of $B_{F2}\cos(k_{F2}x - \Phi_{F2}) + B_{T1}\cos(k_{T1}x - \Phi_{T1})$ to the real part of the z-displacement (same blue curve as in Fig.53a), and **(d)** to the real part of the y-displacement (same blue curve as in Fig.53b). The length of lossy aluminum part equals to $4\lambda_{T0}$ with loss factor $\beta = 4 \times 10^{-3}$. 125

54 For $\Omega_z = 2\pi 30$ rad/s in Case 1 of Example 3, the displacement at the top z-nodes of lossless cylindrical aluminum rod along the x axis **(a)** in the z direction, **(b)** in the y direction, **(c)** wavenumber, amplitude and phase calculations of the numerical result by fitting the sinusoidal wave of $B_{F2}\cos(k_{F2}x - \Phi_{F2}) + B_{T1}\cos(k_{T1}x - \Phi_{T1})$ to the real part of the z-displacement (same blue curve as in Fig.54a), and **(d)** to the real part of the y-displacement (same blue curve as in Fig.54b). The length of lossy aluminum part equals to $4\lambda_{T0}$ with loss factor $\beta = 2 \times 10^{-3}$. 126

55 For $\Omega_z = 2\pi 5$ rad/s in Case 2 of Example 3, the displacement at the top z-nodes of lossless cylindrical aluminum rod along the x axis **(a)** in the z direction, **(b)** in the y direction, **(c)** wavenumber, amplitude and phase calculations of the numerical result by fitting the sinusoidal wave of $B_{T1}\cos(k_{T1}x - \Phi_{T1}) + B_{F2}\cos(k_{F2}x - \Phi_{F2})$ to the real part of the z-displacement (same blue curve as in Fig.55a), and **(d)** to the real part of the y-displacement (same blue curve as in Fig.55b). The length of lossy aluminum part equals to $4\lambda_{T0}$ with loss factor $\beta = 4 \times 10^{-3}$. 127

56 For $\Omega_z = 2\pi 30$ rad/s in Case 2 of Example 3, the displacement at the top z-nodes of lossless cylindrical aluminum rod along the x axis **(a)** in the z direction, **(b)** in the y direction, **(c)** wavenumber, amplitude and phase calculations of the numerical result by fitting the sinusoidal wave of $B_{T1}\cos(k_{T1}x - \Phi_{T1}) + B_{F2}\cos(k_{F2}x - \Phi_{F2})$ to the real part of the z-displacement (same blue curve as in Fig.56a), and **(d)** to the real part of the y-displacement (same blue curve as in Fig.56b). The length of lossy aluminum part equals to $4\lambda_{T0}$ with loss factor $\beta = 2 \times 10^{-3}$. 128

57 Novel gyroscope design. 131

58 Heat map of ratio of the phase difference (output) to input rate is calculated for the radii of rod in the range of 1 μm to 1 mm and the operating frequency range of 100 Hz to 100 kHz. Red curve indicates the designs where the rod length is 10 times larger than the wavelength of flexural wave. Below the red curve, the flexural waves in rods have larger wavelengths where 10 wavelengths are larger than the rod length. L equals to 10 cm. 132

CHAPTER I

INTRODUCTION

An inertial sensor used for navigation systems consists of an accelerometer and a gyroscope. In general, the construction of the gyroscope is more difficult and complex than the construction of the accelerometer. A comprehensive review of gyroscopes has been presented in [1, 2]. There are two types of gyroscopes; optical gyroscopes and mechanical gyroscopes. Optical gyroscopes have been reviewed in [3, 4, 5, 6]. In general, highly sensitive optical gyroscopes, including Fiber Optic Gyroscopes (FOGs) and Ring Laser Gyroscopes, have been used in applications such as robotic guidance and inertial navigation for a variety of vehicles, aerospace and military hardware; very demanding high resolution measurements in seismology, geodesy, geophysics and fundamental physics. Optical gyroscopes are relatively bulky and expensive. Mechanical gyroscopes were discovered in the 19th century by Jean-Bernard-Léon Foucault and the first workable gyro compass was developed by H. Anschtz-Kaempfe in 1908. At first, mechanical gyroscopes have been used for the automatic steering in missiles, stabilized bomb sights, and platforms to carry guns in World War II. More recently, these traditional gyroscopes are still used for inertial guidance systems, where they are used by orbital spacecraft and control systems of some satellites [7]. With the advancement of MEMS technology, mechanical gyroscopes have been miniaturized and they become very cost effective. MEMS vibratory gyroscopes have been reviewed in [8, 9]. Various MEMS gyroscope architectures have been proposed and analyzed in detail [10, 11, 12, 13]. More recently, mode matched vibratory gyroscopes have been studied [14, 15, 16].

The first commercial integrated micro-machined gyroscope was emerged in 2002 by the Analog Devices Inc. [17] and then, various micro-machined gyroscope

devices have been released to the market [13]. MEMS (Micro-electromechanical System) vibratory gyroscopes have the advantages of small size, low cost, high precision and easy integration, which make their way to consumer products. The first adapted application was image stabilization for cameras [18]. Later MEMS gyroscopes had been used in gaming and user interfaces. The usage area of MEMS gyroscopes is further expanding to more demanding applications such as automotive, GPS assisted personal navigation (PND) and location-based services (LBS) [19, 20]. However, the stability of the MEMS gyroscopes (Angle random walk: $\sim$ 0.1 deg/$\sqrt{\text{h}}$, Bias stability: $\sim$10 deg/h) is worse than that of optical gyroscopes (Angle random walk: $\sim$0.001 deg/$\sqrt{\text{h}}$, Bias stability: $\sim$1 deg/h). This limits the use of MEMS gyroscopes over against the optical gyroscopes for inertial navigation based applications. On the other hand, mode matched gyroscopes are considered one of the best candidates for more demanding applications. Therefore, many scientists recently have studied on mode matched vibratory gyroscopes that offer higher rate sensitivity, ability to implement whole-angle operation mode, exceptional scale factor stability, and a potential for self-calibration. As a result, the trends in the research and development of MEMS gyroscopes starts to shift from high-volume production of split mode vibratory gyroscopes to high performance mode-matched vibratory gyroscopes. The emerging interest of mode matched vibratory gyroscopes creates a need for careful analyses to improve the performance. However, the mode matched vibratory gyroscopes provides high sensitivity, it also suffer from the coupling between drive and sense modes due to the Coriolis effect while in rotation. The resonance splitting occurs due to the Coriolis coupling and this may deteriorate the stability performance of mode matched gyros [21]. One of the aim of this thesis is to explore the effect of Coriolis coupling on the stability of mode matched vibratory gyroscopes, while in rotation.

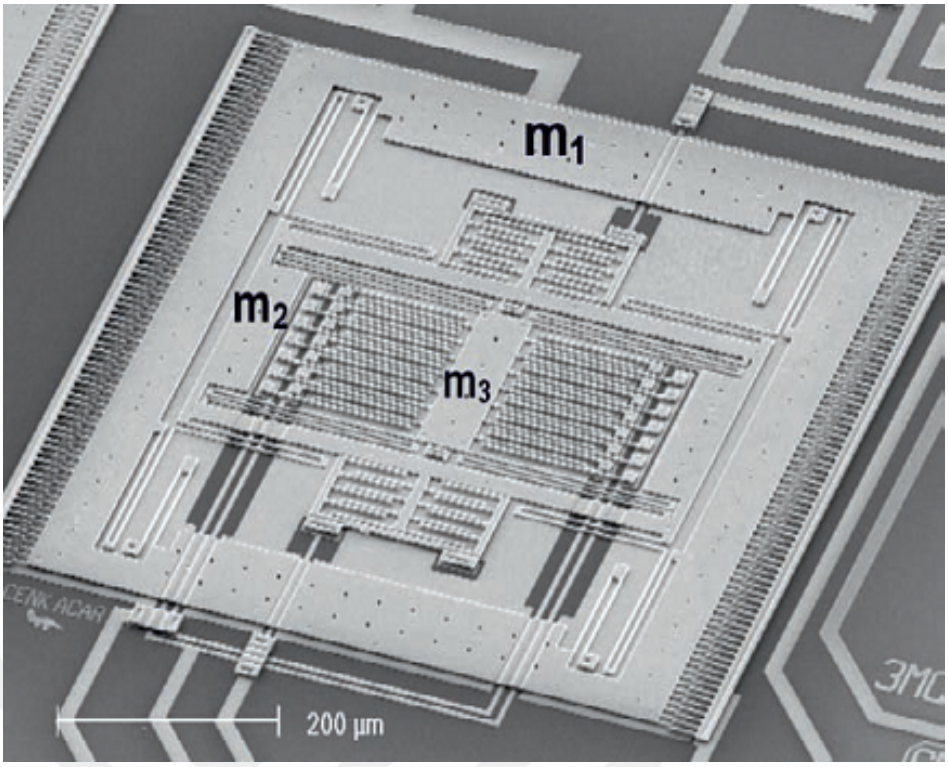
Another aim of this thesis is to discover the design method of a gyroscope that will not only have the potential to reach the stability of the fiber optic gyroscopes

but also compete with MEMS-based gyroscope in respect to size and power consumption. The main reason of using acoustic wave is that these waves have much slower speed compared to the speed of light. A gyroscope can be made by using much smaller waveguides than optical fibers, because speed of the acoustic wave is one million times smaller than the speed of light. Besides piezoelectric transducers consume much less power than laser diodes do. Therefore, one can built more power efficient gyroscopes using acoustic waves.

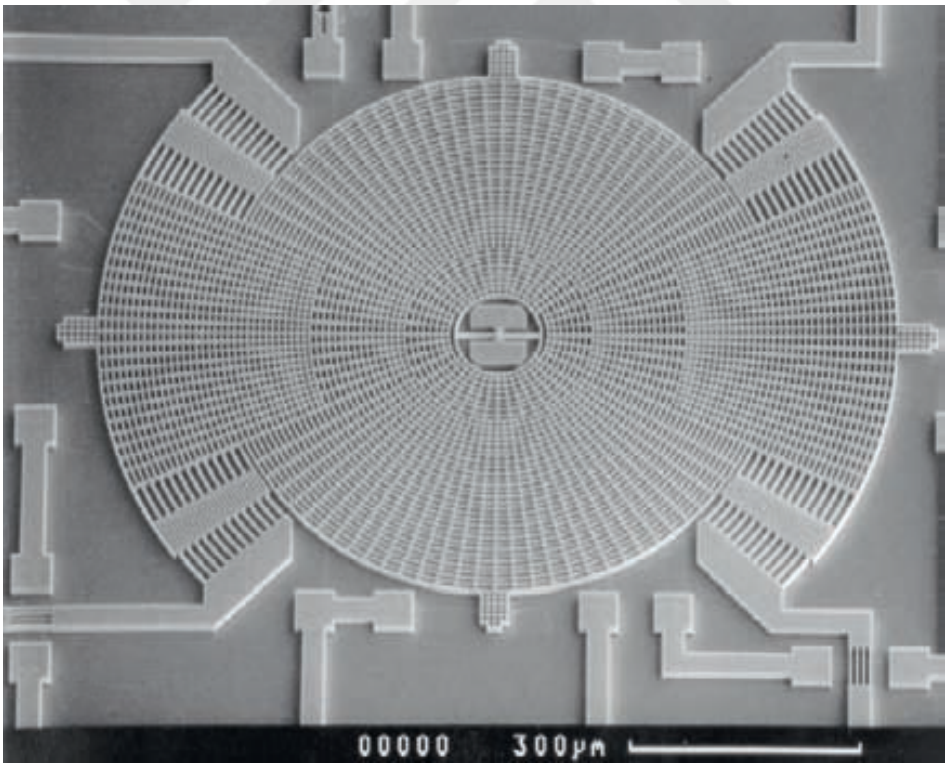
1.1 MEMS Vibratory Gyroscopes

In traditional gyroscopes, rotating parts have been used for a long time, which causes bearing wear and friction problems due to their operation principles. Because of these problems, researchers avoid using rotating parts in MEMS gyroscopes. Moreover, freely rotating parts are nor feasible to build using micromachining techniques. Thus, most of the MEMS gyroscopes in the industry start to utilize the vibrating mechanical elements to sense angular rate instead of the rotating parts. Further, not having any detached moving parts makes the fabrication of gyroscopes easier and suitable for miniaturization by micromachining processes, which leads them to be a competitive alternative. These types of gyroscope are called MEMS vibratory gyroscopes.

A MEMS vibratory gyroscope is composed of two mechanical systems; drive system and sense system. The drive system has a vibratory motion which is coupled to the sense system, as the gyroscope is subjected to a rotational motion. In most of the MEMS gyros, energy transfer is occurred between two modes of the system due to Coriolis acceleration since the drive system excites the first mode. There are two types of MEMS vibratory gyroscopes, which are linear vibratory gyroscope as shown in Fig.1a and torsional vibratory gyroscope as shown in Fig.1b. In the figures, the gyros have drive-mode oscillators that generate constant linear momentum for linear gyros and angular momentum for torsional gyros. The linear or torsional vibration excited by the drive-mode oscillator is



(a)



(b)

Figure 1: Lumped-mass systems; **(a)** linear vibratory gyroscope [10], and **(b)** torsional vibratory gyroscope [22].

coupled with the orthogonal Coriolis force or Coriolis torque due to the applied rotation, respectively. Thus, the angular rotation can be detected by sensing the Coriolis coupling between the drive and sense modes, which is measured by the sense-mode accelerometer.

Typical MEMS 2-DOF (two degree of freedom) vibratory gyroscopes employ proof masses or axi-symmetric architectures such as ring, disk and shell structures coupled by a network of spring system, as shown in Fig.2. The configurations illustrated in Fig.2 will be explained with the examples of previously studied gyroscopes in Section 2.1.4. Further, vibratory gyroscopes can operate in either mode-matched or split-mode. In split-mode, the drive and sense modes have different resonant frequencies, whereas drive and sense modes have the same resonant frequency in the mode matched operation. The resonant frequencies of the gyroscope must be matched to reach an ultimate MEMS gyroscope performance. However, matching the mechanical resonances is generally difficult to implement due to the fabrication restrictions. Typically matching is achieved by using the spring softening effect.The resonant frequency of a mechanical structure vibrating in an E-filed is dependent on the magnitude of the field. Typically the voltage over the sense system is adjusted until the sense resonance is as same as the drive resonance [23]. The mode matching method will be explained further in Section 2.1.3. This method allows increasing the sensitivity by the quality factor of the sense system. Therefore, mode matched vibratory gyroscopes have higher sensitivity and better resolution [24, 25, 26, 27, 28].

The design, modelling and simulation of mode matched vibratory gyroscopes are relatively more complex compared to split mode gyroscopes. However, it is important to develop analytical and numerical models for these gyroscopes to be able to optimize their performance. There are two design configurations for the mode matched operation; vibratory rate gyroscopes and vibratory rate integrating gyroscopes. For the control of vibratory rate gyroscopes, there are two operation modes available such as open loop operation mode and force to re-balance (FTR)

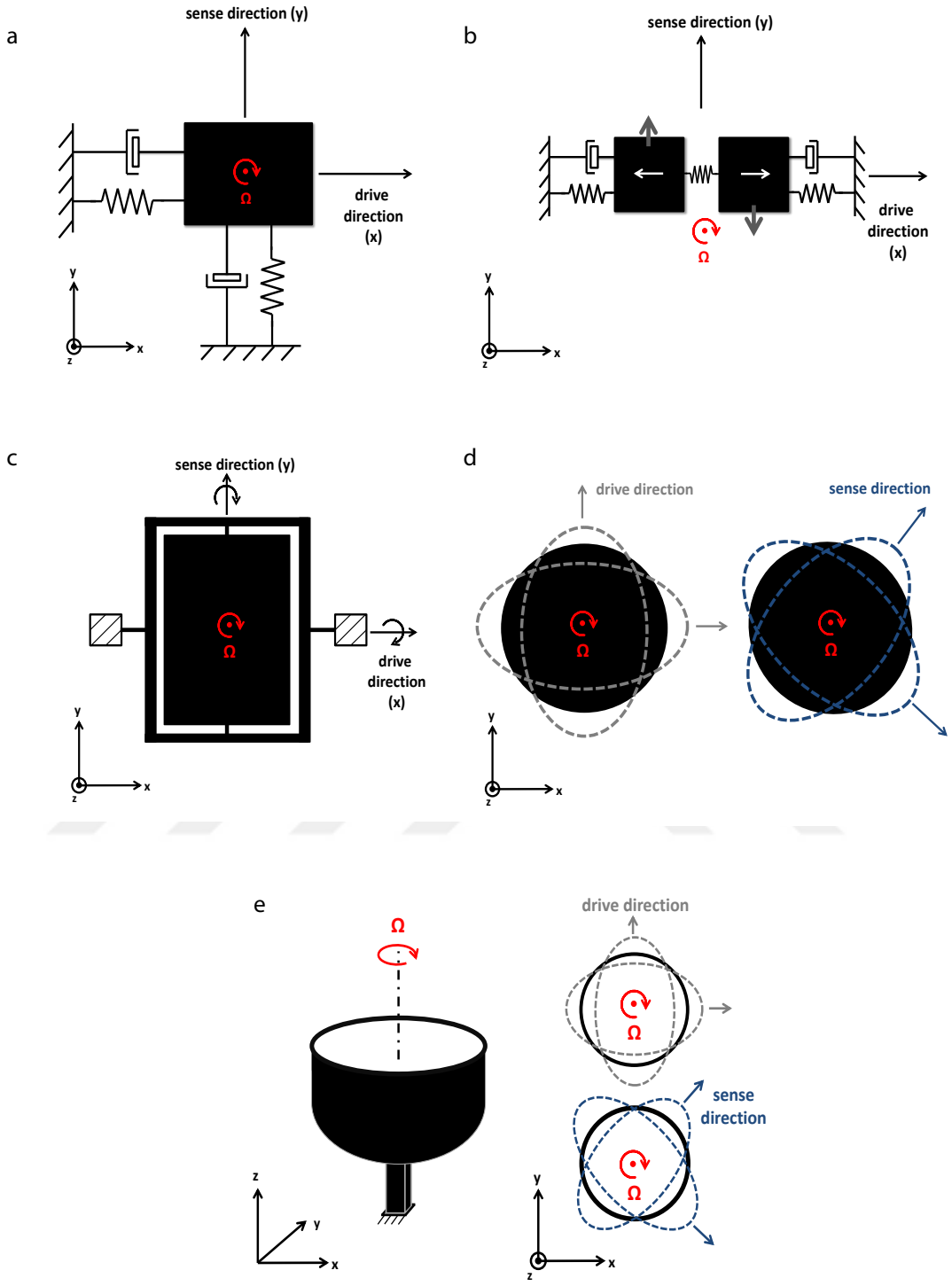


Figure 2: Mode matched vibratory gyroscope architectures; **(a)** lumped-mass system, **(b)** tuning fork system, **(c)** torsional vibratory/gimbal system, **(d)** ring/disk system and **(e)** hemispherical shell/wineglass system.

operation mode. In the open loop operation mode, the control system consists of drive mode oscillator circuit, amplitude gain controller (AGC), phase locked loop (PLL)/demodulation and quadrature cancellation. The drive system oscillates at the resonant frequency in closed loop feedback systems by the drive mode oscillator circuit. The amplitude of drive oscillation is kept constant by the AGC, where the PLL provides the necessary phase shift to keep the drive oscillator in the drive mode resonance. For the sense system, the sense mode output contains two AC signals with strictly 90° phase delay called as quadrature signal and Coriolis signal. The quadrature signal can be separated from Coriolis signal via synchronous demodulation which carries out the process of the demodulation of the sense mode output to calculate the quadrature amplitude and the rate output [29]. Then, the quadrature signal is fed back to the sense system for the quadrature cancellation. As the quadrature signal is cancelled, the rate output is obtained by the demodulation of the sense mode output while the rotation is applied. For the force to re-balance operation mode, the open loop rate output demodulation is modified by a closed-loop control for the sense system [30]. The closed-loop control consists of a PID controller, which controls the corresponding Coriolis signal (control variable) based on the sense mode output (measured process variable) where the desired-point is set to zero. Therefore, the amplitude of sense mode output is fed to the PID controller and output of the PID controller becomes the Coriolis force amplitude, which equals to the rate output. The rate output is converted to an AC signal at drive frequency which is in phase with the actual Coriolis force and then, the AC signal is fed back to the sense system. Due to the force feedback, the sense system does not move. The force to rebalance operation mode provides improved linearity, higher bandwidth and better scale factor stability, whereas it causes increased complexity, higher cost, and higher power consumption. The control systems of vibratory rate gyroscopes will be further discussed in Section 2.1.5.

For the vibratory rate integrating gyroscopes, the whole angle operation mode

is used to measure absolute angles of rotation. In the whole angle operation mode, the mechanical component acts as a mechanical integrator of angular velocity (Ω) [31]. Two modes oscillates freely since the damping of the both drive and sense modes are canceled by the closed loop control system. In the ideal case, the free oscillation of a proof mass system consists of constant straight line trajectory for nonzero initial velocity and in the absence of rotation, damping, and anisoelasticity. As a result, the output of a rotating gyro system equals to $\theta = -\int \Omega dt = -\theta_{actual}$ for an ideal rate integrating gyroscope, where the angle (θ) between two modes equals to the orientation of the drive mode that precesses in time due to the Coriolis Effect (θ_{actual}). In other words, the orientation of precession pattern (θ) becomes a measure of actual rotation measured by the gyroscope (θ_{actual}). The control system of vibratory rate integrating gyroscopes will be discussed in Section 2.1.6.1.

1.2 Applications of MEMS Gyroscopes

MEMS technology enabled the fabrication of miniaturized and low-cost gyroscopes which becomes a feasible alternative to bulky and high-cost conventional inertial sensors. However, the conventional inertial sensors such as fiber-optic gyroscopes, ring laser gyroscopes and rotating wheel gyroscopes provide high-performance, they are usually too expensive and too large for use in most emerging consumer applications. It is enabled to cut costs by miniaturizing the mechanical sensor elements and embedding the electronics on the same silicon chip. Therefore, MEMS vibratory gyroscopes have attracted a lot of interest recently with the development of innovative micro-fabrication processes and have become an attractive solution to market needs. MEMS gyroscopes are finding wide range of applications in aerospace industry, military, automotive and consumer electronics. In automotive, they are being used for vehicle stability control, roll over detection and advanced navigation systems. Consumer electronics applications include gesture recognition for smart phones and tablets, image stabilization for cameras and

camcorders, virtual reality products, inertial pointing devices, and computer gaming industry [18, 32, 33]. These markets are demanding lower cost, smaller size, low power and high performance. Especially, recently emerged applications, devices such as GPS assisted personal navigation (PND) and location-based services (LBS) for cell phones require low noise, high stability and high linearity [19, 20]. Currently, researchers have studied on structural approaches to improve robustness of MEMS vibratory gyroscopes for those emerging consumer applications required more precise sensing.

1.3 Performance Specifications of Gyroscopes

The quality of the gyroscopes is specified by the performance specifications regarding the application areas. The critical performance specifications of the gyroscopes involve resolution (noise floor), angle random walk, bias instability, scale factor, linearity, dynamic range and bandwidth. The definitions of the parameters are presented from IEEE Standard for Inertial Sensor Terminology as below [34]:

Resolution: The largest value of the minimum change in input, for inputs greater than the noise level, that produces a change in output equal to some specified percentage (at least 50%) of the change in output expected using the nominal scale factor.

Angle Random Walk: The angular error buildup with time that is due to white noise in angular rate, typically expressed in $^\circ/\sqrt{\text{hr}}$.

Bias Instability: The random variation in bias as computed over specified finite sample time and averaging time intervals, characterized by a $1/f$ power spectral density, typically expressed in $^\circ$/hr.

Linearity: The property that can be graphically represented as a straight line to show the deviation between the rate output voltage and the desired output voltage in response to the rotation rate.

Scale Factor: The ratio of a change in output to a change in the input intended to be measured, typically specified in V/°/s, and evaluated as the slope

Parameter	Rate Grade	Tactical Grade	Inertial Grade	Unit
Angle Random Walk	>0.5	0.5-0.05	<0.001	$^\circ/\sqrt{\text{hr}}$
Bias Instability	10-1000	0.1-10	<0.01	$^\circ$/hr
Scale Factor Linearity	0.1-1	0.01-0.1	<0.001	%
Dynamic Range	50-10000	>500	>400	$^\circ$/sec
Bandwidth	>70	∼100	∼100	Hz

Table 1: Performance requirements for different classes of gyroscopes [24].

of the straight line that can be fitted by the method of least squares to input-output data.

Dynamic Range: The ratio of the input range to the resolution. It is typically expressed in °/sec.

Bandwidth: The range of frequency of the angular rate input that the gyroscope can detect. It is typically specified as the cutoff frequency coinciding to the -3 dB point, expressed in Hz.

In general, the gyroscopes are classified into three categories based on the performance parameters explained above; inertial grade, tactical grade, and the rate grade gyroscopes as presented in Table 1. Typically, ring laser gyroscopes have achieved inertial-grade performance accurately, while fiber optic gyroscopes are used in tactical-grade applications. For the mechanical gyroscopes, the hemispherical resonator gyroscope (HRG) has achieved inertial-grade performance [35]. But, these devices are too expensive and bulky for many low cost applications. Therefore, the mechanical gyroscopes have received more attention after the MEMS technology provides small and cost effective mechanical gyroscopes. Recently, the rate grade and tactical grade applications have been performed by the micromachined vibratory gyroscopes. In Sections 2.1.4 and 2.1.6, the performance of micromachined vibratory gyroscopes studied between 1991 and 2021 will be reviewed.

1.4 The Robustness Challenge

Micro-fabrication methods and miniaturization processes are still insufficient to manufacture the inertial grade sensors that are able to achieve the requirements

of the emerging high performance applications. The characteristic fault in the micro-fabrication is the flaws in the design of mechanical components, which limits the sensor performance [36, 37]. In order to produce the robust and stable MEMS gyroscopes, the level of miniaturization processes must enable the MEMS gyroscopes to measure the sensitivity of picometer-scale displacements, but this is very challenging process to be achieved [24, 38].

One of the drawbacks in the micromachined gyro structures is the shifting in the drive and sense mode resonant frequencies due to the micro-fabrication difficulties. The maximum gain can be obtained by matching the drive and sense resonances of MEMS gyroscopes, which is crucial to carry out the high performance in applications. However, the fabrication difficulties cause the imperfections in the geometry and the material properties of MEMS structure, which decreases its sensitivity and stability [37]. Another common fabrication error is the anisoelasticity of suspension systems which causes the undesired mode coupling. Due to the anisoelasticity, the elastic cross-coupling occurs between the principle elastic axes and causes the off-diagonal stiffness. As the off-diagonal stiffness generates the undesired signal, which often much larger than the Coriolis motion, increases the noise floor of gyroscopes. In addition, the changes in the temperature during the micro-fabrication process may also affect the temperature dependent material properties (Young's Modulus), the damping and quality factor of the drive and sense systems. Further, the slight variations in micro-fabrication steps may also cause the deviations in mechanical properties from device to device. Therefore, the process control in micro-fabrication is vital to minimize the variations for each sensor device.

In order to solve the micro-fabrication issues mentioned above, electronic compensation is used to minimize the errors. For example, force to rebalance closed loop system is implemented to the sense system to alleviate the cross couplings between drive and sense system and also increase the sensor bandwidth to eliminate the resonant frequency and damping variation problems. But, the closed loop

systems in MEMS devices increases the cost of the product due the requirement of additional feedback electrodes. Thus, the resonant structures employed for MEMS gyroscopes are prone to production difficulties due to the complex construction requirements, and they are susceptible to external shock and vibration. On the other hand, travelling waves in an acoustic waveguide can be used as in SAW based MEMS gyroscopes. This configuration utilize the counter propagating waves in the same rotating waveguide and detect the change in velocities of travelling waves induced by the rotation [39, 40]. This method may reduce the susceptibility to external shock and vibration, temperature effects and packaging induced stresses, which have already demonstrated in SAW based MEMS gyroscopes [41]. However, SAW propagation is not dispersive and to miniaturize the device geometry one needs to use high frequencies which requires high frequency operation and complex electronics. Dispersive waves travelling in an acoustic waveguide allow more flexibility to choose the operation frequency and the device geometry, where low velocity waves with smaller wavelengths are available. Potentially, wave coupling between different waves can lead to more sensitive gyroscopes. In Chapter 4, the wave couplings due to the Coriolis Effect in rotating rod systems will be explained and analyzed in order to provide a basis for robust gyroscope structures.

1.5 Thesis Contribution

Journals

Cetin, H., Yaralioglu, G. (2020). Coriolis Effect on elastic waves propagating in rods. Journal of Sound and Vibration, 485, 115545.

Cetin, H., Yaralioglu, G. (2021). Noise Analysis of Mode Matched Vibratory Gyroscopes. Sensors and Actuators A: Physical, submitted.

Cetin, H., Yaralioglu, G. (2021). Mode Matched Vibratory Gyroscopes: A Review, in preparation.

CHAPTER II

BACKGROUND

2.1 Micromachined Vibratory Gyroscopes

2.1.1 Coriolis Effect

The Coriolis Effect is utilized by all micromachined vibratory gyroscopes in order to detect the rotation rate. In the rotating reference frame, the Coriolis acceleration is activated, when the rotation is applied to vibratory gyro systems. Thus, the principle of operation for micro-machined vibratory gyroscopes can be comprehended better by analyzing the motion of a rotation-induced body, as long as the body is observed in a rotating reference frame.

In Fig.3, the stationary reference frame is shown by Frame A and the rotating reference frame is shown by Frame B. An object located at r_A in Frame A can be also represented in Frame B as an object located at r_B. The position of Frame B is located at R in Frame A. Θ represents the orientation of rotating Frame B and Ω is the angular velocity vector of Frame B, ($\Omega = \dot{\Theta}$).

The time derivatives of a position vector r_A and r_B are given as:

$$\dot{r_A}(t) = \dot{r_B}(t) + \dot{\Theta} \times r_B(t) \tag{2.1}$$

The acceleration of a body in Frame B is calculated as:

$$r_A(t) = R(t) + r_B(t) \tag{2.2}$$

$$\dot{r_A}(t) = \dot{R}(t) + \dot{r_B}(t) + \dot{\Theta} \times r_B(t) \tag{2.3}$$

$$\ddot{r_A}(t) = \ddot{R}(t) + \ddot{r_B}(t) + \dot{\Theta} \times \dot{r_B}(t) + \dot{\Theta} \times (\dot{\Theta} \times r_B(t)) + \ddot{\Theta} \times r_B(t) + \dot{\Theta} \times \dot{r_B}(t) \tag{2.4}$$

For the sake of simplicity, v_B and a_B can be defined as the velocity and acceleration vectors in Frame B respectively. a_A denotes the acceleration vector in Frame A

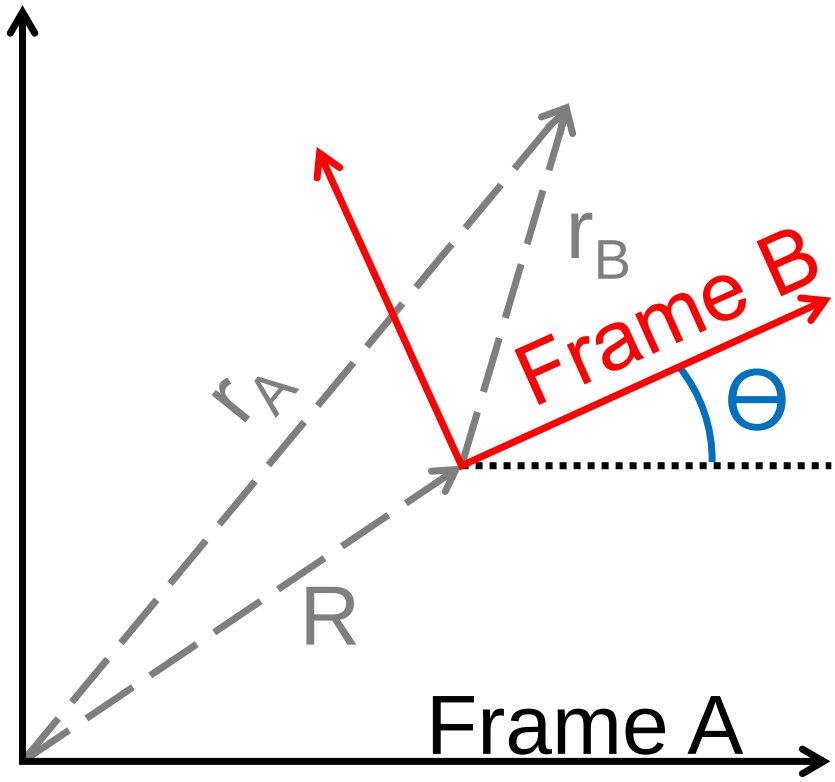


Figure 3: Representation of the position vector relative to the inertial reference frame (Frame A) and the rotating reference frame (Frame B).

and A denotes the linear acceleration in Frame B.

$$a_A = A + a_B + \dot{\Omega} \times r_B + \Omega \times (\Omega \times r_B) + 2\Omega \times v_B \tag{2.5}$$

The translational motion between the two reference frames A can be negligible, as we focus on the rotational motion. Thus, the Eq.(2.5) can be rewritten in terms of a_B:

$$a_B = a_A - \dot{\Omega} \times r_B - \Omega \times (\Omega \times r_B) - 2\Omega \times v_B \tag{2.6}$$

This analysis can be applied for the proof-mass of vibratory gyroscopes in order to understand their dynamics. According to Newton's second law of motion, the force coming from the Eq.(2.6) consists of two components: $F_B = F_A + F_{Fict}$. Therefore, the fictitious force is described as:

$$F_{Fict} = F_{Coriolis} + F_{Euler} + F_{Centrifugal} \tag{2.7}$$

where,

$$F_{Coriolis} = -2m(\Omega \times v_B) \tag{2.8}$$

$$F_{Euler} = -m(\dot{\Omega} \times r_B) \tag{2.9}$$

$$F_{Centrifugal} = -m(\Omega \times (\Omega \times r_B)) \tag{2.10}$$

In this work, the Euler force goes to zero in Eq.(2.7), since the rotation rate is considered as constant value. The Coriolis and centrifugal terms will be considered in calculations for the modelling of vibratory gyroscopes in the following section.

2.1.2 Basic Modelling of Vibratory Gyroscopes

A generic 2-DOF z-axis vibratory gyroscope is shown in Fig.4a, which detects the rotation along the z-axis. For vibratory rate gyroscopes, the proof mass vibrates in the drive direction (x) and the sense system measures the amplitude of the vibration in the sense direction (y) induced by the Coriolis force, as the input rate (Ω_z) is applied. We assumed the rotation axis goes through the point mass 'm'. This does not reduce the generality of the equations but helps us to ignore the DC component of the centripetal force [21]. According to [10], if the angular input rate is constant then the equation of motion is given by Eq.(2.11) for a 2-DOF vibratory rate gyroscope in a rotating reference frame as below:

$$\begin{aligned} m\ddot{x} + c_x\dot{x} + k_x x &= F_X + 2\Omega_z m\dot{y} + xm\Omega_z^2 \\ m\ddot{y} + c_y\dot{y} + k_y y &= F_Y - 2\Omega_z m\dot{x} + ym\Omega_z^2 \end{aligned} \tag{2.11}$$

where $2\Omega_z m\dot{y}$ and $-2\Omega_z m\dot{x}$ denote Coriolis forces and $xm\Omega_z^2$ and $ym\Omega_z^2$ are centripetal forces. k_x, k_y and c_x, c_y denote spring and damping constants in x and y directions, respectively. F_X is the harmonic force with the amplitude of F_0 which maintains constant drive oscillation (x_0) at the frequency of ω. F_Y is the control signal with the amplitude of F_C which equals to zero for the open loop operation mode, whereas it is used in force to rebalance operation mode for the in-phase error compensation. The operation modes of vibratory gyroscopes will be explained fully in Section 2.1.5.

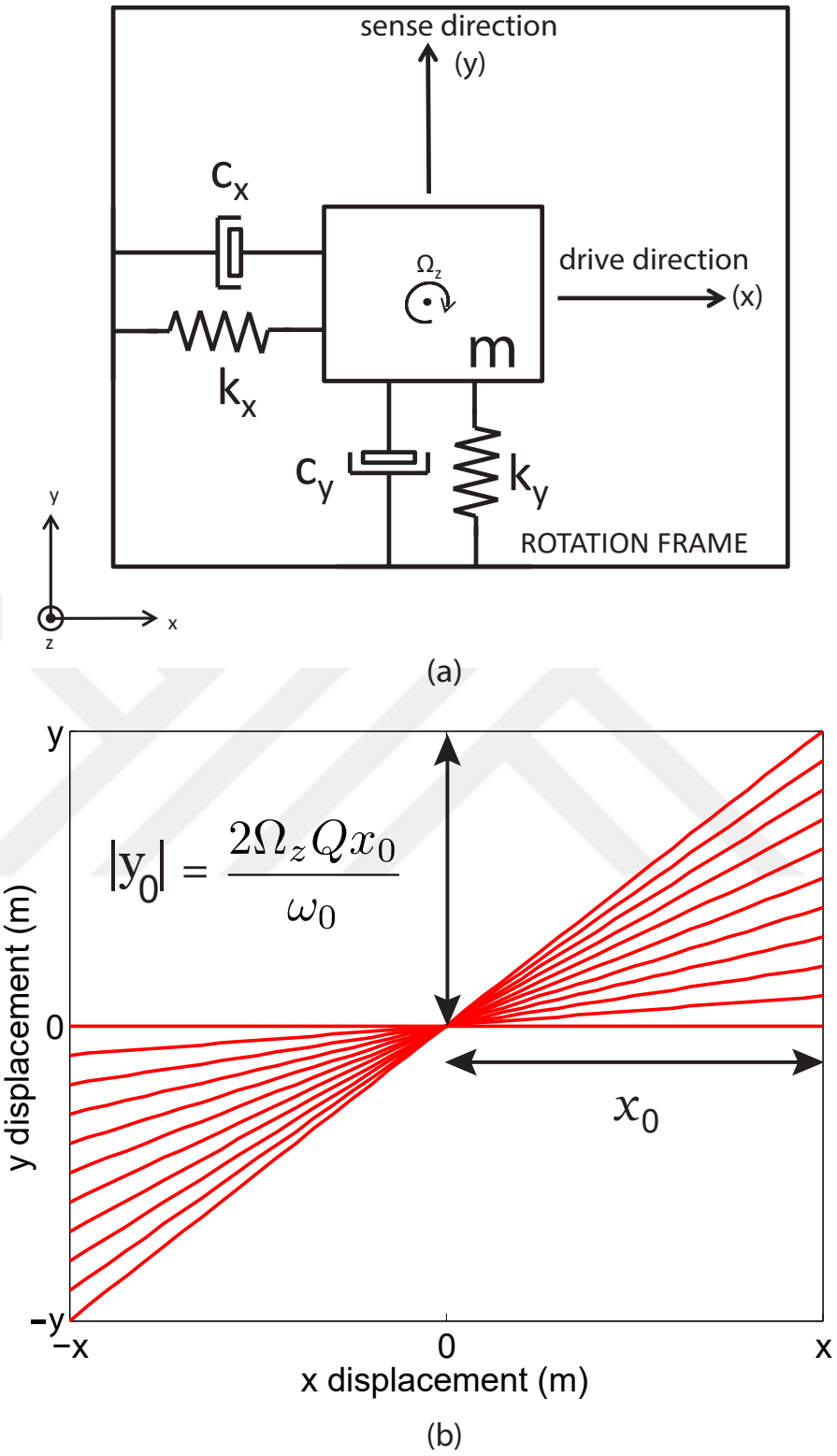


Figure 4: **(a)** Mass-spring-damper system of the 2-DOF vibratory gyroscope, where the rotation axis is going through the point mass, and **(b)** the steady-state response of vibratory rate gyroscopes for various input rates.

For an ideal mode matched operation, spring constants and damping coefficients are the same for both drive and sense systems ($k = k_x = k_y$, $c = c_x = c_y$). Damping coefficients can be calculated as in Eq.(2.12) where the quality factor is $Q = Q_d = Q_s$. For the drive and sense resonators of 2-DOF vibratory gyroscopes with a known Q factor, the relation between the oscillation amplitude and the force at resonance can be calculated using Eq.(2.13).

$$c_x = \frac{\sqrt{k_x m}}{Q_d},\ c_y = \frac{\sqrt{k_y m}}{Q_s} \tag{2.12}$$

$$F_0 = k_x \frac{x_0}{Q_d},\ F_C = k_y \frac{y_0}{Q_s} \tag{2.13}$$

When the drive system is excited by a harmonic force $F_X = F_0 \cos(\omega_0 t)$, the solutions for the steady-state responses of both drive and sense modes are given as

$$\begin{aligned} x &= x_0 \cos(\omega_x t - \phi_x) \\ y &= y_0 \cos(\omega_y t - \phi_y) \qquad\qquad \text{for } \ \Omega_z \neq 0 \end{aligned} \tag{2.14}$$

In the steady state system, the phase of the drive system (ϕ_x) equals to $-90°$, since the drive resonator is oscillated at its resonant frequency ($\omega_x = \omega_0 = \sqrt{k/m}$). For the sense system induced by the Coriolis force, the sense mode phase (ϕ_y) equals to $-270°$ where the drive and sense modes are matched ($\omega_x = \omega_y$). As a result, the steady-state responses for the mode matched gyro system driven in resonance equal to:

$$\begin{aligned} x &= x_0 \sin(\omega_0 t) \qquad\qquad \text{where } \ x_0 = \frac{F_0 Q}{k} \\ y &= y_0 \sin(\omega_0 t) \qquad\qquad \text{where } \ y_0 = -\frac{2\Omega_z Q x_0}{\omega_0} \end{aligned} \tag{2.15}$$

The steady-state response of a vibratory gyroscope given in Eq.(2.15) is illustrated in Fig.4b. In the figure, as the rotating gyro system maintains the constant drive oscillation (x_0) at the frequency of ω_0, the sense displacement (y_0) increases with increasing rotation rate due to the Coriolis force.

Another important point is to understand the nature of the gyro system. The gyro system can be modeled as a second-order system with the transfer function derived from Eq.(2.11) as below:

$$\frac{Y(s)}{A(s)} = \frac{1}{s^2 + \frac{\omega_0}{Q}s + \omega_0^2} \qquad \text{where} \quad \Omega_z < BW \tag{2.16}$$

where Y is the position of the mass; A is the input acceleration. In Eq.(2.16), we assumed that centripetal forces and the Coriolis force acting on the drive resonator are negligible for $\Omega_z < BW$, where $BW = \omega_0/2Q_s$ [21]. The characteristics of the sense system will be explained in the following section by using the transfer function given in Eq.(2.16).

For $\Omega_z > BW$, the resonant frequencies (ω_x, ω_y) shift between the drive and sense mode due to the Coriolis force, as reported in [21]. We calculate the Eigen values of the state matrix constructed from Eq.2.11 where $F_X = F_Y = 0$. In the Eigen values, the real part equals to the bandwidth and the imaginary part equals the resonant frequency for the gyro system. For the mode matched gyroscopes, both drive and sense systems have the resonance modes at the same frequency $(\omega_0 = \omega_x = \omega_y)$, when the input rate is zero. But for non-zero input rates, resonance splitting occurs and there appear two resonances for both drive and sense modes (total of 4 resonances; drive system has two resonances, sense system has two resonances) in their frequency spectra. One set of the resonances shifts down with the increased input rate whereas the other set shifts up. The resonance splitting deteriorates the linearity of mode matched vibratory rate gyroscopes for open loop operations [21]. The effect of the resonance splitting on the noise characteristics of mode matched vibratory gyroscopes will be discussed in Chapter 3.

2.1.3 Mode Matching

In gyro systems, mode matching occurs when the drive and sense modes have the same resonant frequency. When the gyro system achieves the mode matched condition, the spring constants of the both modes are identical and the magnitude

of mechanical response reaches its maximum for the sense system. To illustrate the effect of the mode matching, we calculated the bode diagram of the transfer function given in Eq.(2.16), as shown in the Fig.5. Fig.5 shows how the relationship between ω_x and ω_y changes the magnitude of the mechanical response. When $\omega_x < \omega_y$, the magnitude of the mechanical response is modest and the phase of the response is near 0°. When $\omega_x > \omega_y$, the magnitude of the mechanical response decreases with increasing ω_y and the phase of the response is near -180° shifted from the input acceleration. For the mode-matched case ($\omega_x = \omega_y$), the mechanical response is at its maximum and the phase of the response is near -90° shifted from the input acceleration. By increasing the mechanical response in gyro systems, it is possible to improve the signal to noise ratio and the effect of the electrical noise can be diminished.

In synchronous demodulation, it is important to know if the gyro system operates in mode matched condition or in split mode condition to demodulate the sense output for the calculation of in-phase and quadrature components properly. In gyro systems, when the input acceleration ($I \sin \omega_x t + Q \cos \omega_x t$) passes through the sense system, the phase of the sense output is determined in the range of 0° to -180° depending the relation between ω_x and ω_y, as shown in Fig.5. For the synchronous demodulation, the sense output is multiplied by the reference signals ($\sin \omega_x t$, $\cos \omega_x t$) separately and then, two modulated signals pass from the LPFs to calculate the amplitudes of in-phase and quadrature components (I, Q), where the reference signals are provided by the PLL system [29]. Based on the corresponding phase of the sense output, the signs of the calculated amplitudes (I, Q) may change during the synchronous demodulation and further, the outputs of the synchronous demodulation may switch in between. Hence, mode matching of gyro structures must be performed carefully in order to get the output properly by the synchronous demodulation in the detection system.

In 2-DOF gyro systems, the spring constants of the drive mode and the sense mode characterize the mode matching. It is difficult to adjust the spring constants

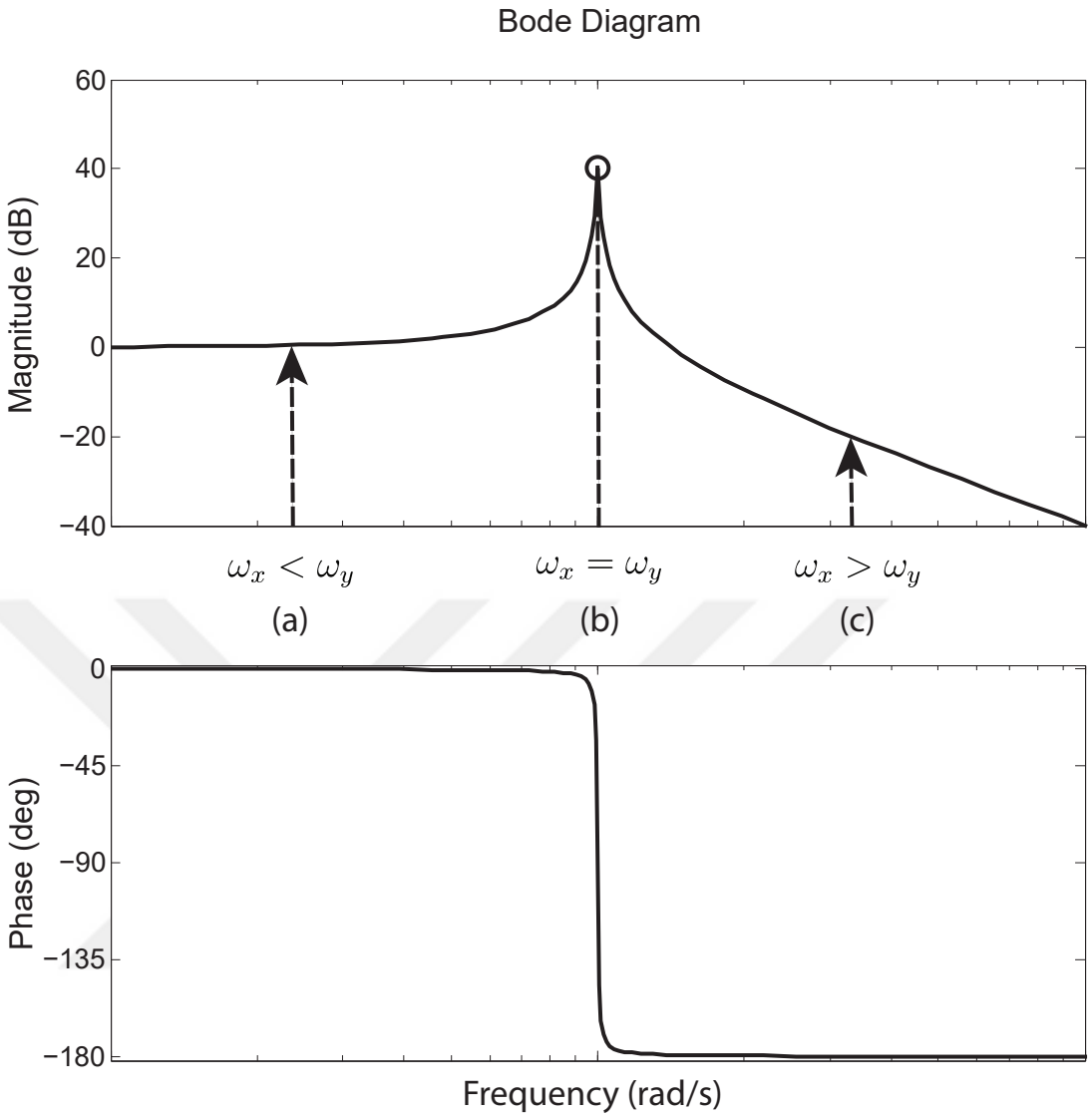


Figure 5: Bode diagram of the transfer function given in Eq. (2.16). **(a)** The mechanical output is modest when $\omega_x < \omega_y$. **(b)** The mechanical output reaches its maximum when $\omega_x = \omega_y$. **(c)** The mechanical output is low when $\omega_x > \omega_y$.

identical due to the failure in MEMS manufacturing. However, there is an technique used frequently in this field to adjust the spring constants electrostatically. This technique provides the ability to decrease the spring constant of the sense mode for matching the resonant frequencies of both drive and sense modes, which is called electrostatic spring softening. In order to identify the electrostatic spring softening, the forces acting on the structure are illustrated for one of the fingers of sense frame as shown in Fig.6a. In Fig.6a, one of the fingers of sense frame is modeled as a set of parallel plates, where one plate moves with a spring (k_{mech})

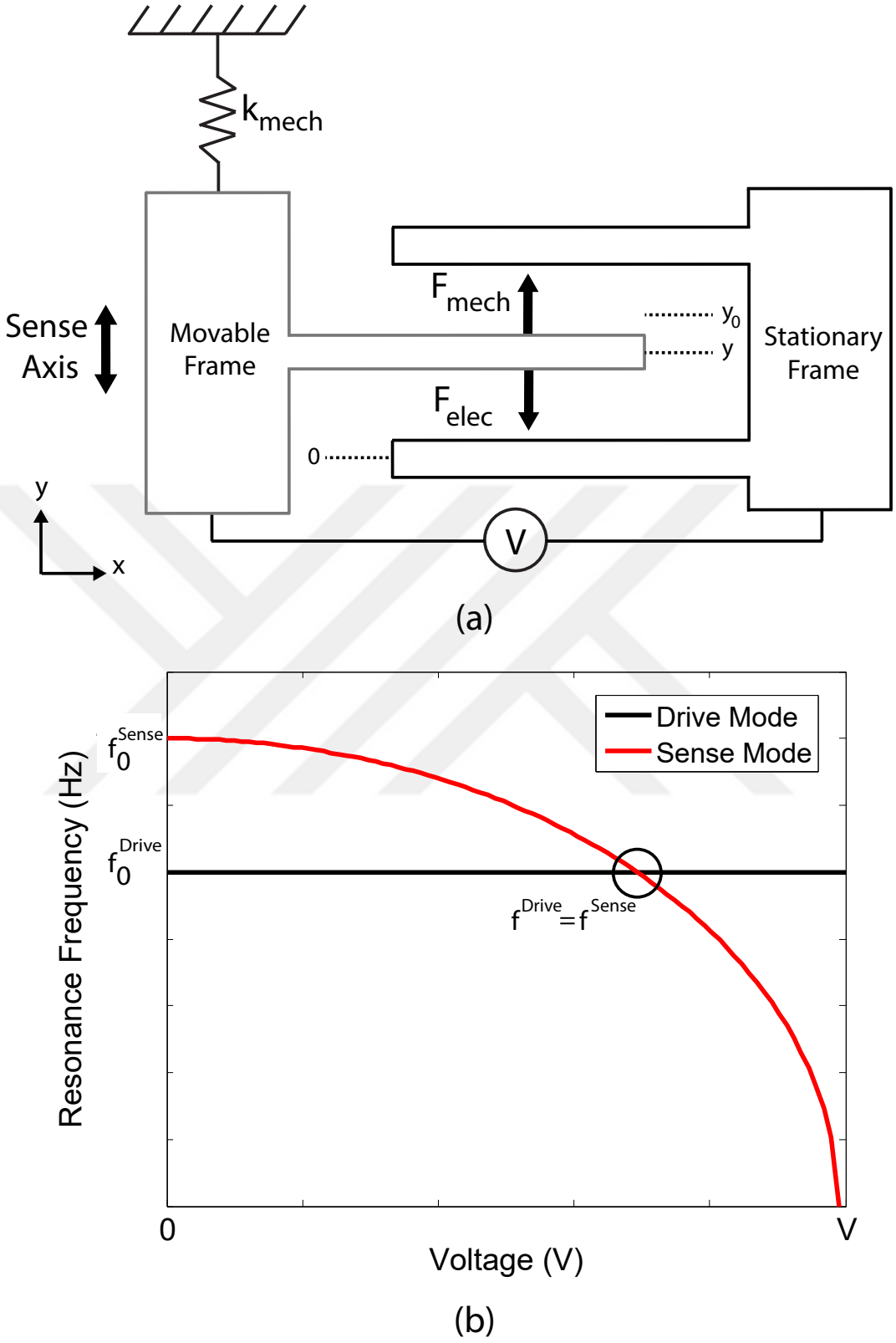


Figure 6: (a) Configuration of the frequency tuning electrodes, and (b) frequency tuning characteristics of the drive and sense modes as a function of voltage.

and the other is stationary. The movable plate represents the accelerometer finger, and the stationary plate represents the sense elements that are fixed to the substrate and interdigitated between the accelerometer fingers. There are two forces acting on the frame; a mechanical spring force acts on the frame tethered to the substrate with flexural beams, and an electrostatic force acts on the frame from the poly-silicon elements that form capacitors with each of its fingers, as shown in Fig.6a. As the movable plate is deflected from its equilibrium position of y_0, the forces on the movable plate is given as below:

$$\begin{aligned} F_{mech} &= -k_{mech}(y - y_0) \\ F_{elec} &= -\frac{1}{2}\frac{A\varepsilon_0}{y^2}V^2 \end{aligned} \tag{2.17}$$

where $F_{mech},\ F_{elec},\ y_0,\ y,\ \varepsilon_0$ and A denote the mechanical force, electrostatic force, the equilibrium position, the position of deflection, the vacuum permittivity and the overlap area of parallel plates, respectively. As the deflection of the movable frame is insignificant in gyro systems, one can use the linear approximation on the forces as below:

$$\begin{aligned} F_{mech} &= \left(\frac{dF_{mech}}{dy}\right)_{y=y_0} y = -k_{mech}y \\ F_{elec} &\approx \left(\frac{dF_{elec}}{dy}\right)_{y=y_0} y = \frac{A\varepsilon_0}{y_0^3}V^2 y \end{aligned} \tag{2.18}$$

The total force acting on the movable sense frame is calculated as:

$$\begin{aligned} F_{total} &= F_{mech} + F_{elec} \\ &= -k_{mech}y + \frac{A\varepsilon_0}{y_0^3}V^2 y \\ &= -\left(k_{mech} - \frac{A\varepsilon_0}{y_0^3}V^2\right) y \\ &= -k_{eff}y \end{aligned} \tag{2.19}$$

where

$$k_{eff} = \left(k_{mech} - \frac{A\varepsilon_0}{y_0^3}V^2\right) \tag{2.20}$$

The inherent mechanical spring constant, k_{mech}, is changed to get an effective spring constant k_{eff} which is basically regulated by the square of the DC voltage

applied on the frames. This configuration enables only to decrease k_{eff} by varying DC voltage, that is why it is known as electrostatic spring softening. While k_{eff} is reduced by DC voltage, one can change the resonant frequency for that axis, as presented below:

$$\omega_y = \sqrt{\frac{k_{eff}}{m}} = \sqrt{\frac{\left(k_{mech} - \frac{A\varepsilon_0}{y_0^3}V^2\right)}{m}} \tag{2.21}$$

As expected, Eq.(2.21) shows that there is always a softening in stiffness of the MEMS structure which reduces the resonant frequency of the sense mode to match with the drive mode, as illustrated in Fig.6b. It is important to note that as one of the fingers of sense frame is modeled in this section, the calculation of the total applied force on the sense frame must be reconsidered for the deflection of the every set of fingers.

2.1.4 Mode Matched Vibratory Rate Gyroscopes

In this section, review of state-of-the-art mode matched vibratory rate gyroscope architectures is presented. The architectures of the vibratory rate gyroscopes can be divided into five categories based on the resonator geometry: lumped mass systems, tuning fork systems, torsional vibratory/gimbal systems, ring/disk systems and hemispherical shell/wineglass systems. In the following sections, the design and performance of various mode matched vibratory rate gyroscopes will be reviewed, where the noise performance of the gyroscopes are presented in Table 2 and Table 3.

2.1.4.1 Lumped Mass Systems

A generic micromachined vibratory gyroscope with a lumped mass system is illustrated in Fig.7a. In Fig.7a, Alper et al. presented a symmetric micro machined vibratory gyroscope with decoupled oscillation modes [42]. Fig.7a shows the architecture of the symmetric and decoupled gyroscope. The anchors are placed at the outermost corners and connected to the movable drive and sense electrodes by the suspension beams. This configuration prevents the cross coupling between drive

References	Architecture	Resolution ($^\circ$/hr/$\sqrt{\text{Hz}}$)	Angle Random Walk ($^\circ/\sqrt{\text{hr}}$)	Bias Instability ($^\circ$/hr)
P. Greiff et. al. (1991) [46]	Gimbal system	14400		
J. Bernstein et al. (1993) [47]	Tuning fork system	681		
M. W. Putty et al. (1994) [48]	Ring system	1800		
K. Tanaka et al. (1995) [49]	Lumped mass system	7200		
P. Greiff et al. (1996) [50]	Gimbal system	43.2		
W. A. Clark et al. (1996) [38]	Lumped mass system	3600		
T. Juneau et al. (1997) [44]	Torsional vibratory system	864	2	
M. Lutz et al. (1997) [51]	Tuning fork system	1440		
T. K. Tang et al. (1997) [52]	Gimbal system		6.3	70
D. R. Sparks et al. (1997) [53]	Ring system	360		
Y. Oh et al. (1997) [54]	Lumped mass system	360		
K.Y. Park et al. (1998) [55]	Lumped mass system	360		
R. Hulsing et al. (1998) [56]	Lumped mass system	18	0.4	100
A. Kourepenis et al. (1998) [57]	Tuning fork system	10		
Y. Mochida et al. (1999) [58]	Lumped mass system	252		
K. Funk et al. (1999) [59]	Torsional vibratory system	1440		
S. Lee et al. (2000) [60]	Lumped mass system	9		
X. Jiang et al. (2000) [61]	Lumped mass system	10800		
Farrokh Ayazi (2001) [25]	Ring system	3600		
H. Xie et al. (2001) [62]	Lumped mass system	1800		
H. Luo et al. (2002) [63]	Lumped mass system	1800		
W. Geiger et al. (2002) [64]	Torsional vibratory system	25		1080
J. A. Geen et al. (2002) [17]	Tuning fork system	180		50
A. A. Seshia et. al. (2002) [65]	Lumped mass system	1080		
G. He et al. (2002) [66]	Ring system	10.4		

Table 2: Vibratory rate gyroscopes studied between 1991 and 2002. Gray colored rows represent the mode matched gyro systems and white colored rows represent the split mode gyro systems.

References	Architecture	Resolution (°/hr/√Hz)	Angle Random Walk (°/√hr)	Bias Instability (°/hr)
H. Xie et al. (2003) [67]	Lumped mass system	72		
D. Karnick et al. (2004) [68]	Tuning fork system		0.05	30
B. Choi et al. (2005) [69]	Lumped mass system	2.27		0.3
H. Johari et al. (2007) [70]	Disk system	40.8	0.28	17
M. F. Zaman et al. (2008) [15]	Tuning fork system	0.5	0.007	0.15
A. A. Trusov et al. (2008) [71]	Lumped mass system	324		288
S. E. Alper et al. (2008) [72]	Lumped mass system	6.9	0.115	14.3
M. F. Zaman et al. (2009) [73]	Ring system	2.3	0.09	3.5
D. M. Rozelle et al. (2009) [7]	Wineglass system	0.001	0.00006	0.0005
W.K. Sung et al. (2011) [74]	Disk system	86.4		648
R. Wang et al. (2011) [75]	Tuning fork system	0.37	6.67	95
Y. Tao et al. (2011) [76]	Ring system		0.05	1.5
I.P. Prikhodko et al. (2011) [77]	Tuning fork system	0.01	0.06	0.88
S. Nitzan et al. (2013) [78]	Disk system		0.36	3.29
P. T. Therani et. al. (2014) [79]	Hemispherical shell system		0.66	
S. Sonmezoglu et al. (2014) [16]	Lumped mass system	2.46	0.025	0.54
A.D. Challoner et al. (2014) [80]	Disk system		0.0033	0.01
J. Y. Cho et al. (2014) [81]	Hemispherical shell system		0.1	1
P. Shao et al. (2015) [45]	Wineglass system	24.73		
A. Efimovskaya et al. (2017) [82]	Ring system		0.78	17
A. Efimovskaya et al. (2017) [82]	Lumped mass system		0.11	1.3
N. V. Lavrik et al. (2019) [83]	Tuning fork system		10	< 0.5
D.Wang et al. (2019) [84]	Lumped mass system		0.0096	0.09
J. Y. Cho et al. (2019) [85]	Hemispherical shell system			0.01
H. Wen et al. (2020) [86]	Disk system	1.8	0.06	0.85
S. Askari et. al. (2021) [87]	Tuning fork system		0.006	0.07

Table 3: Vibratory rate gyroscopes studied between 2003 and 2021. Gray colored rows represent the mode matched gyro systems and white colored rows represent the split mode gyro systems.

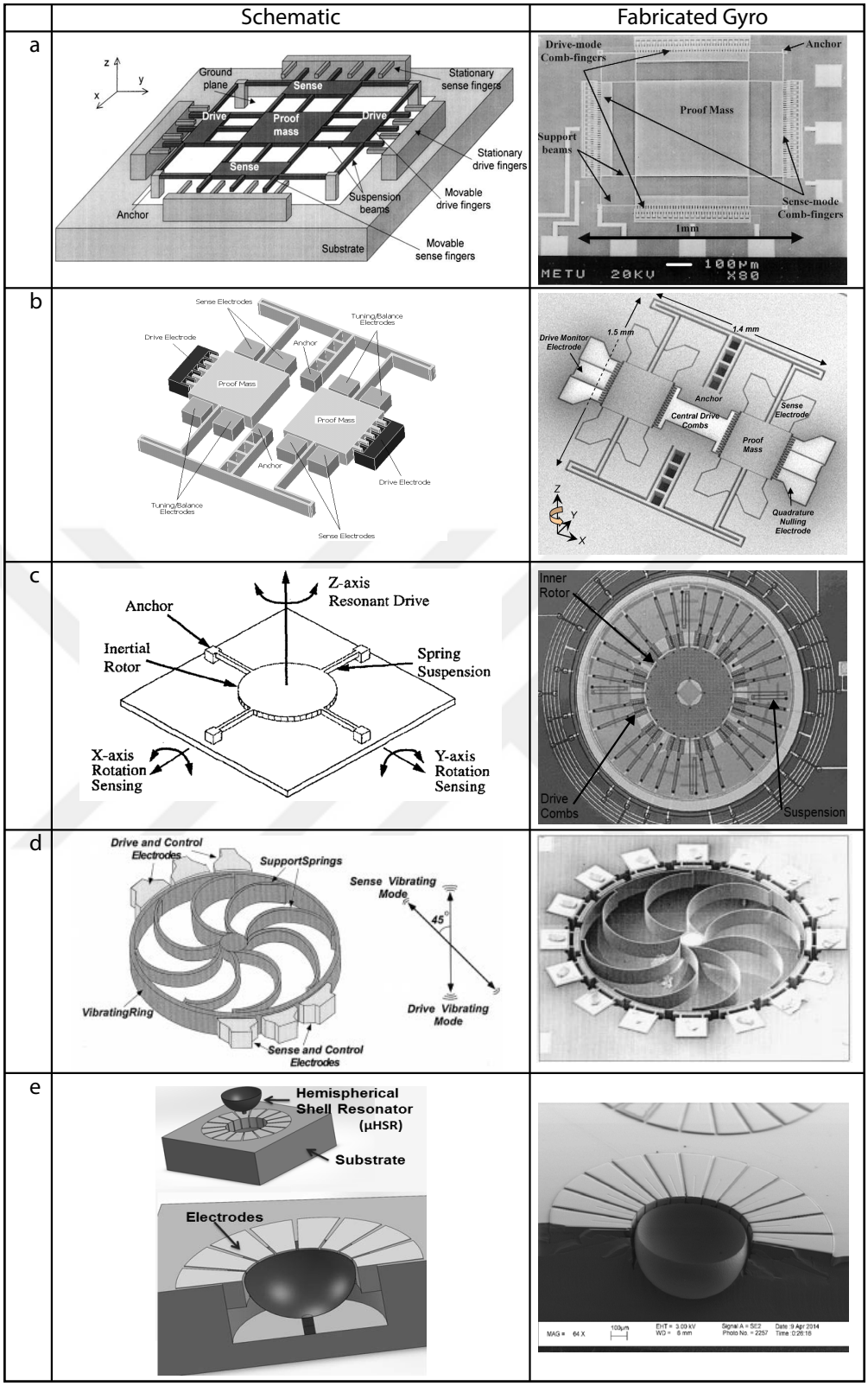


Figure 7: Mode matched vibratory rate gyroscope examples; **(a)** lumped-mass system [42], **(b)** tuning fork system [43, 15], **(c)** torsional vibratory/gimbal system [44], **(d)** ring/disk system [25] and **(e)** hemispherical shell/wineglass system [45].

and sense modes. The suspension beams supporting the proof mass are attached to the movable drive and sense electrodes to preserve the symmetry. Due to the micro-fabrication errors, the fabricated device had a small mismatch between the drive and sense mode resonant frequencies, which were measured as 28,535 Hz and 30,306 Hz, respectively. The device demonstrated the rate sensitivity better than 1.6 $^{\circ}/s$ with the scale factor of 0.9 mV/$^{\circ}$/s. Furthermore, the evolution of mode matched micromachined gyroscopes with the lumped mass systems is investigated in chronological order as below:

In 1996, Clark et al. developed an integrated z-axis gyroscope [38]. The z-axis gyroscope with a resolution of 3600 $^{\circ}/\mathrm{hr}/\sqrt{\mathrm{Hz}}$ is fabricated by the Analog Devices Inc. as a single proof-mass driven into resonance in-plane. Drive and sense modes were electrostatically tuned to match at 12 kHz operating frequency and the quadrature error were compensated electrostatically.

In 1997, Oh et al. presented a 7.5 μm thick deposited polysilicon gyroscope in [54]. The resolution was measured as 360 $^{\circ}/\mathrm{hr}/\sqrt{\mathrm{Hz}}$ with vacuum-packaging. Drive and sense modes were electrostatically tuned to match at 10.52 kHz operating frequency. A fish hook shaped spring suspension system for the micromachined gyroscope operating at 8.1 kHz was developed by Park et al. with the resolution of 360 $^{\circ}/\mathrm{hr}/\sqrt{\mathrm{Hz}}$, as reported in [55].

In 1999, Mochida et al. developed a DRIE-based 50 μm thick bulk micromachined single crystal silicon gyroscope with independent beams for drive and detection modes [58]. This configuration prevents the coupling between the drive and sense modes. The resolution of 252 $^{\circ}/\mathrm{hr}/\sqrt{\mathrm{Hz}}$ was demonstrated at 10 Hz bandwidth, as presented in Table 2.

In 2000, Lee et al. presented a single-crystalline-silicon micro-gyroscope in [60]. In [60], a new isolation method using the sandwiched oxide, polysilicon, and metal films was developed, which can be well suited for high aspect ratio structures. The device operating at 4.6 kHz with 40 μm thick single crystal silicon demonstrated the resolution of 9 $^{\circ}/\mathrm{hr}/\sqrt{\mathrm{Hz}}$ at 100 Hz bandwidth, as presented in Table 2.

In 2001, Xie et al. demonstrated lateral-axis integrated gyroscopes with the out of plane actuation in [62]. The lateral-axis gyroscope with 5 μm thick structure was fabricated by the thin-film CMOS process. The resolution of about 1800 °/hr/$\sqrt{}$Hz was measured, as presented in Table 2. The packaged gyroscope operates at atmospheric pressure with the sensitivity of 0.12 mV/°/s. Drive and sense modes were thermomechanically tuned to match between 4.2 kHz and 5.1 kHz operating frequencies, where the mode matching operation was performed by integrating a polysilicon heater inside the spring beams.

In 2005, Choi et al. presented a bulk micromachined gyroscope with the bandwidth of 58 Hz and the bias instability of 0.3 °/hr tested in 10 mTorr pressure [69]. The measured NER (Noise Equivalent Resolution) equals to 2.27 °/hr/$\sqrt{}$Hz, as presented in Table 3.

In 2008, Alper et al. presented the design and fabrication of a 100 μm thick single-crystal silicon MEMS gyroscope [72]. In this work, the gyroscope was developed by an improved decoupling arrangement between the drive and sense modes, which minimizes the cross coupling between the resonance modes. The size of the fabricated gyro is 4.6 mm x 4.2 mm. The device demonstrated the bias instability of 14.3 °/hr, the ARW of 0.115 °/$\sqrt{}$hr and resolution of 6.9 °/hr/$\sqrt{}$Hz, as presented in Table 3. The scale factor non-linearity was measured as ±0.6 % in the full scale range of ±50 °/s.

In 2014, Sonmezoglu et al. presented the architecture and experimental verification of the automatic mode-matching system for a MEMS gyroscope with wide and tunable bandwidth [16]. In this work, the usage of the phase relationship between the residual quadrature and drive signals was performed in order to achieve automatic frequency matching between the resonance modes, where the resonance modes with the $\sim$ 100 Hz frequency separation was matched by using the proposed method. The device demonstrated the bias instability of 0.54 °/hr, the ARW of 0.025 °/$\sqrt{}$hr and resolution of 2.46 °/hr/$\sqrt{}$Hz, as presented in Table 3. The scale factor was measured as 24.8 mV/°/s.

In 2017, Efimovskaya et al. presented a miniature 50 mm^3 inertial measurement unit (IMU) implemented using a folded MEMS process [82]. In [82], the results of experimental characterization of inertial sensors were also illustrated for the feasibility of the proposed approach of the compact IMU. A micromachined gyroscope operating at 8 kHz was used in the IMU with the size of 3.1 x 3.1 mm. The device demonstrated the bias instability of 1.3 °/hr and the ARW of 0.11 °/$\sqrt{}$hr, as presented in Table 3.

In 2019, Wang et al. presented the experimental results of an amplitude amplified dual-mass MEMS gyroscope [84]. In [84], the frequency mismatch was compensated electrostatically down to 0.5 Hz and the proposed mitigation strategies was implemented for the noise reduction. The MEMS gyroscope with the size of 6.6 mm x 6.6 mm operates at 4.3 kHz. The device demonstrated the bias instability of 0.09 °/hr and the ARW of 0.009 °/$\sqrt{}$hr, as presented in Table 3.

2.1.4.2 Tuning Fork Systems

A generic micromachined vibratory gyroscope with a tuning fork system is illustrated in Fig.7b. In Fig.7b, Zaman et al. presented the design, fabrication, and characterization of an in-plane mode-matched tuning-fork gyroscope [43, 15]. The device is comprised of two proof-masses supported by suspension beams. The suspended mechanical structure is anchored to the central post. The two proof masses are driven in-plane through the x axis in the opposite direction like the tines of tuning fork. As the rotation applied along the z axis, the two proof masses vibrate in-plane through the y axis in the opposite direction and the resulting displacement is sensed by the capacitive detection system to measure the rotation rate. The size of the device is 1.5 mm to 1.7 mm for a 60 μm thick. The ARW of the device was measured as 0.007 °/$\sqrt{}$hr and the bias stability of the device was measured as 0.15 °/hr [15], as presented in Table 3.

In 2011, Wang et al. presented the design, theoretical analysis, fabrication, and experimental results of a multiple beam tuning fork gyroscope [75]. The Q factors between 84,000 and 145,000 were measured for the sense mode, where

the 13 devices operating between 15 kHz and 17 kHz were studied. The best performance achieved by the fabricated devices demonstrated the bias instability of 95 °/hr, the ARW of 6.67 °/$\sqrt{}$hr and the resolution of 0.37 °/hr/$\sqrt{}$Hz, as presented in Table 3. Further, Prikhodko et al. presented the characterization of a silicon micromachined quadruple mass gyroscope in 2011 [77]. Similarly to the tuning fork devices with dual mass, the quadruple mass gyroscope comprises four identical symmetrically decoupled tines. The Q factor of the device was measured as 1.1 million for the 0.1 mTorr vacuum packaged device, where there was a 0.2 Hz frequency split between the resonance modes. The device demonstrated the bias instability of 0.88 °/hr, the ARW of 0.06 °/$\sqrt{}$hr and the resolution of 0.01 °/hr/$\sqrt{}$Hz, as presented in Table 3. In 2021, Askari et al. presented the characterization of a silicon micromachined quadruple mass gyroscope, similar to the device reported by Prikhodko et al. in [87]. The device demonstrated the bias instability of 0.07 °/hr and the ARW of 0.006 °/$\sqrt{}$hr, as presented in Table 3.

2.1.4.3 Torsional Vibratory/Gimbal Systems

A generic micromachined vibratory gyroscope with a gimbal system is illustrated in Fig.7c. In Fig.7c, Juneau et al. presented the dual axis operation of a micromachined rate gyroscope in 1997 [44]. The 2 μm thick disk (inner rotor) with a 150 μm radius serves as a gimbal system, which is suspended by four symmetrically placed beams anchored to the substrate. In Fig.7c, the disk is tilted about the z axis at the resonant frequency. As the rotation applied along the x or y axes, the disk starts to tilt about the y or x axes due to the Coriolis angular acceleration, respectively. Thus, this configuration allows the dual axis rotation rate measurement. The ARW of the device was measured as 2 °/$\sqrt{}$hr and the noise floor of the device was measured as 864 °/hr/$\sqrt{}$Hz [44], as presented in Table 2. Further, Tang et al. presented a bulk micromachined clover-leaf shaped gyroscope in 1997 [52]. The size of the device is 2.54 cm x 2.54 cm x 1.78 cm. The scale factor was measured as 24 mV/°/s. The temperature dependent frequency shift was noted as 0.23 Hz/° for the resonance modes, where 7 Hz frequency split was measured

between drive and sense modes. The ARW of the device was measured as 6.3 $^\circ/\sqrt{\text{hr}}$ and the bias instability of the device was measured as 70 °/hr, as presented in Table 2.

2.1.4.4 Ring/Disk Systems

A generic micromachined vibratory gyroscope with a ring system is illustrated in Fig.7d. In Fig.7d, Ayazi et al. presented the design, fabrication, and testing of a micromachined vibrating ring gyroscope [25]. The device consists of a ring, eight semicircular support springs, and drive, sense and control electrodes. This symmetric design allows two identical elliptically-shaped flexural modes that have equal resonance frequencies and are 45° apart from each other. The ring is driven by the primary flexural mode (drive vibrating mode) with constant amplitude. As the rotation applied around the normal axis, the secondary flexural mode (sense vibrating mode) of the ring starts to vibrate due to the Coriolis force. The resulting displacement is sensed by the capacitive detection system, which is proportional to the rotation rate. The drive frequency and the Q factor of the device were measured as approximately 29 kHz and 1200,respectively. Further, the open loop sensitivity of 200 $\mu V/^\circ/s$ in a dynamic range of $\pm 250^\circ/s$ was measured. The noise floor of the device was measured as 3600 $^\circ/\text{hr}/\sqrt{\text{Hz}}$ [44], as presented in Table 2. Furthermore, the evolution of mode matched micromachined gyroscopes with the ring/disk systems is investigated in chronological order as below:

In 1994, Putty et al. presented a micromachined vibrating ring gyroscope [48]. The ring has a dimater of 1 mm, a thickness of 19 μm and a width of 5 μm. The Q factor was measured as 4000 and the device operates at 33.3 kHz. The device demonstrated the resolution of 1800 $^\circ/\text{hr}/\sqrt{\text{Hz}}$ in 10 Hz bandwidth, as presented in Table 2.

In 2002, He et al. reported a bulk micromachined single crystal silicon vibrating ring gyroscope [66]. The diameter of the ring equals to 2.7 mm and the thickness of the ring equals to 150 μm. The gyro has the following measured performance: the Q factor is 12,000, the non-linearity is 0.02 %, the sensitivity is 132 mV/°/s.

The device demonstrated the resolution of 10.4 °/hr/$\sqrt{}$Hz, as presented in Table 2.

In 2007, Jahori et al. presented the design and implementation of capacitive bulk acoustic wave disk gyroscope in single crystal silicon [70]. The diameter of the disk equals to 1.2 mm and the thickness of the disk equals to 35 μm. The gyro has the following measured performance: the Q factor is 66,000, the bandwidth is 45 Hz, the drive frequency is 2.9 MHz, the sensitivity is 0.32 mV/°/s. The ARW of the device was measured as 0.28 °/$\sqrt{}$hr and the bias instability of the device was measured as 17 °/hr, as presented in Table 3.

In 2009, Zaman et al. reported on the design, fabrication and characterization of a novel multiple-shell silicon vibratory micro-gyroscope [73]. The resonating structure was fabricated in the shape of a star. The diameter of the star resonator equals to 2.5 mm and the thickness of the star resonator equals to 40 μm. The gyro has the following measured performance: the Q factor is 30,000, the bandwidth is 1.5 Hz, the drive frequency is 90 kHz, the sensitivity is 16 mV/°/s. The ARW of the device was measured as 0.09 °/$\sqrt{}$hr and the bias instability of the device was measured as 3.5 °/hr, as presented in Table 3.

In 2011, Sung et al. reported on the design, fabrication, and characterization of a high-frequency dual-axis hollow disk gyroscope [74]. The device utilizes an in-plane elliptical drive mode and two orthogonal out-of-plane sense modes (X-mode,Y-mode). The configuration allows to measure the rotation rate about the two axes. The diameter of the disk equals to 0.8 mm and the thickness of the disk equals to 40 μm. The gyro has the following measured performance: the Q factor of X-mode is 13,000 and the Q factor of Y-mode is 10,000, the drive frequency is 898 kHz, the sensitivities are 0.12 mV/°/s for the X-mode and 0.21 mV/°/s for the Y-mode. The device demonstrated the bias instability of 648 °/hr for X-mode and the bias instability of 1080 °/hr for Y-mode.

In 2011, Tao et al. presented the design, analysis, simulation and experiment of a novel ring vibratory gyroscope based on piezoelectric effect [76]. The device

has vertically aligned eight thin beams which are fixed to the substrate at one end and support a vibrating ring at the other end. The mechanical structure is symmetrical about z axis. The drive and sense piezoelectric elements are attached to the outer surface of the beams for the actuation and the detection, respectively. The diameter of the ring equals to 50 mm and the thickness of the ring equals to 1 mm. The frequency split was noted as 0.06 Hz. The gyro has the following measured performance: the Q factor is 5,000 in atmosphere, the drive frequency is 2.9 kHz, the scale factor is 65.5 mV/°/s. The ARW of the device was measured as 0.05 °/$\sqrt{}$hr and the bias instability of the device was measured as 1.5 °/hr, as presented in Table 3.

In 2013, Nitzan et al. presented an epitaxially-encapsulated polysilicon disk resonator gyroscope [78]. The diameter of the disk equals to 0.6 mm and the thickness of the disk equals to 20 μm. The Q factor was measured as 50,000 and the device operates at 264 kHz, where scale factor was noted as 0.286 mV/°/s. The ARW of the device was measured as 0.36 °/$\sqrt{}$hr and the bias instability of the device was measured as 3.29 °/hr, as presented in Table 3.

In 2017, Efimovskaya et al. presented a miniature 15 mm^3 inertial measurement unit (IMU) implemented using a folded MEMS process [82]. In [82], a toroidal ring micromachined gyroscope operating at 14 kHz was used in the IMU with the size of 2.8 mm x 2.8 mm. The device demonstrated the bias instability of 17 °/hr and ARW of 0.78 °/$\sqrt{}$hr, as presented in Table 3.

In 2020, Wen et al. reported on a wafer-level-packaged capacitive bulk-acoustic-wave gyroscope using a near-solid disk resonator [86]. The size of the gyro was noted as 2.8 mm x 2.8 mm x 0.45 mm. The gyro has the following measured performance: the Q factor is 165,000, the bandwidth is 1.5 Hz, the drive frequency is 2.92 MHz, the scale factor is 3.2 nV/°/s with the full-scale range of ±1000 °/s. The ARW of the device was measured as 0.06 °/$\sqrt{}$hr and the bias instability of the device was measured as 0.85 °/hr, as presented in Table 3.

2.1.4.5 Hemispherical Shell/Wineglass Systems

A generic micromachined vibratory gyroscope with a hemispherical shell system is illustrated in Fig.7e. In Fig.7e, Shao et al. presented the analysis, design, fabrication and characterization of a micro-hemispherical resonating gyroscope [45]. The device consists of a hemispherical shell and multiple electrodes that are fabricated on the same silicon substrate during the process. 16 electrodes are uniformly placed around the hemispherical shell. This symmetric design allows two identical n=2 wineglass modes that have equal resonance frequencies and are 45° apart from each other. The hemisphere is driven by the primary wineglass mode with constant amplitude. As the rotation applied around the normal axis, the secondary wineglass mode starts to vibrate due to the Coriolis force. The resulting displacement is sensed by the capacitive detection system to measure the rotation rate. In this study, two designs with different shell diameters were fabricated and studied also for higher order modes(n=3, n=4). The operating frequencies of the devices are 6.7 kHz and 5.6 kHz for the the n=2 mode. The Q factors of the devices are 8,500 kHz and 17,600 for the the n=2 mode. It was reported that that higher order modes (n=3, n=4) usually have higher Q factors. Further, the closed loop sensitivity of 8.57 mV/°/s was measured. The noise floor of the device was measured as 24.73 °/hr/$\sqrt{}$Hz [45], as presented in Table 3.

In 2014, Therani et al. presented a micro-scale gyroscope based on a 1 mm diameter diamond hemispherical resonator with embedded polysilicon electrodes [79]. In this paper, the mode matching operation and the wineglass modes were studied. For n=2 wineglass mode gyroscope, the drive frequency and the Q-factor were measured as 26.7 kHz and 14,800, respectively. The frequency split between resonance modes was decreased from 75 Hz to 28 Hz. The scale factor is 140 μV/°/s. The ARW of the device was measured as 0.66 °/$\sqrt{}$hr, as presented in Table 3. Further, Cho et al. presented a 3-D fused-silica micro-scale shell gyroscope, called the birdbath resonator gyroscope (BRG) in 2014 [81]. The device has n=2 wine-glass mode at 10.5 kHz, where the closest parasitic mode has a large

frequency separation from the n=2 wine-glass mode. The size of the device is 8 mm x 8 mm x 2.5 mm. The gyro has the following measured performance: the Q factor is 252,640, the angular gain is 0.317, the drive frequency is 10.4 kHz, the scale factor is 27.9 mV/°/s with the full-scale range of ±400 °/s. The frequency split was decreased from 14 Hz to 0.22 Hz. The ARW of the device was measured as 0.106 $^\circ/\sqrt{\text{hr}}$ and the bias instability of the device was measured as 1 °/hr, as presented in Table 3. In 2019, Cho et al. presented a 1.5 million Q factor vacuum packaged birdbath resonator gyroscope (BRG) [85]. They decreased the bias instability of the BRG operating at 10.5 kHz to 0.01 °/hr and increased the Q factor to 1.54 million.

2.1.5 Operation Modes of the Sense System

2.1.5.1 Open Loop Operation Mode

In a typical rate-mode vibratory gyroscope, the drive system is oscillated in a closed loop system and the rate is measured by demodulating the sense output. Fig.8a show the most common model for the gyro system with the drive mode oscillation control loop operating in the open loop operation mode. The control system consists of drive mode oscillator circuit, amplitude gain controller (AGC), phase locked loop (PLL)/demodulation and quadrature cancellation.

Eq.(2.11) is implemented by the Vibratory Gyroscope box as shown in Fig.9a. In1/Out1 represents the drive system; In2/Out2 represents the sense system. The most important feature of this implementation is the inclusion of Coriolis force in the feedback for both the drive system and the sense system. Note that the rate input which is denoted by Ω_z in Fig.9a, affects both the drive and sense frequency response due to the Coriolis Effect. This manifests itself as two resonance peaks in the drive and sense frequency spectra [21]. Moreover, centripetal forces are included to the spring forces in Fig.9a.

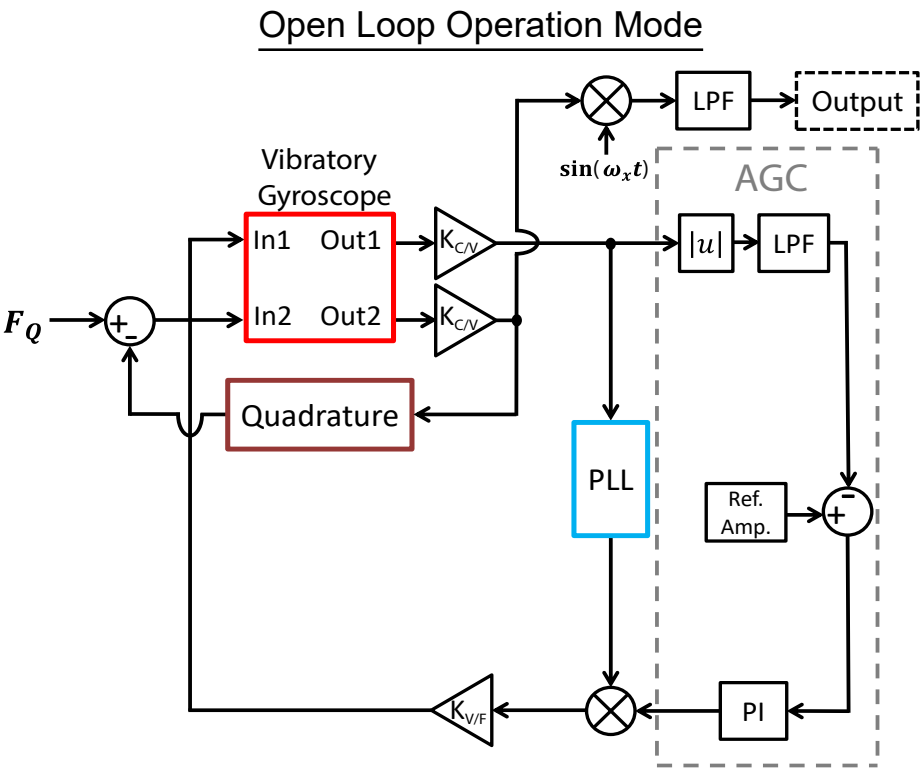
The drive system oscillates at the resonant frequency in closed loop feedback systems by the drive mode oscillator circuit. This circuit is responsible for electrostatic actuation and capacitive detection of the drive mode. The electrostatic

actuation is used for exciting the drive mode oscillator and the capacitive detection is used for measuring the drive displacement. For driving the gyro system, the drive mode oscillator is excited with the initial force. After measuring the drive displacement by the capacitive detection, the capacitance is converted to voltage through a circuit with the conversion gain ($K_{C/V}$) and the converted signal is processed by the drive oscillation controller as shown in Fig.8a. Then, the voltage of processed signal is converted to electrostatic force F_0 through actuators to excite back the gyroscope with the conversion gain ($K_{V/F}$). The mechanical vibration amplitude of the drive mode oscillation is sustained at constant level.

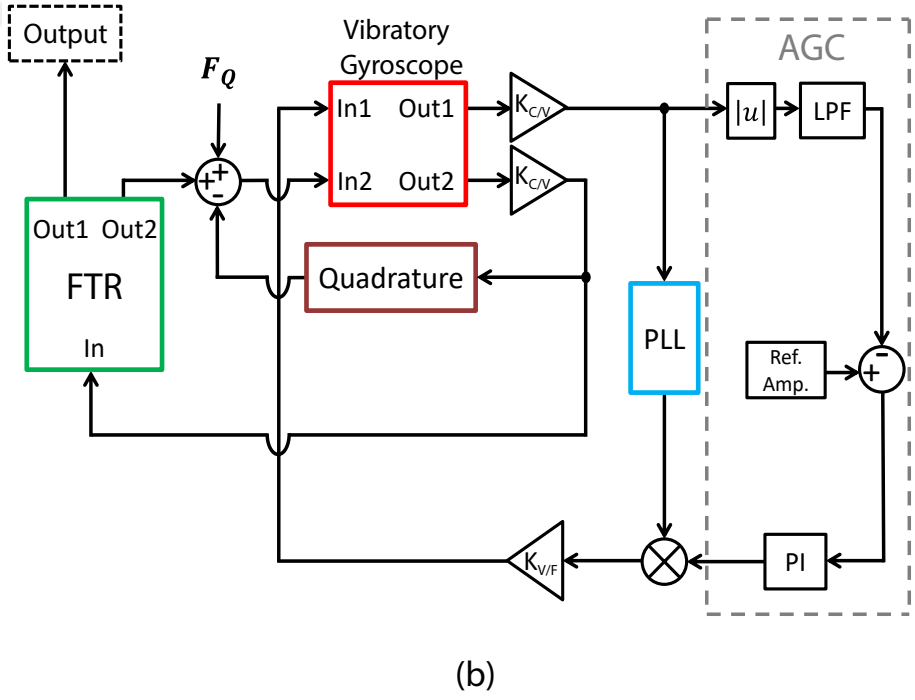
The amplitude of drive oscillation is kept constant by the amplitude gain control (AGC). Components of the AGC are rectifier, low pass filter (LPF), reference amplitude and proportional integral derivative (PID) controller as shown in Fig.8a. The AGC enables a good scale factor stability by providing the constant drive amplitude, as the scale factor of gyroscopes is dependent on drive velocity. The rectifier and the LPF form a subsystem for detecting the drive oscillation amplitude; the PLL controller controls the required excitation force for sustaining the target drive excitation level, which is calculated by subtracting the detected drive amplitude from the reference signal. In the AGC, it is important to adjust the target drive excitation level and tuning of the PID parameters.

PLL provides the necessary phase shift to keep the drive oscillator in the drive mode resonance. Components of the PLL are LPF, PID controller and voltage control oscillator (VCO) where the output of the VCO is used as reference signals ($sin(\omega_x t), cos(\omega_x t)$) as shown in Fig.9a.

For the sense system, the output contains two AC signals with strictly 90° phase delay called as quadrature signal (F_Q) and Coriolis signal. The quadrature signal (F_Q) can be separated from the Coriolis signal via demodulation of the sense mode output to calculate the quadrature amplitude and the rate output. Due to the micro-fabrication difficulties, the cross-coupling occurs between drive and sense mode, which generates the undesired quadrature signal in the



(a)



(b)

Figure 8: Block diagram of **(a)** the drive mode oscillation control with the open loop operation mode, and **(b)** the drive mode oscillation control with force to rebalance operation mode.

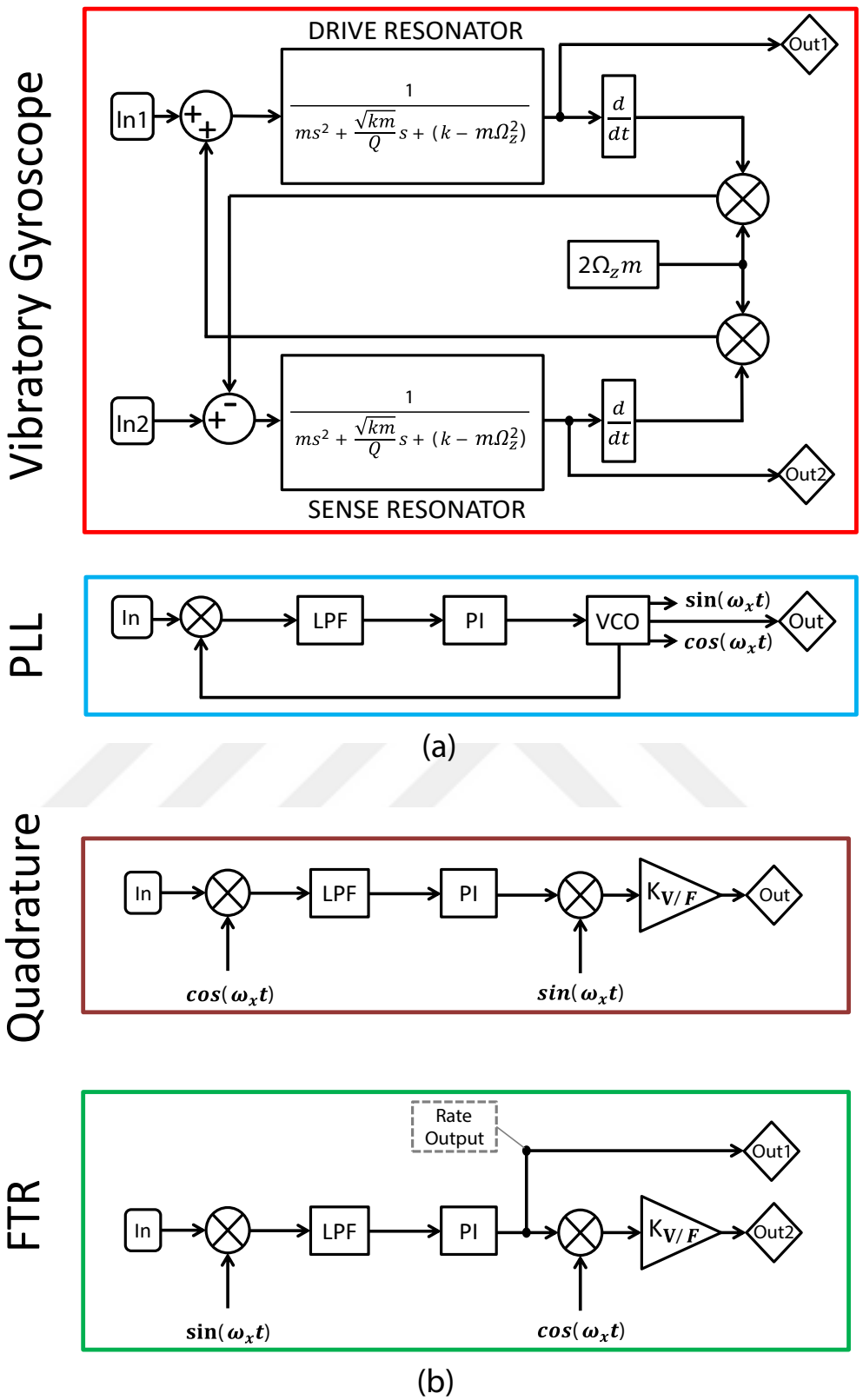
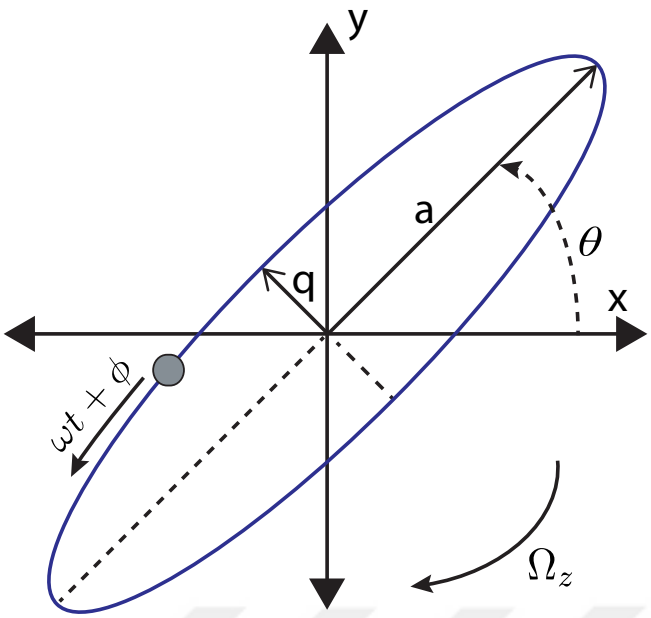


Figure 9: Block diagram of **(a)** vibratory gyroscope box, phase locked loop (PLL) box, and **(b)** quadrature box and force to rebalance (FTR) box.

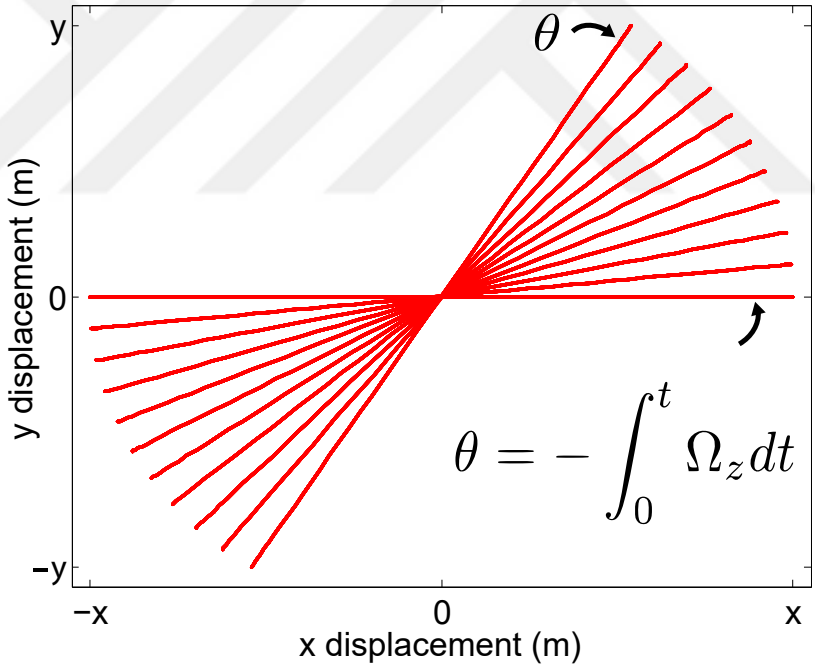
output. The quadrature signal can be drastically larger than the Coriolis signal, so the cancellation of the quadrature signal in the gyro systems is critical. Fig.9b illustrates the common model of quadrature cancellation loop, where the the quadrature signal (F_Q) is added to the sense system externally, as shown in Fig.8a. The components of quadrature box shown in Fig.9b are demonstrated as LPF, PI controller and reference signals ($\sin(\omega_x t)$, $\cos(\omega_x t)$). The sense output is represented as In; the quadrature loop output is represented as Out. In the quadrature box, the sense output is multiplied by the reference signal ($\cos(\omega_x t)$) and then the quadrature amplitude is calculated, as the modulated signal passes through the LPF and the PI controller. The quadrature signal (F_Q) is calculated by multiplying the quadrature amplitude with the reference signal ($\sin(\omega_x t)$) and the conversion gain $K_{V/F}$. $K_{V/F}$ is calculated as x_0/F_0 from the Eq.(2.13) for the conversion of the quadrature displacement to the quadrature signal (F_Q). Then, the quadrature signal (F_Q) is fed back to the sense system for the quadrature cancellation. As the quadrature signal is cancelled, the rate output, which is shown as the black dashed box in Fig.8a, is obtained by the demodulation of the sense system output while the rotation is applied.

2.1.5.2 Force to Rebalance Operation Mode

In the force to rebalance operation mode, the control signal (F_Y) is used to drive the sense system to zero, which equals to the Coriolis force ($2\Omega_z m\dot{x}$) from the Eq.(2.11). In Fig.9b, components of the force to rebalance (FTR) box are demonstrated as LPF, PI controller and reference signals ($\sin(\omega_x t)$, $\cos(\omega_x t)$). The sense output is represented as In; the gyro output and the control signal (F_Y) are represented as Out1 and Out2, respectively. In the FTR box, the sense output is multiplied by the reference signal ($\sin(\omega_x t)$) and then the rate output (y_0) is calculated, as the modulated signal passes through the LPF and the PI controller. The PI controller regulates the control signal (F_Y) to make $y \approx 0$ with a corresponding feedback signal. For the force to rebalance feedback signal, the Coriolis force is calculated by multiplying the rate output (y_0) with the reference signal



(a)



(b)

Figure 10: (a) Orbital trajectory of a proof-mass motion in response to the rotation rate Ω_z in x–y plane, where the amplitude of the proof-mass motion, the quadrature of the proof-mass motion, the inclination angle, the vibration frequency and the phase are denoted as a, q, θ, ω and ϕ respectively, and (b) the steady-state response of vibratory rate integrating gyroscopes.

$(\cos(\omega_x t))$ and the conversion gain $K_{V/F}$. $K_{V/F}$ is calculated as y_0/F_C from the Eq.(2.13) for the conversion of the sense displacement (y) to the control signal (F_Y). Finally, the Coriolis signal fed back to the sense system as the control signal (F_Y) from the Out2 box and the gyro output is measured from the Out1 box.

2.1.6 Mode Matched Vibratory Rate Integrating Gyroscopes

For rate integrating operations, the vibratory gyroscope shown in Fig.4a detects the absolute angles of rotation. In the ideal case, two modes oscillate freely for nonzero initial velocity and in the absence of rotation and anisoelasticity, where the damping coefficients of both modes (c_x, c_y) are canceled by a closed loop control system. When the zero damping condition is achieved to maintain the free oscillation of a gyro structure, the only perturbation is the Coriolis force in a rate integrating gyro system. Then, the equations of motion for a 2-DOF vibratory rate integrating gyroscope in a rotating reference frame are given as:

$$\begin{aligned} \ddot{x} + (\omega_x^2 - \Omega_z^2)x &= +2\Omega_z \dot{y} \\ \ddot{y} + (\omega_y^2 - \Omega_z^2)y &= -2\Omega_z \dot{x} \end{aligned} \tag{2.22}$$

The general solution of Eq. (2.22) is:

$$\begin{aligned} x =& a\cos\left(\theta_0 - \int_{t_0}^{t} \Omega_z(\tau)d\tau\right)\cos(\omega t + \phi) - q\sin\left(\theta_0 - \int_{t_0}^{t} \Omega_z(\tau)d\tau\right)\sin(\omega t + \phi) \\ y =& a\sin\left(\theta_0 - \int_{t_0}^{t} \Omega_z(\tau)d\tau\right)\cos(\omega t + \phi) + q\cos\left(\theta_0 - \int_{t_0}^{t} \Omega_z(\tau)d\tau\right)\sin(\omega t + \phi) \end{aligned} \tag{2.23}$$

where the solution given in Eq.(2.23) represents the orbital trajectory of a proof-mass motion in response to the rotation rate Ω_z in x–y plane, which is illustrated in Fig.10a. In Fig.10a, the trajectory of the proof mass induced by the rotation rate (Ω_z) can be equals to a straight line or an elliptical trajectory motion with parameters of the major radius (a), the minor radius (q), the initial inclination angle (θ_0) and the orbital phase (ϕ). The parameters a and q denote the amplitude

and quadrature of the proof-mass motion in x–y plane. For the zero quadrature case ($q = 0$), the solution given in Eq.(2.23) can be rewritten as:

$$\begin{aligned} x =& a\cos\left(\theta_0 - \int_{t_0}^{t} \Omega_z(\tau)d\tau\right)\cos\left(\omega t + \phi\right) \\ y =& a\sin\left(\theta_0 - \int_{t_0}^{t} \Omega_z(\tau)d\tau\right)\cos\left(\omega t + \phi\right) \end{aligned} \tag{2.24}$$

where the vibration pattern tracks a straight line and precesses with the rotation rate (Ω_z), as shown in Fig.10b. In Eq.(2.24), the inclination angle θ equals to

$$\theta = \theta_0 - \int_{t_0}^{t} \Omega_z(\tau)d\tau \tag{2.25}$$

where the angle of an orbital inclination can be directly measured from the x and y displacement components given in Eq.(2.24) at any time:

$$\theta = \arctan\left(\frac{y}{x}\right) \tag{2.26}$$

Thus, the instantaneous changes in the inclination angle θ can be detected by monitoring x and y displacements in order to measure the rotation rate (Ω_z), as shown in Fig.10b. In other words, Eq.(2.26) describes the governing principle for the whole-angle operation mode of gyro systems, which will be explained in the following section.

2.1.6.1 Whole Angle Operation Mode

In vibratory rate integrating gyroscopes, there are always mechanical imperfections like structural asymmetry and undesired damping that deteriorate the precession pattern. To compensate the effects of the imperfections, a closed loop control system should be implemented to the gyro system. The closed loop control system needs to estimate the orientation of the precession pattern θ to measure the rotation rate. Further, the constant amplitude of oscillation (E) must be sustained by adding the required energy along the orientation of the precession pattern (θ). Due to the imperfections, quadrature error (Q), which makes the vibration pattern elliptic by adding the system quadrature (q) as shown in Fig.10a, needs to be nulled. Thus, the control system is responsible for driving

the gyroscope at constant amplitude, suppressing the quadrature error, tracking and controlling the θ. To fulfill the tasks mentioned above, the required control loops are PLL, AGC and quadrature loop as explained below [88]:

Amplitude Gain Control (AGC): It keeps the amplitude of oscillation (E) stable.

Quadrature Loop: It actively drives the quadrature error (Q) to zero.

Phase Locked Loop (PLL): It is used for the demodulation of the gyro output and provides the reference sinusoidal signals.

As in the open-loop operation mode for the vibratory rate gyroscopes, the PLL is used to demodulate in-phase and quadrature signals. By using these demodulated signals, the slow moving variables amplitude (E), quadrature error (Q), and pattern angle (θ) can be calculated by using the Lynch's method reported in [89] as below:

$$\begin{aligned} E &= c_x^2 + s_x^2 + c_y^2 + s_y^2 \\ Q &= 2(c_x s_y - c_y s_x) \\ R &= c_x^2 + s_x^2 - c_y^2 - s_y^2 \\ S &= 2(c_x c_y + s_x s_y) \\ L &= c_x^2 - s_x^2 + c_y^2 - s_y^2 + 2i(c_x s_x + c_y s_y) \end{aligned} \tag{2.27}$$

where E denotes the energy within the system which is used for the constant amplitude oscillation; Q denotes the quadrature error. The imaginary part of L denotes the phase error which is used for the phase locking by the PLL. R and S are the projections of pattern angle on the x and y axis that is used for the calculation of the orientation of the precession pattern θ as given below:

$$\theta = \frac{1}{2} \arctan\left(\frac{S}{R}\right) \tag{2.28}$$

The parameters given in Eq.(2.27) are regulated by PID controllers. The PID controller in FTR loop controls the pattern angle (θ). It is important to note that FTR loop is disabled for the actual whole angle mode. So, the FTR loop in whole-angle gyroscopes is used to initialize the orientation of the precession pattern to

set the initial inclination angle (θ_0) and to control the pattern angle during the operation. The PID controllers in AGC loop and quadrature loop regulates E to control its amplitude and regulates Q to cancel the quadrature, respectively. As the F_E, F_Q and F_θ established by the PID controllers, the required forces for the two gyro channels (x,y) can be calculated as below:

$$\begin{aligned} F_{c_x} &= F_E \cos\theta - F_\theta \sin\theta \\ F_{c_y} &= F_E \sin\theta + F_\theta \cos\theta \\ F_{s_x} &= -F_Q \sin\theta \\ F_{s_y} &= F_Q \cos\theta \end{aligned} \tag{2.29}$$

where the coordinate transformation around θ is applied to get the corresponding Cartesian components. Then, the signals given in Eq.(2.29) are modulated at the PLL frequency to be fed back to the corresponding gyro channels.

2.1.6.2 Literature Review

In this section, review of state-of-the-art the mode matched vibratory rate integrating gyroscope architectures is presented. The architectures of the vibratory rate integrating gyroscopes can be divided into five categories based on the resonator geometry: lumped mass systems, tuning fork systems, ring/disk systems, cylindrical shell systems and wineglass systems.

In the lumped mass systems, Painter et al. presented a lumped mass micromachined rate integrating gyroscope [90]. The implementation and evaluation of a feedback control system was proposed to achieve the ideal motion of an angle measuring gyroscope by compensating the energy dissipation and suppressing the anisoelasticity. Further, Senkal et al. presented a micro machined vibratory gyroscope that utilizes the principle of dual Foucault pendulum as shown in Fig.11a [101, 102]. The mechanical structure is suspended by four anchors placed in between the two proof masses. The device has two dynamically equivalent, mechanically coupled proof masses that vibrate in the anti-phase motion. This dual axis behavior of the masses provides the oscillation with x–y symmetry where the

References	**Architecture**	**Resolution ($^\circ$/hr/$\sqrt{\text{Hz}}$)**	**Angle Random Walk ($^\circ/\sqrt{\text{hr}}$)**	**Bias Instability ($^\circ$/hr)**
C. C. Painter et al. (2005) [90]	Lumped mass system			
A. A. Trusov et al. (2011) [91]	Tuning fork system	0.01		0.9
J. Cho et al. (2011) [92]	Cylindrical shell system	3.6	0.06	576
J. Cho et al. (2012) [93]	Cylindrical shell system		0.09	129
J. A. Gregory et al. (2012) [94]	Cylindrical shell system		2.6	203
I. P. Prikhodko et al. (2012) [95]	Tuning fork system	0.01	0.06	0.9
J. K. Woo et al. (2014) [96]	Wineglass system		0.1	1
B. R. Johnson et al. (2014) [97]	Cylindrical shell system			
D. Senkal et al. (2014) [98]	Ring system		0.05	0.65
A. A.Trusov et al. (2014) [99]	Tuning fork system		0.05	0.2
P. T. Tehrani et al. (2015) [100]	Disk system			
D. Senkal et al. (2015) [101], [102]	Lumped mass system		0.003	0.27
S. Askari et al. (2018) [103]	Tuning fork system			

Table 4: Mode matched vibratory rate integrating gyroscopes.

frequency and the damping of both gyro modes are matched. The center of masses of each proof mass is aligned for the dynamic balance, which makes the center of mass of the whole system maintain its stationary mode during the oscillation as shown in Fig.11a. This configuration sustains the force and moment balance for both x and y modes, that reduces the susceptibility to external vibration and shock. For the rate integrating operation, the ARW was measured as 0.003 $^\circ/\sqrt{\text{hr}}$ and the bias stability was measured as 0.27 °/hr, as presented in Table 4. For the rate operation with FRB closed loop, the ARW of the device is 0.06 $^\circ/\sqrt{\text{hr}}$ and the bias stability of the device is 1.5 °/hr. The higher noise in rate operation was associated with the feedback noise from the digital to analog converters.

In the tuning fork systems, Shkel et al. presented a quadruple mass gyroscope as shown in Fig.11b [91]. Similarly to the tuning fork devices with dual mass, the quadruple mass gyroscope comprises four identical symmetrically decoupled tines. This configuration can be thought of as two levered dual mass gyroscopes coupled together with additional mechanisms. The anti-phase motion of the masses for both vibration axes (x and y modes) is shown in Fig.11b. For the open loop rate integrating operation, the resolution of the device is 0.01 $^\circ/\text{hr}/\sqrt{\text{Hz}}$ and the bias stability of the device is 0.9 °/hr, as presented in Table 4. Then, the closed-loop rate integrating operation was demonstrated in [99, 103]. In [99], the ARW was measured as 0.05 $^\circ/\sqrt{\text{hr}}$ and the bias stability was measured as 0.2 °/hr, as presented in Table 4.

Senkal et al. presented a micromachined toroidal ring vibratory gyroscope as shown in Fig.11c [98] which uses ring/disk system. This configuration has an outer anchor that encircles the device, a distributed ring support structure and an inner electrode assembly, as shown in Fig.11c. The suspension system consists of 44 concentric rings that are connected to each other using 12 spokes between the rings. The distributed ring support structure decouples the conjugate flexural modes, where the device operates in n = 3 wineglass mode. The ARW was measured as 0.05 $^\circ/\sqrt{\text{hr}}$ and the bias stability was measured as 0.65 °/hr,

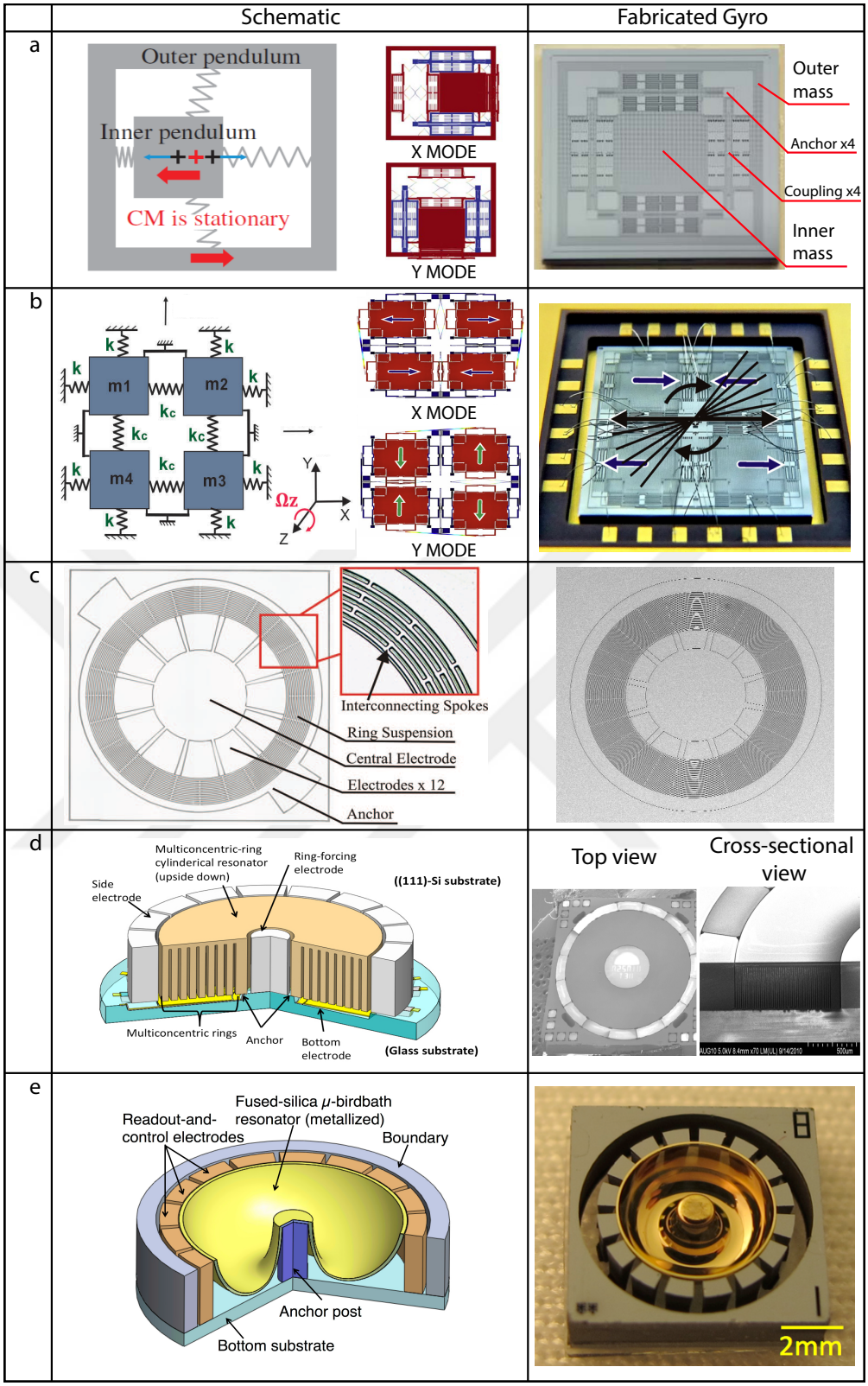


Figure 11: Mode matched vibratory rate integrating gyroscope examples; **(a)** lumped-mass system [101], **(b)** tuning fork system [91], **(c)** ring and disk systems [98], **(d)** cylindrical shell system [92] and **(e)** wineglass system [96].

as presented in Table 4. Further, Tehrani et al. presented a micromachined disk vibratory gyroscope with whole angle operation mode [100]. The Q factor of the device is approximately 80,000 and the drive frequency is 250 kHz. Discrete-time control system based on the Lynch's algorithm were implemented [89]. For the rate gyro operation, the ARW of the device was measured as low as 0.12 $^\circ/\sqrt{\text{hr}}$ and the bias stability of the device was measured as low as 1.5 °/hr [104].

In the cylindrical shell systems, Cho et al. presented a micromachined vibratory Cylindrical Rate Integrating Gyroscope (CING) in [92, 93], as shown in Fig.11d. The gyro structure consists of a resonator, resembling a cylinder with multiple rings, sixteen circumferential electrodes; sixteen bottom electrodes; and a ring electrode at the center of the device, as shown in Fig.11d. This configuration has the self-aligned and axi-symmetric geometry, and the large separation between the operating mode (n = 2 wineglass mode) and the parasitic modes. The drive frequency of the device is 3 kHz and the Q factor of the device is approximately 100,000 as reported in [93]. The ARW of the device was measured as 0.09 $^\circ/\sqrt{\text{hr}}$ and the bias stability of the device was measured as 129 °/hr, as presented in Table 4. In [94], Gregory et al. proposed a high-performance, low-cost system for control and characterization of MEMS rate and rate-integrating gyroscopes by using the Cylindrical Rate-Integrating Gyro (CING) reported in [92, 93]. The ARW of the device was measured as 2.6 $^\circ/\sqrt{\text{hr}}$ and the bias stability of the device was measured as 203 °/hr, as presented in Table 4. Further, Johnson et al. presented a half-toroidal vibratory rate integrating gyroscope [97]. Experimental results of resonance decay time as a function of frequency, temperature and pressure were presented for various resonators. It was also reported that the reduction in frequency mismatch was achieved by eliminating the lip at the perimeter of the resonator, where the device operates in n = 2 wineglass mode.

In the wineglass systems, Woo et al. presented a fused-silica micromachined birdbath resonator gyroscope in [96], as shown in Fig.11e. In Fig.11e, this gyro structure consists of a resonator and sixteen electrodes surrounding the outer

perimeter for the control and readout. Further, the frequency difference between the operating mode (n = 2 wineglass mode) and the parasitic modes is high enough to achieve good vibration stability. The Q factor of the device is approximately 70,000 and the drive frequency is 10.46 kHz. The ARW of the device was measured as 0.1 $^\circ/\sqrt{\text{hr}}$ and the bias stability of the device was measured as 1 $^\circ$/hr, as presented in Table 4.

2.2 Waveguide Based Gyroscopes

2.2.1 Wave Propagation In Elastic Solids

Elastic waves propagating in solids are also known as bulk acoustic waves (BAWs). The BAWs are categorized into a dilatational (longitudinal) wave and a shear wave as shown in Fig.12. The governing wave equations for isotropic bulk materials are given as below [105]:

$$\begin{aligned}(\lambda + 2\mu)\frac{\partial^2 u}{\partial x^2} &= \rho\frac{\partial^2 u}{\partial t^2} \\ \mu\frac{\partial^2 w}{\partial x^2} &= \rho\frac{\partial^2 w}{\partial t^2}\end{aligned} \tag{2.30}$$

where μ and λ are Lame's coefficients. ρ denotes the material density and the displacements are denoted by u and w. The velocities of the dilatational and shear waves (c_d, c_s) are derived by the Eq.(2.30) as below:

$$c_d = \sqrt{\frac{\lambda + 2\mu}{\rho}},\ c_s = \sqrt{\frac{\mu}{\rho}} \tag{2.31}$$

, respectively. Eq.(2.31) shows that dilatational waves propagates faster than the shear waves in a bulk elastic media. To understand the effect of the rotation on propagating elastic waves, the characteristics of propagating elastic waves will be presented for a rotating media in the following section.

2.2.2 Coriolis Effect On Propagating Waves

In an infinite elastic media, the particle motions of dilatational and shear waves are orthogonal to each other, as shown in Fig.12. In Fig.12, the dilatational wave (u) and the shear wave (w) vibrate in the x and z directions respectively, while

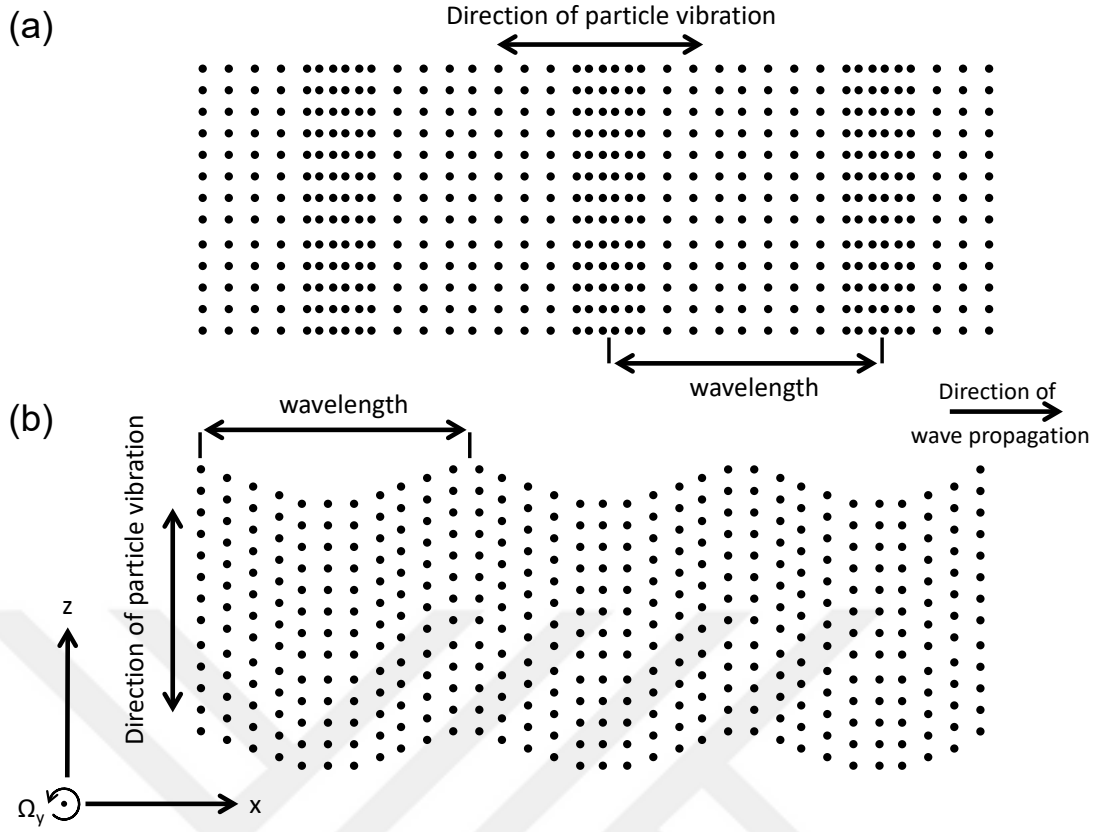


Figure 12: Particle motions of **(a)** the dilatational wave and **(b)** the shear wave.

constant rotation (Ω_y) is applied from the origin through the normal axis (y). As a result, the equations of motion for the dilatational and the shear wave in a rotating reference frame are given as:

$$\begin{aligned}(u+|OP|)\Omega_y^2 + 2\Omega_y \times \frac{\partial w}{\partial t} &= \frac{\partial^2 u}{\partial t^2} - \frac{(\lambda+2\mu)}{\rho}\frac{\partial^2 u}{\partial x^2} \\ w\Omega_y^2 - 2\Omega_y \times \frac{\partial u}{\partial t} &= \frac{\partial^2 w}{\partial t^2} - \frac{\mu}{\rho}\frac{\partial^2 w}{\partial x^2}\end{aligned} \tag{2.32}$$

where $(u+|OP|)\Omega_y^2$ and $w\Omega_y^2$ are the total Centrifugal accelerations and $2\rho\Omega_y \times \frac{\partial w}{\partial t}$, $-2\rho\Omega_y \times \frac{\partial u}{\partial t}$ are the Coriolis accelerations. $|OP|$ denotes the actual position of the particle. The displacement u can be decomposed into a static displacement u_s and a vibrational displacement u_v. As the static displacement is time independent, we only consider the vibrational part of the displacement for the vibration analysis of a rotating media. So, we neglected the $|OP|$ in calculations which affects only the static displacement u_s as reported in [106]. Thus, we consider the harmonic

waves propagating in an infinite elastic media as:

$$u = B_1 e^{j(kx-\omega t)}, w = B_2 e^{j(kx-\omega t)} \tag{2.33}$$

and substitute Eq.(2.33) in Eq.(2.32) by subtracting the static displacement. The following two homogenous equations in B_1, B_2 are obtained as

$$(\lambda + 2\mu)k^2 B_1 = \rho(\omega^2 + \Omega_y^2)B_1 - 2i\rho\Omega_y\omega B_2 \tag{2.34}$$

$$\mu k^2 B_2 = \rho(\omega^2 + \Omega_y^2)B_2 + 2i\rho\Omega_y\omega B_1 \tag{2.35}$$

Eq.(2.34) and Eq.(2.35) can be rewritten in the matrix form as

$$\begin{bmatrix} (\frac{\lambda+2\mu}{\rho}k^2 - \Omega_y^2) - \omega^2 & +i2\Omega_y\omega \\ -i2\Omega_y\omega & (\frac{\mu}{\rho}k^2 - \Omega_y^2) - \omega^2 \end{bmatrix} \begin{bmatrix} B_1 \\ B_2 \end{bmatrix} = 0 \tag{2.36}$$

where the elastic waves are generated by constant frequency ($\omega = \omega_0$). Equating the determinant of coefficients to zero in Eq.(2.36) gives the wavenumber equation induced by the rotation (Ω_y) as

$$\frac{\mu(\lambda + 2\mu)}{\rho^2}k^4 - (\omega_0^2 + \Omega_y^2)(\frac{\lambda + 3\mu}{\rho})k^2 + (\omega_0^2 - \Omega_y^2)^2 = 0 \tag{2.37}$$

where c equals to c_d and c_s for the inertial medium ($\Omega_y = 0$) as $c = \frac{\omega_0}{k}$. This recovers the uncoupled velocities given in Eq.(2.31). As the two elastic waves couple, the solution of Eq.(2.37) gives the wavenumbers for the dilatational wave and the shear wave separately:

$$k_{1,2}^2 = \frac{\rho\omega_0^2}{2\mu(\lambda + 2\mu)}(1 + \frac{\Omega_y^2}{\omega_0^2}) \left(\lambda + 3\mu \pm \sqrt{(\lambda + 3\mu)^2 - 4\mu(\lambda + 2\mu)(\frac{\omega_0^2 - \Omega_y^2}{\omega_0^2 + \Omega_y^2})^2} \right). \tag{2.38}$$

Eq.(2.38) implies that the wavenumber (k) changes for the propagating elastic waves, while the rotation is applied. Thus, the change in velocities of dilatational and shear waves can be used to measure the rotation rate and one can build a gyro structure based on an acoustic waveguide by utilizing that phenomenon. In the following sections, the gyroscopes based on acoustic waveguides will be presented.

2.2.3 Elastic Wave Based Gyroscopes

In general, different architectures like plates, rods, beams and elongated structures are used to guide elastic waves. The elastic waves propagating in the rotating media exhibit different characteristics compared to the wave propagation in the stationary media, as mentioned in the previous section. In many studies, the Coriolis Effect on the elastic waves propagating in the different elastic media such as plates [107, 108], rods [109, 110], cylindrical shells [111, 112] and beams [113] have been examined, when the medium is subjected to the rotation. In all of these researches, it was demonstrated that the elastic waves propagating in a waveguide are coupled due to the Coriolis Effect, as the rotation is applied. This Coriolis coupling changes the velocities of the propagating elastic waves.

In 1981, a rotation rate sensor by using the flexural waves propagating in a ring was firstly proposed in theory by Tiersten et al. in [40]. Tiersten et al. presented that the change in the resonant frequencies of flexural waves can form a basis for a rotation rate sensor. Then, the theoretical results of elastic wave propagation into rotating solid-state media are presented by Yasemin et al. in [114]. Yasemin et al. proposed that the change in the velocities of longitudinal and transverse waves can form a basis for the sensor device. However, the theoretical studies of a novel gyroscope based an acoustic waveguide have been performed many years ago, the experimental works have been studied recently. In 2020, Yasemin et al. presented the experimental results of a novel gyro design which utilizes the propagation of longitudinal and transverse waves in a fused quartz rod [115]. As reported by this study, a dispersion in the phase velocity of the transverse and longitudinal BAW is observed, while the rod system is rotated about the radial axis. In the paper, it was illustrated that the theoretical calculations of the linearity of the proposed device were well matched with the experimental results. In 2021, Shevelko et al. presented the experimental results of a novel gyro design which utilizes the propagation of two transverse waves orthogonal to each other in a fused quartz rod [116]. It was noted that the dispersion in the phase velocity of

the two orthogonal transverse BAWs is observed, while the rod system is rotated about the longitudinal axis. In the paper, it was illustrated that the theoretical calculations of the linearity of the proposed device were well matched with the experimental results. The sensitivity of the developed device was estimated to be 340 μV/r/s, where the rotation was applied up to 4 r/s.

As it is clearly seen that there was a limited number of studies performed for elastic wave based gyroscopes, whereas the wave coupling between different waves can lead to more sensitive gyroscopes. In addition, Yu et al. presented the design, fabrication and preliminary test results of a novel gyro design based on an acoustic waveguide [117, 118]. As reported by this study, the operation mechanism of the device is based on the acoustic version of the Sagnac effect in fiber-optic gyros, where the circular air duct is used as an acoustic waveguide. In this configuration, the phase difference between two acoustic waves travelling in opposite directions is measured to detect the rotation rate by correlating the signal to the angular velocity of the hosting frame, where the drive frequency of the developed device is 1.6 Mhz. However, the sound waves are not dispersive and to achieve relatively small device geometry one needs to use high frequencies which necessitate high frequency operation and complex electronics. Further, the fluid mechanics of internal flows under the micro-meter scaled designs does not cover the continuum assumptions, which adds a complexity in the miniaturized sensor designs [119]. These facts limit the miniaturization of a gyroscope based on the acoustic waveguide using the sound waves. On the other hand, dispersive elastic waves propagating in waveguides allow more freedom in selection of the operation frequency and the device geometry where one can choose low velocity waves with smaller wavelengths. Therefore, we focused on elastic waves propagating in rotating rod system to choose the feasible coupling type for a miniaturized gyro design. The coupling of elastic waves propagating in the rotating rod system will be discussed in Chapter 4.

2.2.4 SAW Based MEMS Gyroscopes

Lord Rayleigh discovered the surface acoustic waves (SAWs) in 1885. The SAWs propagate along the surface of elastic mediums. The amplitudes of SAWs decay exponentially regarding to depth into the substrate, while the energy of SAWS is concentrated on the substrate surface, as shown in Fig.13a. Typically, piezoelectric substrates such as lithium niobate, lithium tantalate, and quartz are mostly preferred as the acoustic waveguide. The piezoelectric materials, that have the electromechanical interaction between mechanical stress and electrical charges of the material, allow converting the mechanical energy to the electrical energy and vice versa, which is called piezoelectric effect. The piezoelectric effect is used for the generation and detection of the SAWs. The configuration consists of piezoelectric material and interdigital transducers (IDTs) that are patterned on the piezoelectric material. The IDTs can be divided into three categories as transmitters, receivers and reflectors. For the wave generation, the particle motion is excited by applying electrical input on the electrodes, where the electric field is formed between transmitter IDTs and the piezoelectric effect induces the wave propagation. For the wave detection, the receiver IDTs, which are charged by the arrived acoustic waves, detect the excited SAWs by the help of the reciprocity of the piezoelectricity.

As shown in Fig.13b and Fig.13c, the SAWs are a combination of longitudinal wave and shear wave due to their particle motion in both z and y direction with a phase difference of $\pi/2$. For the particle motion of SAWs, the crucial point is the change of compressional motion to dilatational motion regarding to depth into the substrate, where u_y and u_z decay exponentially with depth inside the substrate material, as shown in Fig.13d. Thus, it had better to use substrates whose thickness is at least five wavelengths in order to avoid any reflection from the bottom surface as reported by Supriyo Datta in [120].

The SAW based gyroscopes have been studied by researchers [121, 122, 123, 124, 125, 126, 127, 128, 40]. The simple device was used by all researchers, which

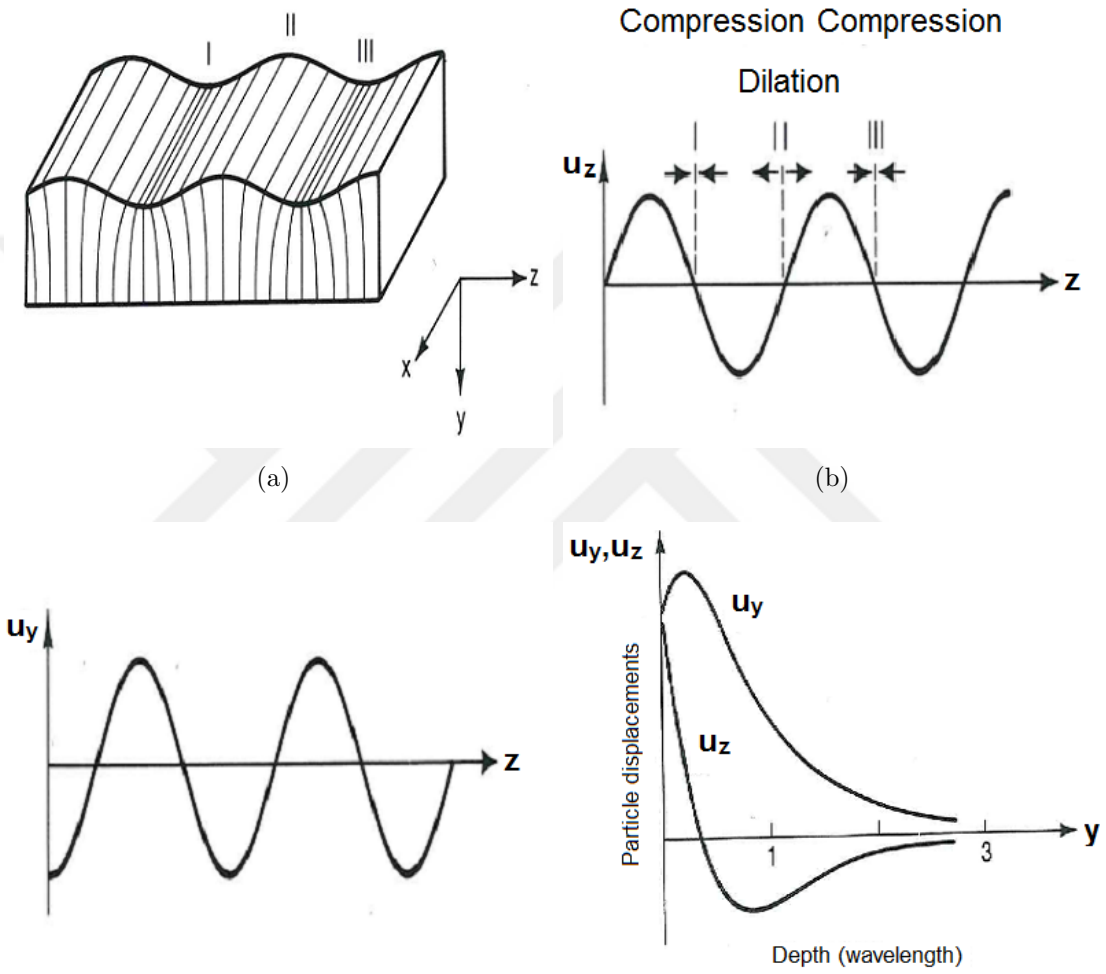


Figure 13: (a) Surface wave in a semi-infinite solid; (b) u_z vs. z at the surface; (c) u_y vs. z at the surface; (d) variation of particle displacement with depth [120].

has a piezoelectric substrate with IDTs, in order to measure the rotation rate as shown in Fig.14. In Fig.14, SAWs are generated on a piezoelectric substrate with two IDTs. The transmitter IDT produces the SAWs and the receiver IDT detects the arrived waves by converting them into electrical signals. When the device is rotated around the x_2-axis, the velocity of the SAW changes. Thus, the applied rotation causes a phase shift on the received signal. The phase shift can be detected by an oscillatory circuit. The oscillation frequency, which is determined by the SAW velocity, can be measured to monitor the rotation rate.

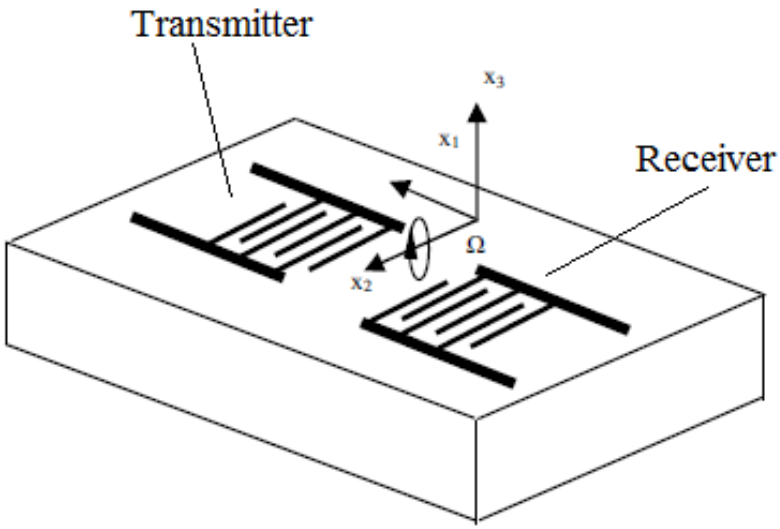


Figure 14: Piezoelectric substrate with IDTs [124].

In general, it is not possible to build a gyroscope by using the SAWs with high sensitivity. The Coriolis force affects the particle motion near and away from the surface oppositely, as shown in Fig.13. That is why the effect of Coriolis force on SAWs is minimal. Further, this Coriolis Effect can be equal to zero for some materials as mentioned in Lao's study [39]. In [39], it was presented that the Coriolis effect on the velocity of SAWs depends on the Poisson's ratio. When the Poisson's ratio is 0.27, the Coriolis Effect is zero. Therefore, SAW based gyroscopes are not the best choice for using as gyroscopes.

Varadan et al. designed a different SAW based gyroscope in order to solve the problem mentioned above [128]. The size of the device is 5 mm to 5 mm. Metal

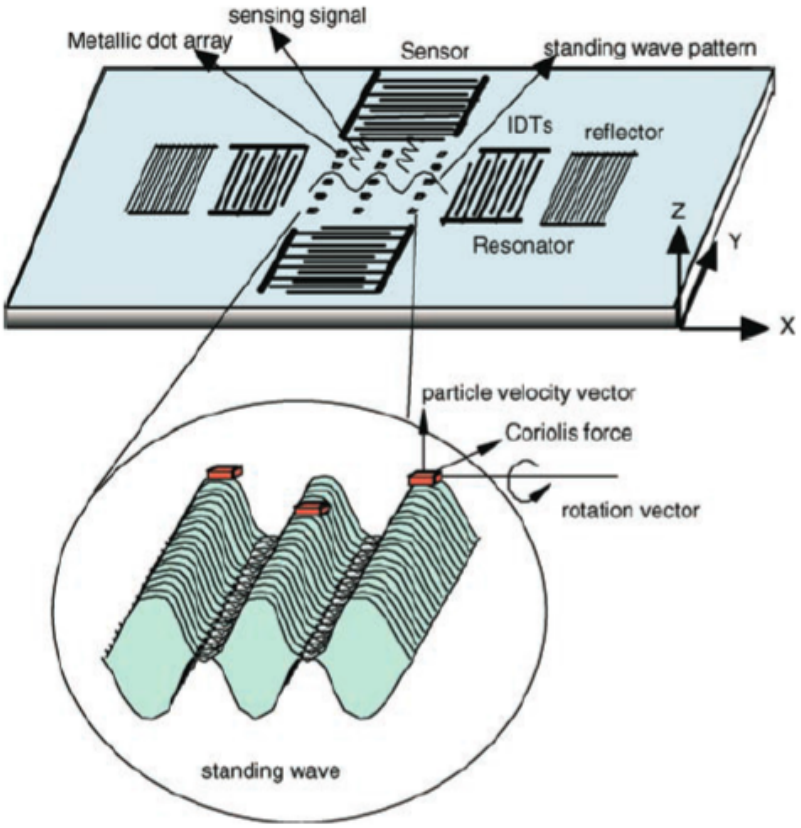


Figure 15: SAW based gyroscope [128].

squares are placed on the propagation path of SAW, as shown in Fig.15. These metal squares start to move up-down (orthogonal to surface) and back-forward (in the propagation direction), while the SAWs propagate through them. As the rotation is applied about the X-axis during the wave propagation, the Coriolis force is exposed to the metal squares about the Y-axis, which is orthogonal to up-down movement of metal squares. Coriolis force generates a second SAW orthogonal to the first SAW. The amplitude of the second SAW is directly proportional to the rotation rate. So, the second SAW can be detected and converted to electrical signals by the receiver IDTs to measure the rotation rate. As a result, it is possible to make a gyroscope in that way. But, the sensitivity of this device is significantly low, where the Coriolis Effect remains again insignificant due to the limitation of the size of metal squares. The main reason of the size limitation is the reflection of SAWs from the metal squares. If thicker metal squares are placed in the propagation path, then the acoustic wave starts to reflect from these metal squares. Thus,

this approach causes the problem of high noise level on the detection systems and it is difficult to make a Z-axis gyroscope in the same piezoelectric body with this method. In conclusion, it is not possible to miniaturize the SAW based devices in order to make a 3-axis MEMS gyroscope.

CHAPTER III

NOISE ANALYSIS OF MODE MATCHED VIBRATORY GYROSCOPES

MEMS technology enabled fabrication of very small and low-cost gyroscopes which made their way to consumer products. The first adapted application was image stabilization for cameras [18]. Later MEMS gyroscopes had been used in gaming and user interfaces. The usage area of MEMS gyroscopes is further expanding to more demanding applications such as automotive, GPS assisted personal navigation (PND) and location-based services (LBS) [19, 20]. Typically, civil and military navigation applications require very high precision optical gyroscopes which are very bulky and expensive. These gyroscopes can deliver very low noise performances which are not attainable by the existing MEMS gyroscopes. To offer a solution for more demanding applications, various MEMS sensor structures have been proposed for improved noise and stability performance [25, 26]. Mode matched gyroscopes are considered one of the best candidates for more demanding applications [129, 16, 130, 28] such as dead reckoning. In a mode matched gyroscope, the sense and drive frequencies are adjusted such that they are as close as possible to each other. The quality factor amplification improves resolution, overall noise floor and bias stability of the sensor [24].

Typical MEMS 2-DOF (two degree of freedom) vibratory gyroscopes employ proof masses coupled by a network of spring system. The drive system oscillates at its resonance and when the rotation is applied, the oscillation couples to the sense system due to Coriolis force. For the mode matched gyroscopes, drive and sense modes have the same resonant frequency. However, matching the mechanical resonances is generally hard to implement due to the fabrication difficulties. One of the common fabrication errors is the anisoelasticity of spring systems which is the

main reason of mechanical quadrature error. Due to the anisoelasticity, the elastic cross-coupling occurs between the principle elastic axes and causes the off-diagonal stiffness. As the off-diagonal stiffness generates the mechanical quadrature signal which increases the noise floor of gyroscopes, the force to rebalance feedback system is used to compensate the quadrature signal by the electrostatic force [30]. Then, the matching typically is achieved by electrostatically modifying the resonant frequencies [23]. This allows increasing the sensitivity by the quality factor of the sense system. Therefore, mode matched vibratory gyroscopes have higher sensitivity and better resolution [25, 26, 28, 24, 27]. In this study, we neglected the anisoelasticity in gyroscopes and focused on Coriolis coupling effect which causes the in-phase error for gyro systems. The aim is to understand how the Coriolis coupling between the drive and sense systems affects the noise floor of mode matched gyroscopes for the open and closed loop operation modes.

Whole angle gyroscopes were introduced to address some of the short comings of the rate-based mode matched gyroscopes [27]. In both regimes, drive and sense sub-systems are coupled together through the Coriolis force [131, 132, 133, 134]. This coupling causes a shift in the resonant frequencies of both systems whereas angle mode gyro is not affected by this shift. However, whole angle gyroscopes have a noise floor which is typically higher than that of rate gyroscopes [135]. On the other hand, the effect of the frequency shift could be ignored for non-mode matched gyroscopes, whereas the effect has impact on the sensitivity of the mode-matched gyroscopes [21]. When a mode matched gyroscope experiences a rotation along its sensitive axis, the performance deteriorates [21]. In this study, we show that these gyroscopes should be evaluated not only for zero rate output performance but also in dynamic cases when they experience a rotation input. In our analyses, we included the Coriolis coupling between the drive and sense systems and calculated the noise performance for rate-mode vibratory gyroscopes.

A comprehensive analysis of noise in MEMS sensors has been presented in [136, 137]. MEMS gyroscopes have been analyzed in [138, 139]. There are two types

of main noise sources; the electrical noise such as thermal (Johnson or Nyquist) noise, generation–recombination noise, flicker noise and the mechanical noise due to the Brownian motion. The electrical noise has received relatively less attention since the ultimate noise of the sensor is determined by the Brownian motion [140]. The mechanical-thermal noise in MEMS gyroscopes has been investigated in terms of angle random walk (ARW), noise equivalent rate (NER) and the power spectral noise density (PSD) of the rate [141]. The Allan deviation is a method of choice to determine the angle random walk [142]. Typically the noise analyses of vibratory gyroscopes have always been carried out for zero-rate input and the dynamic case where the gyro is exposed to an input rotation has been ignored [143, 144, 145].

Here, we perform rigorous noise analyses of mode matched gyro systems by using Allan deviation and power spectral density (PSD) method [146]. We focus on dynamic noise analysis where the sensor is exposed to an input rate and operated in the open loop and force to rebalance modes. We consider only the effect of mechanical noise in mode matched vibratory gyroscopes and neglected the noise of the electronics. We utilized the same approach demonstrated in [131, 132, 133, 134, 21, 141] and extended the analysis for noise calculation where we included the Coriolis coupling between the sense and drive systems. Under rotation input, the resonances of the mode matched gyro shift, which increases the angle random walk in both operation modes. For both operation modes, we further show that the Coriolis coupling between the drive and sense system affects the power spectral density of the mode matched gyro with the generation of low frequency oscillations. In Section 3.1, we present the dynamic model and the Matlab Simulink model. The noise analysis is presented in Section 3.3 where we also discuss the results. In Section 3.4, we used the developed model for a mode-matched gyro which was characterized in terms noise and stability. We verified our model experimentally when the gyro is stationary and try to estimate the noise performance while the gyro experiences rotation.

3.1 Vibratory Gyroscopes System Model

3.1.1 Dynamic Model of Vibratory Gyroscopes

A generic z-axis gyroscope which detects the rotation along the z-axis is shown in Fig.4a. The proof mass vibrates in the drive direction (x) and the sense system detects the vibration of the proof mass in the sense direction (y) due to Coriolis force, as the input rate (Ω_z) is applied. We assumed the rotation axis goes through the point mass 'm'. This does not reduce the generality of the equations but helps us to ignore the DC component of the centripetal force [21]. According to [10], if the angular input rate is constant then the equation of motion is given by Eq.(3.1) for a 2-DOF vibratory gyroscope in a rotating reference frame.

$$\begin{aligned} m\ddot{x} + c_x\dot{x} + k_x x &= +2\Omega_z m\dot{y} + xm\Omega_z^2 + F_X + F_n \\ m\ddot{y} + c_y\dot{y} + k_y y &= -2\Omega_z m\dot{x} + ym\Omega_z^2 + F_Y + F_n \end{aligned} \tag{3.1}$$

where $2\Omega_z m\dot{y}$ and $-2\Omega_z m\dot{x}$ denote Coriolis forces and $xm\Omega_z^2$ and $ym\Omega_z^2$ are centripetal forces. k_x, k_y and c_x, c_y denote spring and damping constants in x and y directions, respectively. F_X is the harmonic force with the amplitude of F_0 which maintains constant drive oscillation (x_0) at the frequency ω. F_Y is the control signal with the amplitude of F_C which equals to zero for the open loop operation mode, whereas it is used in force to rebalance operation mode for the in-phase error compensation. The ensemble averaged mechanical noise force applied at drive and sense systems is calculated as in Eq.(3.2),

$$\langle F_n^2 \rangle = 4k_B T c \tag{3.2}$$

where k_B is the Boltzman constant, T is the temperature and c is the damping of the corresponding system.

For mode matched operations, we assumed that spring constants and damping coefficients are the same for both drive and sense systems ($k = k_x = k_y$, $c = c_x = c_y$). Damping coefficients can be calculated as in Eq.(3.3) where the quality factor is $Q = Q_d = Q_s$. For the drive and sense resonators of 2-DOF vibratory

Parameter	Value	Unit
Resonance Frequency (f)	5000	Hz
Mass (m)	1.01×10^{-6}	kg
Damping Coefficient (c)	3.18×10^{-5}	N.s/m
Spring Constant (k)	1000	N/m
Quality Factor (Q)	1000	1
Bandwidth (BW)	15.7	rad/s
Drive Mode Amplitude (x_0)	1	µm

Table 5: The mode matched vibratory gyroscope parameters.

gyroscopes with a known Q factor, the relation between the oscillation amplitude and the force at resonance can be calculated using Eq.(3.4). In our simulations, we assumed that the drive mode amplitude (x_0) is 1 µm.

$$c_x = \frac{\sqrt{k_x m}}{Q_d},\ c_y = \frac{\sqrt{k_y m}}{Q_s},\ \zeta = \frac{1}{2Q} \tag{3.3}$$

$$F_0 = k_x \frac{x_0}{Q_d},\ F_C = k_y \frac{y_0}{Q_s} \tag{3.4}$$

We designed a mode matched vibratory gyroscope with the Q factor of 1000 where the parameters are presented in Table 5. For our design, the natural frequency ($\omega_0 = 2\pi f$) of both drive and sense mode is calculated as $\sqrt{\frac{k}{m}}$ where the gyro system is lightly damped ($\zeta \ll 1$). When the damping ratio (ζ) is significantly low, the gyro system can be easily disturbed by the random vibrations causing the high level of noise. Therefore, we consider the mechanical noise response in our calculations as the approximated solution for the lightly damped resonators reported in [147]. In [147], the noise response of a lightly damped resonator is defined as a sinusoidal vibration in resonance with the amplitude (C_{ij}) and phase (θ_{ij}) which are slowly varying functions of $\omega_0 t$. The noise response of the gyro system defined in Eq.(3.1) is given as

$$\begin{aligned} &C_{ij}\cos(\omega_0 t - \theta_{ij}) = A_1\cos(\omega_0 t) + A_2\sin(\omega_0 t) \\ &C_{ij} = \sqrt{A_1^2 + A_2^2},\ \theta_{ij} = \tan^{-1}\frac{A_2}{A_1} \qquad \text{for } i = x, y \text{ and } j = x, y \end{aligned} \tag{3.5}$$

where the subscripts (i) and (j) denote the directions of oscillating systems that the mechanical noise force (F_n) is applied on and the mechanical noise response

is resulted in, respectively. When the drive system is excited by a harmonic force $F_X = F_0 \cos(\omega t)$ with the mechanical noise force (F_n), the solutions for the response of both lightly damped drive and sense modes are given as

$$\begin{aligned} x &= C_{xx}\cos(\omega_x t - \theta_{xx}) + C_{xy}\cos(\omega_y t - \theta_{xy}) + \quad x_0\cos(\omega t - \phi_x) \\ y &= \underbrace{C_{yx}\cos(\omega_x t - \theta_{yx}) + C_{yy}\cos(\omega_y t - \theta_{yy})}_{Mechanical\ \ Noise\ \ Response} + \underbrace{y_0\cos(\omega t - \phi_y)}_{Steady-State\ \ Response} \quad \text{for} \quad \Omega_z \neq 0 \end{aligned} \tag{3.6}$$

where $x_0\cos(\omega t - \phi_x)$ and $y_0\cos(\omega t - \phi_y)$ are the steady-state responses; $C_{ij}\cos(\omega_x t + \theta_{ij})$ and $C_{ij}\cos(\omega_y t + \theta_{ij})$ are the noise responses. In the steady state system, the phase of the drive system (ϕ_x) equals to $-90°$, since the drive resonator is oscillated at its resonant frequency ($\omega = \omega_x = \omega_0$). For the sense system induced by the Coriolis force, the sense mode phase (ϕ_y) equals to $-270°$ where the drive and sense modes are matched ($\omega_x = \omega_y$). As a result, the steady-state responses for the mode matched gyro system driven in resonance equal to

$$\begin{aligned} x &= x_0\sin(\omega_0 t) \\ y &= y_0\sin(\omega_0 t) \qquad\qquad \text{where} \quad y_0 = -\Omega_z\frac{2Qx_0}{\omega_0} \end{aligned} \tag{3.7}$$

For the 2-DOF vibratory gyroscope, the resonant frequencies (ω_x, ω_y) shift between the drive and sense mode due to the Coriolis force, as reported in our previous publication [21]. We calculate the Eigen values of the state matrix constructed from Eq.(3.1) where $F_X = F_Y = F_n = 0$. In the Eigen values, the real part equals to the bandwidth and the imaginary part equals the resonant frequency for the gyro system. For the mode matched gyroscopes, both drive and sense systems have the resonance modes at the same frequency ($\omega_0 = \omega_x = \omega_y$), when the input rate is zero. But for non-zero input rates, resonance splitting occurs and there appear two resonances for both drive and sense modes (total of 4 resonances; drive system has two resonances, sense system has two resonances) in their frequency spectra. One set of the resonances shifts down with the increased input rate whereas the other set shifts up. For the mode matched gyro systems,

we showed that the resonant frequency and the bandwidth are solely determined by the input rate as shown below:

$$\omega_{1,2} = \sqrt{\frac{k}{m}} \mp \Omega_z \tag{3.8}$$

$$BW = \frac{\omega_0}{2Q_s} \tag{3.9}$$

where the bandwidth (BW) is calculated as 2.5 Hz (15.7 rad/sec). Based on the Eq.(3.8) and Eq.(3.9), if the rotation rate is less than the gyro bandwidth ($\Omega_z < BW$), the resonances are not separable. But when the input rate is larger than the bandwidth ($\Omega_z > BW$), the two resonance peaks are distinguishable in the frequency domain. Therefore, in the gyro system considered here the frequency shift is negligible up to input rates of 15.7 rad/sec.

For the output detection of the gyro system, the sense amplitude (y) given in Eq.(3.6) is multiplied by the reference signal ($\sin(\omega_x t)$) and the modulated signal passes through the low pass filter (LPF) to detect the rate output (y_0) which is proportional to the rotation rate. In this study, we analyzed two operation modes for the output detection which are open loop operation mode and force to rebalance operation mode. For $\Omega_z < BW$, ω_0 is the resonant frequency for both drive and sense systems ($\omega_x = \omega_y = \omega_0$) where the frequencies of mechanical noise response in the sense system are same with the drive frequency in Eq.(3.6). As a result, the output equals to y_0 with the mechanical noise, since the gyro system is driven at ω_0 for both operation modes. For $\Omega_z > BW$, ω_1 and ω_2 are the resonant frequencies of the drive and sense system, respectively ($\omega_x = \omega_1, \omega_y = \omega_2$) where the frequencies of mechanical noise response in the sense system differs from the drive frequency in Eq.(3.6). In the open loop operation mode, the output equals to

$$Output_{open\ loop\ mode} = y_1 + A\cos(2\Omega_z t - \theta) \qquad \text{for} \quad \Omega_z > BW \tag{3.10}$$

since the gyro system is driven at the higher frequency ($\omega_x = \omega_1$) as in the simulation. y_1 is the degraded sense amplitude (y_0) due to the frequency mismatch

between the drive and sense modes. In Eq.(3.10), the oscillation at the frequency of $2\Omega_z$ appears where A and θ are the corresponding noise amplitude and phase, respectively. In the force to rebalance operation mode, there is only mechanical noise response left in the sense system, as the sense oscillation is forced to zero by FTR feedback system. Hence, the Coriolis coupling between the steady state responses is eliminated, but the Coriolis coupling still occurs between the mechanical noise responses of lightly damped drive and sense systems. In addition to the output detection described above, PI controller adjusts the amplitude of the modulated signal to the Coriolis force after passing through the LPF and then the rate output is obtained in this operation mode. The output equals to

$$Output_{FTR\ mode} = y_0 + A\cos(\Omega_z t) \qquad \text{for} \quad \Omega_z > BW \tag{3.11}$$

since the gyro system is driven at the initial resonant frequency ($\omega_x = \omega_0$) as in the simulation. In Eq.(3.11), the oscillation at the frequency of Ω_z appears where A is the corresponding noise amplitude. Due to the mechanical noise response in the lightly damped gyro system, the low frequency oscillations are generated as in Eq.(3.10) and Eq.(3.11) during the operation of output detection. The low frequency oscillations appear as the peaks in the frequency response of the gyro system which is discussed in the Section 3.3.

3.1.2 MATLAB Simulink Model of Vibratory Gyroscopes

In a typical rate-mode vibratory gyroscope, the drive system is oscillated in a closed loop system and the rate is measured by demodulating the sense output. Fig.16 and Fig.17 show our MATLAB Simulink models for the gyro system with the drive mode oscillation control loop operating in the open loop mode and force to rebalance mode, respectively. In both Simulink models, two noise signals are added to the inputs of the mechanical gyro system in order to simulate the ensemble averaged mechanical noise force given in Eq.(3.2) where the noise signals are generated using the noise tool box in Matlab Simulink. Eq.(3.1) is implemented by the Vibratory Gyroscope box where the Simulink model is shown in Fig.18.

In1/Out1 represents the drive system; In2/Out2 represents the sense system. The most important feature of this implementation is the inclusion of Coriolis force in the feedback for both the drive system and the sense system. Note that the rate input which is denoted by Ω_z in Fig.18, affects both the drive and sense frequency response due to the Coriolis Effect. This manifests itself as two resonance peaks in the drive and sense frequency spectra as in Eq.(3.8). Moreover, centripetal forces are included to the spring forces in Fig.18.

The drive system is oscillated at the resonant frequency in closed loop feedback systems as shown in Fig.16 and Fig.17. The amplitude of drive oscillation is kept constant by the AGC (automated gain control) loop. Components of the AGC are rectifier, low pass filter (LPF), reference amplitude and PI controller. The LPF is a Butterworth filter (8^{th} order) with cut-off frequency of 100 Hz. Other important component is the phase locked loop (PLL) that provides the necessary phase shift to keep the drive oscillator in the drive mode resonance. As we noted earlier, there are two peaks in the frequency spectrum of the drive system as the rotation is applied. For the simulation model, the PLL controller tracks the peak at the higher frequency (ω_1) in the open loop operation mode and holds the operating frequency at the initial resonance (ω_0) in the force to rebalance operation mode. In Fig.19, components of the PLL are demonstrated as low pass filter (LPF), PI controller and voltage control oscillator (VCO) where the output of the VCO is used as reference signals ($\sin(\omega_x t)$, $\cos(\omega_x t)$). We used the same 8^{th} order Butterworth filter with cut-off frequency of 100 Hz in the PLL. Table 6 presents the parameters used in the Matlab Simulink model for both operation modes.

The electrostatic actuation and the capacitive detection are required for driving the gyro system and acquiring the output. In this work, the gain of the capacitance to voltage amplifier ($K_{C/V}$) and voltage to force amplifier ($K_{V/F}$) are set to 1 as shown in Table 6.

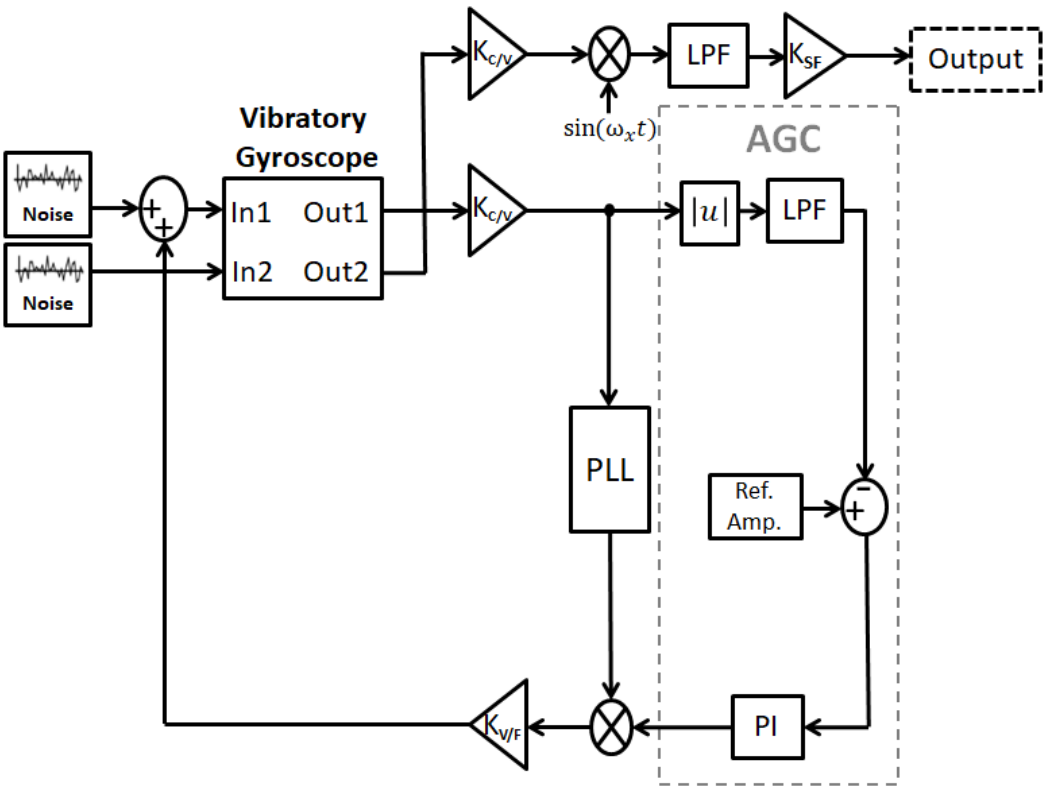


Figure 16: Block diagram of the drive mode oscillation control with the open loop operation mode.

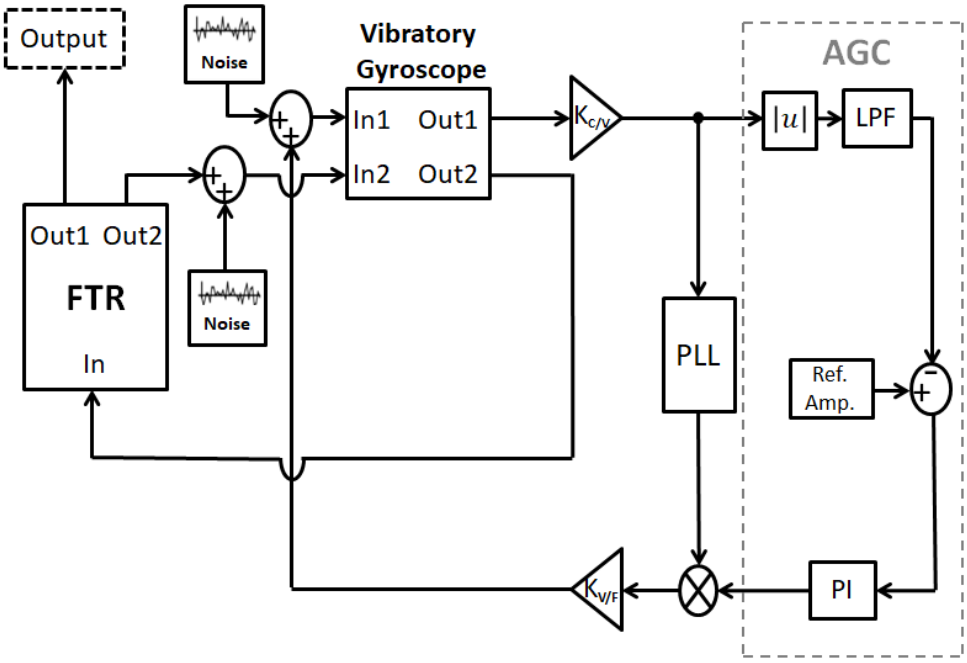


Figure 17: Block diagram of the drive mode oscillation control with the force to rebalance operation mode.

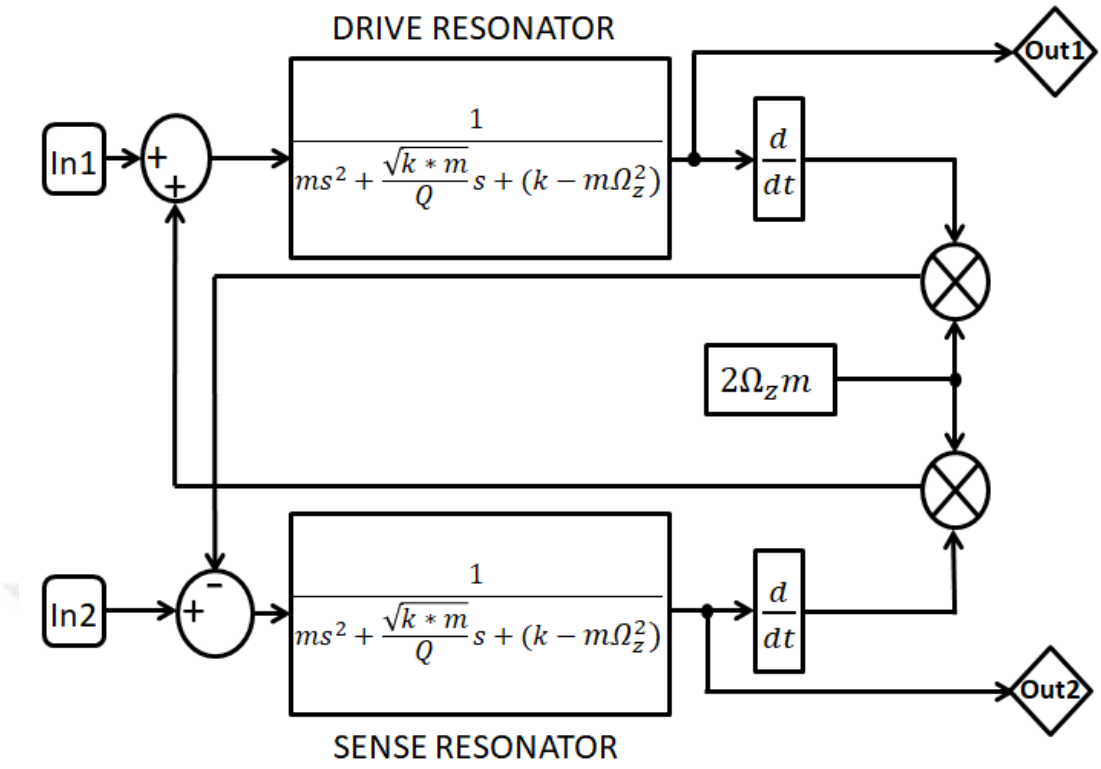


Figure 18: Block diagram of the vibratory gyroscope box.

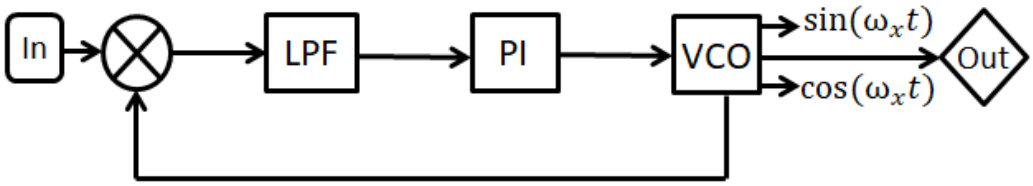


Figure 19: Block diagram of the phase locked loop (PLL) box.

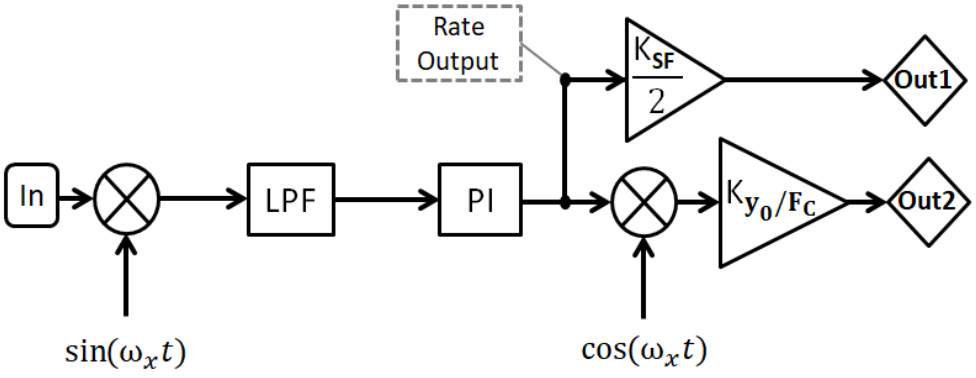


Figure 20: Block diagram of the force to rebalance (FTR) box.

Parameter	Value
$K_{C/V}, K_{V/F}$	1
K_{SF}	$-\omega/(Qx_0)$
K_{y_0/F_C}	k_y/Q_s
Butterworth 8^{th} order LPFs cut-off frequency	100 Hz
Reference Amplitude	$x_0/\frac{\pi}{2}$
PI Controller Constants (AGC)	$K_p = 1$ $K_i = 10$
PI Controller Constants (PLL)	$K_p = 2 \times 10^7$ $K_i = 10^8$
PI Controller Constants (FTR)	$K_p = 1$ $K_i = 50$

Table 6: MATLAB Simulink model parameters.

In the open loop operation mode, the output is obtained by multiplying the sense output with a reference signal as shown in Fig.16. The low pass filter eliminates the AC component and passes the DC component halved in the multiplication which is proportional to the input rate. For the operation of this detection system, the phase of the reference signal should be equal to the phase of the sense signal and thus the VCO output ($\sin(\omega_x t)$) can be used as a reference signal. In our simulations, we chose the scale factor K_{SF} to be

$$K_{SF} = -\frac{\omega}{Qx_0} \tag{3.12}$$

for lower input rates. Therefore, the gyro output is equal to Ω_z. However, for higher input rates the frequency shift in the system becomes considerable and the gyro output deviates from its nominal value. As a result, the system described in Fig.18 does not work linearly. To linearize the system, we multiplied the output by an appropriate scale factor by adjusting K_{SF}. For commercial gyros, this step can be performed during test and calibration. A look-up table is typically used to reduce non-linearity.

In the force to rebalance operation mode, the control signal (F_Y) is used to drive the sense system to zero, which equals to the Coriolis force ($2\Omega_z m\dot{x}$) from

the Eq.(3.1). In Fig.20, components of the force to rebalance (FTR) box are demonstrated as LPF, PI controller and reference signals ($\sin(\omega_x t)$, $\cos(\omega_x t)$). The sense output is represented as In; the gyro output and the control signal (F_Y) are represented as Out1 and Out2, respectively. In the FTR box, the sense output is multiplied by the reference signal ($\sin(\omega_x t)$) and then the rate output (y_0) is calculated, as the modulated signal passes through the LPF and the PI controller. The PI controller regulates the control signal (F_Y) to make $y \approx 0$ with a corresponding feedback signal. For the force to rebalance feedback signal, the Coriolis force is calculated by multiplying the rate output (y_0) with the reference signal ($\cos(\omega_x t)$) and the conversion gain K_{y_0/F_C}. K_{y_0/F_C} is calculated from the Eq.(3.4) for the conversion of the sense displacement (y) to the control signal (F_Y), as shown in Table 6. Finally, the Coriolis signal fed back to the sense system as the control signal (F_Y). The gyro output is determined as Ω_z by scaling the rate output (y_0) with $\frac{K_{SF}}{2}$. Due to the suppression of the sense vibration, Coriolis coupling is eliminated for the steady state response as the linearity is achieved for the gyro system and so, K_{SF} is not adjusted in the force to rebalance operation mode.

3.2 Allan Variance

There are three types of main noise sources for the vibratory gyroscopes; white noise, flicker ($1/f$) noise, and quantization noise. The Allan variance and the Allan deviation are the most common noise analysis method for the vibratory gyroscopes. First, Allan et al. presented the Allan variance method to analyze the frequency stability of clocks and oscillators and later, it is used to represent various noise performances of inertial sensors, such as gyroscopes [142]. This noise analysis is performed for the zero rate inputs at constant temperature, as the gyroscope output is acquired over a period of time. Then, the data binning into groups of different integration times is applied as follows:

$$\overline{\Omega}_n(\tau) = \frac{1}{\tau} \int_{n\tau_0}^{n\tau_0+\tau} \Omega(t) dt \tag{3.13}$$

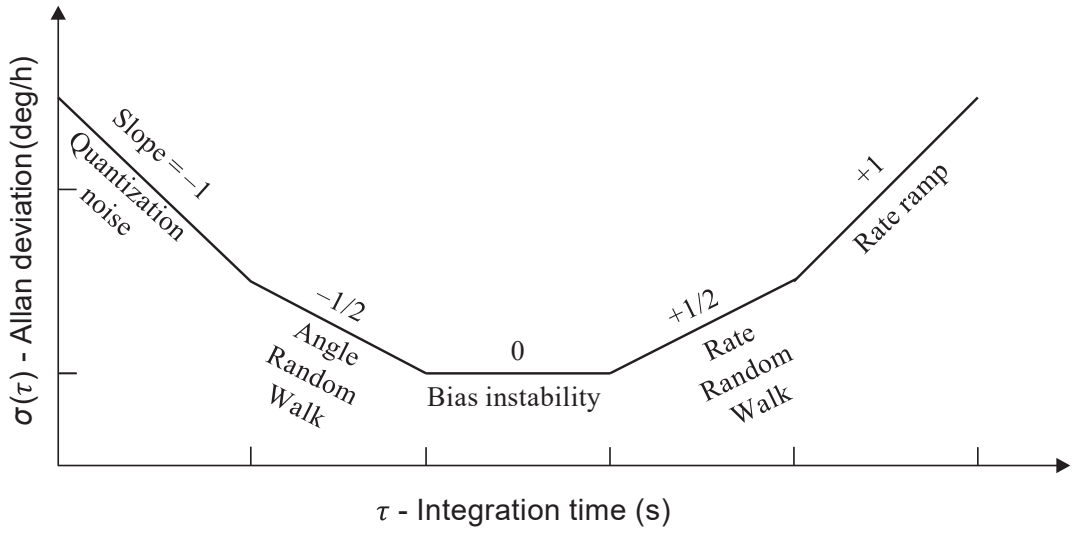


Figure 21: Allan variance analysis of gyroscope output.

where τ_0 denotes the sampling time, n denotes the sample number, and $\tau = m\tau_0$ denotes the bin size. The ensemble average is used to calculate the uncertainty between bins of same integration times:

$$\sigma^2(\tau) = \frac{1}{2}\langle(\overline{\Omega}_{n+m}(\tau) - \overline{\Omega}_n(\tau))^2\rangle \tag{3.14}$$

Eq.3.14 represents the definition of Allan variance. $\sigma^2(\tau)$ denotes the Allan variance as a function of τ and $\langle\rangle$ denotes the ensemble average. The Allan deviation ($\sigma(\tau)$) over integration time is illustrated to get information about various noise processes within the gyroscope in Fig.21. The noise parameters on the Allan deviation curve are explained as below [34]:

Quantization noise: The random variation in the digitized output signal due to sampling and quantizing a continuous signal with a finite word length conversion. It shows up with a slope of τ^{-1}.

Angle Random Walk: The angular error buildup with time that is due to white noise in angular rate, typically expressed in $^\circ/\sqrt{\text{hr}}$. It shows up with a slope of $\tau^{-1/2}$

Bias Instability: The random variation in bias as computed over specified finite sample time and averaging time intervals, characterized by a $1/f$ power

spectral density, typically expressed in °/hr. It shows up with a slope of zero.

Rate Random Walk (RRW): It is the random drift term within the gyroscope and shows up with a slope of $\tau^{+1/2}$ opposite of ARW.

Rate ramp: It is also called the thermal ramp, is caused by temperature changes in the environment and shows up with a slope of τ^{+1}.

In addition, periodic oscillations reveal as peaks in the Allan deviation curve with an integration time of 1/frequency (not shown in the Allan deviation curve). The frequency shift of the drive and sense modes causes the oscillation peaks on the Allan deviation curve for the non-zero rate inputs, which will be shown in the following section.

3.3 Simulation and Results

3.3.1 Open Loop Operation Mode

We calculated the output noise of the gyro described in Section 3.1 by using the model shown in Fig.16 where two separate independent noise sources were added for sense and drive systems separately as described above. Fig.22 shows the PSD of gyro output for various rate inputs. For each curve, we ran the simulations up to 2000 seconds and we ignored the data for the first 10 sec as the transients decayed out within this time frame. We used 1 micro-second time steps (1 MHz sampling rate). Therefore, we obtained almost 2000 second long output data sampled at 1 micro-seconds. We divided this output data in to smaller arrays (total of $\sim$ 500 arrays) and calculated the Fourier transforms of each array. Then we averaged all the Fourier transforms to obtain smoother curves that were shown in Fig.22. The curve corresponding to the zero-rate input is very typical of a gyro output. Above 100 Hz, one can see the effect of the 100 Hz low pass filter at the output which has a slope of 160 dB/dec (8 th order filter). Above 150 Hz the response is determined by the numerical noise and aliasing effects. As the frequency shift is negligible up to the bandwidth of the system (15.7 rad/s), the outputs of PSDs are very similar to each other for zero rate and 10 rad/sec inputs. For higher input rates, the

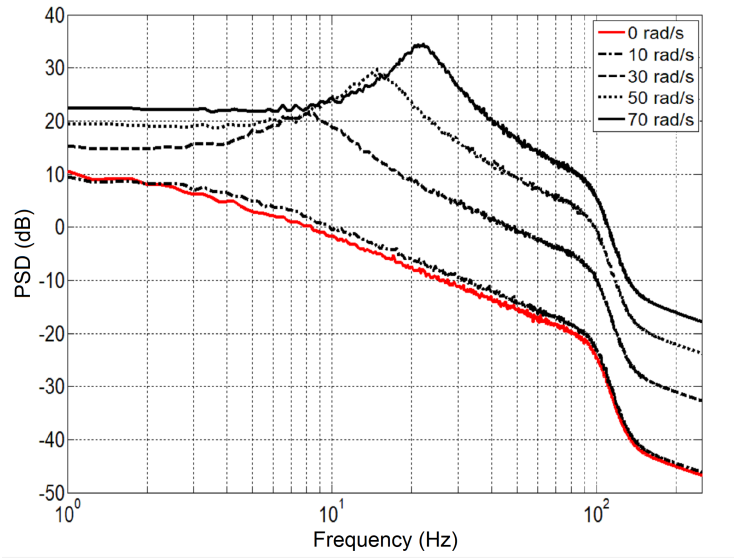


Figure 22: Frequency response of the mode matched vibratory gyroscope for the open loop operation mode where 0 dB = 1 $(^\circ/\text{hr})^2/\text{Hz}$.

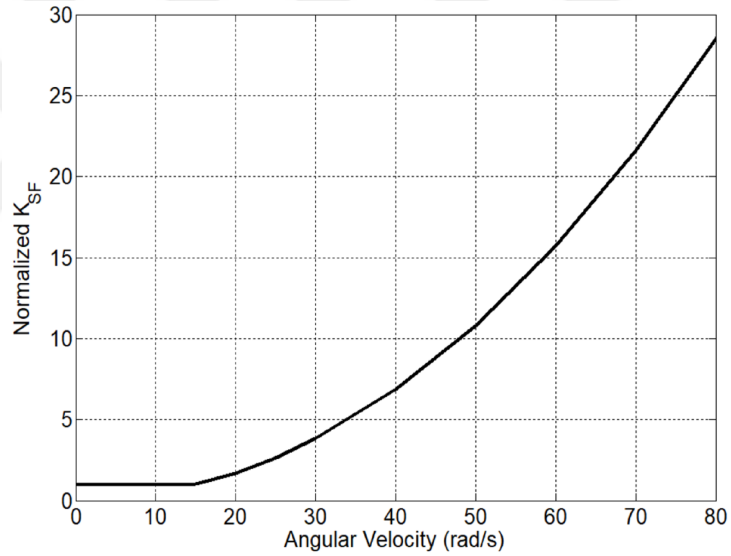


Figure 23: Normalized scale factor K_{SF} as a function of input rate for the open loop operation mode.

resonance shift and splitting become important. Above 15.7 rad/sec, there appear two distinct drive resonances. The PLL controller tracks the higher drive resonance in our model. The amplitude of the sense system which is proportional to the input rate is detected by a simple heterodyne detection (multiplication and low pass filtering) as shown in Fig.16. Typically, the drive output and the sense output are in phase. However, because of the resonance shift and the splitting at higher input rates ($>$ 15.7 rad/sec), there is an additional phase difference between the

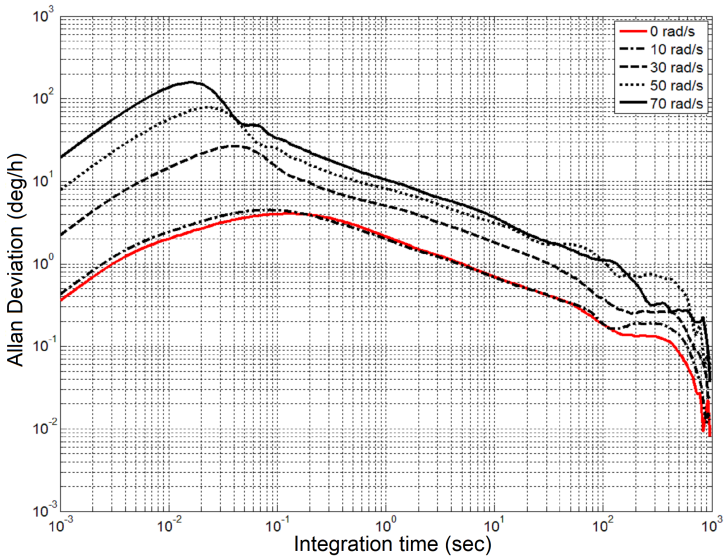


Figure 24: Allan deviation of the mode matched vibratory gyroscope for the open loop operation mode.

drive and the sense. Therefore, gyro output is not accurate for inputs above 15.7 rad/sec. Thus, to linearize the system we adjusted the gain K_{SF} accordingly for 30, 50 and 70 rad/sec inputs. Fig.23 shows normalized K_{SF} as a function of input rate where the normalized K_{SF} is the ratio of adjusted K_{SF} to $-\frac{\omega}{Qx_0}$. As expected normalized K_{SF} is equal to 1 for lower input rates and it increases for higher input rates. Due to this scaling, the noise of gyro system increases for higher input rates (30, 50, 70 rad/sec) as shown in Fig.22. Another drawback of the detection system described above is the generation of a low frequency oscillation which manifest itself as a peaking as shown in Fig.22 for 30, 50, 70 rad/sec inputs between 10 and 20 Hz. As the gyro system has two resonances and PLL tracks the higher resonance ($\omega = \omega_1$), a low frequency oscillation occurs at the output due to the nature of the heterodyne detection. The frequency of the oscillation is determined by the difference between the high and low resonances as calculated in Eq.(3.10). The frequency difference ($\triangle\omega = \omega_1 - \omega_2$) equals to $2\Omega_z$ which corresponds to 9.5, 15.9 and 22.3 Hz for 30, 50 and 70 rad/sec inputs, respectively.

Fig.24 shows the Allan deviation of the outputs calculated in Fig.22. The Allan deviation curves are accurate up to 200 seconds beyond that time the number of points is reduced so much in each bin and the calculation becomes noisier. As

expected higher noise floor in Fig.22 results in higher Allan deviation.

Another important stability parameter is the angle random walk (ARW). For the open loop operation mode, ARW is calculated using the following equation [141]:

$$ARW = \frac{1}{A_g x_0}\sqrt{\frac{k_B T}{mQ\omega}}(\frac{180}{\pi} \times 60) \ \ ^\circ/\sqrt{\text{hr}} \tag{3.15}$$

where the angular gain (A_g) is a proportionality constant which is between 0 and 1. The angular gain is also called as Bryan's factor and the definition of A_g is the ratio of measured rotation output of vibrating pattern to the theoretical rotation output of vibrating body [148]. In our model, the A_g of gyro system decreases, as the measured rotation output deviates from the theoretical output due to the inaccurate output detection for inputs above 15.7 rad/sec. In order to calculate the ARW, we note the value at 1 sec on the Allan deviation curve. ARW is 0.036 $^\circ/\sqrt{\text{hr}}$ in Fig.24 for lower input rates. This value is also in agreement with the result obtained using Eq.(3.15) where $A_g = 1$. ARW increases for higher input rates above 15.7 rad/sec. For higher input rates K_{SF} increases which can be used to estimate $1/A_g$.

3.3.2 Force to Rebalance Operation Mode

We calculated the output noise of the gyro described in Section 3.1 by using the model shown in Fig.17 where we again obtained almost 2000 second long output data sampled at 1 micro-seconds. As described in Section 3.1, the Coriolis coupling between the steady state responses in Eq.(3.6) is eliminated by the suppression of the sense system, but the Coriolis coupling still occurs between the mechanical noise responses of lightly damped drive and sense systems for the FTR mode. In Fig.25, the PSD of the outputs is illustrated for various rate inputs. In the figure, -3dB bandwidth of the FTR mode (BW_{FTR}) is noted as the frequency where the initial value is decreased by 3 dB for each PSD curves. For the zero-rate output, BW_{FTR} is 4.53 Hz (28.5 rad/s). In the FTR mode, the system bandwidth is increased and PLL tracks the initial resonance ($\omega = \omega_0$) of the gyro system. The

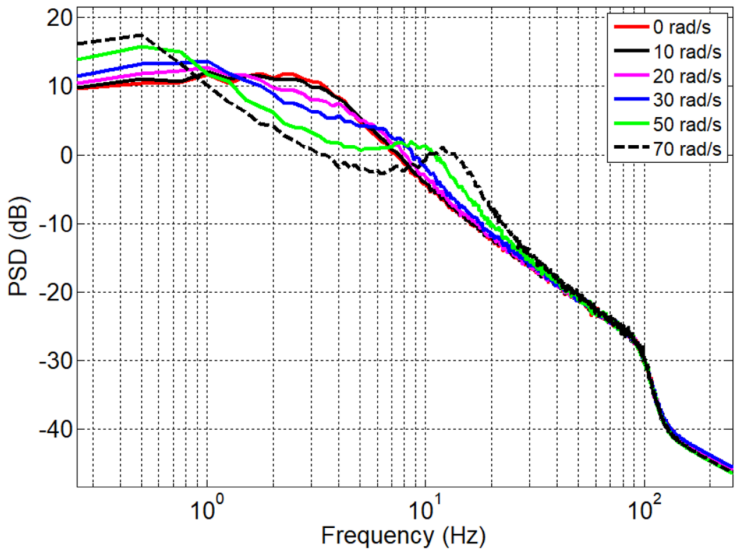


Figure 25: Frequency response of the mode matched vibratory gyroscope for the force to rebalance operation mode where 0 dB = 1 $(^\circ/\text{hr})^2/\text{Hz}$.

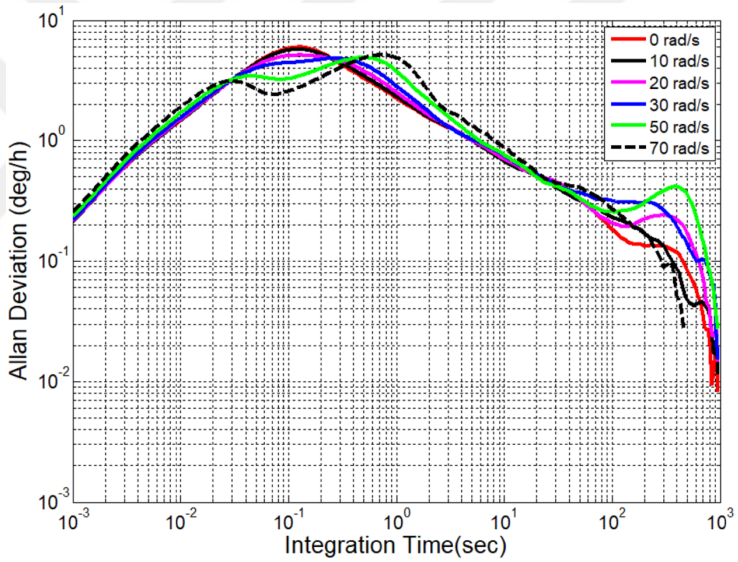


Figure 26: Allan deviation of the mode matched vibratory gyroscope for the force to rebalance operation mode.

PSDs for zero-rate and 10 rad/sec cases are very similar. Input rates above the gyro bandwidth BW, the noise floors increase proportionally with the rotation rate and the low frequency oscillation peaks appears in the spectrum.

For higher input rates, the frequency of the oscillation is calculated as in Eq.(3.11). The frequency equals to Ω_z which corresponds to 3.18, 4.75, 7.95 and 11.15 Hz for 20,30, 50 and 70 rad/sec inputs, respectively. Another drawback of this detection system is the reduction of the system bandwidth, as the rotation is

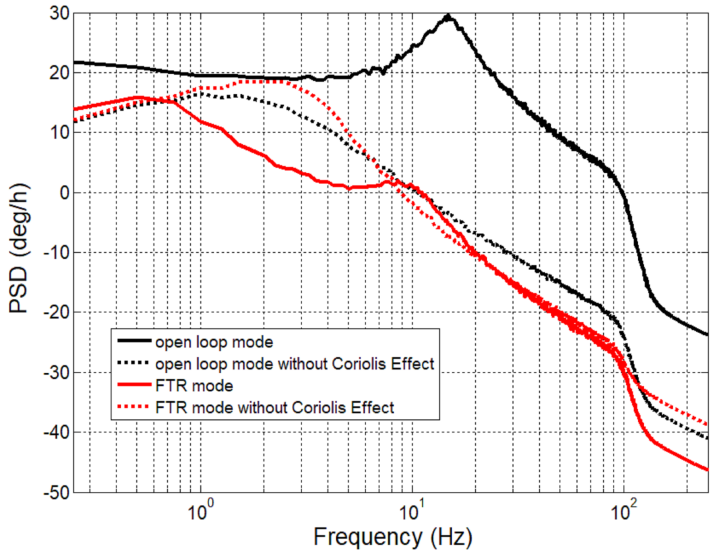


Figure 27: Frequency response of the mode matched vibratory gyroscope for $\Omega_z = 50$ rad/s with and without the Coriolis effect where 0 dB = 1 $(^\circ/\text{hr})^2/\text{Hz}$.

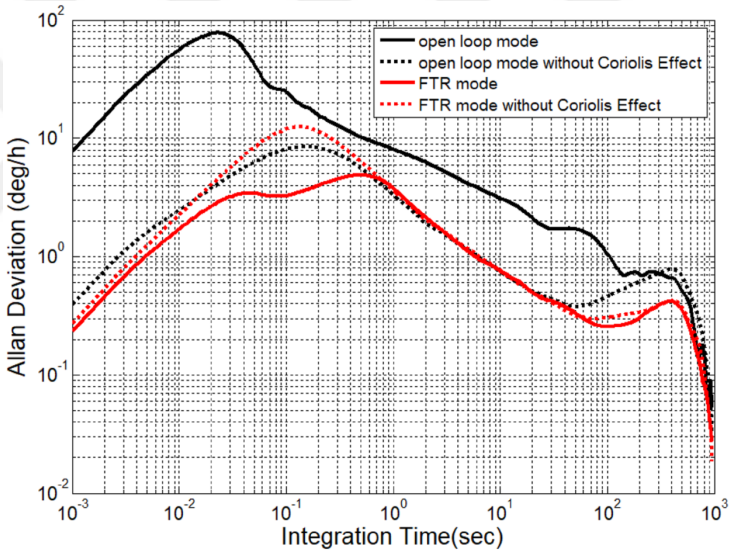


Figure 28: Allan deviation of the mode matched vibratory gyroscope for $\Omega_z = 50$ rad/s with and without the Coriolis Effect.

applied. The BW_{FTR} decreases to 3.6, 2.1, 1.2 and 0.7 Hz for 20, 30, 50 and 70 rad/sec inputs, respectively. In Fig.26, the Allan deviation of the outputs calculated in Fig.25 is illustrated. While the low frequency oscillations are introduced to the output detection due to the Coriolis coupling effect, the bandwidth peak starts to shift from the initial gyro bandwidth (2.5 Hz) to the corresponding system bandwidths for the higher input rates in the Allan deviation plot. This system bandwidth shift increases the ARWs as shown in Fig.26.

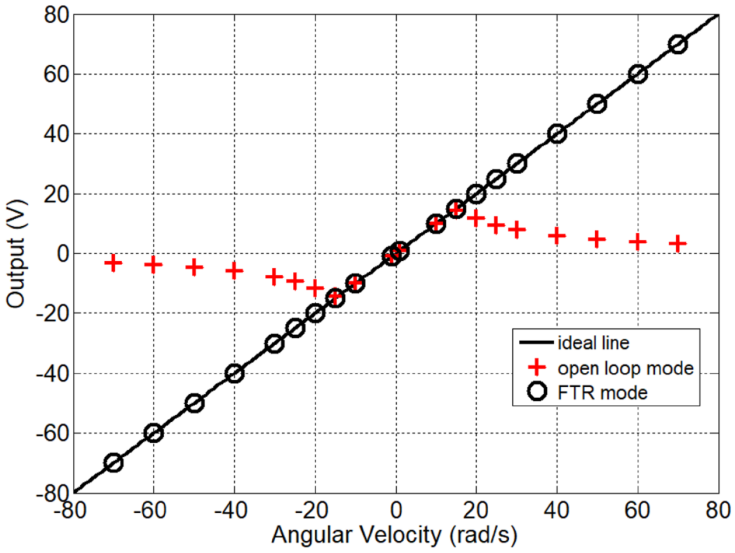


Figure 29: Linearity of the mode matched vibratory gyroscope.

In Fig.27, the PSD of the outputs is illustrated corresponding to the 50 rad/s input rate in order to illustrate the Coriolis Effect. As shown in the figure, the main source of low frequency oscillations is the Coriolis Effect. When we remove the Coriolis force from the input of the drive resonator in Fig.18, we do not observe any low frequency oscillations in the spectrum. In Fig.28, the Allan deviation of the outputs calculated in Fig.27 is illustrated. While the Coriolis force coming from the sense system is ignored, the ARWs are almost similar and the system bandwidth peaks appear at the initial gyro bandwidth (2.5 Hz) for both operation modes.

Fig.29 shows the linearity of gyro system for the two operation systems that we analyzed. The linearity of gyro system shown in Fig.16 is labeled by 'open loop mode' in the figure. As shown in the figure this gyro can only work between -15.7 rad/sec and 15.7 rad/sec. The linearity of gyro system shown in Fig.17 which is labeled by 'FTR mode' in Fig.29. As expected, this gyro system achieves the linearity.

Fig.30 shows corresponding ARWs for the two operation systems described above assuming outputs are linearized using K_{SF}. In the figure, ARWs for the two systems (open loop mode, FTR mode) are noted as the values at 1 sec of

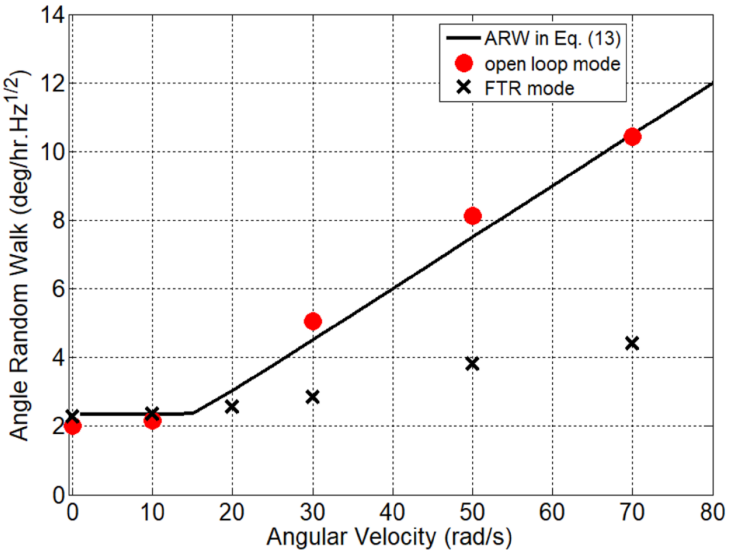


Figure 30: Angle random walk of the mode matched vibratory gyroscope.

each Allan deviation curves in Fig.24 and Fig.26 respectively. The ARW is also calculated by the Eq.(3.15) for the open loop mode which is labeled by 'ARW in Eq.(13)'. In Eq.(3.15), A_g is estimated by the K_{SF}. The 'open loop mode' and 'FTR mode' in Fig.30 matched for the first output calculations. The results of both operation systems show that the output detections may decrease the stability for the rotations above the gyro bandwidth (BW).

3.4 Application of the Model

In this section, we demonstrate the application of the developed model for a mode-matched gyroscope presented in [16], where the mode-matched gyro was characterized in terms of noise and stability and all gyro parameters were readily available. The mode matched gyro of [16] consists of three suspended structures, namely the drive frame, the proof mass frame, and the sense frame. The drive and sense frames are restricted to vibrate along only in one direction (1-DOF), whereas the proof mass frame can vibrate along two orthogonal directions (2-DOF) to achieve Coriolis coupling between the drive and sense systems. Nevertheless, the dynamics

Parameter	Value	Unit
Mechanical Parameters		
Resonance Frequency* (f)	14,182	Hz
Sense Mode Mass* (m_y)	8.43×10^{-8}	kg
Drive Mode Mass** (m_x)	5.22×10^{-8}	kg
Proof Mass* (m_{pm})	3.41×10^{-8}	kg
Sense Mode Damping Coefficient** (c_y)	4.37×10^{-6}	N.s/m
Drive Mode Damping Coefficient** (c_x)	1.39×10^{-7}	N.s/m
Sense Mode Spring Constant** (k_y)	669.36	N/m
Drive Mode Spring Constant** (k_x)	414.48	N/m
Sense Mode Quality Factor* (Q_s)	1719	1
Drive Mode Quality Factor* (Q_d)	33457	1
Bandwidth** (BW^{exp})	4.12	Hz
System Bandwidth* (BW^{exp}_{FTR})	~ 50	Hz
Drive Mode Amplitude* (x_0)	4	μm
Performance Parameters		
Theoretical Mechanical Noise Density*	2.27	$^\circ/\mathrm{hr}\sqrt{\mathrm{Hz}}$
Theoretical Electronic Noise Density*	0.95	$^\circ/\mathrm{hr}\sqrt{\mathrm{Hz}}$
Angle Random Walk* (ARW_{exp})	0.04	$^\circ/\sqrt{\mathrm{hr}}$

* Parameter given in [16].
** Calculated by detailed parameters given in [149].

Table 7: The mode matched vibratory gyroscope parameters of the experiment presented in [16].

of the system can be calculated using the Eq.3.1:

$$\begin{aligned} m_x\ddot{x} + c_x\dot{x} + k_x x &= +2\Omega_z m_{pm}\dot{y} + x m_x\Omega_z^2 + F_X + F_n \\ m_y\ddot{y} + c_y\dot{y} + k_y y &= -2\Omega_z m_{pm}\dot{x} + y m_y\Omega_z^2 + F_Y + F_n \end{aligned} \tag{3.16}$$

where m_{pm} denotes the mass of the proof mass frame. $2\Omega_z m_{pm}\dot{y}$ and $-2\Omega_z m_{pm}\dot{x}$ denote Coriolis forces and $x m_x\Omega_z^2$ and $y m_y\Omega_z^2$ are centripetal forces. m_x denotes the mass of the drive mode, which consists of drive and proof mass frames; m_y denotes the mass of the sense mode, which consists of sense and proof mass frames. In the Simulink model shown in Fig.18, m's should be replaced by the corresponding mass parameters (m_x, m_y, m_{pm}); m_x and m_y are included in the drive and sense resonators, respectively and m_{pm} is used in the Coriolis force term.

The gyro structure studied in [16] operates at 14,182 Hz, where the quality factors of drive and sense modes are equal to 33,457 and 1719, respectively. The drive mode amplitude is kept constant at 4 μm by the AGC and the PLL. The

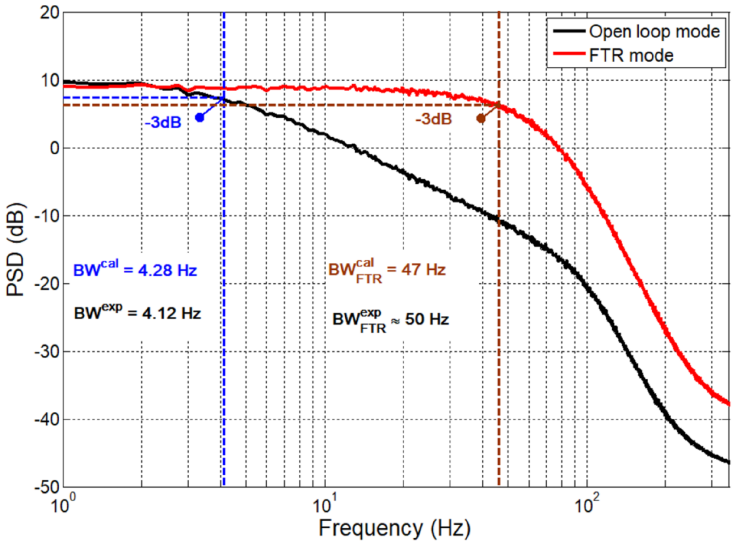


Figure 31: Frequency response of the mode matched vibratory gyroscope model of the experiment for both open loop and force to rebalance operation modes where $\Omega_z = 0$ rad/s and 0 dB = 1 $(^\circ/\text{hr})^2/\text{Hz}$.

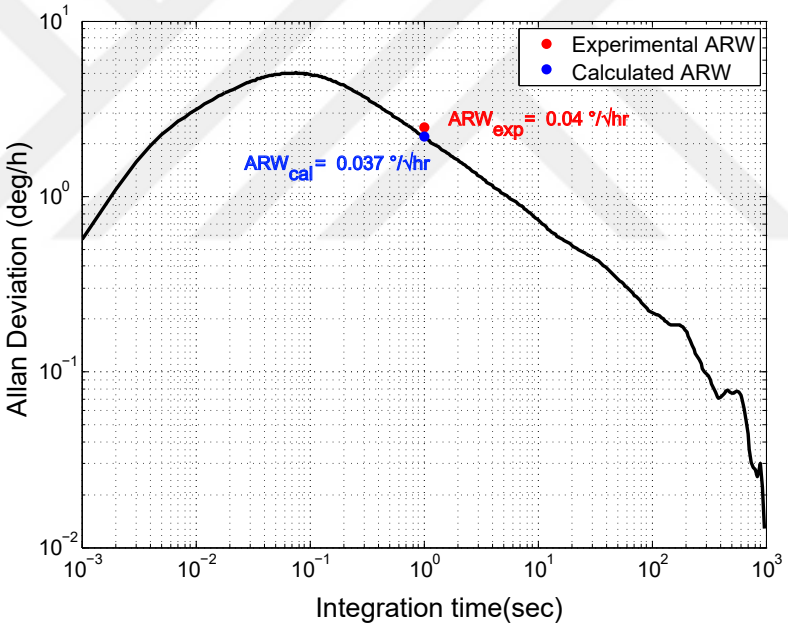


Figure 32: Allan deviation of the mode matched vibratory gyroscope model of the experiment for the force to rebalance operation mode where $\Omega_z = 0$ rad/s.

sense system is operated in the force to rebalance operation mode with the system bandwidth (BW_{FTR}^{exp}) around 50 Hz, where the system bandwidth is adjusted by the PI controller parameters. The mode matched vibratory gyroscope parameters of the experiment are presented in the Table 7.

For the Simulink model of the experimental gyro system, we calculated the

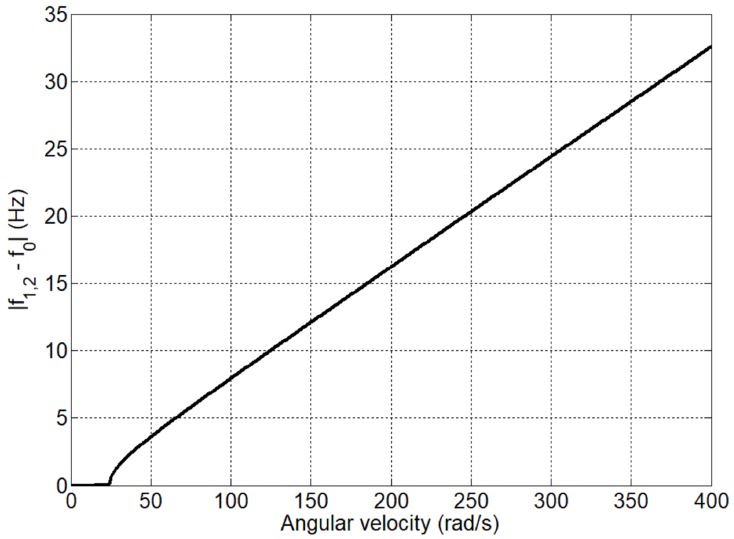


Figure 33: Frequency shift of the drive and sense modes for the mode matched vibratory gyroscope model of the experiment where $\Omega_z \neq 0$ rad/s.

output noise of the gyro by using the models shown in Fig.16 and Fig.17, where we obtained 2000 second long output sampled at 1 micro-seconds. The drive mode amplitude was adjusted to 4 μm by using the AGC and PLL controller parameters presented in Table 8. In the simulation, we chose the scale factor K_{SF} to be

$$K_{SF} = -\frac{\omega m_y}{Q x_0 m_{pm}} \tag{3.17}$$

for the fully decoupled MEMS gyroscopes, where $m_y \neq m_{pm}$. Therefore, the gyro output is equal to Ω_z. First, we performed the simulations for both open loop and FTR modes, where $\Omega_z = 0$ rad/s. In Fig.31, the PSD of the outputs is illustrated for the open loop and FTR modes. In the figure, -3dB bandwidth of the open loop mode (BW^{cal}) is 4.28 Hz, which is in good agreement with the experimental bandwidth (BW^{exp}) of 4.12 Hz. For the FTR mode, we determined the system bandwidth (BW^{cal}_{FTR}) as 47 Hz by adjusting the PI controller parameters of FTR closed loop system box as presented in Table 8. We obtained good match between calculated and experimental system bandwidths, where $BW^{exp}_{FTR} \approx 50Hz$. Fig.32 shows the Allan deviation of the noise curves shown in Fig.31. We calculated the ARW as 0.037 $^\circ/\sqrt{\text{hr}}$, which is in good agreement with the experimental ARW (ARW_{exp}) of 0.04 $^\circ/\sqrt{\text{hr}}$. As expected, the calculated ARW is quite close to the

Parameter	Value
$K_{C/V}, K_{V/F}$	1
K_{SF}	$-\omega m_y/(Qx_0 m_{pm})$
K_{y_0/F_C}	k_y/Q_s
Butterworth 3^{th} order LPFs cut-off frequency	100 Hz
Reference Amplitude	$x_0/\frac{\pi}{2}$
PI Controller Constants (AGC)	$K_p = 0.1$ $K_i = 0.1$
PI Controller Constants (PLL)	$K_p = 5 \times 10^6$ $K_i = 25 \times 10^6$
PI Controller Constants (FTR)	$K_p = 10$ $K_i = 50$

Table 8: MATLAB Simulink model parameters for gyro system presented in [16].

theoretically-calculated mechanical noise, where the thermal noise generated by the electronic system has little effect on the experimental ARW as presented in Table 7. As shown above, we demonstrated a good match between the calculated and measured noise values when the gyro is stationary.

For the dynamic case, the frequency shift between the drive and sense modes can be calculated by the state space model of the gyro, as reported in our previous publication [21]. We calculate the Eigen values of the state matrix constructed from Eq.3.16 where $F_X = F_Y = F_n = 0$. In the Eigen values, the imaginary part equals the resonant frequency for the gyro system. In Fig.33, we calculate the corresponding frequency shift of the drive and sense modes ($|f_{1,2} - f_0|$), as the rotation is applied to the gyro system. As previously presented, the frequency shift of the drive and sense modes causes low oscillation peaks at the frequency response of gyro system. So, the output for the FTR mode given in the Eq.3.11, where $|w_{1,2} - w_0| = \Omega_z$, can be calculated as below:

$$Output^{exp}_{FTR\ mode} = y_0 + A\cos(|w_{1,2} - w_0|t) \qquad \text{for } \Omega_z > BW^{exp} \tag{3.18}$$

for the experimental gyro model. In Fig.34, the PSD is illustrated for various rate inputs. The PSDs for zero-rate and 25 rad/sec cases are very similar, where

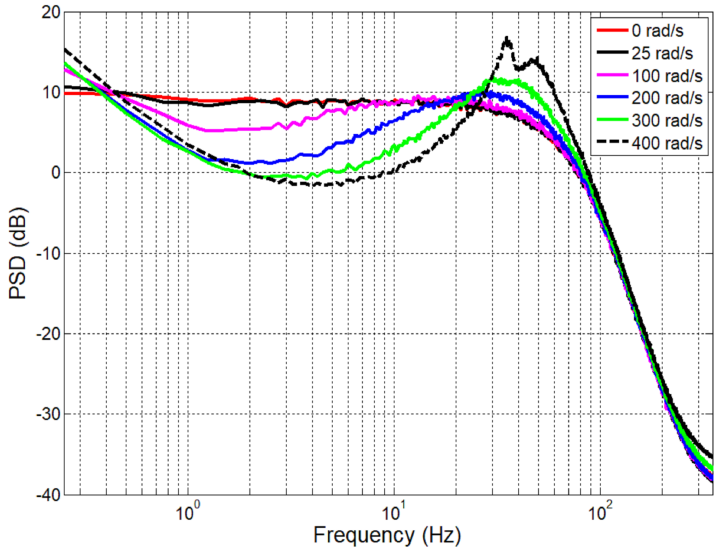


Figure 34: Frequency response of the mode matched vibratory gyroscope model of the experiment for the force to rebalance operation mode where 0 dB = 1 $(^\circ/\text{hr})^2/\text{Hz}$.

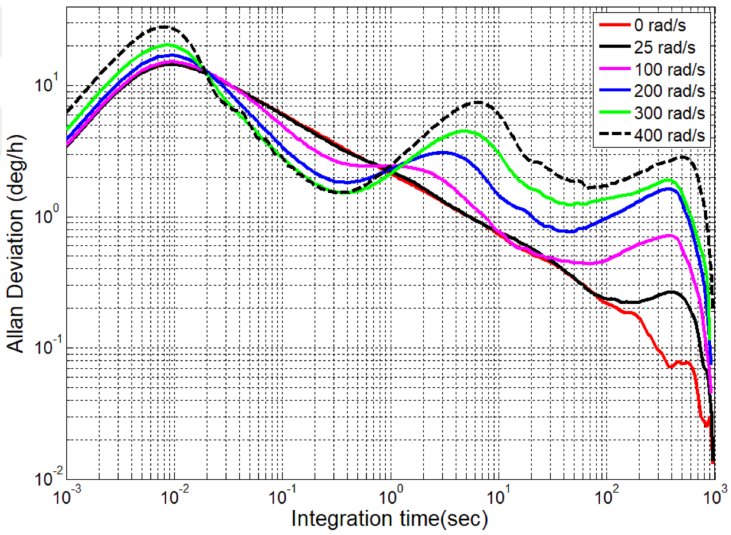


Figure 35: Allan deviation of the mode matched vibratory gyroscope model of the experiment for the force to rebalance operation mode.

$\Omega_z < BW^{exp}$. Input rates above the gyro bandwidth (25.9 rad/s), the noise floor increases proportionally with the rotation rate and noise peaks start to appear in the spectrum for high input rates. For high input rates, the frequency of the oscillation is calculated as in Eq. 3.18. As shown in Fig.33, the frequency equals to $|f_{1,2} - f_0|$ which corresponds to 33 Hz for 400 rad/sec input, where $\Omega_z > BW^{exp}_{FTR}$. This shows that noise peaks can be eliminated by increasing the system bandwidth.

Further, the Allan deviation of Fig.34 is shown in Fig.35. The noise peaks result in overall increase in ARW as shown in Fig.35. As a result, it is clearly seen that the noise performance of a rotating gyro can be significantly different from that of a gyro that does not experience any rotation for mode-matched gyros.

3.5 Discussion

We presented a thorough analysis of mode-matched gyroscope systems. We included the coupling between the drive and sense systems due to Coriolis force in our analysis for rate-mode vibratory gyroscopes. This is the key to see the effect of resonance shift in the performance of the gyro. The most important finding of the analysis is the fact that the phases of the drive and sense modes shift with the input rotation and multiple resonances of the mechanical system appear. When the input rate is above a certain value which can be calculated by the bandwidth of the drive and sense system, the gyro linearity and noise performance degrade a lot. Based on our analyses, the phase shift increases the ARW of the gyroscope system with the typical drive oscillation control system and output detection. It is illustrated that the resonance splitting due to Coriolis Effect results in the generation of peaks at the noise spectrum of the output while the gyro is experiencing high input rotation. Force to rebalance method addresses some of the issues that is associated with the Coriolis coupling. However, under rotation the noise performance is still worse when it is compared to zero input rate case, especially at low frequencies. Further, we show that our results are in good agreement with the experimental results of a gyro studied previously for the static case and we tried to estimate the noise performance of the same gyro under rotation.

CHAPTER IV

CORIOLIS EFFECT ON PROPAGATING WAVES IN RODS

Rotating rod systems have attracted widespread interest in fields such as high power aero-engines [150], gas turbines [151, 152], mass flow meters [153], centrifugal separators, rotor systems and gyroscopes [154, 155]. In many studies, the Coriolis Effect on the elastic waves propagating in the different media such as rods [109, 110], cylindrical shells [111, 112] and beams [113] have been examined, when the medium is subjected to rotation. The coupling of the flexural vibrations in a rotating media was demonstrated for the first time in Bryan's study [156]. In this study, although the Coriolis force was not considered in the calculations, it was found that for a vibrating bell or a cylinder the resonant frequencies shift due to the centrifugal force. Then, Johnson performed theoretical calculations for the in-plane vibration of rotating systems like rotors, shafts and blades [157]. In this research, the coupling of flexural modes due to the Coriolis force was illustrated theoretically, where the resonant frequencies shift. Besides the standing waves examined in the previous work, the Coriolis Effect on the travelling waves in cylindrical shells were presented theoretically for the flexural waves by Srinivasan and Lauterbach [158]. It was reported that the velocity of the forward travelling wave increases whereas the wave velocity corresponding to the backward travelling wave decreases, as the rotation is applied. The coupling of flexural modes due to the Coriolis force was shown experimentally for the first time by the study of Endo et al. [159]. In this study, the flexural vibration of a thin rotating ring was evaluated, where the theoretical calculations of Bryan, Johnson and Srinivasan et al. were compared with the experimental results. Coriolis Effect on rotating rods have been further studied by many scientists [111, 112, 160, 161].

Torsional waves where the particle motion is along the propagation direction have been investigated for the rotors and shafts [162, 163]. In rotor systems which consist of a cylindrical rod with a disk in the middle, the frequency shift has been observed and analyzed. As the external rotation is applied on the radial axis of the rotating rod, the disk starts to move out of plane due to the Coriolis torque. Later, this phenomenon has been also utilized in torsional vibratory gyroscopes [164, 165]. Furthermore, numerous studies have been done to analyze the rods theoretically for various boundary and load conditions in the rotating media, where the elastic waves are coupled due to the Coriolis Effect [166, 167, 168, 169].

The axis of rotation is the determinant factor for the type of the coupling of elastic waves such as flexural-flexural or longitudinal-flexural wave coupling for a finite media; the shear-longitudinal wave coupling for a semi-infinite media. For the flexural-flexural wave coupling, it was found that the resonant frequency of the flexural modes shifts linearly for thin rings by Eley et al., as the rotation is applied perpendicularly to the particle motion of the pair of flexural modes [170]. As reported by this study, the resonant frequency of primary flexural mode increases, whereas the resonant frequency of secondary flexural mode decreases linearly due to the Coriolis force. Recently, this phenomenon has been utilized for the mode-matched gyroscopes using the frequency modulation [171, 172, 173, 174]. For the longitudinal-flexural wave coupling, the effect of constant rotation on the propagation of elastic impact-induced longitudinal and flexural waves in radially rotated rods that undergo large displacement is examined by the Shabana's group [175, 176]. It was shown that dispersion occurs as a result of the applied constant rotation for the longitudinal and flexural waves. For the shear-longitudinal wave coupling, Auriault found that the velocity of the shear and longitudinal wave shift non-linearly, as the rotation is applied perpendicular to the particle motion of the shear and longitudinal wave in a half-space [106]. The velocity of the shear wave decreases, whereas the velocity of the longitudinal wave increases due to the Coriolis force. Furthermore, Ogden et al. presented a similar work for

the plane waves and surface acoustic waves (SAW) where the axis of rotation is applied perpendicularly to the particle motion of the waves [177]. It was noted that the velocities shift non-linearly for both plane and surface acoustic waves due to the Coriolis force in this study. This phenomenon has been also utilized for SAW based gyroscopes, recently [39, 178, 179, 180, 181]. However, the significant analysis performed for the various coupling of the elastic waves propagating in the rotating mediums, the rotating rods have not been studied yet for each type of coupling of elastic waves regarding the axis of rotation.

Here, we present the fundamental governing equations of the wave propagation in a rod experiencing Coriolis Effect. To the author's knowledge, the coupling between various types of waves that may exist in a rod like structure has not been studied in the literature. Our main motivation in this analysis is to present wave equations for the researchers that are working on gyroscopic structures where dispersive waves can be launched in rods. The wavenumber change can be utilized in a gyroscopic sensor to monitor rate of rotation. In the past, the flexural waves have been used in rotating rods to detect rotation rate [182, 25]. Typically, resonant structures have been employed for MEMS gyroscopes. These structures are prone to production difficulties due to the complex construction requirements, and they are susceptible to external shock and vibration. Alternatively, travelling waves can be used as in SAW based MEMS gyroscopes. The main advantage of this configuration is that one can use counter propagating waves in the same rotating waveguide and detect the difference of the velocity change of each propagating wave [39, 40]. This method may reduce the susceptibility to external shock and vibration, temperature effects and packaging induced stresses, which have already demonstrated in SAW based MEMS gyroscopes [41]. However, SAW propagation is not dispersive and to achieve relatively small device geometry one needs to use high frequencies which necessitate high frequency operation and complex electronics. Dispersive waves propagating in rods allow more freedom in selection of the

operation frequency and the device geometry where one can choose low velocity waves with smaller wavelengths. Potentially, wave coupling between different waves can lead to more sensitive gyroscopes. The main purpose of this study is to understand and analyze the wave couplings due to the Coriolis Effect in rotating rod systems in order to provide a basis for novel gyroscope structures. In this study, we analyze fexural-fexural, fexural-longitudinal and fexural-torsional wave coupling separately. We present FEM analysis which confirms our analytical findings and we demonstrate how to use FEA for modeling wave propagation in rods when it is difficult to find analytical solution. We also observed evanescent waves as shown in Fig.40c up to $\sim$ 10 mm where the evanescent wave amplitude quickly decays to zero and the displacement field amplitude converges to the traveling wave amplitude (black curve).

4.1 Theory

4.1.1 Waveguide modes of solid cylindrical rods

Acoustical modes of cylindrical rods have been studied previously by various scientists [183, 184, 185]. In a rod-like waveguide, three types of transverse modes exist; flexural, longitudinal and torsional. Fig.36 shows the particle displacement of the zeroth order of each mode on the cross-section of the waveguide.

Fig.37 shows the wave velocity as a function of frequency in a cylindrical rod. Longitudinal and flexural waves are dispersive whereas torsional waves are not. As shown in Fig.37, for low frequencies 3 modes exist below certain cut-off frequency which is approximately 1 MHz for a 1 mm thick aluminum cylindrical rod.

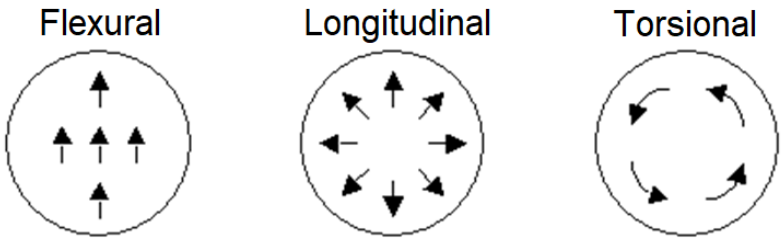


Figure 36: Fundamental modes in a cylindrical waveguide.

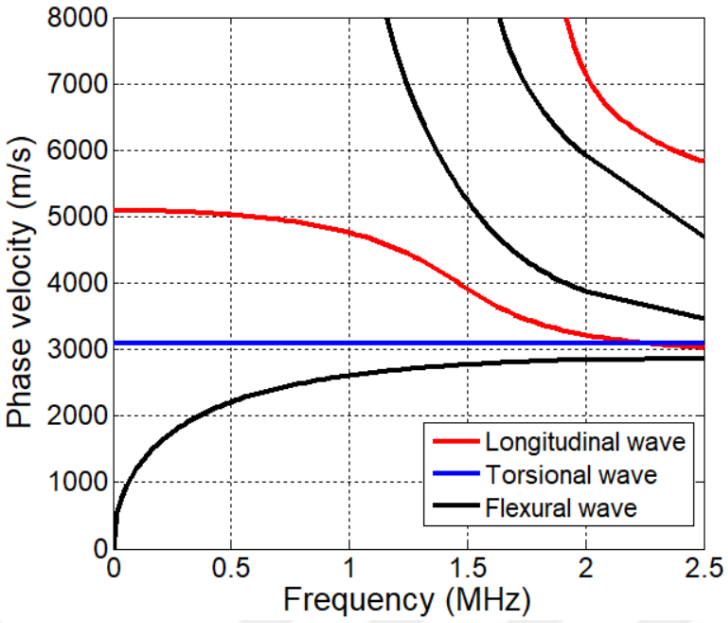


Figure 37: Dispersion curves for a 1 mm thick aluminum cylindrical rod.

Typically, in sensor applications multiple modes are not desirable and a single wave below cut-off frequency is excited. In this study, initially, we assume the wavelength is much larger than the radius ($\frac{r}{\lambda} \leq 0.1$) where typically the first order wave is excited. In this case, one can use one dimensional Euler Bernoulli equations. In the first part of this study, we will perform analytical calculations and then the results will be verified using FEM analysis. Note that FEA analysis can be used for more general cases where radius is not much smaller than the wavelength.

The governing equations for flexural, longitudinal and torsional waves propagating in rods with the radius (r) were presented in [105]. In the next sections, they were included to establish the notation. In these equations, only one dimension of the particle motion is considered for the wave propagation in rods, where the particle motion is perpendicular, parallel or along the direction of propagation for flexural, longitudinal and torsional waves, respectively. The particle motion of the elastic waves driven by constant frequency (ω_0) is affected by the Coriolis acceleration, as the rotation is applied. As a result of the Coriolis Effect on the particle motion, the elastic waves in a rotating media couple with each other based

on the axis of rotation. Therefore, the governing equations affected by the Coriolis acceleration are derived for each coupling of elastic waves for the rotating rods. The theoretical calculations for travelling elastic waves in a rotating media show that the Coriolis coupling shifts the wavenumbers of elastic waves. For a typical gyroscopic sensor, the rod length must be much longer than the wavelength to detect the change in the wave number. Long waveguide also allows pulse-mode operation where multiple reflections from the ends of the waveguide can be clearly separated in time domain. In a long waveguide compared to the wavelength, the contribution of near field effects and evanescent waves are negligible, thus we focused only on the travelling waves and the effect of evanescent waves are not considered in the governing equations.

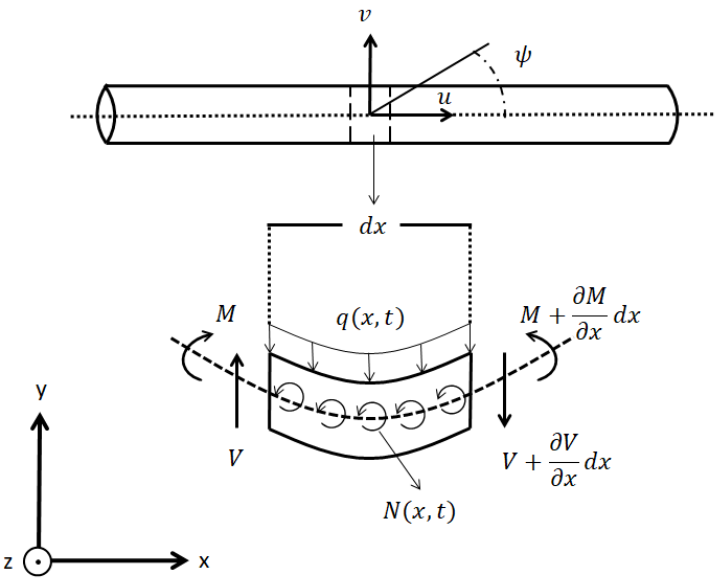
4.1.2 Governing Equations

4.1.2.1 Flexural waves in rods

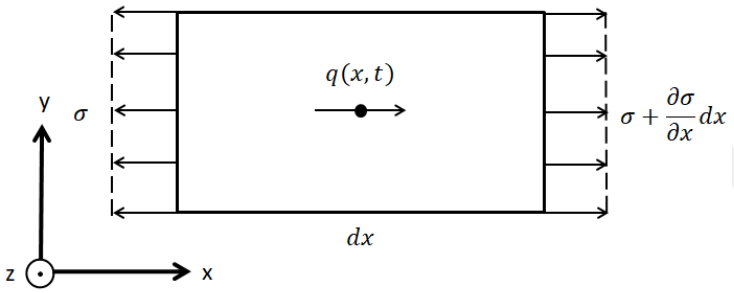
Flexural waves in rods can be analyzed considering the shear force (V) and the bending moment (M) as shown in Fig.38a. In Fig.38a, the particle motion of the flexural wave propagating in the x direction is transversal for a uniform elastic rod, where the $\psi(x,t)$ is the angular displacement along z axis and $v(x,t)$ is the transverse displacement in the y axis for the neutral axis of the rod. The Euler Bernoulli beam theory is the simplest way of explaining the flexural motion in beams, so we utilize this theoretical approach to set the internal force system for flexural waves in the elastic uniform rods. Thus, the equation of motion is given by the Euler Bernoulli beam theory for flexural waves in the uniform rods as

$$q(x,t) = EI\frac{\partial^4 v}{\partial x^4} + \rho A\frac{\partial^2 v}{\partial t^2} \tag{4.1}$$

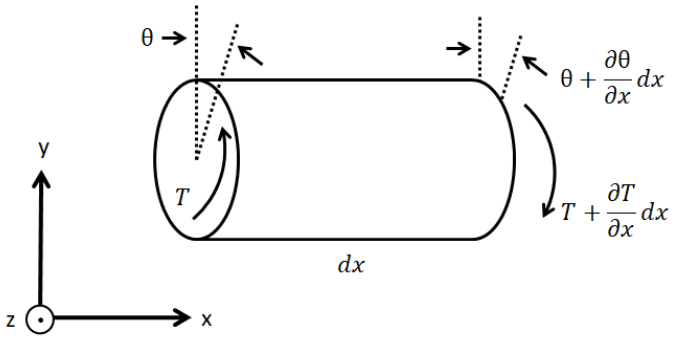
where E, A, ρ and I denote the elasticity modulus, cross-sectional area, density and moment of inertia, respectively. Eq.(4.1) assumes the particle motion is uniform across the cross section of the rod which is the case when the wavelength is larger than the radius. $q(x,t)$ indicates the distributed force load on the rod as



(a)



(b)



(c)

Figure 38: A thin rod with linear displacements u, v and angular displacements θ, ψ where the differential element of rod subjected to **(a)** various transverse loads, **(b)** longitudinal load, and **(c)** torsional load.

shown in Fig.38a. For the distributed couple load $N(x,t)$ on the rod, the equation of momentum for flexural waves by the Euler Bernoulli beam theory is given as

$$-\frac{\partial^2 N(x,t)}{\partial x^2} = EI\frac{\partial^4 \psi}{\partial x^4} + \rho A\frac{\partial^2 \psi}{\partial t^2} \tag{4.2}$$

For a rod, the relation between the frequency (ω) and the wavenumber (k_{F0}) can be derived by using Eq.(4.1) and Eq.(4.2) as

$$\omega = k_{F0}^2\sqrt{\frac{EI}{\rho A}} \tag{4.3}$$

in the absence of body forces and torques where the harmonic wave propagation is considered as $v = B_1 e^{j(kx-\omega t)}$ and $\psi = B_2 e^{j(kx-\omega t)}$. The zero added to the subscript of k_F to indicate that the rod is not experiencing any rotation. We use Eqs.(4.1), (4.2) and (4.3) in our theoretical calculations for the flexural waves in the rotating rods.

4.1.2.2 Longitudinal waves in rods

Longitudinal waves are defined with the distribution of stress fields (σ) on an infinitesimal element of the rod, as shown in Fig.38b. In Fig.38b, the direction of axial particle motion for the longitudinal wave (u) is in the x axis as same with the direction of wave propagation for a uniform elastic rod. For the uniform elastic rod, the axial deformations along the neutral axis of the rod are considered as the same in all points of the cross section, and also the transverse deflections are neglected as reported in [105]. On the basis of these assumptions for longitudinal waves in the uniform rods, the equation of motion is given as

$$E\frac{\partial^2 u}{\partial x^2} + q(x,t) = \rho\frac{\partial^2 u}{\partial t^2} \tag{4.4}$$

where $u(x,t)$ is the displacement in the x direction. $q(x,t)$ indicates the body force per unit volume as shown in Fig.38b. For a rod, the natural frequency (ω) and wavenumber (k_{L0}) of the longitudinal wave are derived by the Eq.(4.4) as

$$\omega = k_{L0}\sqrt{\frac{E}{\rho}} \tag{4.5}$$

in the absence of body forces where the harmonic wave propagation is considered as $u = Be^{j(kx-\omega t)}$. We use the Eq.(4.4) and Eq.(4.5) in our theoretical calculations for the longitudinal waves in the rotating rods.

4.1.2.3 Torsional waves in rods

Torsional waves are defined with an infinitesimal element of the rod subjected to the variable end torques (T), as shown in Fig.38c. In Fig.38c, the angular particle motion of the torsional wave (θ) propagating in the x direction lies in the $y-z$ plane for a uniform elastic rod. For the uniform elastic rod, the angular deformations around the longitudinal axis of the rod are considered as a distribution of stress over the cross section which is proportional to the radial distance, and also the radial deflections are neglected as reported in [105]. According to these assumptions for torsional waves in the uniform rods, the equation of motion is given as

$$C\frac{\partial^2\theta}{\partial x^2} + N(x,t) = \rho J\frac{\partial^2\theta}{\partial t^2} \tag{4.6}$$

where J, C and $\theta(x,t)$ denote polar moment of inertia, shear rigidity and angular displacement about the x axis, respectively. $N(x,t)$ indicates the external body torque on the rod as shown in Fig.38c. For a rod, the natural frequency (ω) and wavenumber (k_{T0}) of the torsional wave are derived by the Eq.(4.6) as

$$\omega = k_{T0}\sqrt{\frac{C}{\rho J}} \tag{4.7}$$

in the absence of body torques where the harmonic wave propagation is considered as $\theta = Be^{j(kx-\omega t)}$. We use the Eq.(4.6) and Eq.(4.7) in our theoretical calculations for the torsional waves in the rotating rods.

4.1.3 Elastic waves in rotating rods

4.1.3.1 Flexural wave - Flexural wave Coupling

In a rod, flexural waves are emerged as the superposition of a pair of elastic waves orthogonal to each other, as shown in Fig.39a. In Fig.39a, the center of the cross section coincides with the x axis where the primary flexural wave (v) and the

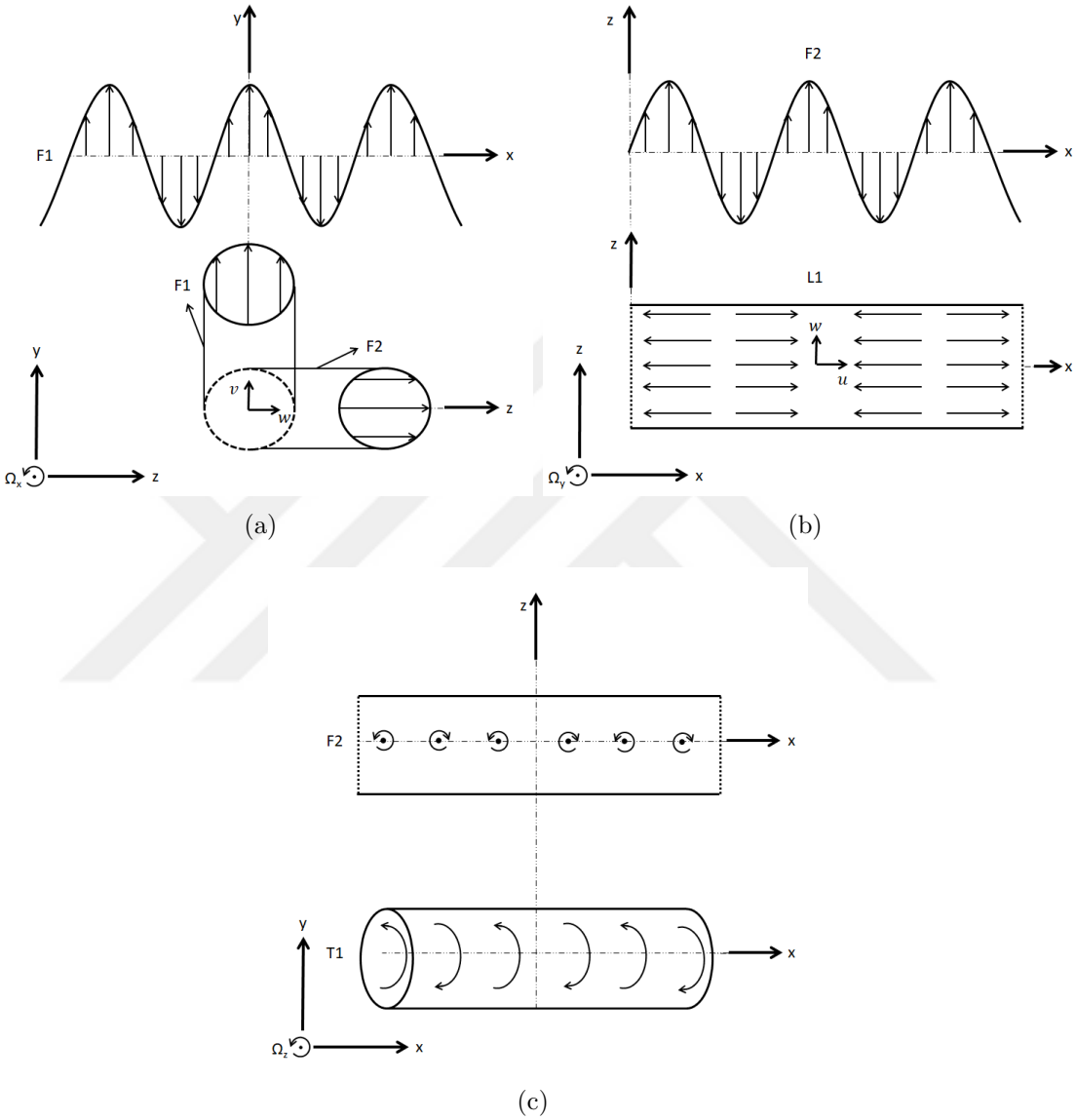


Figure 39: **(a)** Flexural wave-flexural wave coupling between primary flexural wave (F1) and secondary flexural wave (F2), **(b)** flexural wave-longitudinal wave coupling between flexural wave (F2) and longitudinal wave (L1), and **(c)** flexural wave-torsionl wave coupling between flexural wave (F2) and torsional wave (T1).

secondary flexural wave (w) vibrate in the y and z direction, respectively. While constant rotation (Ω_x) is applied about the longitudinal axis (x), the Coriolis force and the centrifugal force are denoted by $q(x,t)$ in Eq.(4.1). For the rotating rod shown in Fig.39a, the secondary flexural wave is induced by the Coriolis force and starts to travel with the primary flexural wave when the primary flexural wave is driven. This causes that the pair of flexural waves is coupled due to the Coriolis force. The Coriolis forces are denoted by $2\rho A(\Omega_x \times \frac{\partial w}{\partial t})$, $-2\rho A(\Omega_x \times \frac{\partial v}{\partial t})$ and the centrifugal forces are denoted by $\rho A v\Omega_x^2$, $\rho A w\Omega_x^2$. As a result, the equations of motion for the pair of flexural waves in a rotating reference frame are given as

$$v\Omega_x^2 + 2(\Omega_x \times \frac{\partial w}{\partial t}) = \frac{EI}{\rho A}\frac{\partial^4 v}{\partial x^4} + \frac{\partial^2 v}{\partial t^2} \tag{4.8}$$

$$w\Omega_x^2 - 2(\Omega_x \times \frac{\partial v}{\partial t}) = \frac{EI}{\rho A}\frac{\partial^4 w}{\partial x^4} + \frac{\partial^2 w}{\partial t^2} \tag{4.9}$$

We consider the harmonic waves propagating in a rod as

$$v = B_1 e^{j(kx-\omega t)}, w = B_2 e^{j(kx-\omega t)} \tag{4.10}$$

and substitute Eq.(4.10) in Eq.(4.8) and Eq.(4.9). The following two homogenous equations in B_1, B_2 are obtained as

$$(\frac{EI}{\rho A}k^4 - \Omega_x^2)B_1 = \omega^2 B_1 - j2\Omega_x\omega B_2 \tag{4.11}$$

$$(\frac{EI}{\rho A}k^4 - \Omega_x^2)B_2 = \omega^2 B_2 + j2\Omega_x\omega B_1 \tag{4.12}$$

Eq.(4.11) and Eq.(4.12) can be rewritten in the matrix form as

$$\begin{bmatrix} (\frac{EI}{\rho A}k^4 - \Omega_x^2) - \omega^2 & +j2\Omega_x\omega \\ -j2\Omega_x\omega & (\frac{EI}{\rho A}k^4 - \Omega_x^2) - \omega^2 \end{bmatrix} \begin{bmatrix} B_1 \\ B_2 \end{bmatrix} = 0 \tag{4.13}$$

where the elastic waves are generated by constant frequency ($\omega = \omega_0$). Equating the determinant of coefficients to zero in Eq.(4.13) gives the wavenumber equation induced by the rotation (Ω_x) as

$$k^8 - k^4(2\omega_0^2 + 2\Omega_x^2)\frac{\rho A}{EI} + (\omega_0^2 - \Omega_x^2)^2(\frac{\rho A}{EI})^2 = 0 \tag{4.14}$$

where k equals to uncoupled wavenumber (k_{F0}) given in Eq.(4.3) for the inertial medium ($\Omega_x = 0$). In our analysis, we assume that the primary flexural (F1) wave is driven initially. When $\Omega_x \neq 0$, the secondary flexural (F2) wave is also driven with the primary flexural wave due to the Coriolis coupling, which causes the change in wavenumbers of both travelling waves, as presented in Eq.(4.14). As the pair of the flexural wave couples, the solution of Eq.(4.14) gives the wavenumbers for the primary and secondary flexural wave separately by the following expression:

$$k^4_{F1,F2} = \frac{\rho A}{EI}\left(\frac{(2\omega_0^2 + 2\Omega_x^2) \pm \sqrt{(2\omega_0^2 + 2\Omega_x^2)^2 - 4(\omega_0^2 - \Omega_x^2)^2}}{2}\right) \tag{4.15}$$

While the ω_0 is the critical point in Eq.(4.15), the wavenumbers equal to

$$\begin{aligned} k_{F1} &= \sqrt[4]{\frac{\rho A}{EI}(\omega_0 + \Omega_x)^2}, \\ k_{F2} &= \sqrt[4]{\frac{\rho A}{EI}(\omega_0 - \Omega_x)^2}, \qquad \text{for } \Omega_x < \omega_0 \end{aligned} \tag{4.16}$$

$$\begin{aligned} k_{F1} &= \sqrt[4]{\frac{4\rho A\omega_0^2}{EI}}, \\ k_{F2} &= 0, \qquad \text{for } \Omega_x = \omega_0 \end{aligned} \tag{4.17}$$

$$\begin{aligned} k_{F1} &= \sqrt[4]{\frac{\rho A}{EI}(\omega_0 + \Omega_x)^2}, \\ k_{F2} &= \sqrt[4]{\frac{\rho A}{EI}(-\omega_0 + \Omega_x)^2}, \qquad \text{for } \Omega_x \geq \omega_0 \end{aligned} \tag{4.18}$$

Eq. (4.16) implies that the wavenumber (k) increases for the primary flexural wave and decreases for the secondary flexural wave, while $\Omega_x < \omega_0$. For $\Omega_x = \omega_0$, the wavenumber becomes zero for the secondary flexural, which causes to stop the wave propagation as given in Eq. (4.17). Eq. (4.18) indicates that the wavenumbers of both flexural waves start to increase, while $\Omega_x > \omega_0$. In our analysis, we use the corresponding wavenumbers calculated from the Eq.(4.14) for the flexural-flexural wave coupling.

4.1.3.2 Longitudinal wave - Flexural wave Coupling

In a rod, the particle motions of longitudinal and flexural waves are orthogonal to each other, as shown in Fig.39b. In Fig.39b, the center of the cross section coincides with the x axis, where the starting point of rod is at the origin. In the figure, it is also shown that the longitudinal wave (u) and the flexural wave (w) vibrate in the x and z directions, respectively. While constant rotation (Ω_y) is applied from the origin through the normal axis (y), $q(x,t)$ is the Coriolis and the centrifugal forces in Eq.(4.1) and Eq.(4.4). For the rotating rod shown in Fig.39b, the longitudinal wave is induced by the Coriolis force and starts to travel with the flexural wave when the flexural wave is driven. This causes the coupling between longitudinal and flexural waves due to the Coriolis force. The Coriolis forces are denoted by $2\rho(\Omega_y \times \frac{\partial w}{\partial t})$, $2\rho A(\Omega_y \times \frac{\partial u}{\partial t})$ and the centrifugal forces are denoted by $\rho(u+x)\Omega_y^2$, $\rho A w\Omega_y^2$. The centrifugal tension force is also included to the equation of motion as $T(x)\frac{\partial^2 w}{\partial x^2}$ where $T(x) = \rho A\Omega_y^2\frac{[L^2-x^2]}{2}$, since the rotation is applied radially to the rod with the length (L). As a result, the equations of motion for the longitudinal and flexural wave in a rotating reference frame are given as

$$(u+x)\Omega_y^2 + 2(\Omega_y \times \frac{\partial w}{\partial t}) = \frac{\partial^2 u}{\partial t^2} - \frac{E}{\rho}\frac{\partial^2 u}{\partial x^2} \tag{4.19}$$

$$w\Omega_y^2 - 2(\Omega_y \times \frac{\partial u}{\partial t}) = \frac{EI}{\rho A}\frac{\partial^4 w}{\partial x^4} - \frac{T(x)}{\rho A}\frac{\partial^2 w}{\partial x^2} + \frac{\partial^2 w}{\partial t^2} \tag{4.20}$$

where $\rho x\Omega_y^2$ and $T(x)$ are negligible for higher excitations and small rotation rates, respectively. Due to the spatially varying loads on the rod, it is impossible to obtain an analytical solution as reported in [110]. In order to ignore the spatial effects in our calculations, we carry out the analysis for the high drive force and the small rotation rates to determine the Coriolis coupling between longitudinal and flexural waves precisely. Thus, we consider the harmonic waves propagating in a rod as

$$u = B_1 e^{j(kx-\omega t)}, w = B_2 e^{j(kx-\omega t)} \tag{4.21}$$

and substitute Eq.(4.21) in Eq.(4.19) and Eq.(4.20) by subtracting the spatially varying parts. The following two homogenous equations in B_1, B_2 are obtained as

$$(\frac{E}{\rho}k^2 - \Omega_y^2)B_1 = \omega^2 B_1 - j2\Omega_y\omega B_2 \tag{4.22}$$

$$(\frac{EI}{\rho A}k^4 - \Omega_y^2)B_2 = \omega^2 B_2 + j2\Omega_y\omega B_1 \tag{4.23}$$

Eq.(4.22) and Eq.(4.23) can be rewritten in the matrix form as

$$\begin{bmatrix} (\frac{E}{A}k^2 - \Omega_y^2) - \omega^2 & +j2\Omega_y\omega \\ -j2\Omega_y\omega & (\frac{EI}{\rho A}k^4 - \Omega_y^2) - \omega^2 \end{bmatrix} \begin{bmatrix} B_1 \\ B_2 \end{bmatrix} = 0 \tag{4.24}$$

where the elastic waves are generated by constant frequency ($\omega = \omega_0$). Equating the determinant of coefficients to zero in Eq.(4.24) gives the wavenumber equation induced by the rotation (Ω_y) as

$$k^6 - k^4(\omega_0^2 + \Omega_y^2)\frac{\rho}{E} - k^2(\omega_0^2 + \Omega_y^2)\frac{\rho A}{EI} + (\omega_0^2 - \Omega_y^2)^2\frac{\rho^2 A}{E^2 I} = 0 \tag{4.25}$$

where k equals to k_{F0} and k_{L0} for the inertial medium ($\Omega_x = 0$), which recovers the uncoupled wavenumbers given in Eqs.(4.3) and (4.5). As the two elastic waves couple, the solution of Eq.(4.25) gives the wavenumbers for the longitudinal wave and the flexural wave separately, however a closed form equation is difficult to find. In general, there are 3 sets of roots (total of 6 roots) corresponding to the flexural wave and the longitudinal wave, where the flexural wave has 2 sets of the roots and longitudinal wave has 1 set of the roots. For the flexural wave, 1 set of the roots is purely imaginary ($ik_{F2}, -ik_{F2}$), which represents the evanescent waves. As the effect of evanescent waves decreases exponentially with increasing distance, we only focus on the travelling waves. The remaining sets of the roots ($k_{F2}, -k_{F2}, k_{L1}, -k_{L1}$) include two positive and two negative real wave numbers that represent forward and backward travelling waves, respectively. Therefore, we use 2 positive roots out of 4 roots to calculate the wavenumbers for flexural and longitudinal waves. One of the 2 roots equals to the wavenumber of flexural wave

(k_{F2}) and the other one equals to the wavenumber of longitudinal wave (k_{L1}). In our analysis, we use the corresponding wavenumbers calculated in Eq.(4.25) for the flexural-longitudinal wave coupling.

4.1.3.3 Torsional wave - Flexural wave Coupling

In a rod, the axes of angular particle motion for torsional waves and flexural waves are orthogonal to each other, as shown in Fig.39c. In Fig.39c, the center of the cross section coincides with the x axis where the torsional wave (θ) and the flexural wave (ϕ) tilt about the x and y axis, respectively. While constant rotation (Ω_z) is applied through the normal axis (z), $N(x,t)$ is the Coriolis and the centrifugal torques in Eq.(4.2) and Eq.(4.6). For the rotating rod shown in Fig.39c, the torsional wave is induced by the Coriolis torque and starts to travel with the flexural wave when the flexural wave is driven. This causes the coupling between torsional and flexural waves due to the Coriolis torque. The Coriolis torques are denoted by $2\rho A(\Omega_z \times \frac{\partial\theta}{\partial t})$, $2\rho J(\Omega_z \times \frac{\partial\phi}{\partial t})$ and the centrifugal torques are denoted by $\rho J\theta\Omega_z^2$, $\rho A\phi\Omega_z^2$. The centrifugal tension force is also included to the equation of motion as $T(x)\frac{\partial^2\phi}{\partial x^2}$. As a result, the equations of motion for the torsional and flexural wave in a rotating reference frame are given as

$$\theta\Omega_z^2 + 2(\Omega_z \times \frac{\partial\phi}{\partial t}) = \frac{\partial^2\theta}{\partial t^2} - \frac{C}{\rho J}\frac{\partial^2\theta}{\partial x^2} \tag{4.26}$$

$$-\frac{\partial^2(\phi\Omega_z^2 - 2(\Omega_z \times \frac{\partial\theta}{\partial t}))}{\partial x^2} = \frac{EI}{\rho A}\frac{\partial^4\phi}{\partial x^4} - \frac{T(x)}{\rho A}\frac{\partial\phi}{\partial x} + \frac{\partial^2\phi}{\partial t^2} \tag{4.27}$$

where $T(x)$ is negligible for small rotation rates. For radially applied rotation on the rod, $\rho x\Omega_z^2$ is also produced and negligible for the higher excitations. In order to ignore the spatial effects in our calculations, we carry out the analysis for the high drive force and small rotation rates to determine the Coriolis coupling between torsional and flexural waves precisely. Thus, we consider the harmonic waves propagating in a rod as

$$\theta = B_1 e^{j(kx-\omega t)}, \phi = B_2 e^{j(kx-\omega t)} \tag{4.28}$$

Parameter	Value	Unit
Density (ρ)	2700	kg/m^3
Poisson ratio (ν)	0.35	-
Young's modulus (E)	70	GPa
Radius (r)	r	m
Area of cross section (A)	πr^2	m^2
Moment of inertia (I)	$\frac{\pi r^4}{4}$	m^4
Polar moment of inertia (J)	$\frac{\pi r^4}{2}$	m^4
Shear rigidity (C)	$\frac{E\pi r^4}{4(1+\nu)}$	Pa.m^4

Table 9: Design parameters for a cylindrical aluminum rod with the radius of r.

and substitute Eq.(4.28) in Eq.(4.26) and Eq.(4.27) by subtracting the spatially varying parts. The following two homogenous equations in B_1, B_2 are obtained as

$$(\frac{C}{\rho J}k^2 - \Omega_z^2)B_1 = \omega^2 B_1 - j2\Omega_z\omega B_2 \tag{4.29}$$

$$(\frac{EI}{\rho A}k^4 - \Omega_z^2 k^2)B_2 = \omega^2 B_2 + j2\Omega_z\omega k^2 B_1 \tag{4.30}$$

Eq.(4.29) and Eq.(4.30) can be rewritten in the matrix form as

$$\begin{bmatrix} (\frac{C}{\rho J}k^2 - \Omega_z^2) - \omega^2 & +j2\Omega_z\omega \\ -j2\Omega_z\omega k^2 & (\frac{EI}{\rho A}k^4 - \Omega_z^2 k^2) - \omega^2 \end{bmatrix} \begin{bmatrix} B_1 \\ B_2 \end{bmatrix} = 0 \tag{4.31}$$

where the elastic waves are generated by constant frequency ($\omega = \omega_0$). Equating the determinant of coefficients to zero in Eq.(4.31) gives the wavenumber equation induced by the rotation (Ω_z) as

$$\frac{EI}{\rho A}\frac{C}{\rho J}k^6 - k^4(\frac{EI}{\rho A}\omega_0^2 + \frac{EI}{\rho A}\Omega_z^2 + \frac{C}{\rho J}\Omega_z^2) - k^2(\frac{C}{\rho J}\omega_0^2 - \Omega_z^4 + 3\Omega_z^2\omega_0^2) + \omega_0^2(\omega_0^2 + \Omega_z^2) = 0 \tag{4.32}$$

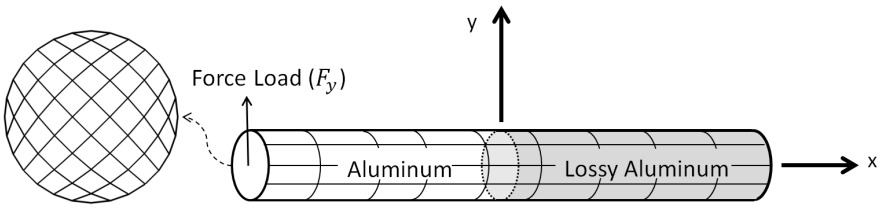
where k equals to k_{F0} and k_{T0} for the inertial medium ($\Omega_z = 0$), which recovers the uncoupled wavenumbers given in Eqs.(4.3) and (4.7). As the two elastic waves couple, the solution of Eq.(4.32) gives the wavenumbers for the torsional wave and the flexural wave separately, however a closed form equation is difficult to find. 2 roots with the positive real parts should be used to calculate the wavenumbers for each coupled elastic waves (k_{T1}, k_{F2}).

4.2 Materials and Methods

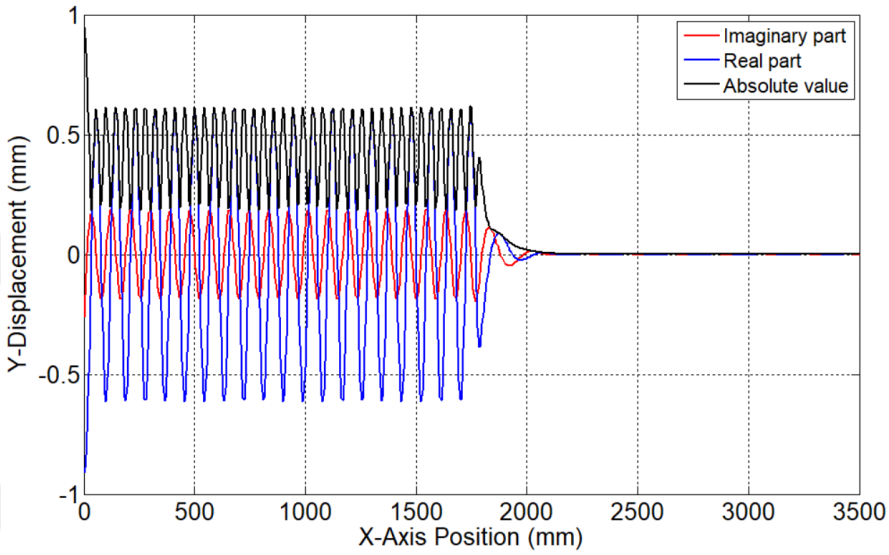
4.2.1 Numerical Methods

In this section, we present finite element method analysis using a commercially available software (ANSYS). Using ANSYS, we demonstrate how to generate travelling waves in rotating rods and verify the analytical calculations derived in the previous section. First, we created a uniform solid model of a rod shown in Fig.40a using SOLID186 elements of the software. We used ANSYS's rotating reference frame option to include the effect of Coriolis force. We used mapped meshing for our model which created regular mesh elements as shown in Fig.40a; the circular cross-section is divided into regular meshes as shown in the figure. The mesh density here was chosen to get quick results without losing the accuracy. Based on our convergence study, we found that 28 divisions along the circular perimeter gave us a good compromise between the accuracy and computation time. The length of the rod is meshed such that there are at least 20 nodes per wavelength. We adjusted the length of the rod to limit the total number of nodes and hence the solution time. In general, our models had 1 million nodes. We applied a uniform force over the circular end of the rod and obtained the real and imaginary parts of the displacement field using harmonic analysis. For a single travelling wave, the displacement amplitude should be uniform across the length of the rod excluding the evanescent wave region which is very close to the source.

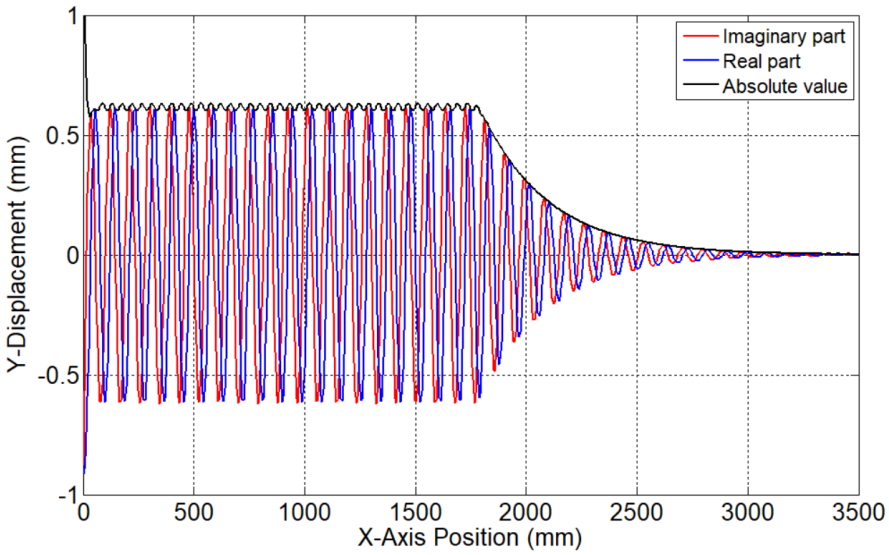
Once the model was constructed, we performed harmonic analysis with the Full method option at specific frequencies to obtain the mode shape [186]. We used Sparse direct solver for harmonic analysis. A typical run at single frequency took 10 minutes on i3-2370 processor with 2.4 GHz clock speed. The uniform elastic rod is made of aluminum where the design parameters are presented for the rod with the radius of r in Table 9. For the circular cross section, the area (A), moment of inertia (I), polar moment of inertia (J) and shear rigidity (C) are calculated as πr^2, $\frac{\pi r^4}{4}$, $\frac{\pi r^4}{2}$ and $\frac{E\pi r^4}{4(1+\nu)}$ in Table 9.



(a)



(b)



(c)

Figure 40: **(a)** Finite element model of the cylindrical rod, **(b)** y-displacement at the top y-nodes of cylindrical aluminum rod along the x-axis for loss factor $\beta = 3 \times 10^{-3}$, and **(c)** for loss factor $\beta = 3 \times 10^{-5}$.

In Fig.40b and Fig.40c, flexural wave (v) propagation in x direction is demonstrated for two aluminum rods with different loss factors. The rod is made from lossless and lossy aluminum as shown in Fig.40a, where the loss is adjusted by the stiffness loss factor (β) of ANSYS. We applied a uniform force in the y-direction on the non-lossy end and performed harmonic analyses at 1 kHz. The lengths of the lossless and lossy sections are determined as $20\lambda_{F0} = 1.788$ m. As reported in [187, 188, 189], the aim of the lossy part is to prevent the reflection of the travelling waves from the end of the rod structure, so the travelling wave is completely absorbed by the lossy medium before reaching to the end by using this method. Another important point of the method is to minimize the mechanical impedance mismatch between the lossy and lossless rod by adjusting the loss factor, since the standing wave is generated by the reflection of waves from the mismatched rod/lossy-rod interface. In Fig.5b, the loss factor is too high, which causes the reflection of travelling wave from the aluminum/lossy-aluminum interface. As a result, this reflection generates a standing wave in the lossless rod where the amplitude of the standing wave is shown with the absolute value (black line). The existence of standing wave pattern causes miscalculation of the wavelength and wavenumber for the travelling wave. In Fig.40c, the loss factor was adjusted such that the impedance mismatched was minimized at the interface while the wave in the lossy part is completely absorbed. In this case, one can easily determine the wavelength of the travelling wave in the lossless aluminum part where the amplitude of the standing wave is significantly small. The calculated wavelength from Fig.40c is 88.91 mm which matches well with the theoretical calculation of 89.41 mm shown in Table 10. Similarly one can generate longitudinal or torsional waves by changing the direction of the applied force and adjusting the length of the aluminum rods to accommodate the changing wavelengths.

4.2.2 Numerical Examples of Coupled Elastic Waves

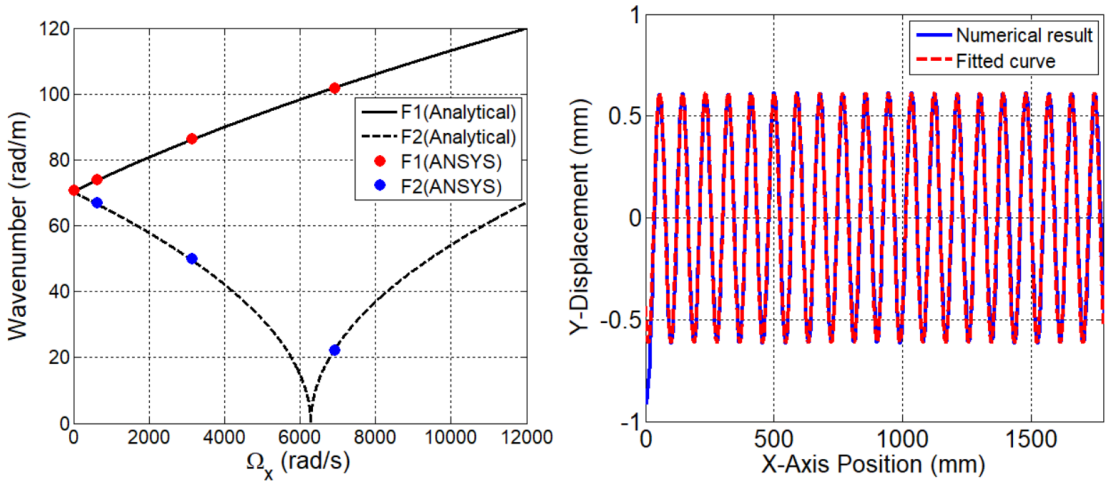
Euler Bernoulli beam theory neglects the shear effect and rotary inertia effect (ρI) on the rod, which restricts the theoretical solution for the rods with the condition

of $\frac{r}{\lambda} \leq 0.1$ as reported in [190]. Therefore, we set the design parameters of the rods based on this condition in order to verify the theoretical calculations. For the numerical examples, three aluminum cylindrical rods with different sizes are designed to analyze the each coupling of elastic waves in a rotating media.

In a rod, the wavelengths of travelling waves differ, where $\lambda_{L0} > \lambda_{T0} > \lambda_{F0}$ for low frequencies. When the wavelengths of coupled two elastic waves are different, the loss factor must be well adjusted and the diameter of the rod must be carefully chosen in order to carry out the wave propagation. In Example 1 presented in Section 4.3.1, the loss factor was easily chosen for the rod with the small diameter ($\sim$ 1 mm), since both coupled elastic waves exist with the same wavelength (λ_{F0}). In Example 2 presented in Section 4.3.2, the selection of the loss factor is relatively difficult for the rods with the small diameter, since both the flexural and longitudinal wave propagation exist; the λ_{L0} is a relatively larger than λ_{F0}, which requires a longer lossy region for the absorption of longitudinal wave. This means that the selection of small diameter for the rod causes very long computation times. Therefore, we design the rod with the larger diameter ($\sim$ 2 m), where λ_{L0} is close to λ_{F0}. In Example 3 presented in Section 4.3.3, we also design the rod with a large diameter, where λ_{T0} is close to λ_{F0}. In order to overcome the computational difficulties explained above, we determine the proper rod diameter to design the length of the lossy rod as short as possible in each example.

4.3 Results

Three different types of coupling were demonstrated in the numerical examples using the method described in the previous section. For the simplicity, we did not illustrate the displacement of lossy rod in the figures and presented only the displacement of lossless part in this section. In general, we found that the wavenumber shifts for the elastic waves propagating in the rods, as the rotation is applied. The results are divided into three parts as follows:



(a) (b)

Figure 41: For the cylindrical aluminum rod induced by the constant rotation (Ω_x) in Example 1, **(a)** wavenumbers of F1 and F2 calculated from Eq.(4.14) and the ANSYS results, **(b)** wavenumber, amplitude and phase calculations of the numerical result by fitting the sinusoidal wave of $B\cos(kx-\Phi)$ to the real part of the y-displacement (same blue curve as in Fig.40c).

4.3.1 Example 1: Flexural wave - Flexural wave Coupling

In this part, the aluminum cylindrical rod is analyzed for various rotation rates of Ω_x about the x-axis in order to illustrate the coupling between the pair of flexural waves explained in Section 4.1 by using the numerical model presented in Section 4.2. In Table 10, the design parameters for Example 1 is given. In Example 1, we drive the primary flexural wave (F1) by applying the force load on the cross section of the lossless rod end with 1 N in the y direction, where the drive frequency (f) equals to 1 kHz. For the static case, the wavelength of flexural wave (λ_{F0}) is calculated as 89.4 mm from Eq.(4.3). For various rotation rates, the loss factor and the length of lossy rod must be chosen carefully, since the difference

Parameter	**Value**	**Unit**
Radius (r)	0.5	mm
Length of lossless aluminum rod ($L = 20\lambda_{F0}$)	1.788	m
Force Load (F_y)	1	N
Drive frequency (f)	1000	Hz
Wavelength of flexural wave (λ_{F0})	89.4	mm
Theoretical condition parameter ($\frac{r}{\lambda} \leq 0.1$)	0.0056	-

Table 10: Example 1: Flexural wave - Flexural wave Coupling.

between wavelengths of flexural waves (λ_{F1}, λ_{F2}) changes. Therefore, the length of lossy rod is designed as $60\lambda_{F0}$ with the proper loss factor, where the length of the lossless rod is $20\lambda_{F0}$. Theoretical condition parameter ($\frac{r}{\lambda_{F0}}$) is fulfilled by 0.0056 for the rod with the radius of 0.5 mm, as presented in Table 10.

In Example 1, the wavenumber shift occurs for the secondary flexural wave (F2) and primary flexural wave (F1) due to the Coriolis force, while the rotation is applied. In Fig.41a, the wavenumbers of F1 and F2 calculated from Eq.(4.14) are illustrated for the rod rotating about the x axis shown in Fig.39a. As expected, the wavenumber increases for F1 and decreases for F2 until $\Omega_x = 2\pi1000$ rad/s. For $\Omega_x = 2\pi1000$ rad/s, wavenumber zero corresponds to infinitely large phase velocity which means rigid body motion. Therefore, the wave propagation stops where $k = 0$. While the rotation rate is higher than $2\pi1000$ rad/s, the wavenumbers of both flexural waves increase. In Fig.41b, we fitted a sinusoidal wave ($B\cos(kx - \Phi)$) to the real part of the displacement, which is calculated from ANSYS as shown in Fig.40c, to find the wave number. In the figure, we find the wavenumber (k) as 70.7 rad/m and the amplitude (B) as 0.61 mm where Φ equals to $\frac{5\pi}{4}$. The theoretical result is 70.26 rad/m for the wavenumber as presented in Fig.41a. Therefore, we got good match between numerical results and theoretical calculations for $\Omega_x = 0$. Further, we study the cases of $\Omega_x = 2\pi100$ rad/s, $2\pi500$ rad/s and $2\pi1100$ rad/s in order to perform thorough analysis of the flexural-flexural wave coupling.

For the dynamic cases, two elastic waves start to propagate together and go in the same direction with the different wavenumbers and amplitudes due to the Coriolis coupling. In other words, the superposition of F1 and F2 gives the y and z displacements of the rod in the x axis in the rotating reference frame. For $\Omega_x = 2\pi100$ rad/s, the y and z displacements are illustrated in Fig.42a and Fig.42b, respectively. In the figures, the interference pattern between F1 and F2 is observed where the amplitude (black curve) is not constant anymore.

In Fig.42c, we fitted a sinusoidal wave ($B_{F1}\cos(k_{F1}x - \Phi_{F1}) + B_{F2}\cos(k_{F2}x - \Phi_{F2})$), which represents the superposition of F1 and F2, to the real part of the

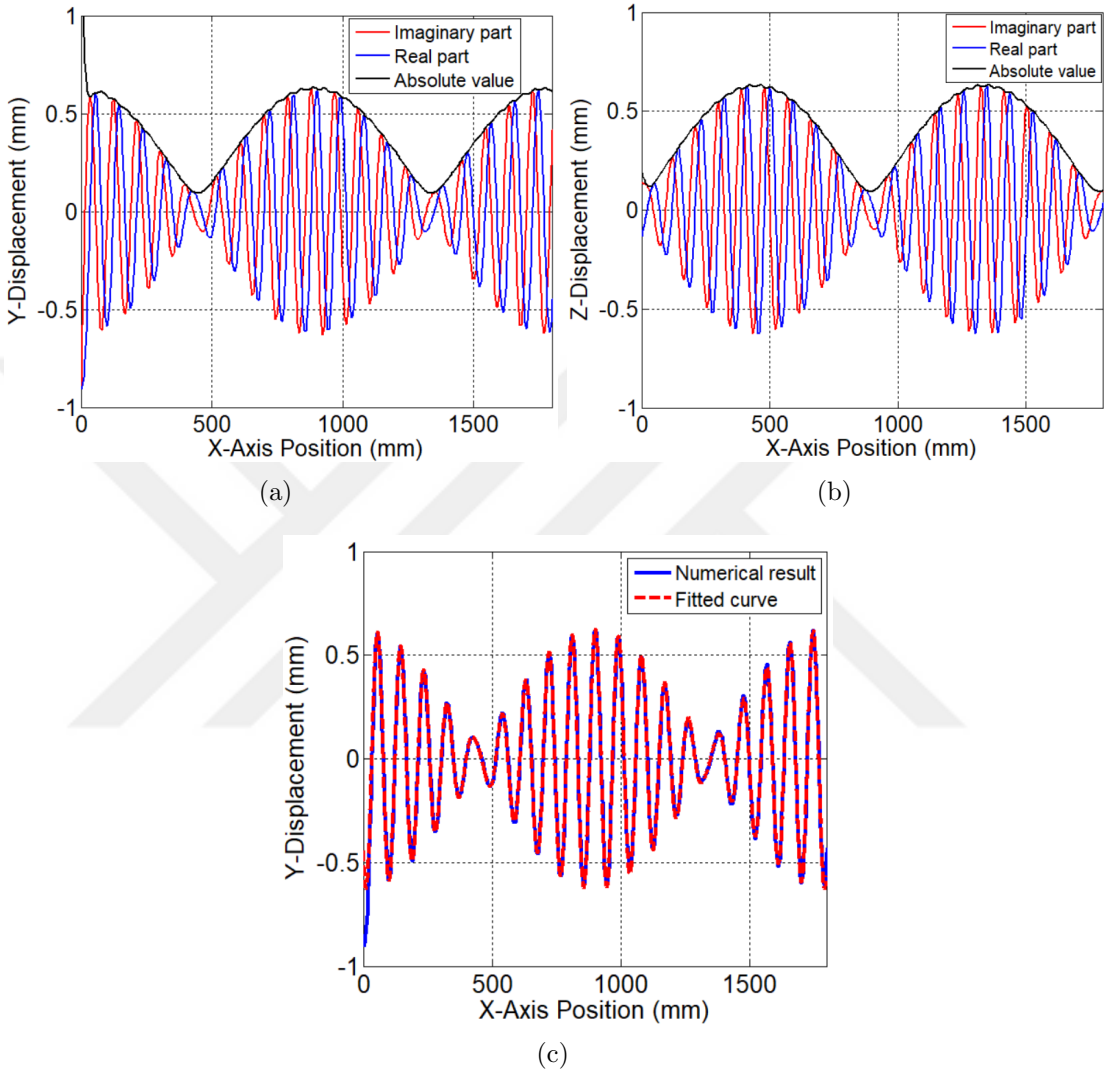


Figure 42: For $\Omega_x = 2\pi 100$ rad/s in Example 1, the displacement at the top y-nodes of lossless cylindrical aluminum rod along the x axis **(a)** in the y direction, **(b)** in the z direction, and **(c)** wavenumber, amplitude and phase calculations of the numerical result by fitting the sinusoidal wave of $B_{F1}\cos(k_{F1}x - \Phi_{F1}) + B_{F2}\cos(k_{F2}x - \Phi_{F2})$ to the real part of the y-displacement (same blue curve as in Fig.42a)). The length of lossy aluminum part equals to $60\lambda_{F0}$ with loss factor $\beta = 10^{-5}$.

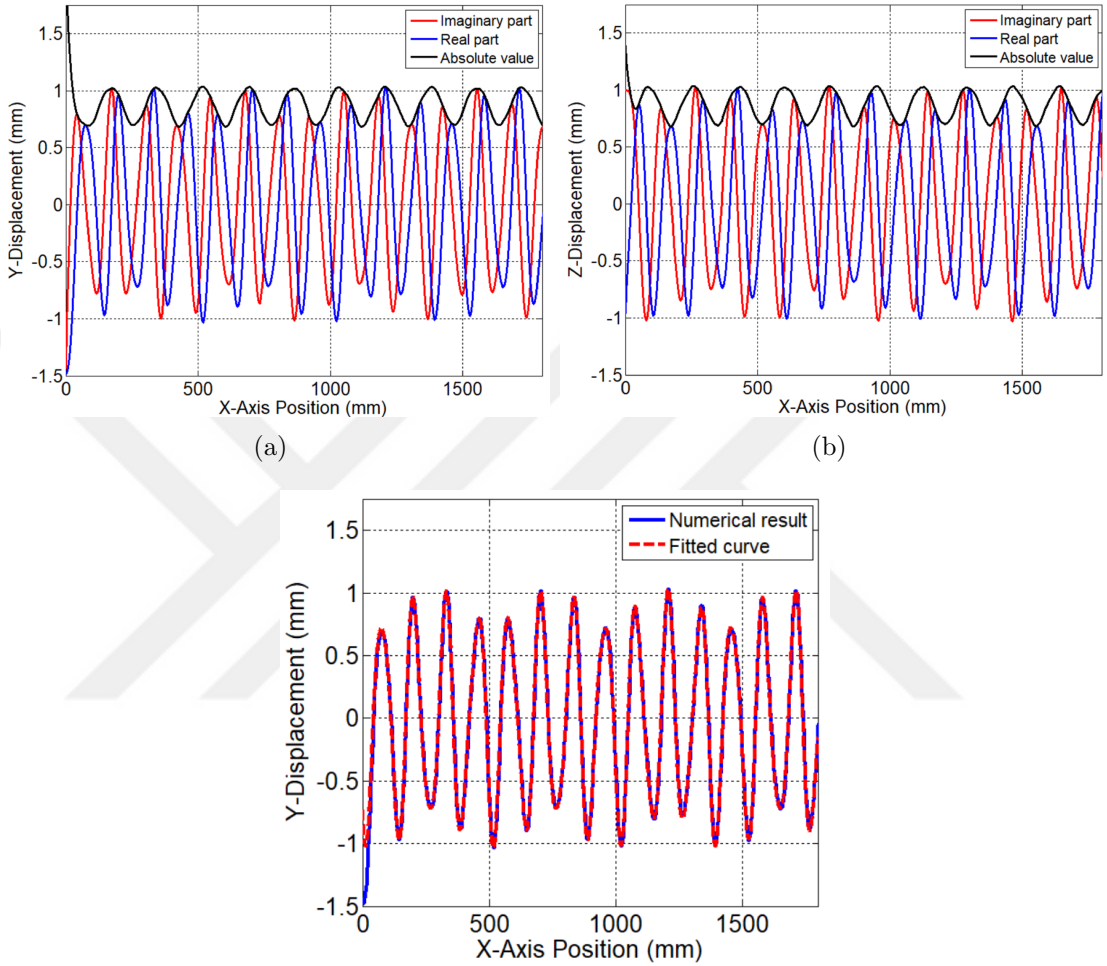


Figure 43: For $\Omega_x = 2\pi 500$ rad/s in Example 1, the displacement at the top y-nodes of lossless cylindrical aluminum rod along the x axis **(a)** in the y direction, **(b)** in the z direction, and **(c)** wavenumber, amplitude and phase calculations of the numerical result by fitting the sinusoidal wave of $B_{F1}\cos(k_{F1}x - \Phi_{F1}) + B_{F2}\cos(k_{F2}x - \Phi_{F2})$ to the real part of the y-displacement (same blue curve as in Fig.43a)). The length of lossy aluminum part equals to $60\lambda_{F0}$ with loss factor $\beta = 2 \times 10^{-5}$.

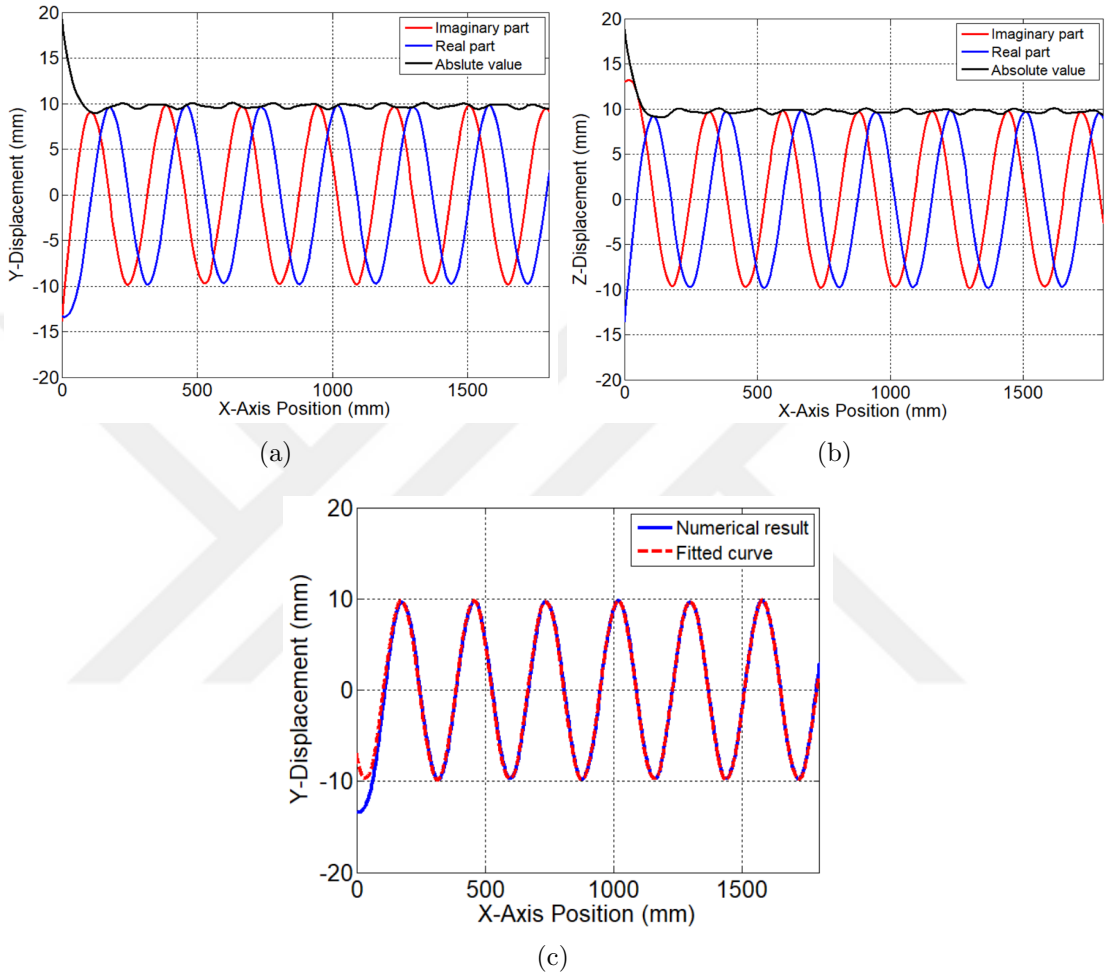


Figure 44: For $\Omega_x = 2\pi 1100$ rad/s in Example 1, the displacement at the top y-nodes of lossless cylindrical aluminum rod along the x axis **(a)** in the y direction, **(b)** in the z direction, and **(c)** wavenumber, amplitude and phase calculations of the numerical result by fitting the sinusoidal wave of $B_{F1}\cos(k_{F1}x - \Phi_{F1}) + B_{F2}\cos(k_{F2}x - \Phi_{F2})$ to the real part of the y-displacement (same blue curve as in Fig.44a)). The length of lossy aluminum part equals to $60\lambda_{F0}$ with loss factor $\beta = 3 \times 10^{-5}$.

displacement shown in Fig.42a. The displacements of F1 and F2 are denoted by $B_{F1}\cos(k_{F1}x - \Phi_{F1})$ and $B_{F2}\cos(k_{F2}x - \Phi_{F2})$, respectively. We found that Φ_{F1} and Φ_{F2} equal to $\frac{5\pi}{4}$ and B_{F1}, B_{F2} are obtained as 0.265 mm and 0.36 mm, respectively. In the figure, we determine k_{F1} as 74.05 rad/m and k_{F2} as 67.05 rad/m. The theoretical results are 73.69 rad/m for k_{F1} and 66.65 rad/m for k_{F2} as presented in Fig.41a. Therefore, we got good match between numerical results and theoretical calculations for the wavenumbers where $\Omega_x = 2\pi100$ rad/s.

For $\Omega_x = 2\pi500$ rad/s, the y displacement of coupled elastic waves (F1+F2) is illustrated in Fig.43a and the z displacement of coupled elastic waves (F1+F2) is illustrated in Fig.43b. In Fig.43c, we fitted a sinusoidal wave ($B_{F1}\cos(k_{F1}x-\Phi_{F1})+ B_{F2}\cos(k_{F2}x - \Phi_{F2})$) to the real part of the displacement shown in Fig.43a. The displacements of F1 and F2 are denoted by $B_{F1}\cos(k_{F1}x - \Phi_{F1})$ and $B_{F2}\cos(k_{F2}x - \Phi_{F2})$, respectively. We found Φ_{F1}, Φ_{F2} as $\frac{5\pi}{4}$ and B_{F1}, B_{F2} are obtained as 0.165 mm and 0.87 mm, respectively. In the figure, we determine k_{F1} as 86.35 rad/m and k_{F2} as 50.05 rad/m. The theoretical results are 86.05 rad/m for k_{F1} and 49.68 rad/m for k_{F2} as presented in Fig.41a. Therefore, we got good match between numerical results and theoretical calculations for the wavenumbers where $\Omega_x = 2\pi500$ rad/s.

For $\Omega_x = 2\pi1100$ rad/s, the y displacement of coupled elastic waves (F1+F2) is illustrated in Fig.44a and the z displacement of coupled elastic waves (F1+F2) is illustrated in Fig.44b. In Fig.44c, the displacements of F1 and F2 are denoted by $B_{F1}\cos(k_{F1}x-\Phi_{F1})$ and $B_{F2}\cos(k_{F2}x-\Phi_{F2})$ for the fitted signal ($B_{F1}\cos(k_{F1}x-\Phi_{F1}) + B_{F2}\cos(k_{F2}x - \Phi_{F2})$), respectively. In the figure, we determine k_{F1} as 101.8 rad/m and k_{F2} as 22.35 rad/m. The theoretical results are 101.8 rad/m for k_{F1} and 22.22 rad/m for k_{F2} as presented in Fig.41a. Therefore, we got also good match between numerical results and theoretical calculations for the wavenumbers where $\Omega_x = 2\pi1100$ rad/s. Further, we found that Φ_{F1} and Φ_{F2} equal to $\frac{5\pi}{4}$ and B_{F1}, B_{F2} are obtained as 0.1 mm and 9.8 mm, respectively. In this case, B_{F2} is relatively higher than B_{F1} and this leads F2 to dominate the wave propagation

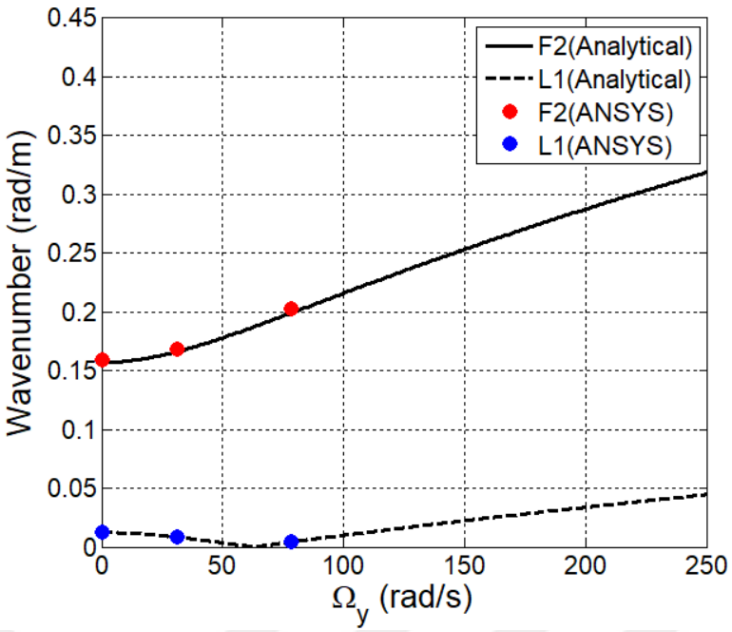


Figure 45: For the cylindrical aluminum rod induced by the constant rotation (Ω_y) in Example 2, the wavenumbers of F2 and L1 calculated from Eq.(4.25) and the ANSYS results.

for $\Omega_x = 2\pi 1100$ rad/s.

4.3.2 Example 2: Longitudinal wave - Flexural wave Coupling

To demonstrate the coupling between longitudinal and flexural waves, we presented two cases (Case1, Case2) where we used two different excitations. In Case 1, we applied the excitation force in the z-direction whereas in Case 2, the excitation is in x-direction. Case 1 generated a flexural wave which couples to longitudinal wave when a rotation along y-axis is introduced. In Case 2, the excitation force creates a longitudinal wave and the longitudinal wave couples to a flexural wave if the rod experiences a rotation along y-axis. In both cases, the excitation

Parameter	**Value**	**Unit**
Radius (r)	1	m
Length of lossless aluminum rod ($L = 2\lambda_{L0}$)	1018.4	m
Force Load (F_z, F_x)	10^{20}	N
Drive frequency (f)	10	Hz
Wavelength of flexural wave (λ_{F0})	39.99	m
Wavelength of longitudinal wave (λ_{L0})	509.2	m
Theoretical condition parameter ($\frac{r}{\lambda} \leq 0.1$)	0.025	-

Table 11: Example 2: Longitudinal wave - Flexural wave Coupling.

amplitudes of the generated waves are quite different depending on the type of the excitation, whereas in both cases corresponding wavenumbers are the same. The design parameters are given in Table 11 for Example 2. In order to minimize the spatial effects (due to centrifugal tension force) as explained in the theory section, we determined a low drive frequency of 10 Hz to analyze the small rotation rates and exaggerated the force loads by 10^{20} N, as presented in Table 11. For the static case, we calculated that the wavelength of flexural wave (λ_{F0}) was 39.99 m from Eq.(4.3) and the wavelength of longitudinal wave (λ_{L0}) was 509.2 m from Eq.(4.5). For various rotation rates, the length of lossy rod was designed to be $6\lambda_{L0}$ with a proper loss factor, where the length of the lossless rod was $2\lambda_{L0}$. For this selection of aluminum rod dimensions, the radius to wavelength ratio is 0.025 where the rod can be treated as a one-dimensional object.

In Example 2, the wavenumber shift occurs for the flexural wave (F2) and longitudinal wave (L1) due to the Coriolis force, while the rotation is applied. In Fig.45, the wavenumbers of F2 and L1 calculated from Eq.(4.25) are illustrated for the rod rotating about the y axis shown in Fig.39b. As expected, the wavenumber increases for F2 and decreases for L1 until $\Omega_y = 2\pi 10$ rad/s. While the rotation rate is higher than $2\pi 10$ rad/s, the wavenumbers of both waves increase. In our analysis, we study the cases of $\Omega_y = 0$, $2\pi 5$ rad/s and $2\pi 12.5$ rad/s in order to perform thorough analysis of the longitudinal-flexural wave coupling.

For $\Omega_y = 0$, the z displacement of F2 in Case 1 is illustrated in Fig.46a and the x displacement of L1 in Case 2 is illustrated in Fig.46b, where the force loads (F_z, F_x) are applied by 10^{20} N. In the figures, there are approximately 25.5 flexural waves and 2 longitudinal waves in the corresponding lossless rods. When we fit the sinusoidal wave ($B\cos(kx - \Phi)$) to the real part of the displacements as shown in Fig.46c and Fig.46d, we find k_{F2} as 0.159 rad/m and k_{L1} as 0.01234 rad/m. The theoretical results are 0.157 rad/m for k_{F2} and 0.01234 rad/m for k_{L1} as presented in Fig.45. Therefore, we got good match between numerical results and theoretical calculations for $\Omega_y = 0$. Further, we found Φ_{F2} as $\frac{5\pi}{4}$ and Φ_{L1} as $-\frac{\pi}{2}$ where B_{F2},

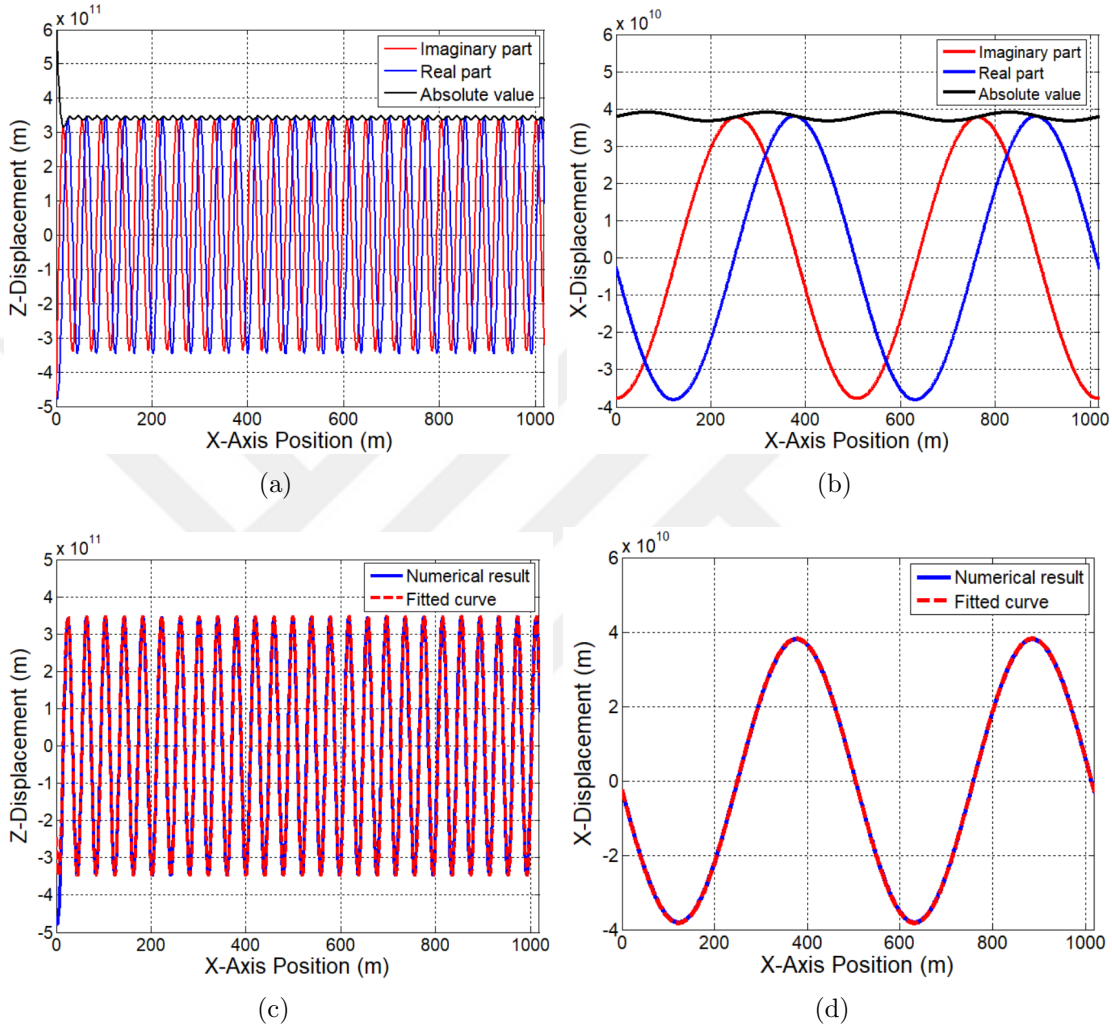


Figure 46: For $\Omega_y = 0$ in Example 2, the displacement at the top z-nodes of lossless cylindrical aluminum rod along the x axis **(a)** in the z direction for Case 1, **(b)** in the x direction for Case 2, **(c)** wavenumber, amplitude and phase calculations of the numerical result by fitting the sinusoidal wave of $B\cos(kx - \Phi)$ to the real part of the z-displacement (same blue curve as in Fig.46a), and **(d)** to the real part of the x-displacement (same blue curve as in Fig.46b). The length of lossy aluminum part equals to $6\lambda_{L0}$ with loss factor $\beta = 2 \times 10^{-3}$.

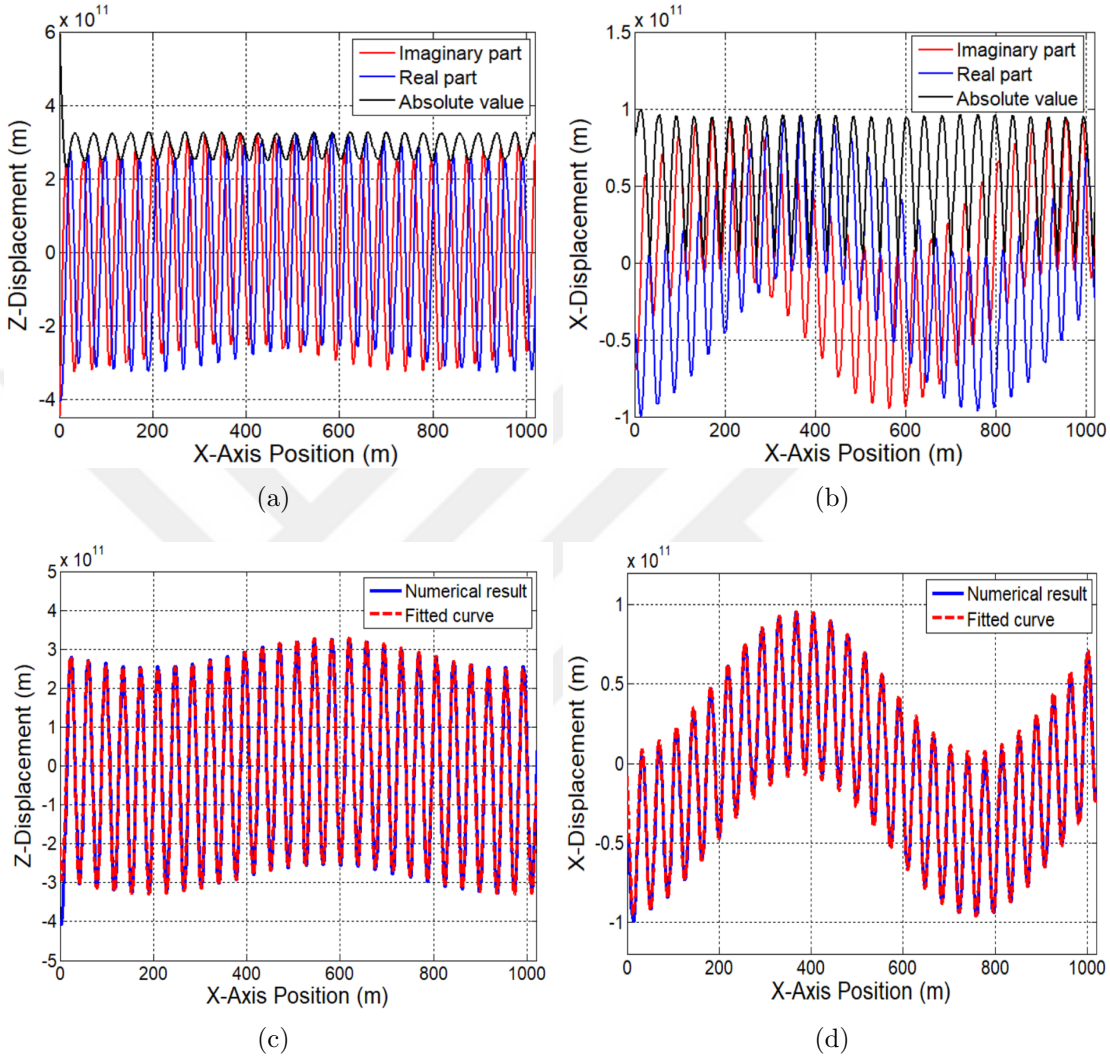


Figure 47: For $\Omega_y = 2\pi 5$ rad/s in Case 1 of Example 2, the displacement at the top z-nodes of lossless cylindrical aluminum rod along the x axis **(a)** in the z direction, **(b)** in the x direction, **(c)** wavenumber, amplitude and phase calculations of the numerical result by fitting the sinusoidal wave of $B_{F2}\cos(k_{F2}x - \Phi_{F2}) + B_{L1}\cos(k_{L1}x - \Phi_{L1})$ to the real part of the z-displacement (same blue curve as in Fig.47a), and **(d)** to the real part of the x-displacement (same blue curve as in Fig.47b). The length of lossy aluminum part equals to $6\lambda_{L0}$ with loss factor $\beta = 4 \times 10^{-3}$.

B_{L1} are obtained as 3.475×10^{11} m and 3.8×10^{10} m, respectively.

For $\Omega_y = 2\pi 5$ rad/s in Case 1, the z displacement of coupled elastic waves (F2+L1) is illustrated in Fig.47a and the x displacement of coupled elastic waves (F2+L1) is illustrated in Fig.47b. When we fit the sinusoidal wave ($B_{F2}\cos(k_{F2}x - \Phi_{F2}) + B_{L1}\cos(k_{L1}x - \Phi_{L1})$) to the real part of the displacements as shown in Fig.47c and Fig.47d, we find k_{F2} as 0.1686 rad/m and k_{L1} as 0.0083 rad/m. The theoretical results are 0.166 rad/m for k_{F2} and 0.0082 rad/m for k_{L1} as presented in Fig.45. Therefore, we got good match between numerical results and theoretical calculations for $\Omega_y = 2\pi 5$ rad/s in Case 1. In Fig.47c, we found Φ_{F2} as $\frac{5\pi}{4}$ and Φ_{L1} as $-\frac{\pi}{2}$ where B_{F2}, B_{L1} are obtained as 2.9×10^{11} m and 4×10^{10} m, respectively. In Fig.47d, we found Φ_{F2} as $\frac{7\pi}{4}$ and Φ_{L1} as $-\pi$ where B_{F2}, B_{L1} are obtained as 5.15×10^{10} m and 4.45×10^{10} m, respectively.

For $\Omega_y = 2\pi 12.5$ rad/s in Case 1, the z displacement of coupled elastic waves (F2+L1) is illustrated in Fig.48a and the x displacement of coupled elastic waves (F2+L1) is illustrated in Fig.48b. When we fit the sinusoidal wave ($B_{F2}\cos(k_{F2}x - \Phi_{F2}) + B_{L1}\cos(k_{L1}x - \Phi_{L1})$) to the real part of the displacements as shown in Fig.48c and Fig.48d, we find k_{F2} as 0.2025 rad/m and k_{L1} as 0.004335 rad/m. The theoretical results are 0.199 rad/m for k_{F2} and 0.00428 rad/m for k_{L1} as presented in Fig.45. Therefore, we got good match between numerical results and theoretical calculations for $\Omega_y = 2\pi 12.5$ rad/s in Case 1. In Fig.48c, we found Φ_{F2} as $\frac{5\pi}{4}$ and Φ_{L1} as $-\frac{\pi}{2}$ where B_{F2}, B_{L1} are obtained as 1.7×10^{11} m and 1×10^{11} m, respectively. In Fig.48d, we found Φ_{F2} as $\frac{7\pi}{4}$ and Φ_{L1} as $-\pi$ where B_{F2}, B_{L1} are obtained as 3.5×10^{10} m and 1×10^{11} m, respectively.

For $\Omega_y = 2\pi 5$ rad/s in Case 2, the z displacement of coupled elastic waves (L1+F2) is illustrated in Fig.49a and the x displacement of coupled elastic waves (L1+F2) is illustrated in Fig.49b. When we fit the sinusoidal wave ($B_{L1}\cos(k_{L1}x - \Phi_{L1}) + B_{F2}\cos(k_{F2}x - \Phi_{F2})$) to the real part of the displacements as shown in Fig.49c and Fig.49d, we find k_{L1} as 0.0083 rad/m and k_{F2} as 0.1686 rad/m. The theoretical results are 0.0082 rad/m for k_{L1} and 0.166 rad/m for k_{F2} as presented

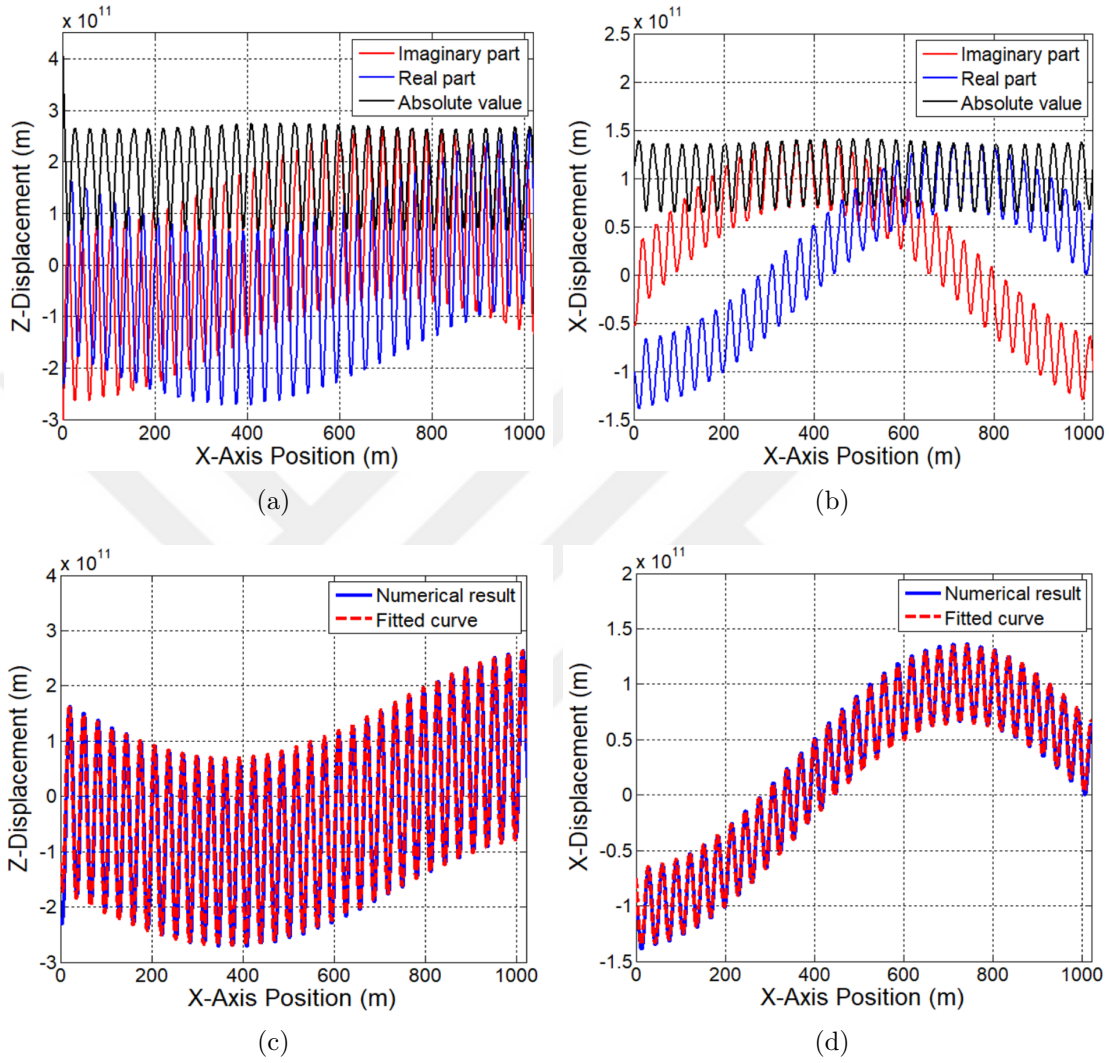


Figure 48: For $\Omega_y = 2\pi 12.5$ rad/s in Case 1 of Example 2, the displacement at the top z-nodes of lossless cylindrical aluminum rod along the x axis **(a)** in the z direction, **(b)** in the x direction, **(c)** wavenumber, amplitude and phase calculations of the numerical result by fitting the sinusoidal wave of $B_{F2}\cos(k_{F2}x - \Phi_{F2}) + B_{L1}\cos(k_{L1}x - \Phi_{L1})$ to the real part of the z-displacement (same blue curve as in Fig.48a), and **(d)** to the real part of the x-displacement (same blue curve as in Fig.48b). The length of lossy aluminum part equals to $6\lambda_{L0}$ with loss factor $\beta = 2 \times 10^{-3}$.

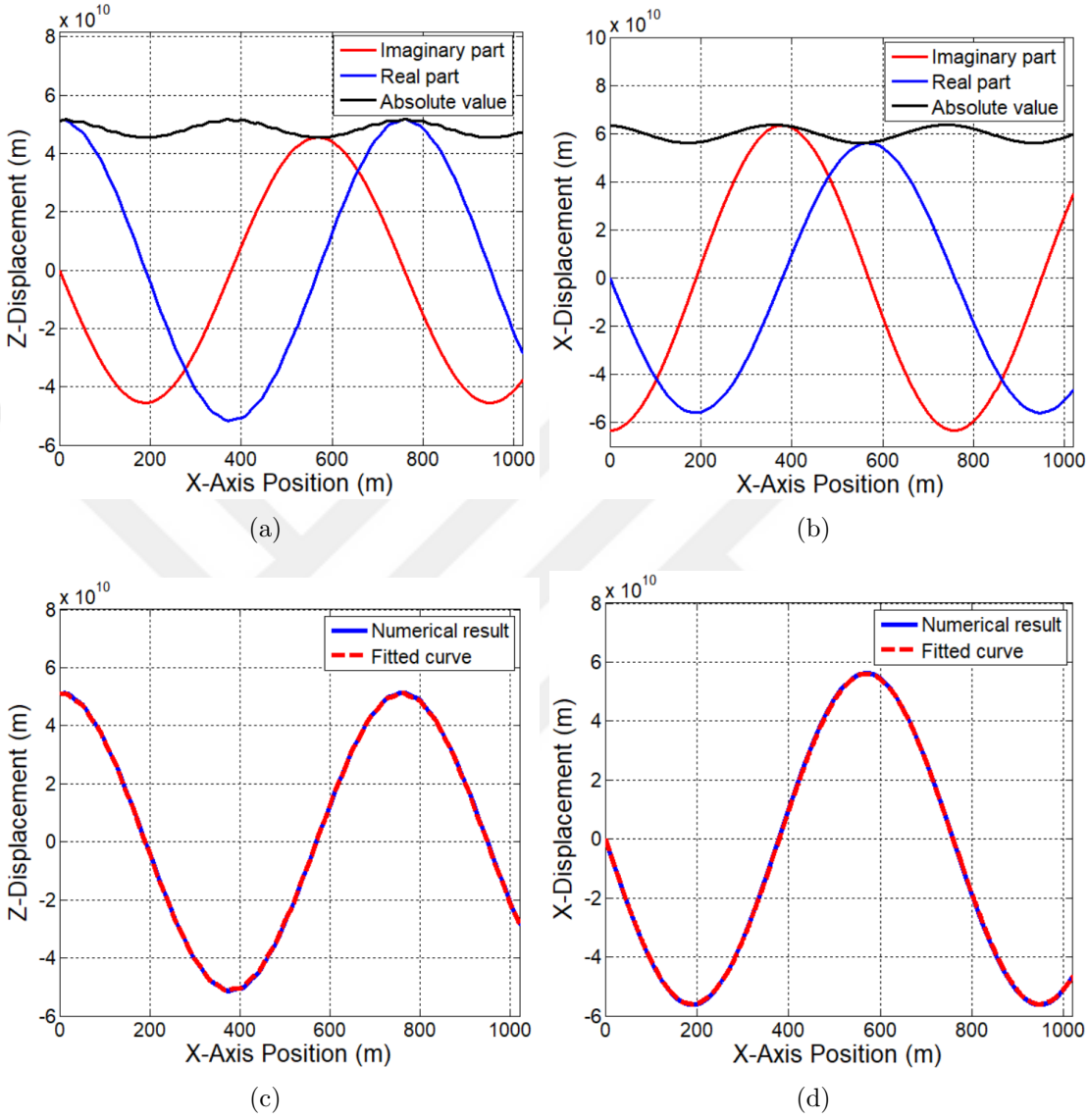


Figure 49: For $\Omega_y = 2\pi 5$ rad/s in Case 2 of Example 2, the displacement at the top z-nodes of lossless cylindrical aluminum rod along the x axis **(a)** in the z direction, **(b)** in the x direction, **(c)** wavenumber, amplitude and phase calculations of the numerical result by fitting the sinusoidal wave of $B_{L1}\cos(k_{L1}x - \Phi_{L1}) + B_{F2}\cos(k_{F2}x - \Phi_{F2})$ to the real part of the z-displacement (same blue curve as in Fig.49a), and **(d)** to the real part of the x-displacement (same blue curve as in Fig.49b). The length of lossy aluminum part equals to $6\lambda_{L0}$ with loss factor $\beta = 4 \times 10^{-3}$.

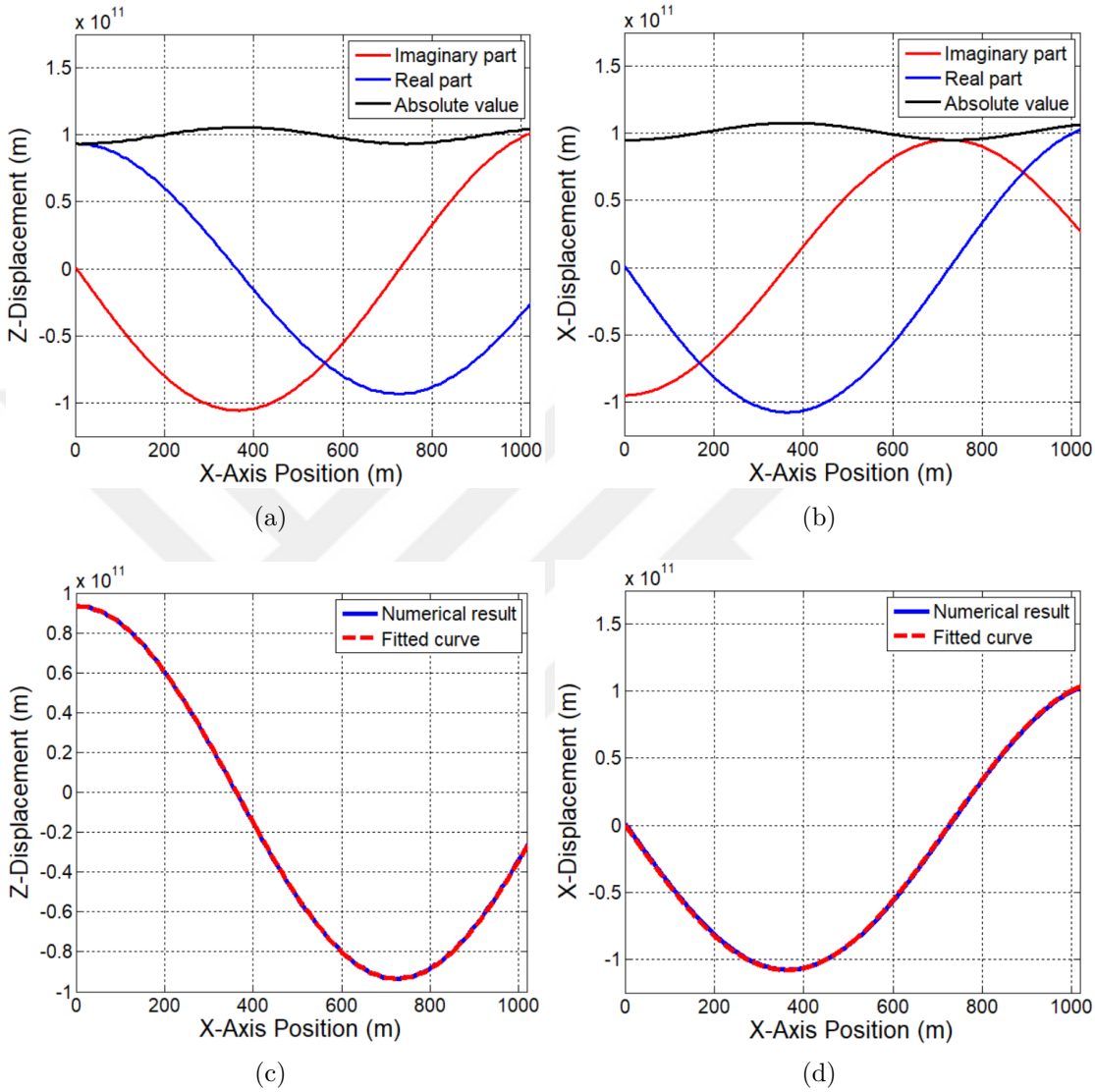


Figure 50: For $\Omega_y = 2\pi 12.5$ rad/s in Case 2 of Example 2, the displacement at the top z-nodes of lossless cylindrical aluminum rod along the x axis **(a)** in the z direction, **(b)** in the x direction, **(c)** wavenumber, amplitude and phase calculations of the numerical result by fitting the sinusoidal wave of $B_{L1}\cos(k_{L1}x - \Phi_{L1}) + B_{F2}\cos(k_{F2}x - \Phi_{F2})$ to the real part of the z-displacement (same blue curve as in Fig.50a), and **(d)** to the real part of the x-displacement (same blue curve as in Fig.50b). The length of lossy aluminum part equals to $6\lambda_{L0}$ with loss factor $\beta = 7 \times 10^{-3}$.

Parameter	Value	Unit
Radius (r)	1	m
Length of lossless aluminum rod ($L = 2\lambda_{T0}$)	619.74	m
Force Load (F)	10^{20}	N
Drive frequency (f)	10	Hz
Wavelength of flexural wave (λ_{F0})	39.99	m
Wavelength of torsional wave (λ_{T0})	309.87	m
Theoretical condition parameter ($\frac{r}{\lambda} \leq 0.1$)	0.025	-

Table 12: Example 3: Torsional wave - Flexural wave Coupling.

in Fig.45. Therefore, we got good match between numerical results and theoretical calculations for $\Omega_y = 2\pi 5$ rad/s in Case 2. In Fig.49c, we found Φ_{L1} as 0 and Φ_{F2} as $-\frac{\pi}{4}$ where B_{L1}, B_{F2} are obtained as 5.1×10^{10} m and 3.5×10^{8} m, respectively. In Fig.49d, we found Φ_{L1} as $-\frac{\pi}{2}$ and Φ_{F2} as $\frac{\pi}{4}$ where B_{L1}, B_{F2} are obtained as 5.6×10^{10} m and 1×10^{8} m, respectively.

For $\Omega_y = 2\pi 12.5$ rad/s in Case 2, the z displacement of coupled elastic waves (L1+F2) is illustrated in Fig.50a and the x displacement of coupled elastic waves (L1+F2) is illustrated in Fig.50b. When we fit the sinusoidal wave ($B_{L1}\cos(k_{L1}x - \Phi_{L1}) + B_{F2}\cos(k_{F2}x - \Phi_{F2})$) to the real part of the displacements as shown in Fig.50c and Fig.50d, we find k_{L1} as 0.004335 rad/m and k_{F2} as 0.2025 rad/m. The theoretical results are 0.00428 rad/m for k_{L1} and 0.199 rad/m for k_{F2} as presented in Fig.45. Therefore, we got good match between numerical results and theoretical calculations for $\Omega_y = 2\pi 12.5$ rad/s in Case 2. In Fig.50c, we found Φ_{L1} as 0 and Φ_{F2} as $-\frac{\pi}{4}$ where B_{L1}, B_{F2} are obtained as 9.34×10^{10} m and 2×10^{8} m, respectively. In Fig.50d, we found Φ_{L1} as $-\frac{\pi}{2}$ and Φ_{F2} as $\frac{\pi}{4}$ where B_{L1}, B_{F2} are obtained as 1.08×10^{11} m and 6×10^{7} m, respectively.

4.3.3 Example 3: Torsional wave - Flexural wave Coupling

In this part, the aluminum cylindrical rod is analyzed for various rotation rates of Ω_z about the z-axis in order to illustrate the coupling between torsional and flexural waves. The design parameters are given in Table 12 for Example 4. In Example 3, we study two different cases for the rotating rods that are categorized as the flexural-torsional wave coupling (Case 1) and the torsional-flexural wave

coupling (Case 2). In Case 1, the flexural wave (F2) is driven in the z direction initially, then the torsional wave (T1) starts to tilt about the x direction and propagate with the flexural wave (F2) due to the Coriolis coupling. In Case 2, the torsional wave (T1) is driven about the x direction initially, then the flexural wave (F2) starts to vibrate in the z direction and propagate with the torsional wave (T1) due to the Coriolis coupling. The force load (F_z) is applied on the cross section of the lossless rod end in the z direction for the actuation of F2 in Case1, where the force load (F_y) is applied on the top and bottom nodes at the z axis of the lossless rod end which are oppositely directed through the y-axis for the actuation of T1 in Case2. In order to minimize the spatial effects as explained in the theory section, we determined a low drive frequency by 10 Hz to analyze the small rotation rates and exaggerated the force loads by 10^{20} N, as presented in Table 12. For the static case, the wavelength of flexural wave (λ_{F0}) is calculated by 39.99 m from Eq.(4.3) and the wavelength of torsional wave (λ_{T0}) is calculated by 309.87 m from Eq.(4.7). For various rotation rates, the length of lossy rod is designed by $4\lambda_{T0}$ with the proper loss factor, where the length of the lossless rod is $2\lambda_{T0}$. Further, theoretical condition parameter ($\frac{r}{\lambda_{F0}}$) is fulfilled by 0.025 for the rod with the radius of 1 m, as presented in Table 12.

In Example 3, the wavenumber shift occurs for the flexural wave (F2) and torsional wave (T1) due to the Coriolis torque, while the rotation is applied. In Fig.51, the wavenumbers of F2 and T1 calculated from Eq.(4.32) are illustrated for the rod rotating about the z axis shown in Fig.39c. In the figure, wavenumbers increase for both F2 and T1 starting from the static case. In our analysis, we study the cases of $\Omega_z = 0$, $2\pi 5$ rad/s and $2\pi 30$ rad/s in order to perform thorough analysis of the torsional-flexural wave coupling.

For $\Omega_z = 0$, the z displacement of F2 in Case 1 is illustrated in Fig.52a and the y displacement of T1 in Case 2 is illustrated in Fig.52b. In the figures, there are approximately 15.5 flexural waves and 2 torsional waves in the corresponding lossless rods. When we fit the sinusoidal wave ($B\cos(kx - \Phi)$) to the real part of

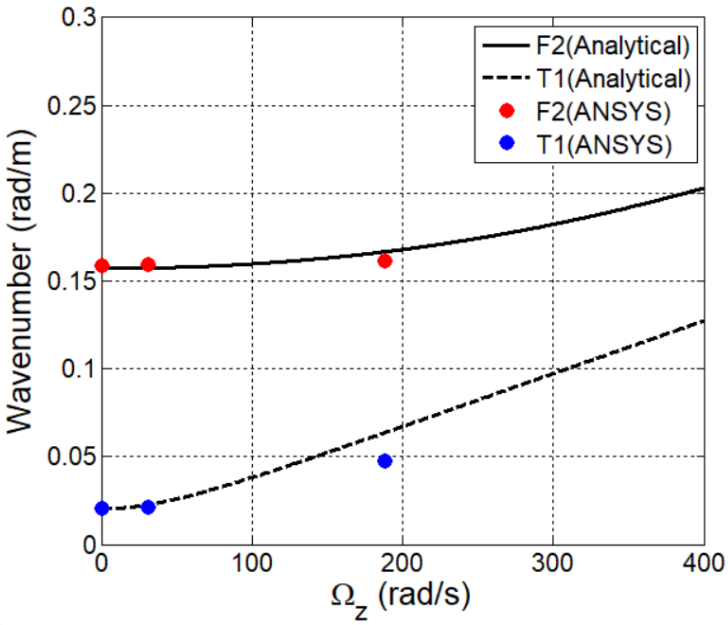


Figure 51: For the cylindrical aluminum rod induced by the constant rotation (Ω_z) in Example 3, the wavenumbers of F2 and T1 calculated from Eq.(4.32) and the ANSYS results.

the displacements as shown in Fig.52c and Fig.52d, we find k_{F2} as 0.159 rad/m and k_{T1} as 0.02028 rad/m. The theoretical results are 0.157 rad/m for k_{F2} and 0.02028 rad/m for k_{T1} as presented in Fig.51. Therefore, we got good match between numerical results and theoretical calculations for $\Omega_z = 0$. Further, we found Φ_{F2} as $\frac{5\pi}{4}$ and Φ_{T1} as -0.5417π where B_{F2}, B_{T1} are obtained as 3.475×10^{11} m and 2.594×10^{11} m, respectively.

For $\Omega_z = 2\pi 5$ rad/s in Case 1, the z displacement of coupled elastic waves (F2+T1) is illustrated in Fig.53a and the y displacement of coupled elastic waves (F2+T1) is illustrated in Fig.53b. When we fit the sinusoidal wave ($B_{F2}\cos(k_{F2}x - \Phi_{F2}) + B_{T1}\cos(k_{T1}x - \Phi_{T1})$) to the real part of the displacements as shown in Fig.53c and Fig.53d, we find k_{F2} as 0.1595 rad/m and k_{T1} as 0.02155 rad/m. The theoretical results are 0.1574 rad/m for k_{F2} and 0.0226 rad/m for k_{T1} as presented in Fig.51. Therefore, we got good match between numerical results and theoretical calculations for $\Omega_z = 2\pi 5$ rad/s in Case 1. In Fig.53c, we found Φ_{F2} as $\frac{5\pi}{4}$ and Φ_{T1} as -0.5417π where B_{F2}, B_{T1} are obtained as 3.45×10^{11} m and 5×10^{9} m, respectively. In Fig.53d, we found Φ_{F2} as $\frac{\pi}{4}$ and Φ_{T1} as 1.26π where B_{F2}, B_{T1} are

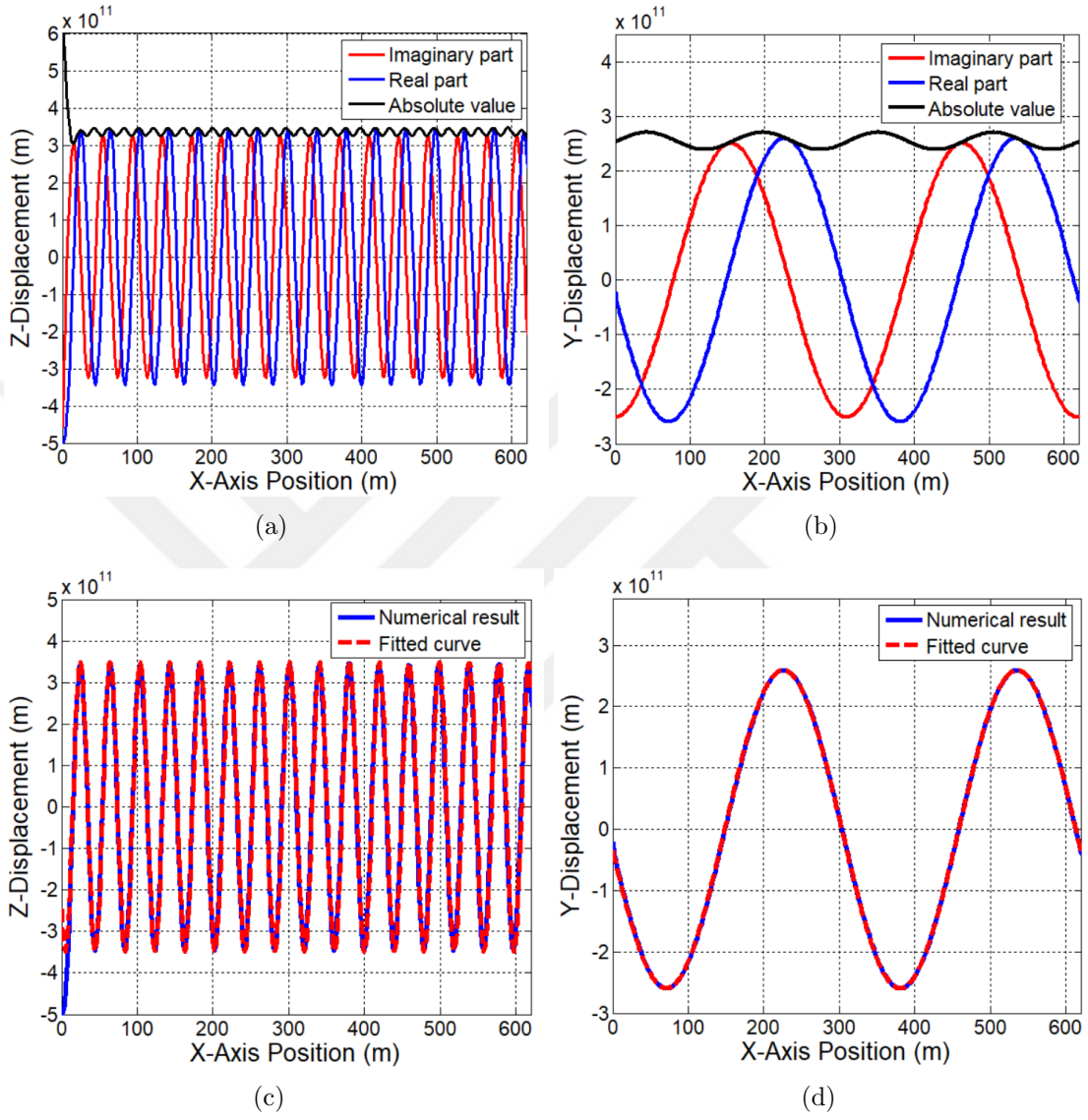


Figure 52: For $\Omega_z = 0$ in Example 3, the displacement at the top z-nodes of lossless cylindrical aluminum rod along the x axis **(a)** in the z direction for Case 1, **(b)** in the y direction for Case 2, **(c)** wavenumber, amplitude and phase calculations of the numerical result by fitting the sinusoidal wave of $B\cos(kx - \Phi)$ to the real part of the z-displacement (same blue curve as in Fig.52a), and **(d)** to the real part of the y-displacement (same blue curve as in Fig.52b). The length of lossy aluminum part equals to $4\lambda_{T0}$ with loss factor $\beta = 4 \times 10^{-3}$.

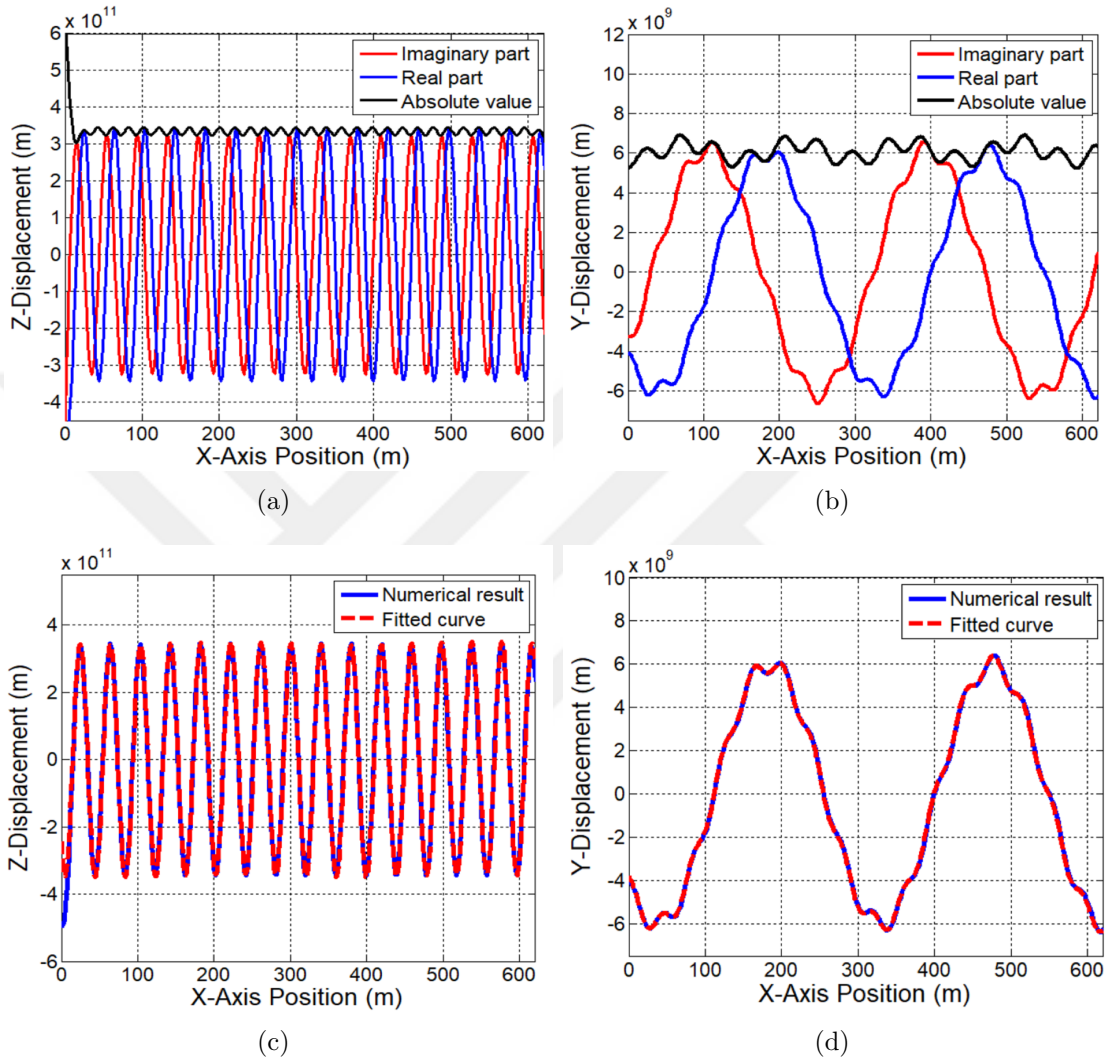


Figure 53: For $\Omega_z = 2\pi 5$ rad/s in Case 1 of Example 3, the displacement at the top z-nodes of lossless cylindrical aluminum rod along the x axis **(a)** in the z direction, **(b)** in the y direction, **(c)** wavenumber, amplitude and phase calculations of the numerical result by fitting the sinusoidal wave of $B_{F2}\cos(k_{F2}x - \Phi_{F2}) + B_{T1}\cos(k_{T1}x - \Phi_{T1})$ to the real part of the z-displacement (same blue curve as in Fig.53a), and **(d)** to the real part of the y-displacement (same blue curve as in Fig.53b). The length of lossy aluminum part equals to $4\lambda_{T0}$ with loss factor $\beta = 4 \times 10^{-3}$.

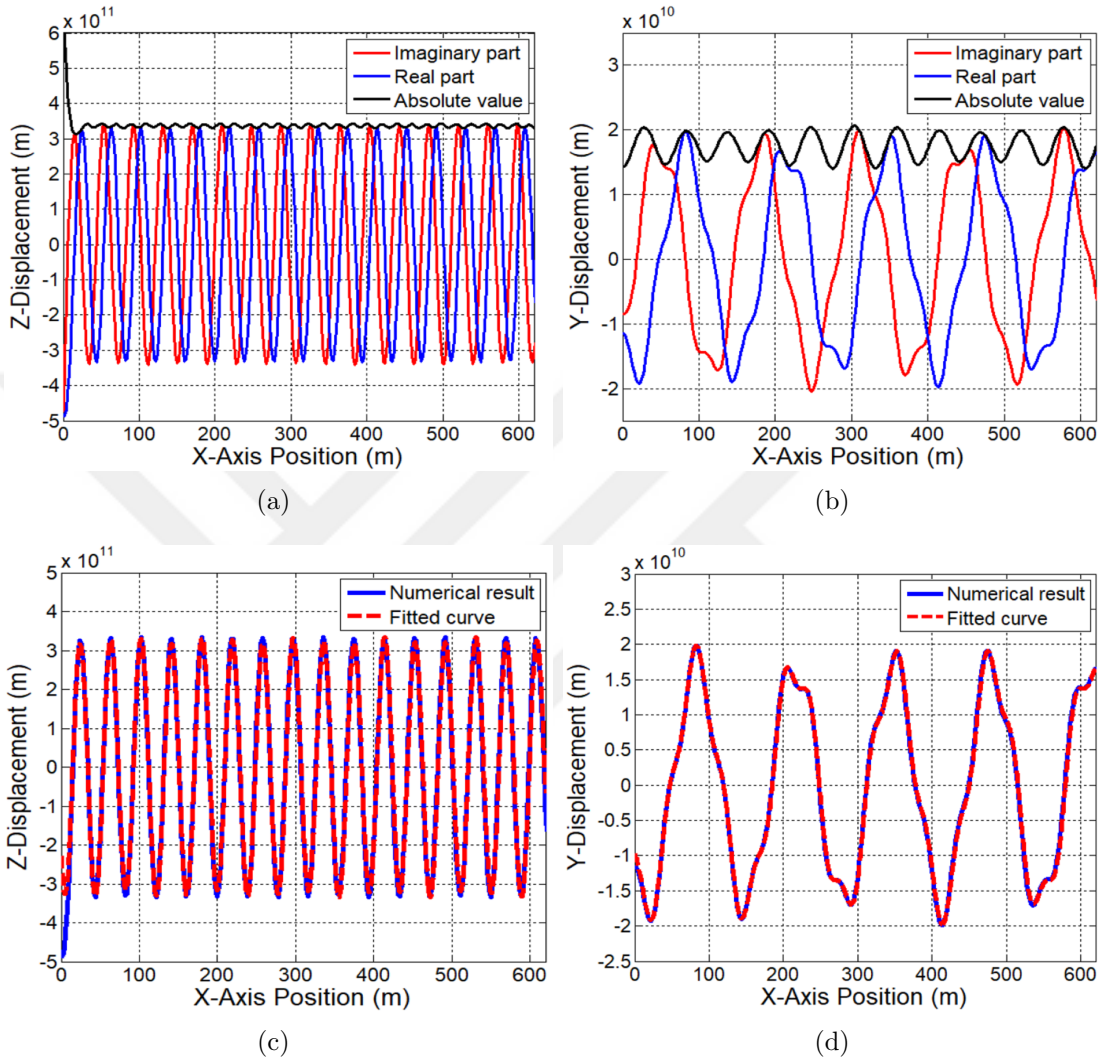


Figure 54: For $\Omega_z = 2\pi 30$ rad/s in Case 1 of Example 3, the displacement at the top z-nodes of lossless cylindrical aluminum rod along the x axis **(a)** in the z direction, **(b)** in the y direction, **(c)** wavenumber, amplitude and phase calculations of the numerical result by fitting the sinusoidal wave of $B_{F2}\cos(k_{F2}x - \Phi_{F2}) + B_{T1}\cos(k_{T1}x - \Phi_{T1})$ to the real part of the z-displacement (same blue curve as in Fig.54a), and **(d)** to the real part of the y-displacement (same blue curve as in Fig.54b). The length of lossy aluminum part equals to $4\lambda_{T0}$ with loss factor $\beta = 2 \times 10^{-3}$.

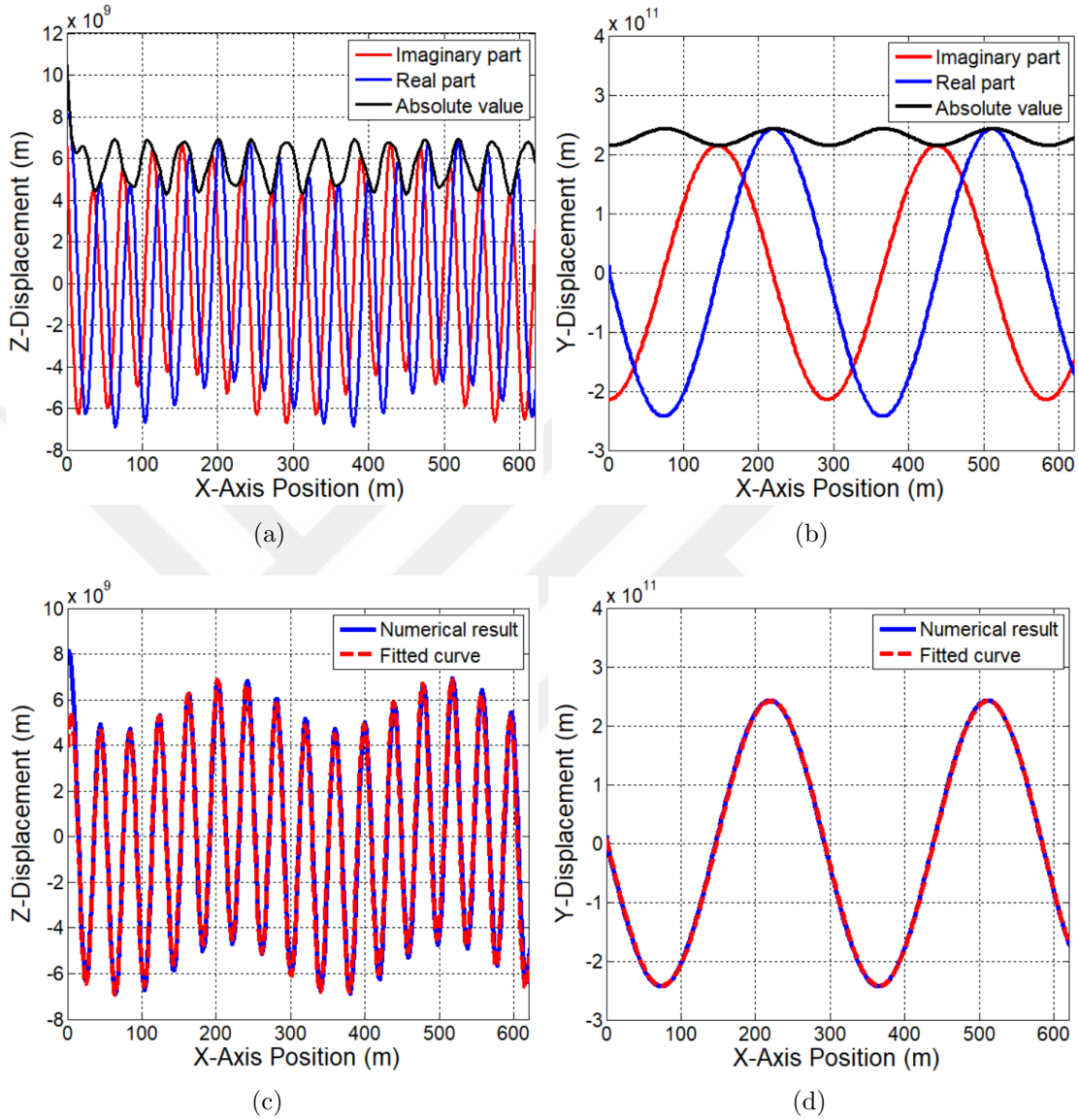


Figure 55: For $\Omega_z = 2\pi 5$ rad/s in Case 2 of Example 3, the displacement at the top z-nodes of lossless cylindrical aluminum rod along the x axis **(a)** in the z direction, **(b)** in the y direction, **(c)** wavenumber, amplitude and phase calculations of the numerical result by fitting the sinusoidal wave of $B_{T1}\cos(k_{T1}x - \Phi_{T1}) + B_{F2}\cos(k_{F2}x - \Phi_{F2})$ to the real part of the z-displacement (same blue curve as in Fig.55a), and **(d)** to the real part of the y-displacement (same blue curve as in Fig.55b). The length of lossy aluminum part equals to $4\lambda_{T0}$ with loss factor $\beta = 4 \times 10^{-3}$.

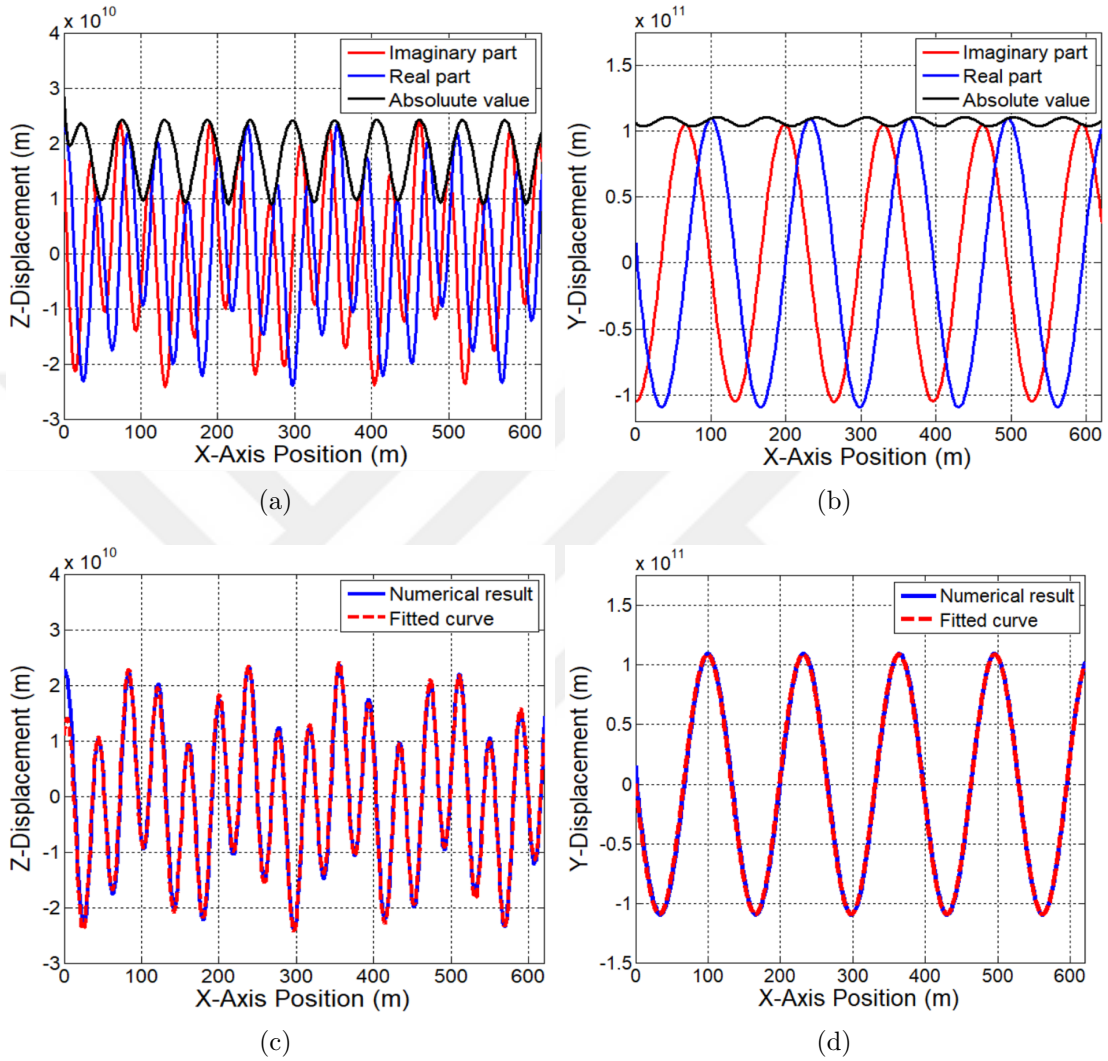


Figure 56: For $\Omega_z = 2\pi 30$ rad/s in Case 2 of Example 3, the displacement at the top z-nodes of lossless cylindrical aluminum rod along the x axis **(a)** in the z direction, **(b)** in the y direction, **(c)** wavenumber, amplitude and phase calculations of the numerical result by fitting the sinusoidal wave of $B_{T1}\cos(k_{T1}x - \Phi_{T1}) + B_{F2}\cos(k_{F2}x - \Phi_{F2})$ to the real part of the z-displacement (same blue curve as in Fig.56a), and **(d)** to the real part of the y-displacement (same blue curve as in Fig.56b). The length of lossy aluminum part equals to $4\lambda_{T0}$ with loss factor $\beta = 2 \times 10^{-3}$.

obtained as 4×10^8 m and 6×10^9 m, respectively.

For $\Omega_z = 2\pi 30$ rad/s in Case 1, the z displacement of coupled elastic waves (F2+T1) is illustrated in Fig.54a and the y displacement of coupled elastic waves (F2+T1) is illustrated in Fig.54b. When we fit the sinusoidal wave ($B_{F2}\cos(k_{F2}x - \Phi_{F2}) + B_{T1}\cos(k_{T1}x - \Phi_{T1})$) to the real part of the displacements as shown in Fig.54c and Fig.54d, we find k_{F2} as 0.1612 rad/m and k_{T1} as 0.0475 rad/m. The theoretical results are 0.1667 rad/m for k_{F2} and 0.0638 rad/m for k_{T1} as presented in Fig.51. Therefore, we got good match between numerical results and theoretical calculations for $\Omega_z = 2\pi 30$ rad/s in Case 1. In Fig.54c, we found Φ_{F2} as $\frac{5\pi}{4}$ and Φ_{T1} as -0.5417π where B_{F2}, B_{T1} are obtained as 3.25×10^{11} m and 9×10^9 m, respectively. In Fig.54d, we found Φ_{F2} as $\frac{\pi}{4}$ and Φ_{T1} as 1.26π where B_{F2}, B_{T1} are obtained as 2.75×10^9 m and 1.7×10^{10} m, respectively.

For $\Omega_z = 2\pi 5$ rad/s in Case 2, the z displacement of coupled elastic waves (T1+F2) is illustrated in Fig.55a and the y displacement of coupled elastic waves (T1+F2) is illustrated in Fig.55b. When we fit the sinusoidal wave ($B_{T1}\cos(k_{T1}x - \Phi_{T1}) + B_{F2}\cos(k_{F2}x - \Phi_{F2})$) to the real part of the displacements as shown in Fig.55c and Fig.55d, we find k_{T1} as 0.02155 rad/m and k_{F2} as 0.1595 rad/m. The theoretical results are 0.0226 rad/m for k_{T1} and 0.1574 rad/m for k_{F2} as presented in Fig.51. Therefore, we got good match between numerical results and theoretical calculations for $\Omega_z = 2\pi 5$ rad/s in Case 2. In Fig.55c, we found Φ_{T1} as -0.5417π and Φ_{F2} as $\frac{9\pi}{4}$ where B_{T1}, B_{F2} are obtained as 1.2×10^9 m and 5.7×10^9 m, respectively. In Fig.55d, we found Φ_{T1} as $\frac{3\pi}{2}$ and Φ_{F2} as $\frac{5\pi}{4}$ where B_{T1}, B_{F2} are obtained as 2.42×10^{11} m and 1×10^8 m, respectively.

For $\Omega_z = 2\pi 30$ rad/s in Case 2, the z displacement of coupled elastic waves (T1+F2) is illustrated in Fig.56a and the y displacement of coupled elastic waves (T1+F2) is illustrated in Fig.56b. When we fit the sinusoidal wave ($B_{T1}\cos(k_{T1}x - \Phi_{T1}) + B_{F2}\cos(k_{F2}x - \Phi_{F2})$) to the real part of the displacements as shown in Fig.56c and Fig.56d, we find k_{T1} as 0.0475 rad/m and k_{F2} as 0.1612 rad/m. The theoretical results are 0.0638 rad/m for k_{T1} and 0.1667 rad/m for k_{F2} as presented

in Fig.51. Therefore, we got good match between numerical results and theoretical calculations for $\Omega_z = 2\pi 30$ rad/s in Case 2. In Fig.56c, we found Φ_{T1} as -0.5417π and Φ_{F2} as $\frac{9\pi}{4}$ where B_{T1}, B_{F2} are obtained as 7.6×10^9 m and 1.67×10^{10} m, respectively. In Fig.56d, we found Φ_{T1} as $\frac{3\pi}{2}$ and Φ_{F2} as $\frac{\pi}{4}$ where B_{T1}, B_{F2} are obtained as 1.09×10^{11} m and 1×10^8 m, respectively.

4.4 A Novel Cylindrical Rod Gyroscope Using Coupled Flexural-Flexural Wave Propagation

In this section, a cylindrical rod waveguide gyroscope is presented as an example of a waveguide based gyroscope. Fig.57 shows the device geometry. The gyroscope is composed of a rod and two transducers located at each end of the rod. Flexural waves are excited and detected by the transducers. Flexural wave propagation is dispersive and multiple modes may exist depending on the operation frequency. In such systems, a single mode, which is the lowest order mode, is excited to avoid signal cluttering. The sensitivity of the gyroscope, that utilizes the elastic waves, is inversely proportional to velocity and wavelength of the elastic wave. Therefore, the size and the operating frequency of the waveguide must be chosen carefully. The modes of cylindrical rod waveguide were discussed and the most appropriate mode was chosen as the flexural modes considering the details in the previous sections. The analytical calculations were presented in order to calculate the wavenumber shift of coupled flexural waves in rotating cylindrical rod waveguides and, the analytical calculations were verified by the finite element analysis. In order to measure the rotation rate in the rotating rods, the phase difference ($\Delta\phi$) between the initial wave and the induced wave can be calculated by $(k_{F1} - k_{F0})L$ as given below:

$$\Delta\phi = k_{F0}L\left(\sqrt{1 + \frac{\Omega_x}{\omega_0}} - 1\right) \tag{4.33}$$

where k_{F0}, k_{F1} are given in Eq.(4.3) and Eq.(4.15), respectively. L denotes the length of the cylindrical rod. As the $\Delta\phi$ is proportional with the Ω_x, one can measure the rotation rate with the configuration presented in Fig.57. In Fig.57,

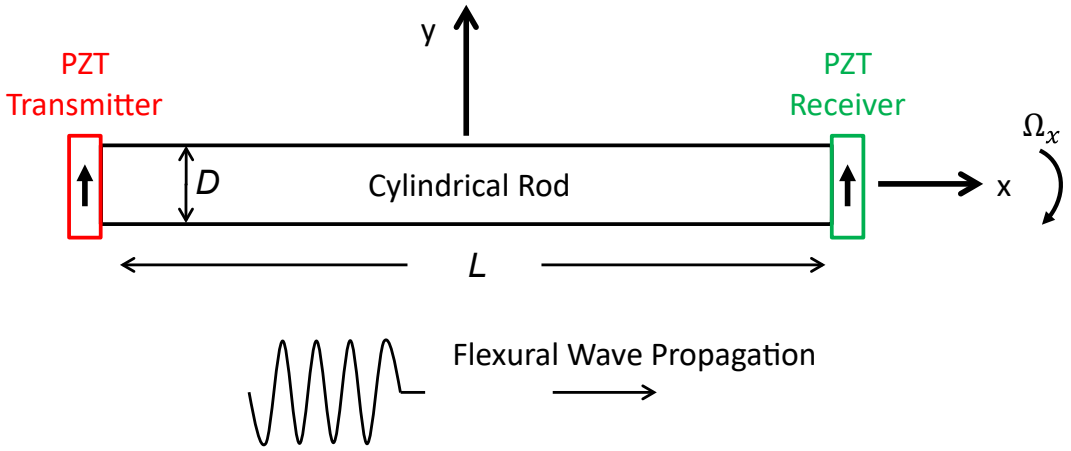


Figure 57: Novel gyroscope design.

PZT transmitter excites the flexural wave in y direction with pulse-mode operation and PZT receiver detects the flexural wave propagating through the x direction induced by the rotation about the x axis. In this configuration, a straight cylindrical rod system is used as a waveguide and the polarization directions of both transducers are identical for the excitation and the detection of the flexural wave propagation. Ideally, when there is no rotation, there exists no phase shift for the travelling wave. The phase shift reveal proportional to the amount of rotation, when the rod system is rotated about the direction of the wave propagation. The sensitivity of the device depends on the phase difference given in Eq.(4.33). Eq.(4.33) shows that the sensitivity decreases for higher operating frequencies and further, the size of the rod also affects the sensitivity as shown in Fig.58.

The sensitivity of the proposed gyroscope can be optimized with the variables of the operating frequency and the rod size. Fig.58 shows the sensitivity of a rod system for the operating frequency range of 100 Hz to 100 kHz and the radii of rod in the range of 1 μm to 1 mm, where the rod length is 10 cm. As expected, the sensitivity decreases when the operating frequency increases in Fig.58. Further, the sensitivity decreases for the larger rod diameters. Thus, the maximum sensitivity is calculated for the minimum operating frequency and the smallest rod diameter as 0.039 degree/dps. However, for the rod design with the maximum sensitivity the wavelength of flexural wave is larger than the rod length as

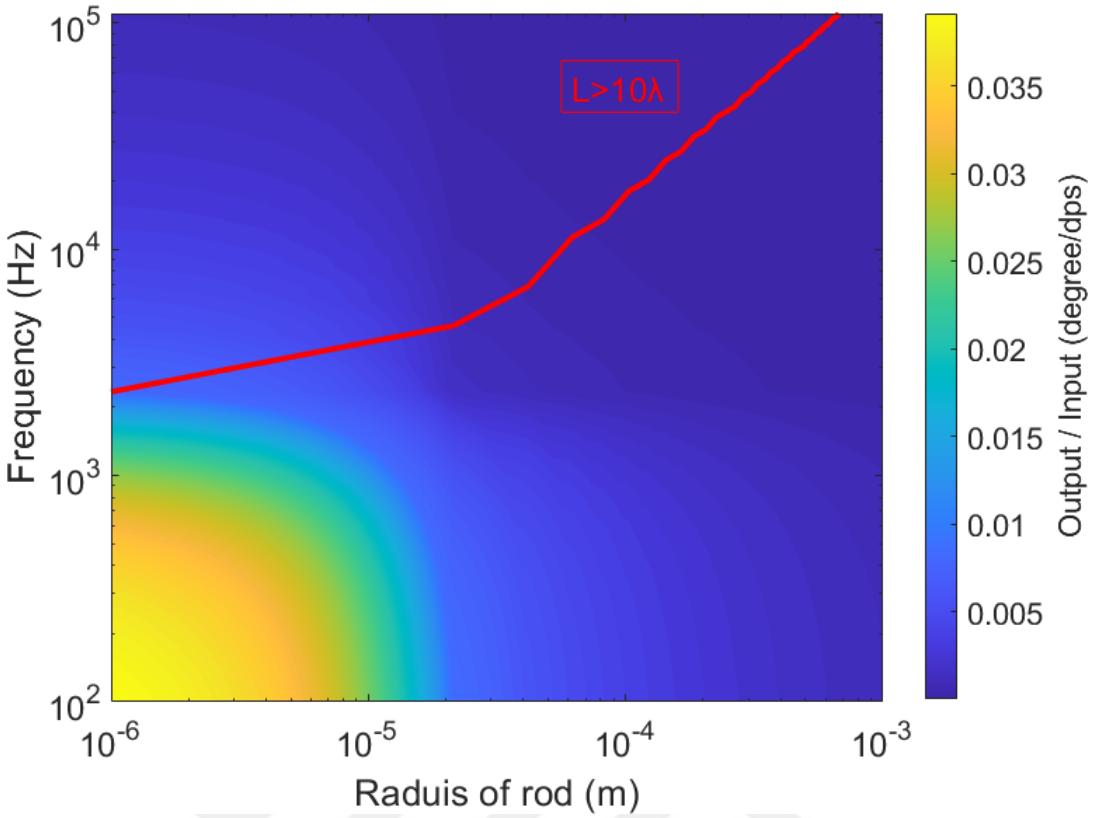


Figure 58: Heat map of ratio of the phase difference (output) to input rate is calculated for the radii of rod in the range of 1 μm to 1 mm and the operating frequency range of 100 Hz to 100 kHz. Red curve indicates the designs where the rod length is 10 times larger than the wavelength of flexural wave. Below the red curve, the flexural waves in rods have larger wavelengths where 10 wavelengths are larger than the rod length. L equals to 10 cm.

calculated in Fig.58. This shows that the ratio of the rod length to wavelength is another important condition to be considered in the design of rod system based gyroscopes. So, we calculated the wavelengths that are 10 times smaller than the rod length in order to perform the wave propagation as shown with the red curve in Fig.58. Below the red curve, the flexural waves in rods have larger wavelengths than the desired wave propagation condition determined as $L > 10\lambda$. Therefore, the operating frequency and the radius of rod were calculated as 2.3 kHz and 1 μm, where the maximum sensitivity was calculated as 0.008 degree/dps under the condition of $L > 10\lambda$. For the fabrication of this configuration, one of the biggest challenges is the high aspect ratio (L/2r) of the rod. So, the aspect ratio of the rod should be reconsidered, where the sensitivity will be sacrificed in this case.

However, such structures can be fabricated from single crystal silicon using micro-machining techniques. The transducers can also be integrated over the waveguide using PZT sputtering techniques.

4.5 Discussion

We presented a thorough vibration analysis of rod systems including the Coriolis coupling between the various propagating elastic waves. It is shown that elastic waves are affected by the rotation rate applied about any axis. Therefore, vibrating rod structures form a feasible basis for a rotation rate sensor, where the type of elastic wave coupling is the determinant factor for the size of the sensor. The main purpose of this work is to explore the most suitable wave type and coupling for the sensor applications. It is demonstrated that flexural-flexural, longitudinal-flexural and torsional-flexural wave coupling occur due to the Coriolis Effect by using the FEM analysis. Our analysis showed that the wavenumber shift occurs for the elastic waves propagating in the rods, as the rotation is applied. In the analysis, we studied several cases for each type of couplings and the analytical calculations are well matched with the numerical results for the shifting wavenumbers of the elastic waves due to the Coriolis Effect. Based on the several case studies, it is found that the sizes of the rod structures are not suitable enough for the sensor applications, except for the case of flexural-flexural wave coupling. In this case, the rod is designed in mm scale for 1 kHz operating frequency and can be miniaturized in smaller scales ($\sim$ μm) for the higher operating frequency range ($\sim$MHz). Thus, the flexural wave that couples with its conjugate flexural mode can be used to measure the rotation rate applied about the direction of propagation, whereas other types of couplings may not be feasible due to the rod size. Future work should focus on the construction of the sensor system as a rod which utilizes the propagating flexural waves and flexural-flexural wave coupling.

CHAPTER V

CONCLUSION AND FUTURE WORK

We performed the noise analysis of mode matched vibrating gyroscope systems and introduced a novel cylindrical rod gyroscope based on our thorough vibration analysis of rotating rod systems. Mode matched MEMS gyroscopes have been considered to be a good candidate for low cost navigation applications due to the fact that they theoretically achieve very low noise and high stability. However, the analysis of mode-matched vibratory gyroscopes have been carried out for zero-rate output. We presented a thorough analysis of mode-matched gyroscope systems where the coupling between the drive and sense systems due to Coriolis force is included. This enabled us to analyze the effect of the Coriolis coupling in the performance of the gyro. In the analysis, we illustrated that as the rotation input is applied, the phases of the drive and sense modes shift and multiple resonances of the gyro system appear. Further, the rotation rates above the bandwidth of the drive and sense system deteriorate the gyro linearity and the noise performance a lot, where the resonance splitting occurs due to Coriolis Effect. For the gyro system with the typical drive oscillation control system and open-loop output detection, the phase shift increases the ARW. Moreover, the resonance splitting due to Coriolis Effect generates peaks in the output noise spectrum, which also results in overall increase in ARW. For the force to rebalance operation mode, some of the issues that is associated with the Coriolis coupling is addressed. However, the noise performance of a rotating gyro can be significantly different from that of a gyro that does not experience any rotation for mode-matched gyros.

The observations we made during the first part of this thesis motivated us to investigate the frequency shift in the resonances of vibratory systems due to the Coriolis force. The frequency shift and the multiple resonances observed are due

to the multiple waves that are traveling in the mechanical structures of the gyroscopes. In the second part of the thesis we analyzed wave propagation in rotating waveguides. This analysis led to development of waveguide based gyroscopes. This novel gyroscope uses the flexural modes of a straight rod shaped waveguide. The rotation measurement method is based on the phase shift of elastic waves. In this thesis, we showed how to calculate the mode couplings in a rotating rod system and choose the most appropriate mode coupling for the detection. Based on our analysis, it was found that the flexural-flexural wave coupling is suitable for the sensor applications. One can excite the flexural wave propagating through the straight rod system by a transmitter transducer attached to the rod end. Ideally, when there is no rotation, there exists no phase shift for the travelling wave. As the rotation is introduced about the direction of the wave propagation, the phase shift generated is proportional to the amount of rotation. The receiver transducer attached to the other rod end collects this modulated travelling wave to measure the rotation rate. The both transmitter and receiver transducers have the same polarization direction.

In the future, we would like to build the novel cylindrical rod gyroscope using coupled flexural-flexural wave propagation experimentally and demonstrate the operation of this device. Further, detailed analysis is required to calculate the sensitivity of these devices.

Bibliography

[1] V. Passaro, A. Cuccovillo, L. Vaiani, M. De Carlo, and C. E. Campanella, "Gyroscope technology and applications: A review in the industrial perspective," *Sensors*, vol. 17, no. 10, p. 2284, 2017.

[2] N. Barbour and G. Schmidt, "Inertial sensor technology trends," *IEEE Sensors Journal*, vol. 1, no. 4, pp. 332–339, 2001.

[3] R. Bergh, H. Lefevre, and H. Shaw, "An overview of fiber-optic gyroscopes," *Journal of Lightwave Technology*, vol. 2, no. 2, pp. 91–107, 1984.

[4] H. C. Lefevre, Y. Bourbin, P. Graindorge, and H. J. Arditty, "Review Of Fiber Optic Gyroscopes," in *Max Born Centenary Conf* (M. J. Colles and D. W. Swift, eds.), vol. 0369, pp. 386 – 394, International Society for Optics and Photonics, SPIE, 1983.

[5] W. W. Chow, J. Gea-Banacloche, L. M. Pedrotti, V. E. Sanders, W. Schleich, and M. O. Scully, "The ring laser gyro," *Rev. Mod. Phys.*, vol. 57, pp. 61–104, Jan 1985.

[6] K. U. Schreiber and J.-P. R. Wells, "Invited review article: Large ring lasers for rotation sensing," *Review of Scientific Instruments*, vol. 84, no. 4, p. 041101, 2013.

[7] D. M. Rozelle, "The hemispherical resonator gyro: From wineglass to the planets," in *Proc. 19th AAS/AIAA Space Flight Mechanics Meeting*, vol. 134, pp. 1157–1178, 2009.

[8] G. Zhanshe, C. Fucheng, L. Boyu, C. Le, L. Chao, and S. Ke, "Research development of silicon MEMS gyroscopes: a review," *Microsystem Technologies*, vol. 21, no. 10, pp. 2053–2066, 2015.

[9] C. Acar, A. R. Schofield, A. A. Trusov, L. E. Costlow, and A. M. Shkel, "Environmentally robust MEMS vibratory gyroscopes for automotive applications," *IEEE Sensors Journal*, vol. 9, no. 12, pp. 1895–1906, 2009.

[10] C. Acar and A. Shkel, *MEMS vibratory gyroscopes: structural approaches to improve robustness*. Springer Science & Business Media, 2008.

[11] J. Yang, "A review of analyses related to vibrations of rotating piezoelectric bodies and gyroscopes," *IEEE Transactions on Ultrasonics, Ferroelectrics, and Frequency Control*, vol. 52, no. 5, pp. 698–706, 2005.

[12] K. Larkin, M. Ghommem, M. Serrano, and A. Abdelkefi, "A review on vibrating beam-based micro/nano-gyroscopes," *Microsystem Technologies*, pp. 1–25, 2021.

[13] R. Antonello and R. Oboe, "MEMS gyroscopes for consumer and industrial applications," *Microsensors, Intech*, pp. 253–280, 2011.

[14] A. A. Trusov, A. R. Schofield, and A. M. Shkel, "Micromachined rate gyroscope architecture with ultra-high quality factor and improved mode ordering," *Sensors and Actuators A: Physical*, vol. 165, no. 1, pp. 26–34, 2011. Transducers 2009.

[15] M. F. Zaman, A. Sharma, Z. Hao, and F. Ayazi, "A mode-matched silicon-yaw tuning-fork gyroscope with subdegree-per-hour allan deviation bias instability," *Journal of Microelectromechanical systems*, vol. 17, no. 6, pp. 1526–1536, 2008.

[16] S. Sonmezoglu, S. E. Alper, and T. Akin, "An automatically mode-matched mems gyroscope with wide and tunable bandwidth," *Journal of microelectromechanical systems*, vol. 23, no. 2, pp. 284–297, 2014.

[17] J. Geen, S. Sherman, J. Chang, and S. Lewis, "Single-chip surface micromachined integrated gyroscope with 50 °/h Allan deviation," *IEEE Journal of Solid-State Circuits*, vol. 37, no. 12, pp. 1860–1866, 2002.

[18] D. Sachs, S. Nasiri, and D. Goehl, "Image stabilization technology overview," *InvenSense Whitepaper*, 2006.

[19] R. H. Dixon and J. Bouchaud, "Markets and applications for MEMS inertial sensors," in *MEMS/MOEMS Components and Their Applications III*, vol. 6113, p. 611306, International Society for Optics and Photonics, 2006.

[20] J. Raper, G. Gartner, H. Karimi, and C. Rizos, "A critical evaluation of location based services and their potential," *Journal of Location Based Services*, vol. 1, no. 1, pp. 5–45, 2007.

[21] H. Cetin and G. G. Yaralioglu, "Analysis of vibratory gyroscopes: drive and sense mode resonance shift by Coriolis force," *IEEE Sensors Journal*, vol. 17, no. 2, pp. 347–358, 2016.

[22] K. Funk, H. Emmerich, A. Schilp, M. Offenberg, R. Neul, and F. Larmer, "A surface micromachined silicon gyroscope using a thick polysilicon layer," in *Technical Digest. IEEE International MEMS 99 Conference. Twelfth IEEE International Conference on Micro Electro Mechanical Systems (Cat. No.99CH36291)*, pp. 57–60, 1999.

[23] B. J. Gallacher, J. Hedley, J. S. Burdess, A. J. Harris, A. Rickard, and D. O. King, "Electrostatic correction of structural imperfections present in a microring gyroscope," *Journal of Microelectromechanical systems*, vol. 14, no. 2, pp. 221–234, 2005.

[24] N. Yazdi, F. Ayazi, and K. Najafi, "Micromachined inertial sensors," *Proceedings of the IEEE*, vol. 86, no. 8, pp. 1640–1659, 1998.

[25] F. Ayazi and K. Najafi, "A HARPSS polysilicon vibrating ring gyroscope," *Journal of Microelectromechanical Systems*, vol. 10, no. 2, pp. 169–179, 2001.

[26] S. Y. Bae, K. J. Hayworth, K. Y. Yee, K. Shcheglov, and D. V. Wiberg, "High-performance MEMS microgyroscope," in *Design, Test, Integration, and Packaging of MEMS/MOEMS 2002*, vol. 4755, pp. 316–324, International Society for Optics and Photonics, 2002.

[27] A. M. Shkel, "Type I and type II micromachined vibratory gyroscopes," in *2006 IEEE/ION Position, Location, And Navigation Symposium*, pp. 586–593, IEEE, 2006.

[28] I. P. Prikhodko, J. A. Gregory, W. A. Clark, J. A. Geen, M. W. Judy, C. H. Ahn, and T. W. Kenny, "Mode-matched MEMS Coriolis vibratory gyroscopes: Myth or reality?," in *2016 IEEE/ION Position, Location and Navigation Symposium (PLANS)*, pp. 1–4, IEEE, 2016.

[29] M. Saukoski, L. Aaltonen, and K. A. I. Halonen, "Effects of synchronous demodulation in vibratory mems gyroscopes: A theoretical study," *IEEE Sensors Journal*, vol. 8, no. 10, pp. 1722–1733, 2008.

[30] Z. Hu and B. Gallacher, "A mode-matched force-rebalance control for a MEMS vibratory gyroscope," *Sensors and Actuators A: Physical*, vol. 273, pp. 1–11, 2018.

[31] D. Senkal and A. M. Shkel, *Whole-Angle MEMS Gyroscopes: Challenges and Opportunities*. John Wiley & Sons, 2020.

[32] D. Chatzopoulos, C. Bermejo, Z. Huang, and P. Hui, "Mobile augmented reality survey: From where we are to where we go," *IEEE Access*, vol. 5, pp. 6917–6950, 2017.

[33] L. Yang, J. Huang, T. Feng, W. Hong-An, and D. Guo-Zhong, "Gesture interaction in virtual reality," *Virtual Reality & Intelligent Hardware*, vol. 1, no. 1, pp. 84–112, 2019.

[34] "IEEE standard for inertial sensor terminology," *IEEE Std 528-2019*, pp. 1–35, 2019.

[35] D. D. Lynch, "Hemispherical resonator gyro," *IEEE Trans. Aerosp. Electron. Syst*, vol. 20, no. 4, pp. 432–433, 1984.

[36] A. M. Shkel, R. Horowitz, A. A. Seshia, S. Park, and R. T. Howe, "Dynamics and control of micromachined gyroscopes," in *Proceedings of the 1999 American Control Conference (Cat. No. 99CH36251)*, vol. 3, pp. 2119–2124, IEEE, 1999.

[37] A. Shkel, R. T. Howe, and R. Horowitz, "Modeling and simulation of micromachined gyroscopes in the presence of imperfections," in *Int. Conf. On Modelling and Simulation of Microsystems*, pp. 605–608, Citeseer, 1999.

[38] W. A. Clark, R. T. Howe, and R. Horowitz, "Surface micromachined z-axis vibratory rate gyroscope," in *Tech. Dig. Solid-State Sensor and Actuator Workshop*, pp. 283–287, 1996.

[39] B. Y. Lao, "Gyroscopic effect in surface acoustic waves," in *1980 Ultrasonics Symposium*, pp. 687–691, IEEE, 1980.

[40] H. Tiersten, D. Stevens, and P. Das, "Circulating flexural wave rotation rate sensor," in *1981 Ultrasonics Symposium*, pp. 163–166, IEEE, 1981.

[41] H. Oh, K. J. Lee, K. Lee, and S. S. Yang, "Gyroscopes based on surface acoustic waves," *Micro and Nano Systems Letters*, vol. 3, no. 1, p. 1, 2015.

[42] S. E. Alper and T. Akin, "A symmetric surface micromachined gyroscope with decoupled oscillation modes," *Sensors and Actuators A: Physical*, vol. 97, pp. 347–358, 2002.

[43] M. Zaman, A. Sharma, B. Amini, and F. Ayazi, "Towards inertial grade vibratory microgyros: A high-q in-plane silicon-on-insulator tuning fork device," in *Proceedings of Solid-State Sensor, Actuator and Microsystems Workshop, Hilton Head Island, SC, USA*, vol. 610, p. 384385, 2004.

[44] T. Juneau, A. Pisano, and J. H. Smith, "Dual axis operation of a micromachined rate gyroscope," in *Proceedings of International Solid State Sensors and Actuators Conference (Transducers' 97)*, vol. 2, pp. 883–886, IEEE, 1997.

[45] P. Shao, V. Tavassoli, C. L. Mayberry, and F. Ayazi, "A 3D-HARPSS polysilicon microhemispherical shell resonating gyroscope: Design, fabrication, and characterization," *IEEE Sensors Journal*, vol. 15, no. 9, pp. 4974–4985, 2015.

[46] P. Greiff, B. Boxenhorn, T. King, and L. Niles, "Silicon monolithic micromechanical gyroscope," in *TRANSDUCERS'91: 1991 International Conference on Solid-State Sensors and Actuators. Digest of Technical Papers*, pp. 966–968, IEEE, 1991.

[47] J. Bernstein, S. Cho, A. King, A. Kourepenis, P. Maciel, and M. Weinberg, "A micromachined comb-drive tuning fork rate gyroscope," in *[1993] Proceedings IEEE Micro Electro Mechanical Systems*, pp. 143–148, IEEE, 1993.

[48] M. Putty and K. Najafi, "A MICROMACHINED VIBRATING RING GYROSCOPE," in *1994 Solid-State, Actuators, and Microsystems Workshop Technical Digest*, Transducer Research Foundation, Inc., June 1994.

[49] K. Tanaka, Y. Mochida, M. Sugimoto, K. Moriya, T. Hasegawa, K. Atsuchi, and K. Ohwada, "A micromachined vibrating gyroscope," *Sensors and Actuators A: Physical*, vol. 50, no. 1-2, pp. 111–115, 1995.

[50] P. Greiff, B. Antkowiak, J. Campbell, and A. Petrovich, "Vibrating wheel micromechanical gyro," in *Proceedings of Position, Location and Navigation Symposium-PLANS'96*, pp. 31–37, IEEE, 1996.

[51] M. Lutz, W. Golderer, J. Gerstenmeier, J. Marek, B. Maihofer, S. Mahler, H. Munzel, and U. Bischof, "A precision yaw rate sensor in silicon micromachining," in *Proceedings of International Solid State Sensors and Actuators Conference (Transducers' 97)*, vol. 2, pp. 847–850, IEEE, 1997.

[52] T. K. Tang, R. C. Gutierrez, C. B. Stell, V. Vorperian, G. A. Arakaki, J. T. Rice, W. J. Li, I. Chakraborty, K. Shcheglov, J. Z. Wilcox, *et al.*, "A packaged silicon mems vibratory gyroscope for microspacecraft," in *Proceedings IEEE The Tenth Annual International Workshop on Micro Electro Mechanical Systems. An Investigation of Micro Structures, Sensors, Actuators, Machines and Robots*, pp. 500–505, IEEE, 1997.

[53] D. Sparks, S. Zarabadi, J. Johnson, Q. Jiang, M. Chia, O. Larsen, W. Higdon, and P. Castillo-Borelley, "A cmos integrated surface micromachined angular rate sensor: its automotive applications," in *Proceedings of International Solid State Sensors and Actuators Conference (Transducers' 97)*, vol. 2, pp. 851–854, IEEE, 1997.

[54] Y. Oh, B. Lee, S. Baek, H. Kim, J. Kim, S. Kang, and C. Song, "A surface-micromachined tunable vibratory gyroscope," in *Proceedings IEEE The Tenth Annual International Workshop on Micro Electro Mechanical Systems. An Investigation of Micro Structures, Sensors, Actuators, Machines and Robots*, pp. 272–277, IEEE, 1997.

[55] K.-Y. Park, C.-W. Lee, Y.-S. Oh, and Y.-H. Cho, "Laterally oscillated and force-balanced micro vibratory rate gyroscope supported by fish-hook-shaped springs," *Sensors and Actuators A: Physical*, vol. 64, no. 1, pp. 69–76, 1998.

[56] R. Hulsing, "Mems inertial rate and acceleration sensor," *IEEE aerospace and electronic systems magazine*, vol. 13, no. 11, pp. 17–23, 1998.

[57] A. Kourepenis, J. Borenstein, J. Connelly, R. Elliott, P. Ward, and M. Weinberg, "Performance of mems inertial sensors," in *IEEE 1998 Position Location and Navigation Symposium (Cat. No. 98CH36153)*, pp. 1–8, IEEE, 1998.

[58] Y. Mochida, M. Tamura, and K. Ohwada, "A micromachined vibrating rate gyroscope with independent beams for the drive and detection modes," *Sensors and Actuators A: Physical*, vol. 80, no. 2, pp. 170–178, 2000.

[59] K. Funk, H. Emmerich, A. Schilp, M. Offenberg, R. Neul, and F. Larmer, "A surface micromachined silicon gyroscope using a thick polysilicon layer," in *Technical Digest. IEEE International MEMS 99 Conference. Twelfth IEEE International Conference on Micro Electro Mechanical Systems (Cat. No.99CH36291)*, pp. 57–60, 1999.

[60] S. Lee, S. Park, J. Kim, S. Lee, and D.-I. Cho, "Surface/bulk micromachined single-crystalline-silicon micro-gyroscope," *Journal of Microelectromechanical Systems*, vol. 9, no. 4, pp. 557–567, 2000.

[61] X. Jiang, J. Seeger, M. Kraft, and B. Boser, "A monolithic surface micromachined z-axis gyroscope with digital output," in *2000 Symposium on VLSI Circuits. Digest of Technical Papers (Cat. No.00CH37103)*, pp. 16–19, 2000.

[62] H. Xie and G. Fedder, "A cmos-mems lateral-axis gyroscope," in *Technical Digest. MEMS 2001. 14th IEEE International Conference on Micro Electro Mechanical Systems (Cat. No.01CH37090)*, pp. 162–165, 2001.

[63] H. Luo, X. Zhu, H. Lakdawala, L. Carley, and G. Fedder, "A copper cmos-mems z-axis gyroscope," in *Technical Digest. MEMS 2002 IEEE International Conference. Fifteenth IEEE International Conference on Micro Electro Mechanical Systems (Cat. No.02CH37266)*, pp. 631–634, 2002.

[64] W. Geiger, W. Butt, A. Gaißer, J. Frech, M. Braxmaier, T. Link, A. Kohne, P. Nommensen, H. Sandmaier, W. Lang, and H. Sandmaier, "Decoupled microgyros and the design principle DAVED," *Sensors and Actuators A: Physical*, vol. 95, no. 2, pp. 239–249, 2002. Papers from the Proceedings of the 14th IEEE Internat. Conf. on MicroElectroMechanical Systems.

[65] A. Seshia, R. Howe, and S. Montague, "An integrated microelectromechanical resonant output gyroscope," in *Technical Digest. MEMS 2002 IEEE International Conference. Fifteenth IEEE International Conference on Micro Electro Mechanical Systems (Cat. No.02CH37266)*, pp. 722–726, 2002.

[66] G. He and K. Najafi, "A single-crystal silicon vibrating ring gyroscope," in *Technical Digest. MEMS 2002 IEEE International Conference. Fifteenth IEEE International Conference on Micro Electro Mechanical Systems (Cat. No.02CH37266)*, pp. 718–721, 2002.

[67] H. Xie and G. K. Fedder, "Fabrication, characterization, and analysis of a drie cmos-mems gyroscope," *IEEE Sensors Journal*, vol. 3, no. 5, pp. 622–631, 2003.

[68] D. Karnick, G. Ballas, L. Koland, M. Secord, T. Braman, and T. Kourepenis, "Honeywell gun-hard inertial measurement unit (IMU) development," in *PLANS 2004. Position Location and Navigation Symposium (IEEE Cat. No.04CH37556)*, pp. 49–55, 2004.

[69] B.-d. Choi, S. Park, H. Ko, S.-J. Paik, Y. Park, G. Lim, A. Lee, S. C. Lee, W. Carr, D. Setiadi, *et al.*, "The first sub-deg/hr bias stability, silicon-microfabricated gyroscope," in *The 13th International Conference on Solid-State Sensors, Actuators and Microsystems, 2005. Digest of Technical Papers. TRANSDUCERS'05.*, vol. 1, pp. 180–183, IEEE, 2005.

[70] H. Johari and F. Ayazi, "High-frequency capacitive disk gyroscopes in (100) and (111) silicon," in *2007 IEEE 20th International Conference on Micro Electro Mechanical Systems (MEMS)*, pp. 47–50, IEEE, 2007.

[71] A. Trusov, A. Schofield, and A. Shkel, "New architectural design of a temperature robust mems gyroscope with improved gain-bandwidth characteristics," in *Proc. A Solid-State Sensors, Actuators and Microsystems Workshop (Hilton Head Workshop 2008)*, pp. 14–17, 2008.

[72] S. E. Alper, Y. Temiz, and T. Akin, "A compact angular rate sensor system using a fully decoupled silicon-on-glass mems gyroscope," *Journal of Microelectromechanical systems*, vol. 17, no. 6, pp. 1418–1429, 2008.

[73] M. F. Zaman, A. Sharma, and F. Ayazi, "The resonating star gyroscope: A novel multiple-shell silicon gyroscope with sub-5 deg/hr allan deviation bias instability," *IEEE Sensors Journal*, vol. 9, no. 6, pp. 616–624, 2009.

[74] W. Sung, M. Dalal, and F. Ayazi, "A mode-matched 0.9 MHz single proof-mass dual-axis gyroscope," in *2011 16th International Solid-State Sensors, Actuators and Microsystems Conference*, pp. 2821–2824, IEEE, 2011.

[75] R. Wang, P. Cheng, F. Xie, D. Young, and Z. Hao, "A multiple-beam tuning-fork gyroscope with high quality factors," *Sensors and Actuators A: Physical*, vol. 166, no. 1, pp. 22–33, 2011.

[76] Y. Tao, X. Wu, D. Xiao, Y. Wu, H. Cui, X. Xi, and B. Zhu, "Design, analysis and experiment of a novel ring vibratory gyroscope," *Sensors and Actuators A: Physical*, vol. 168, no. 2, pp. 286–299, 2011.

[77] I. P. Prikhodko, S. A. Zotov, A. A. Trusov, and A. M. Shkel, "Sub-degree-per-hour silicon mems rate sensor with 1 million Q-factor," in *2011 16th International Solid-State Sensors, Actuators and Microsystems Conference*, pp. 2809–2812, IEEE, 2011.

[78] S. Nitzan, C. Ahn, T.-H. Su, M. Li, E. Ng, S. Wang, Z. Yang, G. O'brien, B. Boser, T. Kenny, *et al.*, "Epitaxially-encapsulated polysilicon disk resonator gyroscope," in *2013 IEEE 26th International Conference on Micro Electro Mechanical Systems (MEMS)*, pp. 625–628, IEEE, 2013.

[79] P. Taheri-Tehrani, T. Su, A. Heidari, G. Jaramillo, C. Yang, S. Akhbari, H. Najar, S. Nitzan, D. Saito, L. Lin, *et al.*, "Micro-scale diamond hemispherical resonator gyroscope," in *Hilton Head Workshop*, pp. 289–292, 2014.

[80] A. D. Challoner, H. G. Howard, and J. Y. Liu, "Boeing disc resonator gyroscope," in *2014 IEEE/ION Position, Location and Navigation Symposium-PLANS 2014*, pp. 504–514, IEEE, 2014.

[81] J. Y. Cho, J.-K. Woo, J. Yan, R. L. Peterson, and K. Najafi, "Fused-silica micro birdbath resonator gyroscope (μ-BRG)," *Journal of Microelectromechanical Systems*, vol. 23, no. 1, pp. 66–77, 2013.

[82] A. Efimovskaya, Y.-W. Lin, and A. M. Shkel, "Origami-like 3-D folded MEMS approach for miniature inertial measurement unit," *Journal of Microelectromechanical Systems*, vol. 26, no. 5, pp. 1030–1039, 2017.

[83] N. V. Lavrik and P. G. Datskos, "Optically read Coriolis vibratory gyroscope based on a silicon tuning fork," *Microsystems & nanoengineering*, vol. 5, no. 1, pp. 1–11, 2019.

[84] D. Wang, A. Efimovskaya, and A. M. Shkel, "Amplitude amplified dual-mass gyroscope: Design architecture and noise mitigation strategies," in *2019 IEEE International Symposium on Inertial Sensors and Systems (INERTIAL)*, pp. 1–4, IEEE, 2019.

[85] J. Y. Cho, J.-K. Woo, G. He, D. Yang, C. Boyd, S. Singh, A. Darvishian, B. Shiari, and K. Najafi, "1.5-million Q-factor vacuum-packaged birdbath resonator gyroscope (BRG)," in *2019 IEEE 32nd International Conference on Micro Electro Mechanical Systems (MEMS)*, pp. 210–213, IEEE, 2019.

[86] H. Wen, A. Daruwalla, C.-S. Liu, and F. Ayazi, "A hermetically-sealed 2.9 MHz N = 3 disk baw gyroscope with sub-degree-per-hour bias instability," in *2020 IEEE 33rd International Conference on Micro Electro Mechanical Systems (MEMS)*, pp. 741–744, IEEE, 2020.

[87] S. Askari, M. H. Asadian, and A. M. Shkel, "Performance of quad mass gyroscope in the angular rate mode," *Micromachines*, vol. 12, no. 3, p. 266, 2021.

[88] D. Lynch, "Coriolis vibratory gyros," *Symposium Gyro Technology, Stuttgart, Germany, September*, pp. 21–23, 1998.

[89] D. D. Lynch, "Vibratory gyro analysis by the method of averaging," in *Proc. 2nd St. Petersburg Conf. on Gyroscopic Technology and Navigation, St. Petersburg*, pp. 26–34, 1995.

[90] C. Painter and A. Shkel, "Experimental evaluation of a control system for an absolute angle measuring micromachined gyroscope," in *SENSORS, 2005 IEEE*, pp. 4–pp, IEEE, 2005.

[91] A. A. Trusov, I. P. Prikhodko, S. A. Zotov, and A. M. Shkel, "Low-dissipation silicon tuning fork gyroscopes for rate and whole angle measurements," *IEEE Sensors Journal*, vol. 11, no. 11, pp. 2763–2770, 2011.

[92] J. Cho, J. Gregory, and K. Najafi, "Single-crystal-silicon vibratory cylindrical rate integrating gyroscope (CING)," in *2011 16th International Solid-State Sensors, Actuators and Microsystems Conference*, pp. 2813–2816, IEEE, 2011.

[93] J. Cho, J. Gregory, and K. Najafi, "High-q, 3khz single-crystal-silicon cylindrical rate-integrating gyro (CING)," in *2012 IEEE 25th International Conference on Micro Electro Mechanical Systems (MEMS)*, pp. 172–175, IEEE, 2012.

[94] J. Gregory, J. Cho, and K. Najafi, "Characterization and control of a high-Q MEMS inertial sensor using low-cost hardware," in *Proceedings of IEEE/ION PLANS 2012*, pp. 239–239, 2012.

[95] I. P. Prikhodko, S. A. Zotov, A. A. Trusov, and A. M. Shkel, "Foucault pendulum on a chip: Rate integrating silicon MEMS gyroscope," *Sensors and Actuators A: Physical*, vol. 177, pp. 67–78, 2012.

[96] J.-K. Woo, J. Y. Cho, C. Boyd, and K. Najafi, "Whole-angle-mode micromachined fused-silica birdbath resonator gyroscope (WA-BRG)," in *2014 IEEE 27th International Conference on Micro Electro Mechanical Systems (MEMS)*, pp. 20–23, IEEE, 2014.

[97] B. R. Johnson, C. Boynton, E. Cabuz, S. Chang, K. Christ, S. Moore, J. Reinke, and K. Winegar, "Toroidal resonators with small frequency mismatch for rate integrating gyroscopes," in *2014 international symposium on inertial sensors and systems (ISISS)*, pp. 1–4, IEEE, 2014.

[98] D. Senkal, S. Askari, M. Ahamed, E. Ng, V. Hong, Y. Yang, C. H. Ahn, T. Kenny, and A. Shkel, "100K Q-factor toroidal ring gyroscope implemented in wafer-level epitaxial silicon encapsulation process," in *2014 IEEE 27th International Conference on Micro Electro Mechanical Systems (MEMS)*, pp. 24–27, IEEE, 2014.

[99] A. Trusov, D. Rozelle, G. Atikyan, S. Zotov, B. Simon, A. Shkel, and A. Meyer, "Non-axisymmetric Coriolis vibratory gyroscope with whole angle, force rebalance, and self-calibration," in *Proceedings of the Technical Digest of IEEE Solid State Sensors, Actuators and Microsystems Workshop, Hilton Head Island, SC, USA*, pp. 8–12, 2014.

[100] P. Taheri-Tehrani, O. Izyumin, I. Izyumin, C. H. Ahn, E. J. Ng, V. A. Hong, Y. Yang, T. W. Kenny, B. E. Boser, and D. A. Horsley, "Disk resonator gyroscope with whole-angle mode operation," in *2015 IEEE International Symposium on Inertial Sensors and Systems (ISISS) Proceedings*, pp. 1–4, IEEE, 2015.

[101] D. Senkal, A. Efimovskaya, and A. M. Shkel, "Dual foucault pendulum gyroscope," in *2015 Transducers-2015 18th International Conference on Solid-State Sensors, Actuators and Microsystems (TRANSDUCERS)*, pp. 1219–1222, IEEE, 2015.

[102] D. Senkal, A. Efimovskaya, and A. M. Shkel, "Minimal realization of dynamically balanced lumped mass WA gyroscope: dual foucault pendulum," in *2015 IEEE International Symposium on Inertial Sensors and Systems (ISISS) Proceedings*, pp. 1–2, IEEE, 2015.

[103] S. Askari, M. H. Asadian, and A. M. Shkel, "High quality factor mems gyroscope with whole angle mode of operation," in *2018 IEEE International Symposium on Inertial Sensors and Systems (INERTIAL)*, pp. 1–4, IEEE, 2018.

[104] S. Nitzan, T.-H. Su, C. Ahn, E. Ng, V. Hong, Y. Yang, T. Kenny, and D. A. Horsley, "Impact of gyroscope operation above the critical bifurcation threshold on scale factor and bias instability," in *2014 IEEE 27th International Conference on Micro Electro Mechanical Systems (MEMS)*, pp. 749–752, 2014.

[105] K. F. Graff, *Wave motion in elastic solids*. Courier Corporation, 2012.

[106] J.-L. Auriault, "Body wave propagation in rotating elastic media," *Mechanics Research Communications*, vol. 31, no. 1, pp. 21–27, 2004.

[107] S. Sreenivasamurthy and V. Ramamurti, "Coriolis effect on the vibration of flat rotating low aspect ratio cantilever plates," *The Journal of Strain Analysis for Engineering Design*, vol. 16, no. 2, pp. 97–106, 1981.

[108] T. H. Young and G. T. Liou, "Coriolis Effect on the Vibration of a Cantilever Plate With Time-Varying Rotating Speed," *Journal of Vibration and Acoustics*, vol. 114, pp. 232–241, 04 1992.

[109] H. F. Bauer, "Vibration of a rotating uniform beam, part I: orientation in the axis of rotation," *Journal of Sound and Vibration*, vol. 72, no. 2, pp. 177–189, 1980.

[110] S. Hashemi and M. Richard, "Natural frequencies of rotating uniform beams with Coriolis effects," *Journal of vibration and acoustics*, vol. 123, no. 4, pp. 444–455, 2001.

[111] D. Guo, Z. Zheng, and F. Chu, "Vibration analysis of spinning cylindrical shells by finite element method," *International Journal of solids and structures*, vol. 39, no. 3, pp. 725–739, 2002.

[112] L. Hua and K. Lam, "Frequency characteristics of a thin rotating cylindrical shell using the generalized differential quadrature method," *International Journal of Mechanical Sciences*, vol. 40, no. 5, pp. 443–459, 1998.

[113] S. Sun, D. Cao, and S. Chu, "Free vibration analysis of thin rotating cylindrical shells using wave propagation approach," *Archive of Applied Mechanics*, vol. 83, no. 4, pp. 521–531, 2013.

[114] Y. Durukan, A. I. Lutovinov, A. N. Peregudov, E. S. Popkova, and M. M. Shevelko, "The characteristics of acoustic wave propagation in rotating solid-state media," in *2018 IEEE Conference of Russian Young Researchers in Electrical and Electronic Engineering (EIConRus)*, pp. 449–452, IEEE, 2018.

[115] Y. Durukan, M. Shevelko, A. Peregudov, E. Popkova, and S. Shevchenko, "The effect of a rotating medium on bulk acoustic wave polarization: From theoretical considerations to perspective angular motion sensor design," *Sensors*, vol. 20, no. 9, p. 2487, 2020.

[116] M. Shevelko, A. Lutovinov, A. Peregudov, E. Popkova, Y. Durukan, and S. Shevchenko, "The sensitive element of acoustic sensor on circular polarized waves: From theoretical considerations towards perspective rotation rate sensors design," *Sensors*, vol. 21, no. 1, p. 32, 2021.

[117] Y. Yu, B. Chen, J. Tao, X. Chen, H. Zhang, W. Pang, D. Zhang, and H. Luo, "A novel high sensitivity mems acoustic gyroscope by measuring phase shift," in *2015 IEEE SENSORS*, pp. 1–4, IEEE, 2015.

[118] Y. Yu, H. Luo, B. Chen, J. Tao, Z. Feng, H. Zhang, W. Guo, and D. Zhang, "Mems gyroscopes based on acoustic sagnac effect," *Micromachines*, vol. 8, no. 1, p. 2, 2017.

[119] A. Beskok and G. Karniadakis, *Microflows and Nanoflows: Fundamentals and Simulation. Interdisciplinary Applied Mathematics*. Springer, 2005.

[120] S. Datta, *Surface acoustic wave devices*. Prentice Hall, 1986.

[121] M. Kurosawa, Y. Fukuda, M. Takasaki, and T. Higuchi, "A surface acoustic wave gyro sensor," in *Solid State Sensors and Actuators, 1997. TRANSDUCERS'97 Chicago., 1997 International Conference on*, vol. 2, pp. 863–866, IEEE, 1997.

[122] K. Jose, W. Suh, P. Xavier, V. Varadan, and V. Varadan, "Surface acoustic wave MEMS gyroscope," *Wave motion*, vol. 36, no. 4, pp. 367–381, 2002.

[123] A. Mehta, K. Jose, and V. K. Varadan, "Numerical simulation of a surface acoustic wave (SAW) gyroscope using HP Eesof," in *SPIE's 9th Annual International Symposium on Smart Structures and Materials*, pp. 169–177, International Society for Optics and Photonics, 2002.

[124] Q. Yan, Y. Wei, M. Shen, J. Zhu, and Y. Li, "Theoretical and experimental study of surface acoustic wave gyroscopic effect," in *2007 International Conference on Mechatronics and Automation*, pp. 3812–3816, IEEE, 2007.

[125] H. Oh, S. Yang, and K. Lee, "Development of surface acoustic wave-based microgyroscope utilizing progressive wave," *Japanese Journal of Applied Physics*, vol. 49, no. 6S, p. 06GN16, 2010.

[126] W. Wang, J. Liu, X. Xie, M. Liu, and S. He, "Development of a new surface acoustic wave based gyroscope on a X-112 Y LiTaO3 substrate," *Sensors*, vol. 11, no. 11, pp. 10894–10906, 2011.

[127] H. Oh, S. S. Yang, and K. Lee, "Development of passive surface acoustic wave gyroscope with standing wave mode," in *Micro Electro Mechanical Systems (MEMS), 2011 IEEE 24th International Conference on*, pp. 565–568, IEEE, 2011.

[128] V. Varadan, W. Suh, P. Xavier, K. Jose, and V. Varadan, "Design and development of a MEMS-IDT gyroscope," *Smart Materials and Structures*, vol. 9, no. 6, p. 898, 2000.

[129] I. P. Prikhodko, S. A. Zotov, A. A. Trusov, and A. M. Shkel, "Sub-degree-per-hour silicon MEMS rate sensor with 1 million Q-factor," in *2011 16th International Solid-State Sensors, Actuators and Microsystems Conference*, pp. 2809–2812, IEEE, 2011.

[130] M. Zaman, A. Sharma, and F. Ayazi, "High performance matched-mode tuning fork gyroscope," in *19th IEEE International Conference on Micro Electro Mechanical Systems*, pp. 66–69, IEEE, 2006.

[131] H. Moussa and R. Bourquin, "Theory of direct frequency output vibrating gyroscopes," *IEEE sensors Journal*, vol. 6, no. 2, pp. 310–315, 2006.

[132] S. A. Zotov, A. A. Trusov, and A. M. Shkel, "High-range angular rate sensor based on mechanical frequency modulation," *Journal of Microelectromechanical Systems*, vol. 21, no. 2, pp. 398–405, 2012.

[133] D. Effa, E. Abdel-Rahman, and M. Yavuz, "Cantilever beam microgyroscope based on frequency modulation," in *2013 IEEE/ASME International Conference on Advanced Intelligent Mechatronics*, pp. 844–849, IEEE, 2013.

[134] B. Eminoglu, Y.-C. Yeh, I. I. Izyumin, I. Nacita, M. Wireman, A. Reinelt, and B. E. Boser, "Comparison of long-term stability of AM versus FM gyroscopes," in *2016 IEEE 29th International Conference on Micro Electro Mechanical Systems (MEMS)*, pp. 954–957, IEEE, 2016.

[135] A. A. Trusov, I. P. Prikhodko, S. A. Zotov, and A. M. Shkel, "Low-dissipation silicon tuning fork gyroscopes for rate and whole angle measurements," *IEEE Sensors Journal*, vol. 11, no. 11, pp. 2763–2770, 2011.

[136] F. Mohd-Yasin, D. Nagel, and C. Korman, "Noise in MEMS," *Measurement Science and Technology*, vol. 21, no. 1, p. 012001, 2009.

[137] T. B. Gabrielson, "Mechanical-thermal noise in micromachined acoustic and vibration sensors," *IEEE transactions on Electron Devices*, vol. 40, no. 5, pp. 903–909, 1993.

[138] V. Annovazzi-Lodi and S. Merlo, "Mechanical–thermal noise in micromachined gyros," *Microelectronics journal*, vol. 30, no. 12, pp. 1227–1230, 1999.

[139] X. Ding, J. Jia, Y. Gao, and H. Li, "Mechanical and electrical noise in sense channel of mems vibratory gyroscopes," *Sensors*, vol. 17, no. 10, p. 2306, 2017.

[140] J. J. Allen, *Micro electro mechanical system design*. CRC Press, 2005.

[141] R. P. Leland, "Mechanical-thermal noise in mems gyroscopes," *IEEE Sensors Journal*, vol. 5, no. 3, pp. 493–500, 2005.

[142] D. W. Allan, "Statistics of atomic frequency standards," *Proceedings of the IEEE*, vol. 54, no. 2, pp. 221–230, 1966.

[143] N. El-Sheimy, H. Hou, and X. Niu, "Analysis and modeling of inertial sensors using Allan variance," *IEEE Transactions on instrumentation and measurement*, vol. 57, no. 1, pp. 140–149, 2007.

[144] M. F. Zaman, A. Sharma, Z. Hao, and F. Ayazi, "A mode-matched silicon-yaw tuning-fork gyroscope with subdegree-per-hour Allan deviation bias instability," *Journal of Microelectromechanical systems*, vol. 17, no. 6, pp. 1526–1536, 2008.

[145] M. Vagner, P. Beneš, and Z. Havránek, "Experience with Allan variance method for mems gyroscope performance characterization," in *2012 IEEE International Instrumentation and Measurement Technology Conference Proceedings*, pp. 1343–1347, IEEE, 2012.

[146] V. Vukmirica, I. Trajkovski, and N. Asanovic, "Two methods for the determination of inertial sensor parameters," *Scientific Technical Review*, vol. 60, pp. 27–33, 2010.

[147] T. Caughey, "Random excitation of a system with bilinear hysteresis," *Journal of Applied Mechanics*, vol. 27, no. 4, pp. 649–652, 1960.

[148] S. V. Joubert, M. Y. Shatalov, and T. H. Fay, "On numerically solving an eigenvalue problem arising in a resonator gyroscope," *Applied Mathematics and Computation*, vol. 246, pp. 561–571, 2014.

[149] S. Sonmezoglu, *A HIGH PERFORMANCE AUTOMATIC MODE-MATCHED MEMS GYROSCOPE*. Master's thesis, Middle East Technical University, Ankara, Turkey, 2012.

[150] E. Armstrong, P. Christie, and T. Hunt, "Vibration in cylindrical shafts," in *Proceedings of the Institution of Mechanical Engineers, Conference Proceedings*, vol. 180, pp. 38–48, SAGE Publications Sage UK: London, England, 1965.

[151] H. Macke, "Traveling-wave vibration of gas-turbine engine shells," *Journal of Engineering for Power*, vol. 88, no. 2, pp. 179–187, 1966.

[152] E. Chatelet, F. D'ambrosio, and G. Jacquet-Richardet, "Toward global modelling approaches for dynamic analyses of rotating assemblies of turbomachines," *Journal of Sound and Vibration*, vol. 282, no. 1-2, pp. 163–178, 2005.

[153] M. Anklin, W. Drahm, and A. Rieder, "Coriolis mass flowmeters: Overview of the current state of the art and latest research," *Flow Measurement and Instrumentation*, vol. 17, no. 6, pp. 317–323, 2006.

[154] H. Abe, T. Yoshida, and K. Turuga, "Piezoelectric-ceramic cylinder vibratory gyroscope," *Japanese journal of applied physics*, vol. 31, no. 9S, p. 3061, 1992.

[155] J. Yang, H. Fang, and Q. Jiang, "A vibrating piezoelectric ceramic shell as a rotation sensor," *Smart Materials and Structures*, vol. 9, no. 4, p. 445, 2000.

[156] G. H. Bryan, "On the beats in the vibrations of a revolving cylinder or bell," in *Proceedings of the Cambridge Philosophical Society*, vol. 7, pp. 101–111, 1890.

[157] D. Johnson, "Free vibration of a rotating elastic body: the general theory and some examples of practical cases," *Aircraft Engineering and Aerospace Technology*, vol. 24, no. 8, pp. 234–236, 1952.

[158] A. Srinivasan and G. Lauterbach, "Traveling waves in rotating cylindrical shells," *Journal of Engineering for Industry*, vol. 93, no. 4, pp. 1229–1232, 1971.

[159] M. Endo, K. Hatamura, M. Sakata, and O. Taniguchi, "Flexural vibration of a thin rotating ring," *Journal of Sound and Vibration*, vol. 92, no. 2, pp. 261–272, 1984.

[160] K. SUZUKI, R. TAKAHASHI, and T. KOSAWADA, "Analysis of vibrations of rotating thin circular cylindrical shells," *JSME international journal. Ser. 3, Vibration, control engineering, engineering for industry*, vol. 34, no. 1, pp. 19–25, 1991.

[161] R. Firouz-Abadi, M. Torkaman-Asadi, and M. Rahmanian, "Whirling frequencies of thin spinning cylindrical shells surrounded by an elastic foundation," *Acta Mechanica*, vol. 224, no. 4, pp. 881–892, 2013.

[162] M. I. Friswell, J. E. Penny, S. D. Garvey, and A. W. Lees, *Dynamics of rotating machines*. Cambridge University Press, 2010.

[163] C.-H. Yang and S.-C. Huang, "Coupling vibrations in rotating shaft-disk-blades system," *Journal of Vibration and Acoustics*, vol. 129, no. 1, pp. 48–57, 2007.

[164] V. Bhadbhade, N. Jalili, and S. N. Mahmoodi, "A novel piezoelectrically actuated flexural/torsional vibrating beam gyroscope," *Journal of Sound and Vibration*, vol. 311, no. 3-5, pp. 1305–1324, 2008.

[165] C. Acar and A. M. Shkel, "Structural design and experimental characterization of torsional micromachined gyroscopes with non-resonant drive mode," *Journal of micromechanics and microengineering*, vol. 14, no. 1, p. 15, 2003.

[166] L. E. PENZES and H. Kraus, "Free vibration of prestressed cylindrical shells having arbitrary homogeneous boundary conditions.," *AIAA Journal*, vol. 10, no. 10, pp. 1309–1313, 1972.

[167] A. Zohar and J. Aboudi, "The free vibrations of a thin circular finite rotating cylinder," *International Journal of Mechanical Sciences*, vol. 15, no. 4, pp. 269–278, 1973.

[168] J. Padovan, "Natural frequencies of rotating prestressed cylinders," *Journal of Sound and Vibration*, vol. 31, no. 4, pp. 469–482, 1973.

[169] J. Padovan, "Traveling waves vibrations and buckling of rotating anisotropic shells of revolution by finite elements," *International Journal of Solids and Structures*, vol. 11, no. 12, pp. 1367–1380, 1975.

[170] R. Eley, C. Fox, and S. McWilliam, "Coriolis coupling effects on the vibration of rotating rings," *Journal of sound and vibration*, vol. 238, no. 3, pp. 459–480, 2000.

[171] D. Effa, E. Abdel-Rahman, and M. Yavuz, "Cantilever beam microgyroscope based on frequency modulation," in *2013 IEEE/ASME International Conference on Advanced Intelligent Mechatronics*, pp. 844–849, IEEE, 2013.

[172] B. Eminoglu, Y.-C. Yeh, I. I. Izyumin, I. Nacita, M. Wireman, A. Reinelt, and B. E. Boser, "Comparison of long-term stability of am versus fm gyroscopes," in *2016 IEEE 29th International Conference on Micro Electro Mechanical Systems (MEMS)*, pp. 954–957, IEEE, 2016.

[173] S. A. Zotov, A. A. Trusov, and A. M. Shkel, "High-range angular rate sensor based on mechanical frequency modulation," *Journal of Microelectromechanical Systems*, vol. 21, no. 2, pp. 398–405, 2012.

[174] H. Moussa and R. Bourquin, "Theory of direct frequency output vibrating gyroscopes," *IEEE sensors Journal*, vol. 6, no. 2, pp. 310–315, 2006.

[175] W.-H. Gau and A. Shabana, "Effect of finite rotation on the propagation of elastic waves in constrained mechanical systems," *Journal of Mechanical Design*, vol. 114, no. 3, pp. 384–393, 1992.

[176] W. Hsu and A. Shabana, "Finite element analysis of impact-induced transverse waves in rotating beams," *Journal of sound and vibration*, vol. 168, no. 2, pp. 355–369, 1993.

[177] R. W. Ogden and B. Singh, "The effect of rotation and initial stress on the propagation of waves in a transversely isotropic elastic solid," *Wave Motion*, vol. 51, no. 7, pp. 1108–1126, 2014.

[178] S. W. Lee, J. W. Rhim, S. W. Park, and S. S. Yang, "A micro rate gyroscope based on the saw gyroscopic effect," *Journal of Micromechanics and Microengineering*, vol. 17, no. 11, p. 2272, 2007.

[179] W. Wang, J. Liu, X. Xie, M. Liu, and S. He, "Development of a new surface acoustic wave based gyroscope on a X-112 Y LiTaO3 substrate," *Sensors*, vol. 11, no. 11, pp. 10894–10906, 2011.

[180] H. Oh, S. Yang, and K. Lee, "Development of surface acoustic wave-based microgyroscope utilizing progressive wave," *Japanese Journal of Applied Physics*, vol. 49, no. 6S, p. 06GN16, 2010.

[181] H. Wegert, L. M. Reindl, W. Ruile, and A. P. Mayer, "On the Coriolis effect in acoustic waveguides," *The Journal of the Acoustical Society of America*, vol. 131, no. 5, pp. 3794–3801, 2012.

[182] K. Sato, A. Ono, and Y. Tomikawa, "Finite element method simulation of double-ended tuning-fork quartz resonator for application to vibratory gyro-sensor," *Japanese journal of applied physics*, vol. 42, no. 5S, p. 3115, 2003.

[183] I. Mirsky, "Wave propagation in transversely isotropic circular cylinders part i: Theory," *The journal of the Acoustical Society of America*, vol. 37, no. 6, pp. 1016–1021, 1965.

[184] F. C. Eliot and G. Mott, "Elastic waves propagation in circular cylinders having hexagonal crystal symmetry," *The Journal of the Acoustical Society of America*, vol. 44, no. 2, pp. 423–430, 1968.

[185] H. McNiven and Y. Mengi, "Dispersion of waves in transversely isotropic rods," *The Journal of the Acoustical Society of America*, vol. 49, no. 1B, pp. 229–236, 1971.

[186] P. Kohnke, "Theory reference for the mechanical APDL and mechanical applications," *Ansys Inc, release*, vol. 12, 2009.

[187] G. Yaralioglu, F. Degertekin, M. Badi, B. Auld, and B. Khuri-Yakub, "Finite element method and normal mode modeling of capacitive micromachined SAW and Lamb wave transducers," in *2000 IEEE Ultrasonics Symposium. Proceedings. An International Symposium (Cat. No. 00CH37121)*, vol. 1, pp. 129–132, IEEE, 2000.

[188] A. Bozkurt, F. Degertekin, A. Atalar, and B. Khuri-Yakub, "Analytic modeling of loss and cross-coupling in capacitive micromachined ultrasonic transducers," in *1998 IEEE Ultrasonics Symposium. Proceedings (Cat. No. 98CH36102)*, vol. 2, pp. 1025–1028, IEEE, 1998.

[189] E. Moulin, J. Assaad, C. Delebarre, and D. Osmont, "Modeling of Lamb waves generated by integrated transducers in composite plates using a coupled finite element–normal modes expansion method," *The Journal of the Acoustical Society of America*, vol. 107, no. 1, pp. 87–94, 2000.

[190] H. Kolsky, *Stress waves in solids*, vol. 1098. Courier Corporation, 1963.

VITA

Hakan Cetin received the B.Sc. and M.Sc. degrees in electrical engineering from Özyeğin University, Istanbul, Turkey, in 2014 and 2016, respectively. He received the Ph.D. degree in electrical engineering from Özyeğin University, Istanbul, Turkey, in June, 2021. His research interest includes vibration, acoustics, acoustofluidics, MEMS sensors and inertial sensors.